

Potential of Multi-Winglet Systems to Improve Aircraft Performance

vorgelegt von
Diplom-Ingenieur
Martin Berens

von der Fakultät V - Verkehrs- und Maschinensysteme -
der Technischen Universität Berlin
zur Erlangung des akademischen Grades

Doktor der Ingenieurwissenschaften
- Dr.-Ing. -

genehmigte Dissertation

Promotionsausschuss:

Vorsitzender:	Prof. Dr.-Ing. W. Nitsche
Gutachter:	Prof. Dr.-Ing. J. Thorbeck
	Prof. Dr.-Ing. F. Thiele

Tag der wissenschaftlichen Aussprache:
28. März 2008

Berlin 2008
D 83

Preface

The work documented in this thesis was mainly performed during my job as an assistant lecturer in the Aircraft Design and Aerostructures Group at the Institute of Aeronautics and Astronautics at the Technical University Berlin.

I would like to express my gratitude to my supervisor, Prof. Dr.-Ing. Jürgen Thorbeck, for giving me the opportunity to freely work on the ideas that finally culminated in the present document. Also I would like to thank for his valuable advice which was not limited to technical matters and last but not least his patience.

Furthermore, I am grateful to Prof. Dr.-Ing. Frank Thiele, who did not hesitate to accept to become second examiner. I also appreciate that Prof. Dr.-Ing. Wolfgang Nitsche agreed to take the chair of the examination board, who succeeded in strengthening my personal interest in the field of aerodynamics in the years of my studies.

I would also like to thank Prof. Dr.-Ing. Karl Heinz Horstmann of the Institute of Aerodynamics and Flow Technology of DLR Braunschweig for the valuable advice on lifting line and vortex lattice methods. Thanks also to Prof. Dr.-Ing. Dietrich Hummel of the Institute of Fluid Mechanics of the Technical University of Braunschweig for recollecting details on the multi-winglet experiments conducted back in the 1970s including an excursion to the loft of the institute building to take some photos of the wind-tunnel model, which were helpful for designing of a CAD model of the configuration. The next person to thank is my colleague Johannes Hartmann for sketching the CATIA model. It is with regret in this context, that I had finally to curtail the project scope and abandon the attempt to analyse the multi-winglet configuration by means of RANS simulations.

Finally I am indebted to Michael Stache for the demonstration of experimental set-ups for the analysis of non-planar wing concepts, the willingness to share ideas and the experience gained in the course of many years of research on multi-winglet configurations at the Institute of Bionics and Evolutionstechnik of the Technical University Berlin.

I could extend the list of persons to whom I am grateful, but it would become too lengthy and it would be extremely difficult not to miss someone. Hence, I prefer to thank groups of persons, the secretariat staff for their patient advises on and practical help in administrative matters, the workshop staff who's assistance I merely requested for non-scientific efforts but who were enduringly interested in the finalisation of my thesis, of course, my direct colleagues and last but not least the students of the KATO team, who, due to their enthusiasm, took a lot of work off my hands and thus indirectly also contributed to the present work.

Furthermore I am indebted to Dipl.-Ing. August Kröger of Airbus Deutschland for his gentle but sustained pushing to bring the project finally to an end.

Last but not least I have to address my special thanks to my parents, my sister Monika and my brother Thomas for their continuing encouragement. Anke, the person who deserves my greatest gratitude coined the working title of the thesis and had to put up with a sometimes less than balanced private life, but also never lost confidence that the project will finally have a happy end.

Martin Berens

Hamburg, June 2008

Contents

ABSTRACT	V
ÜBERSICHT	VI
NOMENCLATURE	VII
1 INTRODUCTION	1
2 NON-PLANAR CONFIGURATIONS FOR LIFT PRODUCTION	4
2.1 Lift, Induced Drag and Related Phenomena	4
2.1.1 The Concept of the Lifting Line	4
2.1.2 Induced Drag of Non-Planar Lifting Systems	8
2.1.3 Classification of Non-planar Lifting Systems According to their Wake Shapes	15
2.1.4 Aircraft Wake Vortices and Associated Effects	22
2.1.5 Design and Off-Design Characteristics of Non-planar Lifting Systems	25
2.2 Further Aspects for the Design of Optimum Lifting Systems	26
2.2.1 Profile Drag	27
2.2.2 Effect of Wing Splitting on Profile Drag	28
2.2.3 Effect of Induced and Profile Drag on Aircraft Performance	30
2.2.4 Compressibility Effects	32
2.2.5 Wing Structure Mass	33
2.3 Multiwinglet Systems in Nature - Outer Primaries of Birds	34
2.3.1 Wing Morphology	35
2.3.2 Correlation of Wing Loading and Aspect Ratio with Fan-Out	39
2.3.3 Functions of Slotted Outer Primaries in Flight	40
2.4 Non-Planar Aircraft Wing Concepts	47
2.4.1 Technically Prevailing Winglet Systems	48
2.4.2 Attempts of Technical Adaptation of Multiwinglet Systems	53
2.5 Synopsis of Trends Affecting Planar and Non-Planar Wing Efficiencies	58
3 NUMERICAL MODEL	61
3.1 Aerodynamics	64
3.1.1 Vortex Lattice Method	64
3.1.2 Profile Drag Estimation	74
3.1.3 Interference Drag Estimation	82
3.1.4 Minimum and Maximum Section Lift Coefficients	84
3.1.5 Non-Linear Lift Effects	86
3.1.6 Cascade Effects	94
3.1.7 Aggregation of Integral Forces and Moments	108
3.2 Structures	109
3.2.1 Simplified Dimensioning of Wing Box	109

3.2.2	Aeroelastic Deformation of Wing	116
3.2.3	Structure Model Performance	119
3.3	VLM⁺⁺ - Suite for Multidisciplinary Analysis of Wing Configurations	122
3.3.1	Programme Modules	122
3.3.2	Numerical Optimisation Mode	123
3.3.3	Parametric Study Mode	124
4	VALIDATION OF NUMERICAL MODEL	125
4.1	Comparison with Multi-Winglet Low Speed Experimental Results	125
4.1.1	Adaptation of Section Characteristics to Reynolds Numbers	126
4.1.2	Comparison of Lift and Drag Characteristics	127
4.2	Comparison with Published Numerical Results	133
4.3	Planform Optimisation with Wing Mass Constraint and Comparison with Analytical Results	134
4.3.1	Wing Planform of Minimum Induced Drag with Wing Mass Constraint	134
4.3.2	Numerically Optimised Wing Planforms	137
4.3.3	Numerical Results	139
5	MULTI-WINGLET PARAMETRIC STUDIES AND OPTIMISATION	142
5.1	Introductory Note - Sensitivity of Results to Planform Parameter Definition	143
5.2	Sensitivity of Aerodynamic Performance to Parameter Changes	145
5.2.1	Variation of Reynolds Number	145
5.2.2	Variation of Camber	147
5.2.3	Variation of Winglet Number	150
5.2.4	Configuration Enhancements	153
5.3	Change of Optimum Slitting Ratio with Stepwise Refinement of Computational Model	158
5.3.1	Effect on Profile Drag, Wing Mass and Aircraft Performance Parameters	158
5.3.2	Incorporation of Refined Aerodynamic Models	173
5.3.3	Consideration of Aeroelastic Effects on Wing Sizing	177
5.3.4	Discussion of Effects Attributable to Sizing and Model Assumptions	181
5.4	Systematic Variation of Geometry Parameters	183
5.4.1	Wing and Winglets with Rectangular Planform	183
5.4.2	Parametric Optimisation of Planform Shape	193
5.4.3	Numerical Multi-Winglet Optimisation	196
6	CONCLUSION	199
	REFERENCES	207
	APPENDIX A : SYNOPSIS OF EXPERIMENTS WITH SPLIT-TIP AND MULTI-WINGLET CONFIGURATIONS DOCUMENTED IN THE OPEN LITERATURE	217
	APPENDIX B : INTERFERENCE DRAG MODEL	223

APPENDIX C : HYBRID METHOD TO ESTIMATE CHORDWISE PRESSURE DISTRIBUTIONS ON THE BASIS OF VLM RESULTS	233
APPENDIX D : EFFECT OF GAP ON THE MAXIMUM LIFT CAPABILITY OF WING-CANARD CONFIGURATIONS - COMPARISON OF COMPUTATIONAL RESULTS WITH EXPERIMENTAL DATA	245

Abstract

The potential of multi-winglet configurations to increase aircraft performance is the subject of the present thesis. Multi-winglet systems are well-known from the avian world. It has repeatedly been attempted to exploit the theoretically predicted potential for technical applications, which, however, was only successful in very few cases. The obvious discrepancy between the success of the multi-winglet configuration in nature as well as the theoretically large potential to reduce induced drag and to mitigate wake vortex intensities on the one hand and the modest results of technical implementations on the other form the motivation to look more closely at the characteristics of multi-winglet configurations.

A multidisciplinary analysis tool, termed VLM++, has been developed on the basis of an implementation of the 3D vortex lattice method. Apart from consideration of profile and interference drag, the method also considers effects that need to be regarded particularly in the case of multi-winglet configurations. The effect of mutual interference among the winglets on the individual surfaces maximum loadabilities is considered, producing values which normally differ from those of the basic airfoil sections. Another module permits to explicitly model the nonlinear lift characteristics on the basis of generalised lift polars.

A comparison of the numerical results with published low speed measurement data of multi-winglet configurations having symmetrical NACA 0015 airfoil sections proves that the extended analysis model correctly predicts the lift and drag behaviour even in the case of partly separated flow. The computational model correctly identifies the root sections of the foremost winglets as the locations where flow separations first occur when the angle of attack is increased. A parametric study going beyond the range of available measurement data shows that cambering the planar inner wing part reduces the aerodynamic loads on the critical winglet and hence extends the attached flow lift range with its comparably small drag figures. Also, the maximum lift coefficients are increased. These findings are expected to hold at least as far as the inner wing sections operate at supercritical Reynolds numbers. No other measure leads to a comparable improvement of multi-winglet efficiency.

An extended parametric study on the basis of a general aviation aircraft scenario was performed. In addition to aerodynamics, wing structure masses were computed by means of a simplified wing sizing approach. For performance computations, employment of an ideal propeller propulsion system was assumed. The results show that the multi-winglet configuration does not offer a significant improvement in payload-specific fuel consumption for range-optimal flight conditions as compared to the corresponding best planar wing with identical prescribed wing total surface area, span and takeoff mass. This is in contrast to flight conditions for maximum endurance where a clear advantage in terms of the aforementioned figure of merit for the multi-winglet configuration is predicted.

Übersicht

Gegenstand der vorliegenden Arbeit ist die Untersuchung des Potenzials von Multi-Winglet Konfigurationen zur Leistungssteigerung von Flugzeugen. Multi-Winglet Systeme sind aus der Vogelwelt bekannt. Die offensichtliche Diskrepanz zwischen dem Erfolg der Multi-Winglet Konfiguration in der Natur sowie dem theoretisch großen Potenzial zur Verringerung des induzierten Widerstands und der damit verbundenen Abschwächung der Intensität der Nachlaufwirbel auf der einen und den gleichzeitig mäßigen Ergebnissen bei technischen Umsetzungen auf der anderen Seite bilden die Motivation, die Besonderheiten der Konfiguration näher zu betrachten.

Hierzu wurde ein multidisziplinäres Analysetool VLM++ auf der Basis eines 3D Wirbelleiterverfahrens entwickelt, das über Erweiterungen zur Berechnung des Profil- und des Interferenzwiderstands hinaus besondere, bei Multi-Winglet Konfigurationen auftretende Effekte explizit berücksichtigt. Zum einen wird der Effekt verschiedener Anordnungen einzelner Winglets auf die jeweilige und in der Regel von den Profilwerten abweichende aerodynamische Belastbarkeit modelliert. Zum anderen erlaubt das Tool den nicht-linearen Auftriebsanstieg bei Erreichen des Grenzauftriebsbeiwerts eines Profilschnitts auf der Basis generalisierter aufgelöster Polaren zu berücksichtigen.

Ein Vergleich der numerischen Ergebnisse mit veröffentlichten Niedergeschwindigkeitsmessdaten für Multi-Winglet Konfigurationen mit symmetrischen NACA 0015 Profilen weist die korrekte Nachbildung des Auftriebs- und Widerstandsverhaltens mit dem erweiterten Simulationsmodell auch für den Fall teilweise abgelöster Strömung nach. Durch das Analysetool werden die Wurzelbereiche der vordersten Winglets als Stellen, an denen bei steigendem Anstellwinkel zuerst Ablösungen auftreten, richtig identifiziert. Eine über den Umfang der Messungen hinausgehende Parameterstudie zeigt, dass die Verwölbung des planaren Innenflügels am besten geeignet ist, diese Belastung zu verringern und damit den ablöse- und widerstandsarmen Auftriebsbereich deutlich zu vergrößern. Weiterhin werden die Maximalauftriebsbeiwerte erhöht. Dies gilt zumindest dann, wenn bei den Innenflügelprofilen überkritische Reynoldszahlen vorliegen. Keine andere Maßnahme führt zu ähnlich großen Leistungsverbesserungen.

Eine umfangreiche Parameterstudie wurde auf Basis eines für die Allgemeine Luftfahrt typischen Kleinflugzeugszenarios durchgeführt. Zusätzlich zur Analyse der aerodynamischen Eigenschaften wurden die Flügelstrukturmassen mittels eines vereinfachten Ansatzes für die Flügeldimensionierung berechnet. Für die Flugleistungsrechnungen wurde die Verwendung eines idealen Propellerantriebs vorausgesetzt. Die Ergebnisse zeigen, dass sich mit der Multi-Winglet Konfiguration keine signifikante Verbesserung des nutzlastspezifischen Kraftstoffverbrauchs bei reichweitenoptimalen Flugbedingungen im Vergleich zum besten planaren Flügel bei vorgeschriebener Gesamtflügelfläche, Spannweite und Abflugmasse erzielen lässt. Dagegen wird ein deutlicher Vorteil der Multi-Winglet Konfiguration hinsichtlich der genannten Gütegröße bei Flugbedingungen für maximale Flugdauer prognostiziert.

Nomenclature

Latin Symbols

Symbol	Unit/Scale	Description
A	-	multiplier, amplification factor
AR	-	wing aspect ratio
b	m	wing span
c	m	chord length
C_d	-	local drag coefficient, section drag coefficient
C_D	-	drag coefficient
C_F	-	chord based friction drag coefficient
C_l	-	local lift coefficient, section lift coefficient
C_L	-	lift coefficient
C_l'	rad^{-1}	$= dC_l / d\alpha$, section or local lift curve slope
$C_{l,i}$	-	section design lift coefficient
C_M	-	pitching moment coefficient
C_p	-	pressure coefficient
$\overline{C_p}$	-	canonical pressure coefficient
ΔC_p	-	pressure difference coefficient between upper and lower side of a lifting element
C_S	-	side force coefficient
D	N	drag force
D_f	m	fuselage diameter
E	N/m^2	Young's modulus of elasticity
e	-	Oswald efficiency factor
E_{kin}	Nm	kinetic energy
\vec{F}_{tot}	N	cut load vector
G	N/m^2	shear modulus
g_0	-	gravitational acceleration
h	m	height
H	m	altitude
I	m^3	moment of inertia
\vec{I}_c	m^{-1}	influence coefficient vector
L	N	lift force
LHV	J/kg	lower heating value
l_f	m	fuselage length

viii

m	kg	mass
m	-	maximum camber, height of mean line above chord line with respect to chord length
M	-	Mach number
M_b	Nm	bending moment
\bar{M}_{tot}	Nm	cut moment vector
n	-	number of elements, load factor
P	Nm/s	power
p	N/m ²	static pressure
p	-	chordwise relative position of maximum camber
p	N/m	tension flow
psfc	(kg s)/(N m)	power specific fuel consumption
\bar{Q}	m/s	total flow velocity vector
q	N/m ²	dynamic pressure
q	N/m	shear flow
\bar{q}	m/s	perturbation velocity
R	m	Range
\bar{R}	N	aerodynamic force vector
r	m	radius
\bar{r}	m	vortex filament vector, distance in space
Re_c	-	chord based Reynolds number
Re_x	-	Reynolds number based on length x
S	m ²	surface area
s	m	semi-span b/2
s	m	coordinate coinciding with vortex filament orientation
$d\bar{s}$	m	section of curved line with infinitesimal length
S'	m ²	area of stream tube analogon
S_{frc}	N	side force component
t	s	time
t	m	thickness of profile section
(t/c)	-	relative thickness of profile section
T	s	duration
T_{wb}	-	coefficient matrix for coordinate transformation from wind to body axes
w	m/s	downwash velocity
W	N	weight
x, y, z	m	Cartesian coordinates

Greek Symbols

Symbol	Unit/Scale	Description
α	rad, (deg)	geometrical angle of attack
β	rad, (deg)	effective angle of attack, sideslip angle
Γ	m ² /s	circulation
γ	rad, (deg)	flight path angle
$\gamma(\varphi)$	m/s	continuous chordwise circulation distribution
γ_{wake}	m/s	circulation strength of vortex sheet $d\Gamma / dy$
Υ	rad, (deg)	dihedral angle
δ	rad, (deg)	correction angle
δ	m	boundary layer thickness
ε	rad, (deg)	geometrical washout, twist angle
η	-	non-dimensional spanwise coordinate $2 \cdot y / b$, efficiency
η^*	-	non-dimensional curvilinear spanwise coordinate following trace of quarter chord line in plane perpendicular to the freestream
ι	rad, (deg)	incidence
ξ, η, ζ	-	non-dimensional coordinates, corresponding to x, y, z
μ	-	shape parameter
ν	m ² /s	kinematic viscosity
ρ	kg/m ³	density
σ	-	implicit boundary layer state parameter
σ	N/m ²	tensile stress
τ	-	span efficiency: induced drag of planar elliptically loaded wing divided by induced drag of actual configuration
φ	rad, (deg)	radial coordinate
Φ	m ² /s	velocity potential

Subscripts

Symbol	Description
\perp	perpendicular
\parallel	parallel
∞, inf	freestream
0	zero, reference
25	quarter chord
2D	two-dimensional
3D	three-dimensional
90	at $\alpha = 90$ degs
b	body, body axes, bending
bas	basic
box	wing box
c	with respect to chord
const	constant
crit	critical
det	deterioration
dih	due to dihedral
ell	elliptical
f	friction
fp	flat plate
fs	front spar
i	induced, index
int	interference
l	local, lower, leading
la	laminar
ldp	lift-dependent profile
le	leading edge
lin	linear
m	mean
main	main wing (centre wing part to which winglets are attached)
max	maximum
min	minimum
minmax	applicable to minimum as well as maximum condition
ml	mean line
n	normal

p	pressure, profile
pan	skin panels
pd	pressure drag
pen	penalty
pln	planar
prim	primary
prof	profile
pst	post-stall
r	root
ref	reference
rs	rear spar
scale	due to scale effects
sec	secondary
sep	separated flow
sc	shear centre
sv	super velocity
sym	symmetry
t	transition, tip, tangential, trailing
te	trailing edge
Tip Ext.	wing tip extension
to	take-off
Trefftz	in Trefftz plane
ts	trailing surfaces
tu	turbulent
u	upper
w	wind axes, wing
wb	wing box
wet	wetted
wl	winglet
wmwl	wing-multiwinglet
ww	wing-wall

Abbreviations

Acronym	Description
BL	Boundary Layer
COC	Cash Operating Costs
DOC	Direct Operating Costs
ICAO	International Civil Aviation Organization
IFR	Instrument Flight Rules
IMC	Instrument Meteorological Conditions
ISA	International Standard Atmosphere
RANS	Reynolds-Averaged Navier-Stokes Equations
RMS	Root Mean Square
SL	Sea Level
VLM	Vortex Lattice Method

1 Introduction

Early theoretical studies already showed that it is possible to reduce induced drag by wing end plates or winglets. Wings utilising such additional surfaces are often referred to as non-planar configurations because the wing tip devices protrude out of the plane of the main lift producing surface. Multi-winglet systems known from the avian world also reduce induced drag. Multi-winglet systems have been technically replicated and practically tested, at times with success.

Up to today, many transport and general aviation aircraft as well as sailplanes have winglets attached to each end of the wing extending more or less upwards in the direction of the lift. This practical success is not only because of the satisfactory performance regarding the reduction of induced drag, but also the fact that the integration into transonic wing designs obviously did not constitute an insurmountable impediment. Aircraft operating in the transonic Mach number range that can be alternatively equipped with winglets have shown specific range improvements of up to 5% compared to versions with conventional wing-tips.

However, there are some potential advantages of equipping aircraft with multi-winglet cascades instead of single-winglet systems such as

- greater surface fraction contributing to the wing lift
- lower wing structural mass, because of smaller wing root bending moments
- greater mitigation of wing tip vortex system core circulation.

There are also potential disadvantages such as

- difficulties in obtaining designs with low interference drag, especially in the transonic Mach number range
- problems associated with low Reynolds numbers at individual winglet surfaces
- need for actuation of winglet incidences requiring a complex additional aircraft system affecting system's total reliability and increasing aircraft mass
- aero-elastic problems.

Considering the potential advantages and disadvantages of multi-winglets, the question can be asked as to whether the single winglet is in fact always the most advantageous solution or could a multi-winglet configuration perhaps perform better.

While this comparison is a worthwhile assignment, it must be realised that only little knowledge is available on the characteristics of multi-winglet configurations with respect to the pros and cons listed above. Hence, the scope of the present work is limited to identifying principal performance effects due to multi-winglet wing tip devices with a

particular emphasis on aircraft application, which is in itself a voluminous task if tackled on an advanced conceptual design level.

A particular difficulty that excludes the direct inference of overall performance implications from observations in the avian world is the fact that nature attempts to satisfy a multitude of additional requirements compared to aircraft designs following Cayley's paradigm such as

- thrust production during the flapping cycle
- requirement to fold the wing away
- requirement of redundancy in case of loss of an outer primary feather
- damage tolerance, e. g. ability to continue flying after wing tip collision with obstacles.

An experimental approach naturally limits the degree of freedom because of difficulties to design and build test models that are arbitrarily configurable. Furthermore, it seems questionable to arrive at a satisfactory multi-winglet design while pursuing a tentative design approach with only limited theoretical understanding of the physical effects involved. For these reasons, a theoretical study is preferable.

Methods, on the one hand, must allow the representation of principal physical effects, but on the other hand, must offer a good efficiency regarding turn around times in order to allow parametric studies and optimisations to be performed, especially in view of limited computer capacity. The state of computer performance had improved so much by the 1970s that methods based on potential theory were established as standard tools in aerodynamic analysis and design. Since vortex-lattice and panel methods cover only a limited range of physical effects, research progressed quickly to more advanced schemes, which are characterised by flow field discretisation. The schemes to solve the Navier-Stokes equations are well known. This process has been accelerated by obvious shortcomings in the older tools.

However, in order to avoid computationally costly generic techniques, methods based on potential theory are still widely used in configurational aerodynamics. The least complex approach for three-dimensional aerodynamic analysis of non-planar wing configurations is the vortex-lattice method (VLM). The computations within the scope of the present thesis will be based on an implementation of this method. The quality of results can be enhanced by applying suitable corrections for the physical effects not taken into account explicitly. Suitable corrections deserve particular attention since the performance of multi-winglet systems has always been significantly over-predicted by methods based on potential theory compared to experiments. The basic VLM will be extended to account for additional physical effects by means of the following models for

- profile drag
- interference drag

- cascade effects, i.e. mutual interference between elements that increase or decrease their aerodynamic loadability
- nonlinear effects at maximum lift

In addition to the aerodynamic effects mentioned above, the wing structural mass as well as static aeroelastic effects will be also considered in order to set-up a comprehensive multidisciplinary wing analysis tool.

Distinguishing of individual effects allows to study how the configuration optima shift depending on the fidelity of the model, i.e. the number of effects actually included. An advantage of using "classic" potential based schemes for aerodynamic analysis is, in this respect, the implicit differentiation of individual effects. Since VLM belongs to the same family of methods that emanated from the well-known lifting-line approach, solutions of the latter lend themselves for validation of the tool. Moreover, they can be taken as reliable starting points for shape optimisations of the winglet cascades by means of parametric studies or numerical optimisation.

Chapter 2 provides an overview on the current state of knowledge regarding non-planar lifting systems. The idea to use wing tip cascades originates from the avian world. This introductory chapter must therefore go beyond the scope of engineering sciences and will incorporate research facts from biologists' and ornithologists' points of view. The chapter also presents a review on technical realisations of non-planar lifting systems with emphasis laid on attempts to adapt multi-winglet concepts to natural examples. The chapter will present a review on different approaches to compute and optimise lifting systems with respect to induced drag.

Chapter 3 documents the implemented numerical tools used in the scope of the present work as well as specific enhancements. The programming of a vortex lattice method as a core element and of accessory models for profile drag, interference drag, cascade effects, non-linear lift effects and structural sizing as well as their incorporation into a comprehensive programme suite will be discussed.

Chapter 4 presents selected comparisons of the present method with analytical solutions, experimental data and selected numerical results documented in the literature for the sake of tool validation. The chapter places particular emphasis on multidisciplinary test cases.

Chapter 5 is dedicated to parametric studies and shape optimisation of multi-winglet configurations. Basic trends regarding non-planar configurations with respect to the disciplines covered by the programme suite are identified and discussed.

Chapter 6 provides a summary of the thesis and the conclusions drawn intended to provide assistance for multi-winglet configuration design as well as an outlook for future work.

2 Non-Planar Configurations for Lift Production

2.1 Lift, Induced Drag and Related Phenomena

2.1.1 The Concept of the Lifting Line

The first widely acknowledged successful method to predict the induced drag of finite wings was the lifting line theory of Prandtl [1]. Outlines of the theory can be found in virtually all textbooks that consider fundamentals of aerodynamic theory ([2], [3], [4], [6]). Prandtl's lifting line theory models the wing as a concentrated, lift generating vortex filament. Since the vortex is rigidly connected to the airframe it is commonly referred to as the bound vortex. In order to obey a vortex theorem of Helmholtz, which states that a vortex can neither start nor end in an unbounded fluid, it was necessary for the vortex systems to be closed by modelling trailing vortices and a starting vortex. The particular novelty of the lifting line concept was that the strength of the vortex, which is usually expressed by the mathematical term circulation, is allowed to vary in the spanwise direction. As a consequence, the two discrete trailing vortex filaments tried before had to be transformed into a continuous trailing vortex sheet (Fig. 1).

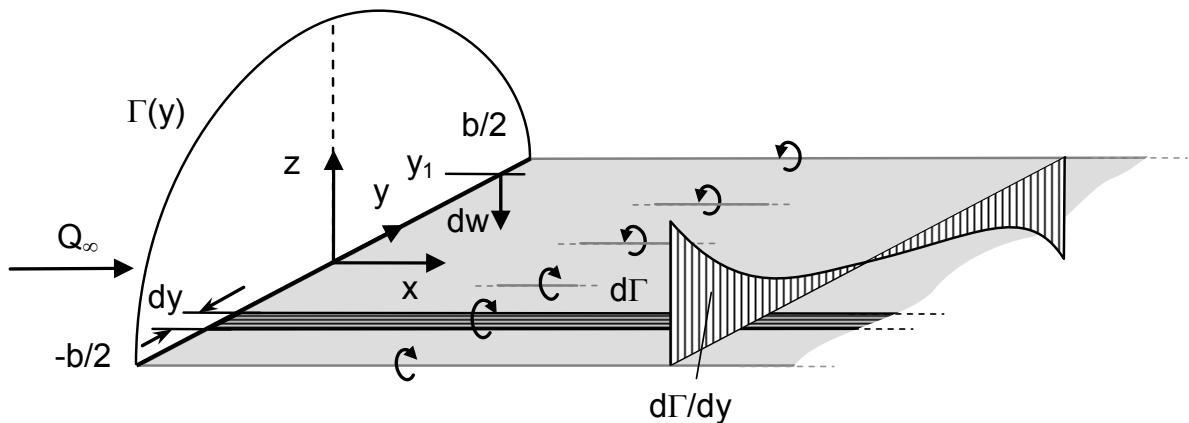


Fig. 1: Induced downwash at lifting line.

For a specified spanwise circulation distribution $\Gamma(y)$, the local strength of the vortex sheet equates to the local variation of bound circulation $\gamma_{\text{wake}} = d\Gamma/dy$. Each infinitesimal element of the vortex sheet induces velocities at all points in the flow according to the Biot-Savart law. However, only the induced velocities at the bound

vortex are required to assess the aerodynamic properties of the wing. A strip of vorticity of width dy induces an incremental velocity

$$dw(y_1) = -\frac{1}{4\pi} \frac{d\Gamma}{dy} \frac{1}{y - y_1} dy$$

at the point y_1 on the lifting line (Fig. 1). Spanwise integration yields the total induced velocity $w(y_1)$ at that point.

Another important effect directly connected to the downwash at the lifting line is the reduction of the lift curve slope. The greater the downwash angle, the lesser the effective angle of attack and the lesser the gradient of the wing lift coefficient with respect to angle of attack.

For a rigorous treatment, the Kutta-Joukowski theorem should also be applied to the wake vortices which are located in a field of downwash that is jointly induced by the bound vortex and by the vortex sheet itself. As a consequence, the wake vortex sheet is not force free, which cannot be physically justified. The physical solution to this theoretical problem is the free convection of the wake vortex sheet so that it becomes a stream surface. Wake roll-up starting from the wing tip region is the most distinct phenomenon in this respect. The justification for the assumption of a rigid wake was based on the observation that roll-up is initially confined to the wake close to the tip and that the process is slow enough to leave the greater part of the wake vortex sheet virtually planar. Another fact supporting the use of a rigid wake model is that the wake vortices closely behind the wing have the greatest influence on the downwash at the lifting line according to the Biot-Savart law. It is worth to mention that computer adaptations of the lifting line theory made it possible to simulate the wake roll-up iteratively. So doing, the physical reality is approached more closely. However, differences between the aerodynamic performance computed with wake roll-up and rigid wake models are normally small.

Some criticism of the lifting line concept is advised in order to prevent misinterpretations that occasionally appear in publications. According to the lifting line concept, the downwash at the lifting line results from the velocities induced by the trailing vortices. This concept is based on the Biot-Savart law and produces mathematically correct and also useful solutions to engineering problems. Nevertheless, the physics of the vortex sheet are not properly modelled. At the end of the day, the concept of the velocity induction by trailing vorticity has to be recognised as a mathematical trick rather than a representation of real physics, though a very powerful and also a very successful one. There are frequently some misunderstandings regarding the Biot-Savart law and its application for trailing vortex sheet induction with the immediate consequence that it appears that too much physical meaning is laid on the behaviour of the vortex sheet and particularly its retroaction onto the wing.

Physically speaking there is only one means to cause a velocity perturbation in a flow - a pressure difference. This fact is readily modelled by the Euler equation. Simplified for steady and inviscid flow in the absence of body forces this momentum equation becomes in differential form

$$\rho (\vec{Q} \circ \nabla \vec{Q}) = -\nabla p \quad (1)$$

which holds for compressible as well as incompressible flows. For constant density it directly states that a spatial change in velocity must correspond to a spatial change in pressure.

In three dimensional space, the velocity vector has three components and together with the pressure there are four unknowns. Equation (1) can be expanded to yield three equations for each direction in space and the systems of equations can be solved using the continuity equation

$$\nabla \circ \rho \vec{Q} = 0 \quad (2)$$

as a fourth equation. However, this is difficult from a practical point of view because the pressure does not appear explicitly in the continuity equation and, except for special cases, solution of the Euler equations can only be achieved numerically. For irrotational flow, useful results for a magnitude of engineering applications can be found by utilising the Laplace equation.

The incompressible form of the continuity equation (2) is

$$\nabla \vec{Q} = 0 \quad (3)$$

For irrotational flow a velocity potential can be defined such that

$$\vec{Q} = \nabla \Phi \quad (4)$$

and inserting into eq. (4) yields the Laplace equation

$$\nabla^2 \Phi = 0 \quad (5)$$

The important advantages of the Laplace equation are that there is only one equation to be solved instead of four and that it is a linear equation regarding the argument. For an irrotational, inviscid, incompressible flow, it now appears that the velocity field can be obtained from a solution of Laplace's equation for the velocity potential. The pressure can then be found from the well known Bernoulli equation. This equation can be derived from the Euler equation and hence it can also be seen as a special form of the momentum equation. The following simplified form for irrotational flow will be sufficient to demonstrate the principle

$$p + \frac{1}{2}\rho Q^2 = \text{const} \quad (6)$$

where the total velocity $Q = (U^2 + V^2 + W^2)^{1/2}$ and the constant has the same value throughout the flow while it is usually set to $p_\infty + 1/2\rho Q_\infty^2$.

It is the lack of direct pressure modelling that can lead to some confusion in the course of analysing induced angle of attack or induced drag by means of methods based on potential theory. Rather than induction by trailing vortices it is primarily the actual three-dimensional pressure distribution around the wing that causes downwash velocities at the locus of the wing. The discussion on how to properly model the wake vortex sheet for wing analysis by means of potential theory appears to be pushed too hard in the light of the real physical relations of cause and effect.

Returning to the lifting line model, distinct results and related boundary conditions deserve attention. Although Prandtl sought a method that makes it possible to analyse the aerodynamic properties of a given wing on the one hand and to solve the design task on the other where an arbitrary lift distribution is prescribed and geometrical properties of the wing are inferred, the first successful solutions were obtained for particular lift distributions of the type $(1-\eta^2)^{n/2}$, where η is the non-dimensional spanwise coordinate $2y/b$ and n is a positive integer. With n set to 1, the equation describes an ellipse. The particular advantage of the elliptical circulation distribution is that it produces finite induced downwash velocities at the wing tips. Moreover, the downwash becomes constant along the lifting line. It was first proved by Munk [7] that a constant downwash is both a necessary and a sufficient condition for minimum induced drag of a wing for given fixed values of lift and span.

Trefftz and later Glauert approximated arbitrary circulation distributions with Fourier series, which are in principle harmonics of the elliptical distribution. For wing aspect ratios exceeding 4, the larger parts of the flow conditions around the wing are virtually two dimensional with the exception of the tip region. If the profile section lift curve slopes, the planform geometry and the local incidences are known at a finite number of spanwise stations, the circulation distribution can now be numerically computed by solving a set of simultaneous linear equations (compare e.g. [6]). The resulting load distribution at large deviates from the elliptical optimum for rectangular or straight tapered planform shapes, to mention but a few. A parameter that relates the actual induced drag to that of an ideal elliptically loaded wing of the same lift and span is the span efficiency $\tau = D_i/D_{i,ell}$. The maximum span efficiency in the limit of the theory discussed so far is 1.0.

2.1.2 Induced Drag of Non-Planar Lifting Systems

The mutual interference of wings was studied shortly after the problem of lift and induced drag generation of single wings was solved by means of the lifting line theory. Munk [7] showed that the induced drag of arbitrary planar and non-planar systems of two or more lifting elements is independent of their individual positions in longitudinal direction as long as their circulations remain unchanged. Considering the induced velocity field in a control plane that is normal to the free stream direction and letting the system of lift producing wings pass through that plane, it will be observed that both the wake and the bound vortices induce velocities at points lying in the plane. However, the influence of the bound vortices diminishes quickly with increasing distance of the lifting system, so that only the induction by the wake vortex sheet remains. The principle of energy conservation applied to the idealized planar wake vortex sheets now requires a unique result irrespective of the actual "near field" arrangement of lifting surfaces that created the vortex sheets. For the induced velocities are independent of the longitudinal arrangement of lifting surfaces, the same must be true for the induced drag.

Of course, the magnitude of the mutually induced velocities at the lifting lines does change with increasing stagger so that the incidences need to be adapted in order to meet the requirement of constant circulations. The individual contribution to induced drag also changes, but the total induced drag does not. The front surface in a tandem arrangement of two longitudinally staggered wings of equal span that produce lift in the same direction experiences downwash velocities induced by the wakes of both wings but also an upwash velocity due to the circulation of the rear wing. Superposition of the contributions yields reduced induced drag on the leading wing. Contrarily, induced drag at the trailing wing is increased above the value that would be expected if it operated as a single surface in an unbounded flow.

A handbook method was derived [8] that made it possible to assess the lift and induced drag properties of two-surface configurations, e. g. conventional wing and horizontal tail, biplane, canard and tandem configurations. A remarkable effect represented by the method is that a biplane produces considerably less induced drag for a given lift than that what would be produced by a single wing of the same span. This result directly leads to the concept of induced drag reduction by means of multiple and vertically separated winglets. In order to produce a given lift force, a wing or a system of wings must impart a definite vertical momentum increase to the airstream and, the kinetic energy of the wake motion must come from the thrust work done by the wing or wings in overcoming the induced drag. For a given momentum change, i. e. a given lift, the wake kinetic energy will decrease if the additional velocity imparted to the flow is decreased but the mass of affected air is increased. This is exactly achieved with a biplane configuration. It can be generalized that the vertical spreading of the wake vorticity

reduces the total kinetic-energy content of a unit length of the vortex wake and hence also reduces induced drag.

Munk [7] also identified the condition for minimum induced drag of configurations where elements of the lifting line are not positioned perpendicular to the overall lift direction. The concept as outlined by Prandtl [9] (see also Kroo [10]) is based on the idea that the induced drag is only a minimum if any alteration of the circulation distribution does not produce smaller induced drag values. Two small circulation increments $\delta\Gamma_1$ and $\delta\Gamma_2$ at different locations are considered. In order to maintain constant lift it is required that

$$\cos \Upsilon_1 \delta\Gamma_1 + \cos \Upsilon_2 \delta\Gamma_2 = 0 \quad (7)$$

where Υ is the dihedral angle of the wake measured from a line that is perpendicular to the lift and the freestream directions (refer to Fig. 2).

The perturbation circulations produce the following induced drag increment if the analysis is confined to first-order effects

$$\delta D = w_{1,n} \delta\Gamma_1 + w_{2,n} \delta\Gamma_2 \quad (8)$$

where w_n are the "normalwash" velocities induced by the trailing vorticity perpendicular to the local slope of the lifting line.

Requiring that $\delta D = 0$ and combining equations (7) and (8) yields the condition

$$\cos \Upsilon_1 w_{1,n} = -\cos \Upsilon_2 w_{2,n}$$

or equivalently with reference to Fig. 2

$$w_n = w_0 \cdot \cos \Upsilon \quad (9)$$

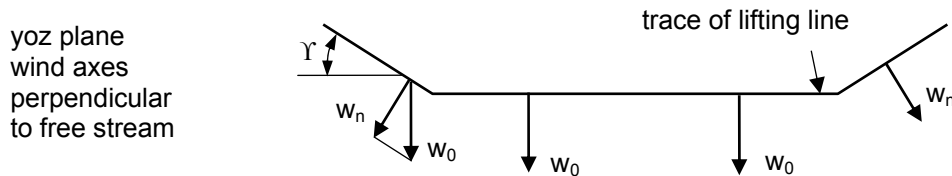


Fig. 2: Optimum downwash of a non-planar lifting configuration.

Equation (9) stipulates zero sidewash velocity for vertical endplates or winglets. Thus the sidewash induced by the loading of the endplates or winglets should just cancel the sidewash induced by the wing for minimum induced drag (refer also to [11]).

It has to be mentioned at this point that the implications of Munk's stagger theorem only apply in idealized potential flow in connection with rigid wake vortex sheets. The span of the horizontal tail of a conventional aircraft configuration is always much smaller than that of the wing and the roll up of the vortex sheets from the wing tips has only little effect on the flow conditions at the tail. The error associated with neglecting roll-up is thus small. A different situation is encountered for a tandem wing, for example. The roll-up of the tip vortices of the leading wing can significantly modify the flow conditions at the trailing wing. The real force-free wake also descends with the consequence that the induced velocities at a trailing wing are in fact a function of the longitudinal distance to the leading wing, which is a difference to Munk's idealised concept. It can be put on record that the Prandtl-Munk theory can be very useful for quick approximations but the limits of the theory need always to be kept in mind.

An intriguing approach that allows the direct comparison of non-planar and planar wing configurations was brought forward by Munk [7]. Prandtl [9] discussed the concept and added illustrative examples, i.e. the comparison of ideally loaded planar, biplane, triplane and boxwing configurations that are constrained to fit into a box of specified span b and height h . The drag can be expressed as

$$D_i = \frac{L^2}{4qS'} \quad (10)$$

where S' is a surface area that only depends on the shape of the projection of the lifting system into a plane perpendicular to the freestream (Trefftz plane). According to Munk, a 2-dimensional potential flow can be found that serves as an analogon for assessing induced drag properties of arbitrary configurations. The idea is directly inferred from Munk's theorem that a lifting system with minimum induced drag must produce a distinct downwash distribution. Again, only the wake properties are of concern. The analogon basically consists of the Trefftz plane with the wake replaced by a two dimensional vortex distribution along the lines where the wake intersects with the plane. A parallel potential flow with velocity w_1 is added so that the effective induced velocities at the projections of the lifting lines come to a halt. The latter condition is only obtained for ideally loaded lifting systems that produce constant downwash velocities as discussed above. Given the optimum lift distribution of the actual wing, the traces of the lifting surfaces now resemble impermeable lines with the resulting potential flow passing around (compare illustration in Fig. 3). The surface S' can be computed as the sum of the velocity potential differences of the individual infinitesimal trace segments integrated over the spanwise coordinate and divided by w_1 . Velocity potential differences between lower and upper side are alternativley expressed by the local circulation.

$$S' = \frac{1}{w_1} \sum \int \Gamma(y) dy$$

The reason for mentioning the analogon is that it allows a simple and illustrative physical interpretation of how the shape of the lifting system influences induced drag. The surface S' can be interpreted as the cross section of a stream tube or that of a pipe. The flow velocity is Q_∞ . The stream tube or the pipe is bend downward so that a vertical velocity w_1 is imposed that is equal to the velocity of the superimposed parallel potential flow discussed above (which in turn equals the downwash velocity far behind the actual wing). Kinetic energy is added because the absolute velocity of the stream tube is increased to $\sqrt{Q_\infty^2 + w_1^2}$ far behind the wing or bend for the pipe flow example. The vertical component of the force that is required to change the flow direction of the streamtube equals the lift and the horizontal component equals the induced drag. This reduces the complexity to the basic momentum relation.

The lift of the whole system is

$$L = w_1 \rho S' Q_\infty$$

Because S' is located in the denominator of equation (10), the induced drag will be minimized by maximizing this quantity. For a given Lift L , the induced downwash velocity w_1 must be reduced accordingly.

S' depends only on the shape of the lifting system traces in the Trefftz plane. Thus, the problem of minimizing induced drag can be tackled by searching for shapes that maximize S' . Fig. 3 shows four optimally loaded configurations of equal span b and the associated surface areas S' reproduced from reference [9] that all fit into a box with an aspect ratio of $h/b = 0.25$. The span efficiency is directly related to S' by

$$\tau = \frac{4S'}{\pi b^2}$$

The most significant difference in span efficiency occurs at transition from the monoplane to the biplane. Adding a third surface yields only little improvements. The best configuration is the boxwing forming a closed line following the outer contour of the prescribed box in the two-dimensional flow. It is worth mentioning that the velocities (and the velocity potentials) inside the box are zero with respect to the box reference frame. The difference to the triplane is again modest. As already stated by Prandtl, the front view of a system of lifting surfaces governs its characteristics with respect to induced drag production. Löbert [12] evaluated performance features of split tip configurations by parametrically varying the location where the main wing was split into two tip surfaces, keeping the overall span and height of the configuration constant. Löbert found that the position of the split had only little impact on the inviscid performance of the configurations, which is fully in accordance with the above statement. Principally, the larger the areas of retarded fluid in the equivalent two-

dimensional flow model, the less the induced drag. Keeping this principle in mind, the interpretation of various configurations to be discussed in the following sections is significantly eased.

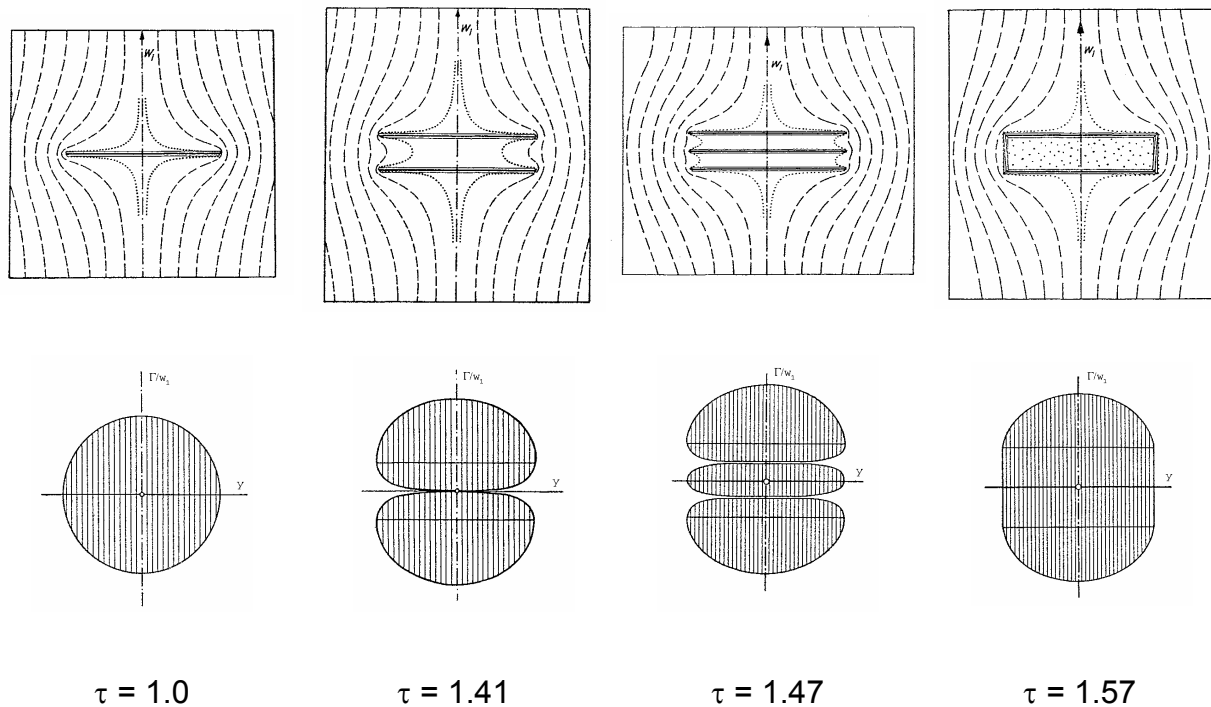


Fig. 3: Streamlines of mono-, bi- and tri-planes as well as box wing (the latter three having height to semispan ratios $h/b = 0.25$). Surfaces S' shown below and associated span efficiencies τ indicated at the bottom (reproduced from [9]).

Cone [13] studied properties of finite wings by means of conformal transformation as well as by means of an intriguing experimental approach based on an electrical potential flow analogue technique. He studied the induced drag properties of various non-planar configurations including winglet, multi-winglet, wing tip loop and box wings.

Concepts also included spanwise cambered wings. Spanwise camber is of relevance in the current context because the outer primaries of soaring birds often bend upwards under aerodynamic loads. A remarkable result of Cone in this respect was that semiellipse arc configurations performed much better than circular arc forms regarding span efficiency τ (refer to Fig. 4).

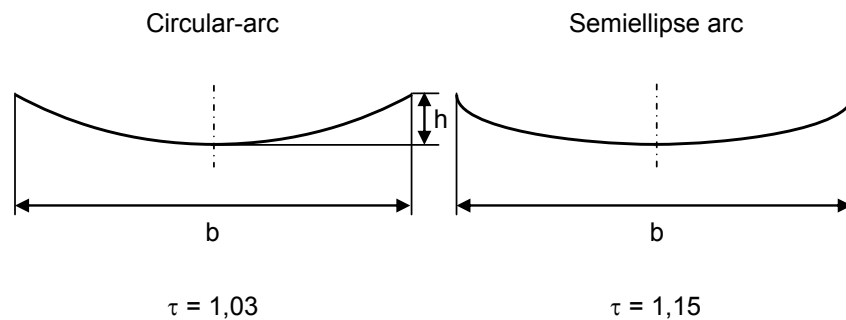


Fig. 4: Span efficiencies of circular and semiellipse arcs with $h/s = 0.25$ [13].

Evaluation by means of the analogy of wings with end plates, vertical fins, curved, spiroid, and branched tips showed that all non-planar configurations had span efficiencies - the figure of merit in the current context - greater than an elliptically loaded wing having the same span (Fig. 5). Due to the experimental determination by means of the electrical analogon, configurations were always unconditionally optimally loaded. Comparison of the various configurations reveals that relatively small deviations in geometry can result in significant differences regarding span efficiencies. Numbers 1 through 4 show the geometries of branched wing tip configurations. Two effects can be seen. First observation is, the greater the vertical extent of the configuration, the greater the span efficiency. Second, if a rectangle of width b and height h is constructed that tightly fit around configuration 2 and 3 it is found that the winglet tips of configuration 3 extend to the boundaries of the enclosing box whereas the corresponding winglet tips of configuration 2, when connected, describe a rounded envelope. This little geometrical difference accounts for the span efficiency of configuration 3 to be 6.3% larger than that of configuration 2. Configuration 6 shows a tip loop concept that evolved as the outer enclosing contour of configuration 4. All inner winglets 2 through 5 are eliminated but a curved sideward boundary has been added. The span efficiency increases slightly by 1.7%. The span efficiency of the blended winglet configuration 5 is somewhat smaller than that of the branched configuration 2 and that of configuration 14, all three having the same height. Nevertheless, τ is significantly smaller than the best branched configuration 3. Although height being much smaller, the winglet at right angle to the main wing (configuration 7) attains almost the same value for the figure of merit as the blended winglet configuration. Performance decays if the winglets are attached further inboard. Obviously, the inability to fill the corners of the enclosing rectangle impairs the magnitude of the figure of merit, which, as discussed above is directly proportional to the surface S' . This effect can also be observed by comparison of configurations 9 through 11 having equal heights.

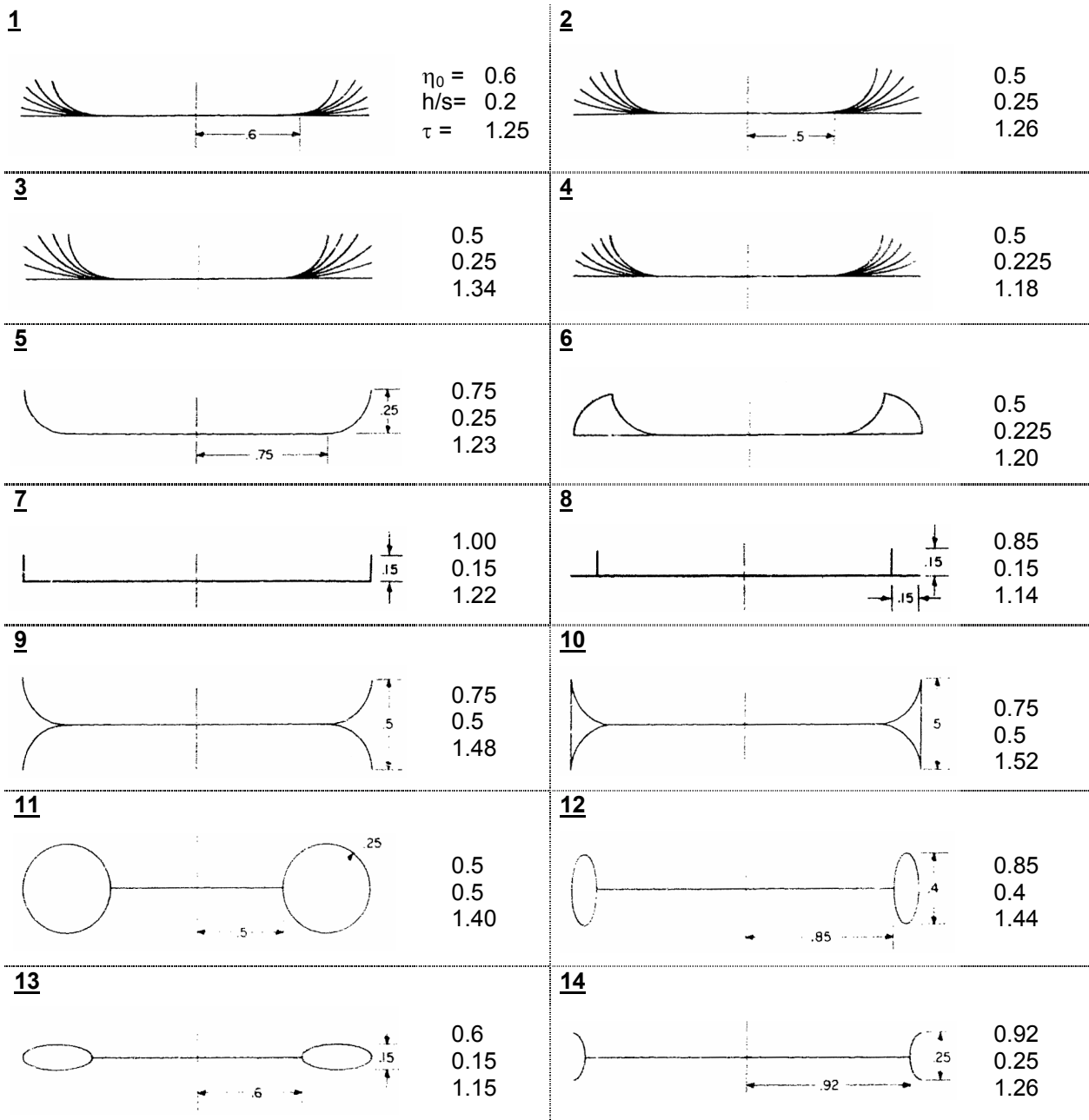


Fig. 5: Efficiency factors and geometries of optimally loaded wings with various non-planar tip forms [13].

Weber [11] analysed the effect of vertical winglets by means of a theoretical treatment of the Trefftz plane properties using conformal transformations. A result that cannot be inferred from Fig. 5 was that configurations where the winglet extends from the wingtip vertically upwards have a greater span efficiency than those where the winglet with the same ratio h/s extends equally upwards and downwards. Configuration 7 in Fig. 5 has a span efficiency of 1.156 according to Weber, a value somewhat smaller than that measured by Cone. The corresponding value for the configuration where the upper and

lower parts of the winglets are equal is 1.146, the difference in relative gain being thus about 9%. A similar result is presented by Kroo [14].

Induced lift can play a decisive role regarding lift to drag properties of non-planar wing configuration, a fact also discussed by Cone. The additional velocities at the wing induced by the bound vortices of the winglets are positive if the winglets point upwards in the lift direction. The effective flow velocity at the horizontal main wing lifting line is reduced if the winglets point downwards. The velocity increments consequently increase respectively decrease the lift according to the generalized Kutta-Joukowski theorem. Due to an increased induced lift, the configuration where the winglets point upwards must have an advantage over the configuration with winglets pointing downwards regarding L/D_i . This is in accord with computational results obtained with panel methods including wake relaxation reported by Eppler [15] and Maughmer [16].

2.1.3 Classification of Non-planar Lifting Systems According to their Wake Shapes

A slightly different approach to those described above is to infer the induced drag from the properties of the fully rolled-up vortex wake (Spreiter and Sacks [28], Zimmer [83]). With the exemption of particular one-sided parabolic circulation distributions [23] this approach has the disadvantage of lacking the possibility of analytical treatment. However, the wake roll-up can be numerically simulated.

Numerical simulation of the roll-up process became a common approach as computational power in the 1960s and 70s increased (compare e.g. Rossow [31], [32]). The usual approach is to discretise the vortex sheet into concentrated vortex filaments by incremental spanwise integration of the wake vortex strength $d\Gamma/dy$. For a two dimensional Trefftz plane representation, the discrete filaments become point vortices. The paths of the vortices can now be simulated by Euler or Runge-Kutta time stepping integration of the induced velocities. While the simulation result from which the induced drag can be computed by means of various methods ([27], [18]) does not constitute an improvement with respect to accuracy compared to the methods discussed in chapters 2.1.4 and 2.1.2, it has the advantage that the topology of the vortex is directly comparable with data obtained from experimental wake surveys. Since linear and momentum quantities as well as energy are conserved in the absence of viscosity during the roll-up process according to Betz [24], these quantities can also be derived from two-dimensional Trefftz-plane analyses, both for numerically determined as well as experimental data.

Spreiter and Sacks [28] discussed wake vortex shapes with reduced kinetic energy content and thus reduced induced drag under the constraint of constant lift. They identified two principle vehicles to achieve reduced kinetic energy in the wake of a wing

which are favourably illustrated by the relaxed, i.e. rolled-up vortex system of a simple wing. The power required to overcome induced drag, which is consumed to create the wake can be reduced either by

1. increasing the distance between the two vortex centroids or by
2. reducing the kinetic energy content of the vortex core regions.

Increasing the distances of the vortex centroids increases the mass of air that descends with the vortex system, which is contained within the limits of the Kelvin oval. The Kelvin oval is formed by dividing streamlines in the Trefftz plane. On the one hand, these streamlines separate the outer fluid, which is just deflected by the disturbance of the descending vortex system but which finally recovers its original position in space, and on the other hand, the fluid which is bound to the system and descending with the counter rotating vortices. One part of kinetic energy content in the wake can be related to the linear translation of the Kelvin oval as it were a rigid body. The other part is basically rotational energy within the oval. In the case of a wake created by an elliptically loaded wing, linear translation makes up about half the energy and rotation the other.

Cone [13] gives a descriptive explanation of how energy expenditure can be reduced by the second vehicle. He starts the discussion defining a symmetrical circulation distribution at a lifting line. The total circulation of the vortex wake can be determined by integrating the velocity components that are tangent to an arbitrary path C enclosing the trailing vortex sheet of one wing half. This circulation equals the circulation at the wing centre section.

$$\Gamma_0 = -\oint_C \vec{Q} \cdot d\vec{s} \quad (11)$$

The lift of practical wings is although not uniquely determined by but closely related to Γ_0 . It is possible to create systems of equal span that have different spanwise circulation distributions but equal values for lift and root circulation. Nevertheless, the kinetic energy content of the wake that corresponds to the induced drag of the wing may vary considerably. Cone proceeds to illustrate the differences in kinetic energy at fixed values of circulation by a comparison of two Rankine vortices of different core diameters. While the velocity of a potential vortex becomes singular at the origin, the Rankine vortex prevents this by modelling the core analogously to a rotating rigid body.

Fig. 6 depicts two Rankine vortices with different core radii. For radii greater than r_1 respectively r_2 it is assumed that the tangential velocities obey the equation for the

potential vortex $Q_\theta = -\frac{\Gamma}{2\pi r}$.

The kinetic energy per unit length in axial direction contained in the vortex systems is

$$E_{\text{kin}}' = \rho\pi \int_0^{\infty} Q_{\theta}(r)^2 \cdot r \, dr$$

and it is obvious that vortex 2 contains less kinetic energy than vortex 1 even though circulations at radii greater than r_2 are equal. Despite the need to preserve the total wing circulation, no unique restriction is placed upon the induced drag which accompanies this circulation.

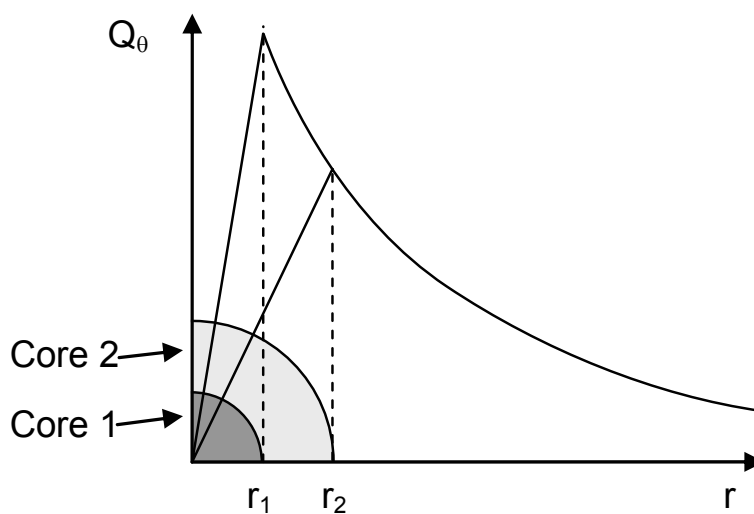


Fig. 6: Distribution of tangential velocities for two vortices of different core radii (adapted from [13]).

For single winglets that are principally perpendicular to the planar wing part, the main vehicle of induced drag reduction is the increased distance between the circulation centroids of both wing halves. The working principle can be illustrated by looking at the Trefftz-plane velocity field. A comparison of the velocity fields of the partly rolled-up vortices in the wake of an elliptically loaded wing (a) and a wing-winglet configuration with optimum circulation distribution for minimum induced drag (b) according to Weber [11] is shown in Fig. 7.

The picture is a result of a time-marching roll-up simulation of the discretised trailing vortex fields using potential vortices. The distances that individual vortices travelled in one time step were obtained by integration of the summed-up induced velocities. A 4th-order accurate Runge-Kutta scheme was employed for the integrations. Trefftz-plane induced velocities at points other than those directly positioned on the wake sheet have been obtained from randomly distributed tracer particles, i.e. dummy vortices with zero

circulation. The velocities at grid points were then interpolated from the velocities of the point vortices and the dummy vortices. This procedure has the advantage over the direct evaluation of induced velocities at grid points that velocities do not become singular.

The coordinates of Fig. 7 are non-dimensionalised by the semi-span s of the wing. The wing shapes in a plane perpendicular to the freestream are depicted above the velocity fields. The winglet configuration is characterised by a ratio of winglet height to semi-span of 0.4. Velocities are given in a moving frame of reference that descends with the sinking velocity of the vortex centroids, which are marked by crosshair symbols. Referring the absolute velocity values to a Trefftz-plane reference velocity yields non-dimensionalised velocities

$$Q_{\text{Trefftz,ref}} = \frac{\Gamma_m^*}{b}$$

where

$$\Gamma_m^* = \frac{L}{\rho Q_\infty b}$$

Trefftz-plane reference velocities are equal for all vector plots shown in Fig. 7. For constant values of Q_∞ , ρ and b , this means that lift is the same for both configurations. The figures are presented for a common instant in non-dimensional time

$$t^* = \frac{t}{T_{\text{ref}}} = 0.811$$

where

$$T_{\text{ref}} = \frac{b^2}{\Gamma_m^*}$$

Velocity plots are presented because of the direct link to kinetic energy respectively kinetic power

$$P = \frac{1}{2} \rho Q_\infty \iint Q_{\text{Trefftz}}^2 dy dz$$

From a macroscopic point of view, velocity fields closely resemble that what is theoretically generated by two counter-rotating potential vortices. Deviations are confined to the vortex core regions. The area enclosed by the Kelvin oval is therefore primarily determined by the distance of vortex centroids b^* .

Statistics in Tab. 1 may ease the interpretation of the simulation results of Fig. 7.

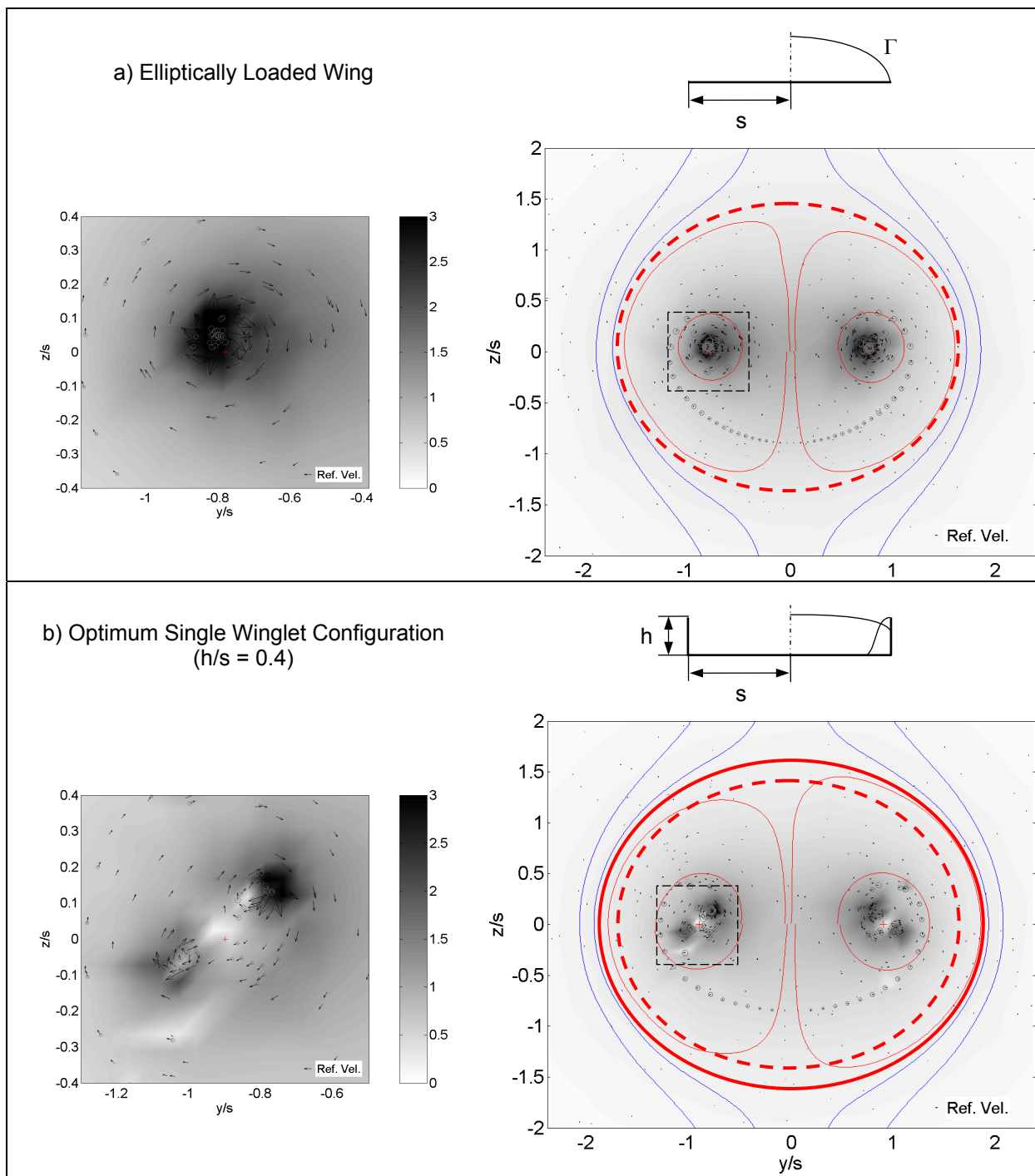


Fig. 7: Trefftz-plane non-dimensional velocity fields generated by partly rolled-up vortex wakes at $t^* = 0.811$. Velocities are given in a vertically moving frame of reference coupled to vortex centroids. Shading represents absolute magnitude of velocities in the Trefftz plane $(v^2 + w^2)^{1/2} / Q_{\text{Trefftz,ref}}$. Core regions enclosed by the dashed rectangles of constant area $= 0.8^2 \cdot s^2$ in the all-up views are shown enlarged on the left hand side. Bullet sizes indicate strengths of point vortices in terms of circulation.

Tab. 1: Induced drag and wake vortex statistics of configuration compared in Fig. 7.

Configuration	Span Efficiency τ	η_{Centroid}	$W_{\text{Centroid}}/Q_{\text{Trefftz,ref}}$	Maximum Power Density Relative to a)
a) Elliptically Loaded Wing	1.0	0.785	0.254	100%
b) Optimum Single Winglet Configuration	1.41	0.903	0.194	48%
[a) - b)] / b)	+ 41 %	+ 15%	- 31%	- 52%

Much of the circulation of the winglet configuration is shed at the outermost span station. This moves the centroids of the trailing vortex sheet apart. Also the core circulation is reduced for the winglet case. The rolled-up vortex system behind an optimally loaded winglet configuration creates two distinct vortices per wing half, one emanating at the winglet top and a second at the winglet root. Fig. 7 represents the roll-up process after the winglet tip and root vortices made just more than one rotation about the centroid. The stronger top vortex thus refers to the winglet tip vortex and the lower vortex to the winglet root vortex. This partition in two centres reduces the induced velocities in the core region and by such vorticity and also kinetic energy content (compare also wake measurements of Kreuzer [62], [72]).

A similar analysis has been made with a rectangular wing and a multi-winglet configuration. Both configurations are uncambered, untwisted, and have load distributions corresponding to aspect ratios of 8.0 (AR is based on span and the wing areas projected into a plane perpendicular to the lift direction in this case). Lift distributions are hence not necessarily optimal with respect to induced drag unlike the configurations of Fig. 7. The data of Fig. 8 and Tab. 2 is presented in a similar fashion as above, though. The rectangular wing has been added because the lift distribution of the multi-winglet configuration closely approximates that of a rectangular wing if circulations are summed up at spanwise coordinates. The lift distribution of a rectangular wing is more pronounced at the tip compared to the elliptically loaded wing. Note that the multi-winglet configuration with a rather "rectangular" spanwise lift distribution approaches the corresponding optimal lift distribution much more closely than the rectangular wing [12]. The rectangular lift distribution has two effects. First the centroid of the wake circulation is moved outwards and second the trailing vorticity is stronger due to the greater bound circulation gradient at the wing tip, which is directly reflected by a higher maximum power density.

These effects act in opposite directions, the first is reducing and the second increasing induced drag. In addition to the reduced root circulation another consequence of the greater centroid span b^* is a reduction in downwash velocity w_{Centroid} . The circulation

centroids of the multi-winglet configuration are shifted towards the wing tip location compared to the rectangular wing but inboard of the centroids of the optimum single winglet configuration of Tab. 1 respectively Fig. 7.

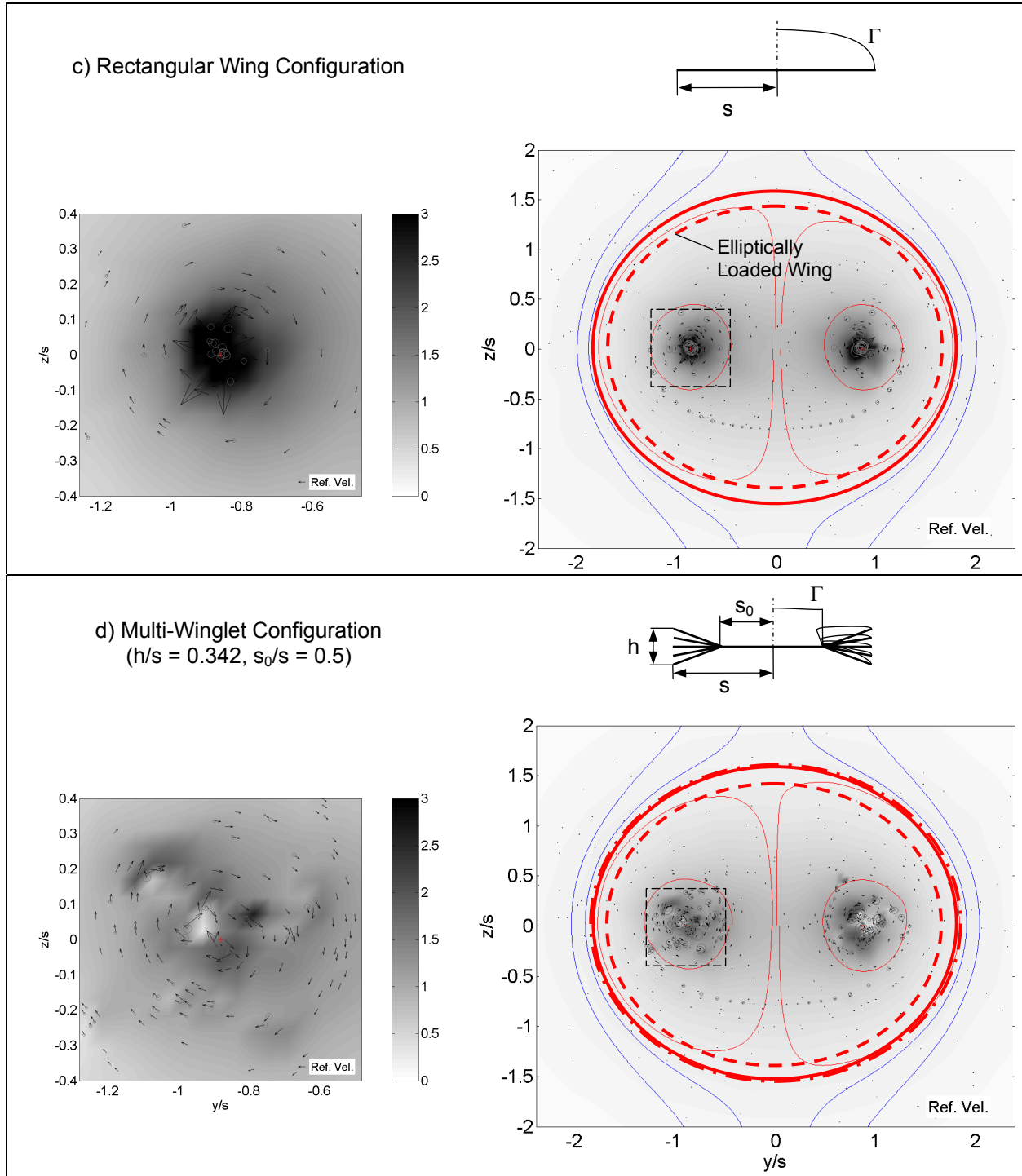


Fig. 8: Trefftz-plane non-dimensional velocity fields generated by partly rolled-up vortex wakes of untwisted rectangular wing and multi-winglet configuration (refer to Fig. 7 for reference data).

Tab. 2: Induced drag and wake vortex statistics of configurations shown in Fig. 8 (configuration a) for reference).

Configuration	Span Efficiency τ	η_{Centroid}	$w_{\text{Centroid}} / Q_{\text{Trefftz,ref}}$	Maximum Power Density Relative to a)
a) Elliptically Loaded Wing	1.0	0.785	0.254	100%
c) Rectangular Wing	0.97	0.863	0.212	182%
d) Multi-Winglet Configuration	1.32	0.885	0.201	31%
[d) - a)] / a)	+ 32 %	+ 13%	- 21%	- 69%

In comparison with the rectangular wing configuration the induced drag reduction clearly originates from the diffused Trefftz-plane velocity field in the vortex core regions. Core circulations are closer to distribution 2 of Fig. 6 than that of distribution 1. This is also indicated by the decreased maximum power density and the rather diffused velocity distribution. Comparison of the single winglet case in Fig. 7 (data in Tab. 1) with the multi-winglet configuration in Fig. 8 (data in Tab. 2) shows that the capabilities to reduce induced drag are of the same order of magnitude but the wake topologies are different.

2.1.4 Aircraft Wake Vortices and Associated Effects

The preceding section showed that the strengths of the wake vortices are directly related to induced drag and that the vortex sheet is subject to a relaxation process, which can physically be observed as the vortex roll-up process. Roll-up of the simplest system of two counter-rotating wake vortices of a planar aircraft wing starts from the tips as far as the high-lift devices are in the retracted position. For ease of discussion a simple elliptically loaded wing is considered.

Circulatory motion of the air in a plane perpendicular to the free stream direction is commonly interpreted as the consequence of the higher lower side pressures causing air to flow around the tip towards the low pressure upper side of the wing. Inspection of the initial roll up in more detail reveals that the cross flow at the tip causes the flow to locally separate, typically at about half tip chord location. The region of vortex flow ends at a reattachment line further inboard on the wing tip suction side. This initial roll-up can also be motivated by the simplified potential flow model depicted in Fig. 1 because the absolute strength of the free vortex sheet $d\Gamma/dy$ is greatest at the tips.



Fig. 9: Contrails visualising cores of flap outer and winglet tip vortices of MD11 [21].

The vast majority of the bound circulation of an elliptically loaded wing is shed near the tips (while for large transport aircraft in the high-lift configuration it might be the outer edge of the flap, Fig. 9). Practically the roll-up is essentially completed within 2-3 chords aft of the trailing edge [22]. The strength of the trailing vortex core is illustrated by peak tangential velocities of up to 100 m/s, a value observed at a B757 tip vortex. The rate at which roll-up takes place increases with circulation. Once rolled-up, the counter rotating vortex system descends due to mutual induction. Tip vortices are known to be extraordinary stable systems that can persist for thousands of chord lengths downstream of a wing. Dissipation rates are small in the first stage of decay until the vortices become unstable and break up when they start to decay more rapidly in the second stage until they have virtually vanished.

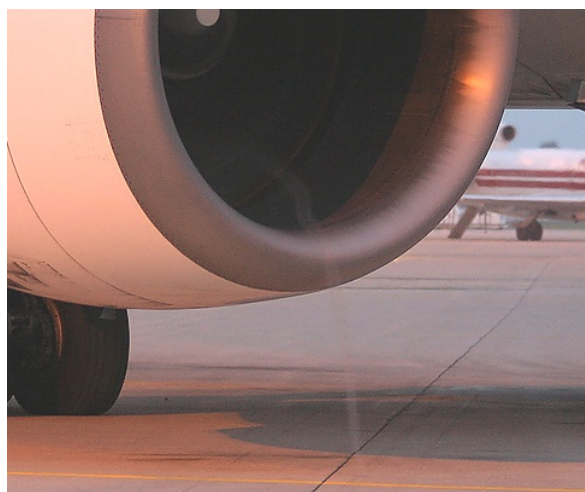


Fig. 10: Intake vortex ending on ground [21].

Another particular effect related to the generation of drag cannot be completely ignored apart from the fundamental interplay of induced drag and the creation of wake vortices as described by potential flow models. Low pressure prevails in the core of the free vortex. This low pressure region cannot just suddenly begin in air but rather sucks itself towards a boundary. This effect can frequently be seen on fan engine intakes of non-moving aircraft on ground when the engine is running (Fig. 10). This behaviour is in accord with Helmholtz's theorem that a vortex can only terminate at the boundaries of a flow if the system is not closed to form a ring.

Since the separation of the vortex or the attachment of the low pressure vortex core to the surface is located at or behind the mid chord position, the lift is increased but also the drag. The lifting line model shown in Fig. 1 does not account for this type of pressure drag. The physics of the effect are similar to the vortex flow dominating the lift and drag production of slender wings. However, the magnitude of this effect is directly related to the aspect ratio of the wing and hence it is small in the normal flight range on aircraft with high aspect ratio wings [20]. However, it may often be this mechanism of drag generation that is tackled by special wing tip shapes, such as sharp edged and downward bend wing tip caps seen on many Cessna aircraft or raked wing tip configurations where the tip section is swept back, rather than their effectiveness in producing a more elliptical lift distribution as is frequently claimed.

Although the present work concentrates on effects of multi-winglet configurations for application on low speed aircraft where hazards due to the generation of wake vortices usually does not play a role, the wake vortex problem in aviation nevertheless deserves mentioning in the current discussion context.

Wake vortices of large aircraft constitute an aviation hazard as several accidents in the past have proved. A wake vortex encounter started a sequence of events that finally ended in the fatal crash of an A300 in 2001 [17]. Increased longitudinal separation of aircraft, particularly during approach, reduces the throughput of runways. Mitigation of wake vortices directly reduces hazards for following aircraft and allows smaller separation distances. Increased runway utilization may make additional runways unnecessary or postpone the need to a later point in time. Increased airport efficiency may be reflected in reduced landing charges with the final consequence of reduced direct operating costs of airlines and finally lower ticket prices. This sequence shows that there is a clear economic component with respect to the wake vortex problem next to the immediate safety implications. Hence, means that allow mitigation of the wake vortices strengths, which is principally possible with single and multi-winglet systems, should attract interest of aircraft manufacturers.

2.1.5 Design and Off-Design Characteristics of Non-planar Lifting Systems

Design and off-design characteristics of single and multi-winglet configurations will be briefly discussed in the following section as far as span efficiency is concerned.

Before, it will shortly be recalled how to arrive at a three-dimensional configuration once theoretically optimum load distributions are established. The chord distribution can be computed if a design sectional lift coefficient is specified (refer e. g. to Stache [18]). Local incidences respectively wing washout must then be chosen so that the optimal load distribution is obtained. Effective adaptation of incidences can also fully or in part be obtained by altering sectional camber.

Disadvantage of a single winglet extending in the lift direction is that it can only be optimised regarding induced drag respectively span efficiency for a single operating point. This is in contrast to an elliptically loaded wing, which has a span efficiency that is independent of the lift coefficient. Circulation as well as its spanwise distribution change linearly with angle of attack if the elliptically loaded planar wing is concerned. The winglet is unlike the wing in that its geometric angle of attack does not vary with aircraft angle of attack but with sideslip angle. Angle of attack increase is thus limited to the angle of attack fraction that is induced by the main wing. However, according to Maughmer [16] the winglet can be designed so that the induced velocities cause its lift coefficient to track very closely with that of the wing. While this is true for small winglets the induced angle of attack becomes smaller the larger the winglet is. It can therefore be inferred that small winglets are less sensitive to deviations from the design point than large winglets. Nevertheless, it has to be mentioned that Ewald [65], for example, used winglets with symmetrical airfoil sections and neither root incidence nor twist but obtained results that clearly favoured the winglet configuration in comparison to a configuration without them.

To illustrate the difference of winglet configurations mounted at right angles to the main wing and multi-winglet configurations with significantly smaller anhedral respectively dihedral angles, the change of the local geometric angle of attack with the global one is considered, which is

$$\alpha_{wl} = \alpha \cdot \cos(\Upsilon) \quad (12)$$

A wing part, which has a dihedral angle of 20° experiences in this way still 94% of the angle of attack increase of a planar wing part, while it drops to 50% for a dihedral of 60° down to 0% for 90°.

In agreement with Prandtl's results for multi-surface configurations [9] and the optimum lift distributions for a multi-winglet configuration with four winglets covering the outer

20% of the span given by Stache [18], the uppermost and the lowermost winglets must bear comparatively high loads. The root loadings of the top and bottom winglets at dihedral angles of 30 and -30 degs were optimised to have 35.2% of the main wing circulation just inboard of that location each, while the circulations of the two centrally located of the otherwise equally distributed winglets were just 14.8% each. In a three dimensional realisation, the winglets would preferably be mounted on top of each other in order to eliminate the mutual influences of the bound circulations on the load distributions of the other winglets. In this set-up, it is guaranteed that angle of attack changes affect all winglets equally. The smaller the anhedral respectively dihedral angles, the smaller the deviation from the optimum operating point during changes in angle of attack. The performance of such a configuration in a potential flow would be good, though not realisable in a real flow. Adjacent winglet surfaces would hinder momentum transfer from the outer flow into the boundary layer resulting in separating boundary layers in the corners. This adverse interference effect would strongly impair the aerodynamic performance. For this reason, the overlap of multi-winglet cascades of birds are staggered in the streamwise direction and overlap of subsequent winglets is limited to small amounts. If one strives for an optimum loading, the main wing must be cambered in order to establish a high incidence of the trailing winglet, which is a prerequisite for the high load required there. However, the influence of the bound circulations would result in different lift curve slopes of the subsequent surfaces descending from the leading to the trailing winglet. The fundamental advantage of independency of the optimum loading from angle of attack cannot be realised without adaptation. In addition it has to be mentioned that high loads at trailing edge lifting elements arranged in accelerating cascades are in general disadvantageous, as they are prone to boundary layer separation. An important consequence is that the theoretical optimum load distribution of a multi-winglet configuration is hardly to be realised in practice (compare practical experience of Sunkomat [81]).

It can be summarised that the single winglet has the disadvantage to optimally work only at one operating point, whereas the multi-winglet configuration must deliberately deviate from the theoretical optimum from scratch in order to exhibit a suitable performance in real flow conditions.

2.2 Further Aspects for the Design of Optimum Lifting Systems

It was also Cone [13] who stated that no final recommendation can be inferred from the mere study of span efficiency regarding the design of a wing. Profile drag and structural design considerations must be regarded for a more general scope to arrive at an optimum aircraft wing design. Cone concluded that the design compromises between aerodynamic and structural considerations are necessary and that their relative

weighting will depend entirely upon the mission requirements of the particular aircraft under consideration.

2.2.1 Profile Drag

Induced drag only depends on the load, the load distribution and the geometry of the lifting system - primarily on the span - but not on the extent of the lifting surface in the flow direction. A wing in a real flow will always experience profile drag. This drag component is therefore an essential element in wing optimisation. Profile drag is mainly due to skin friction. The magnitude of this drag component mainly depends on the size of the wetted surface area. If skin friction were the only profile drag component, profile drag could be minimized by minimizing the wetted area.

For a fixed load, load distribution and span of a single planar wing induced drag is constant. Striving for minimum drag, one opportunity left is to reduce the wetted surface area by reducing the wing chord lengths and by so doing also the profile drag. A direct consequence is the increase of local and wing overall lift coefficients. If the height of the wing section were prescribed in order to meet a structural mass constraint, the sections relative thickness would increase. Increase of the lift coefficients as well as of the relative thickness affects the condition where boundary layer separation has to be expected. The increasing pressure drag then counters the reductions in friction drag. Finally the degree of boundary layer separation yields an extent where the prescribed lift cannot be maintained anymore. Boundary layer separation, to summarise, sets a lower limit to the chordwise extent of the wing.

Stache [18] compared computational results of planar and various non-planar wing configurations, regarding induced drag as well as profile drag. A two dimensional numerical wake model was used, where circulations of discrete trailing vortices were derived from a generic parametric bound circulation distribution. Induced drag was computed by means of the Kirchhoff-Routh function. While chord dimensions were derived from the supposition of a specified fixed lift coefficient applicable to all wing and winglet sections, profile drag was obtained from resulting Reynolds numbers influencing turbulent flat plate skin friction drag. Using fixed lift coefficients avoids the need to model lift dependent profile drag that is associated with pressure drag, which is becoming a dominating profile drag component when boundary layer separation sets in. The lift to drag ratio was optimised using a genetic optimisation algorithm. It was found that the differences in lift to drag ratios among non-planar configurations were only small. For large devices with $h/s = 0.3$, the tip loop configuration had only 91.5% of the drag that an optimum planar wing would have, followed by the split tip and single winglet configurations with virtually identical figures of 92.5% (see also Tab. 3).

Tab. 3: Drag ratios of various non-planar wing configurations constrained to fit into a box with height to semispan ratio of 0.3. Values are given as percentages with respect to optimum planar wing configuration [18].

	Tip Loop $\eta_0 = 0.7$	Split Tip $\eta_0 = 0.7$	Single Winglet (Pointing Upwards)
Profile Drag	107.8 %	105.7 %	110.8 %
Induced Drag	78.0 %	81.2 %	77.1 %
Total Drag	91.5 %	92.5 %	92.5 %

2.2.2 Effect of Wing Splitting on Profile Drag

Splitting a lift producing surface into two or more smaller surfaces so that the chord lengths are integer fractions ($1/2$, $1/3$, ...) of the original single surface chord reduces the Reynolds numbers. Given that the state of the boundary layers does not fundamentally change, the skin friction drag of the smaller surfaces will be higher than that of the single surface. This statement holds for the chord based friction drag coefficient as well as for the total drag. The ratio by which the skin friction drag of the multi-surface configuration will be increased above that of the single surface can be estimated by means of a simple analysis.

The friction drag ratio is

$$\left(\frac{\sum D_{f,2}}{D_{f,1}} \right) = \frac{n_2 \cdot c_{F,2} \cdot c_2}{c_{F,1} \cdot c_1}$$

where the index '2' indicates an individual element of the n_2 elements of the multi-surfaces configuration and '1' the equivalent single surface. Because $n_2 \cdot c_2 = c_1$ the equation simplifies to

$$\left(\frac{\sum D_{f,2}}{D_{f,1}} \right) = \frac{c_{F,2}}{c_{F,1}} \quad (13)$$

The integrated skin friction drag coefficients c_F can be evaluated for three different cases using formulas for flat plate friction drag [91]:

Laminar	Turbulent	Mixed with transition
$c_{F,la,c} = \frac{1.328}{\sqrt{Re_c}}$	$c_{F,tu,c} = \frac{0.455}{\log(Re_c)^{2.58}}$	$c_F = c_{F,tu,c} - x_t / c \cdot (c_{F,tu,t} - c_{F,la,t})$

The coefficients $c_{F,tu,t}$ and $c_{F,la,t}$ are compared with Reynolds numbers based on the distance of the transition location from the leading edge x_t instead of the chord length c .

Fig. 11 shows the results obtained by evaluating equation (13) plotted against the chord Reynolds number of the single surface. For laminar flow, the drag ratio is independent of the Reynolds number. The value of the laminar drag ratio is exactly the square root of the number of elements of the multi surface configuration. The drag is significantly increased in the present case by a factor of $\sqrt{n_2} = \sqrt{5} = 2.24$.

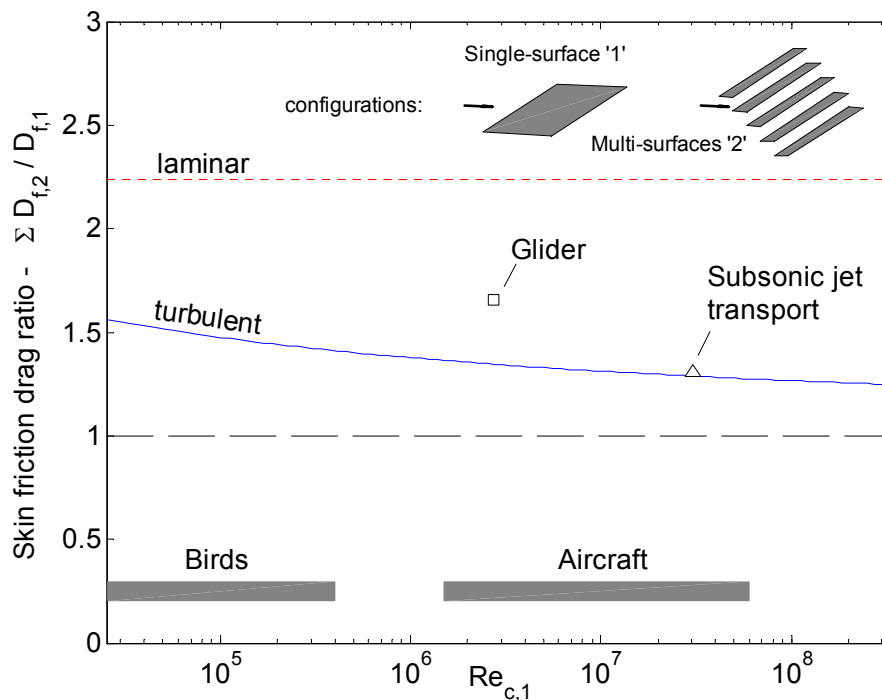


Fig. 11: Effect of splitting a single flat plate into five smaller plates on skin friction drag (Glider: $x_t/c = 65\%$, $c = 1$ m, $Q_\infty = 40$ m/s, $H = 0$; Subsonic jet transport: $x_t/c = 5\%$, $c = 5$ m, $Q_\infty = 250$ m/s, $H = 11.3$ km).

The drag ratio for turbulent flow is lesser and decreases while advancing to higher operational Reynolds numbers. In the Reynolds number range typical for aircraft the skin friction drag of the multi-surface configuration is increased by about 35%. The drag penalty for breaking a given surface down into a multi-surface configuration is thus more severe for laminar designs such as gliders than for turbulent designs such as subsonic jet transport aircraft with swept back wings that only allow small regions of laminar flow. Since it is virtually impossible to arrive at designs where the boundary layer is laminar up to the trailing edge it can be concluded that an increase in the Reynolds number reduces the skin friction penalty of multi-surface designs. This is a particular important aspect because skin friction represents about 80-90% of the profile drag. In the limited scope of flat plate friction, aircraft appear to be less sensitive to slotting of wing surfaces than birds.

2.2.3 Effect of Induced and Profile Drag on Aircraft Performance

Drag polars relate the lift capability of wings to drag and thus illustrate the aerodynamic efficiency of wings. The non-dimensional drag coefficient of a wing can be expressed by a parabolic function. The same approach is also used for the drag characteristics of aircraft for which the model is widely used because its simple mathematical form and the possibility of linearisation that permits an analytical treatment of aircraft performance. In its simplest form only profile drag and induced drag are considered, the second term of eq. (14).

$$c_D = c_{D,p} + \frac{c_L^2}{\tau \cdot AR \cdot \pi} \quad (14)$$

The effects of profile and induced drag on performance figures of gliders and aircraft with power producing engines are illustrated in Fig. 12. For the sake of simplicity it has been assumed that the profile drag coefficient $c_{D,p}$ is a constant.

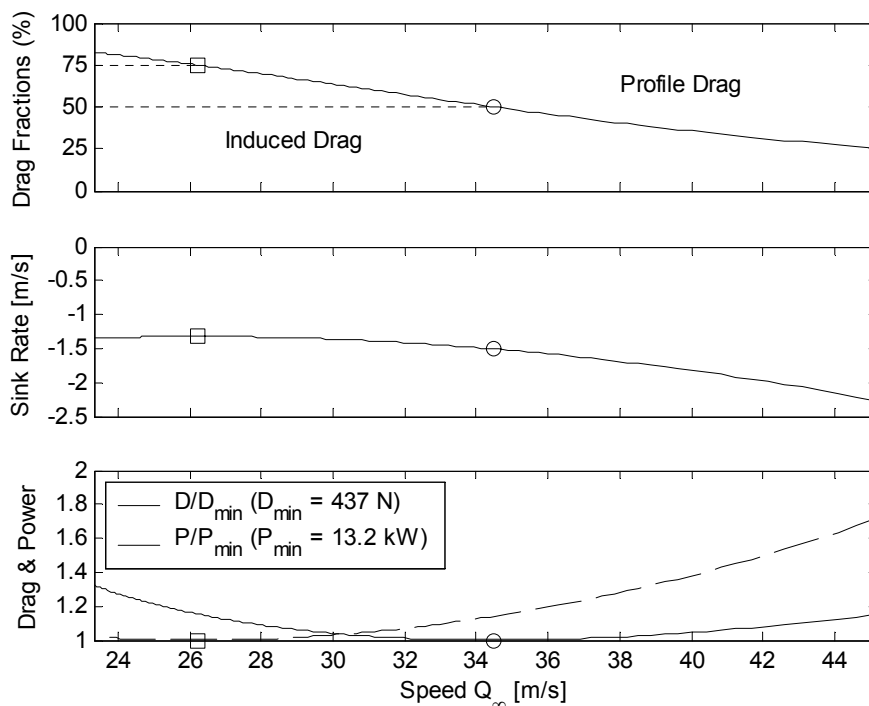


Fig. 12: Drag components according to parabolic drag polar model and symbols indicating particular operating points ($W = 10 \cdot 10^3$ N, $S = 20$ m², $c_{D,0} = 0.015$, $\tau = 1.0$, $AR = 10$, $c_L = 1.5 \dots 0.4$, ISA, SL).

Expanding eq. (14) using the definitions of lift and drag coefficients as well as the definition for aspect ratio $AR = b^2/S$ and the condition of small glide path angles such that $L \approx W$ yields the aircraft drag in dimensional form

$$\begin{aligned}
 D &= D_p + D_i \\
 &= \frac{1}{2} c_{D,p} \rho Q_\infty^2 S + \frac{2W^2}{\rho Q_\infty^2 \tau b^2 \pi}
 \end{aligned} \tag{15}$$

The power is obtained by multiplying equation (15) with the freestream velocity Q_∞ . Drag and power curves in the lower subplot of Fig. 12 have been normalised by their respective minimum values, which were analytically computed. The relative contributions of profile and induced drag are shown in the upper subplot of Fig. 12. Since

$$L/D \approx W/D \approx Q_\infty/w \tag{16}$$

sink speed w is obtained by multiplying equation (15) with Q_∞ / W . Using relation (16), the approximation $Q_\infty \approx dR/dt$ and the definition $w = dH/dt$, one obtains the equation for range of an unpowered aircraft or glider after some manipulations

$$dR = \frac{c_L}{c_D} dH \tag{17}$$

A corresponding equation results for endurance

$$dt = \frac{c_L^{3/2}}{c_D} \cdot \sqrt{\frac{\rho}{2 \cdot W/S}} dH \tag{18}$$

It can be shown that the latter two equations also hold for powered aircraft with power producing (i.e. propeller) engines.

Maximum range is achieved for gliders and propeller driven aircraft if the operating point is chosen so that it corresponds to the maximum lift to drag ratio, indicated by the bullets in Fig. 12. Characteristics of this operating point are firstly that profile and induced drag are equal and secondly that the absolute drag is minimum. A frequently used designation is hence minimum drag operating point.

The operating point for minimum sink speed or maximum endurance coincides with the minimum power condition at a speed that is just 76% of the speed for maximum range. Only 25% of the total drag is profile drag while induced drag constitutes the remaining 75%. The operating point is also characterised by the maximum endurance parameter $c_L^{3/2}/c_D$. It must be born in mind that wing loading directly influences the minimum power operating point.

The higher induced drag fraction indicates that non-planar wing configurations aimed at reducing this drag component will be primarily effective with respect to endurance. The trade-off between additional profile drag and reduction of induced drag is different for maximum endurance and maximum range operating points. An example may help to

illustrate this. Assuming that the induced drag can be reduced by 20%, the profile drag for a neutral performance effect could increase by 60% for the maximum endurance operating point but only by 20% for the maximum range condition.

Gains are thus likely to shrink if the speed increases and the lift coefficient decreases. It might be easier to achieve net benefits with non-planar wing configurations on large aircraft equipped with power producing propeller engines than with thrust producing turbojet engines. This is because conditions for maximum endurance and maximum range are shifted to lower lift coefficients respectively higher speeds for the latter means of propulsion. Turbojet engines were soon replaced by more efficient turbofan engines with characteristics that are more or less half way between the idealisations of thrust and power producing means of propulsion. However, characteristics of the aircraft propulsion system are important with respect to the net benefits obtainable with non-planar lifting systems.

In addition, large commercial transport aircraft usually operate at higher speeds than those for minimum fuel consumption in order to reduce time dependent costs and also to increase passenger appeal by shorter flight durations. These effects further erode the attractiveness of devices for induced drag reduction. However, as will be discussed in a subsequent section, practice proved that non-planar configurations might still offer performance benefits even if the operating point is shifted far to the right of the optimum points shown in Fig. 12 and the fact that only small increments in other drag components such as winglet profile drag are acceptable for a given induced drag reduction.

2.2.4 Compressibility Effects

For a subsonic jet transport aircraft, the optimisation of wing configurations for transonic flow, particularly regarding wave drag and the problem of shock induced boundary layer separation, is another aspect of first order [14]. Early wings of aircraft operating in the transonic Mach number range with sweepback suffered from undesired effects affecting aircraft handling qualities like tip stall and pitch up or high wave drag that curtailed performance to mention but a few. Wing loadings were often comparatively low and the planforms were mostly simple and hence planar because it was believed that this eased to avoid or at least to mitigate the undesired effects stated above. It was not before the 1970s that wing tip devices were suggested for aircraft operating in the transonic Mach number range. A breakthrough was achieved because researchers at NASA developed winglets for aircraft operating in the transonic Mach number range such as the KC135 and validated the designs by extensive wing tunnel and flight test experiments ([55], [59], [58]), thus stealing sceptics' thunder by sheer evidence. One reason of the success was that it was managed to integrate the winglet without significantly deteriorating the drag divergence Mach numbers of the wings because of thorough

tailoring of the winglets to minimise the interference of the pressure fields of wing and winglet surfaces. Modern supercritical wing designs with winglets also show that a particular tailoring of the additional surface for the cruise operating points at Mach numbers around 0.8 is possible [61].

There is less information available on the behaviour of multi-winglet configurations in compressible flow. However, the experimental data in reference [79] shows that favourable performance figures can be maintained up to the transonic Mach number range despite the fact that the deterioration is slightly larger than for a single winglet compared to incompressible flow conditions.

A more extensive survey about the actually much larger cut set of transonics and non-planar wing configurations is out of the scope of the present thesis for the sake of a reduced degree of complexity. Instead, emphasis is placed on the characteristics of multi-winglet configurations in low speed incompressible flow.

2.2.5 Wing Structure Mass

A suitable structural design is a necessity for aircraft safety and efficiency. Improving the aerodynamic efficiency of a planar cantilever wing by increasing span and reducing induced drag has the consequence that the wing bending moments increase due to the larger lever arms. If the condition of a fixed wing loading is set so that the wing lift coefficient remains constant, the greater span requires decreased chord length. Assuming fixed taper ratio and a fixed profile section with constant maximum thickness to chord ratio t/c , it follows that the thickness of the profile must be scaled down proportionally to the chord length. If a wing box is used as the primary structural member, the tension flows are not only increased due to the higher bending moments but also because of the reduced area moment of inertia. For a given material strength, the amount of material in the box upper and lower skin panels must be increased accordingly. While the bending moments at a given relative span station, inevitably increase, the shear forces remain constant. Hence, the growth of material required to resist the shear forces is less than that of the material required to resist bending. The upper and lower panels make up for most of the primary structure mass of wings having intermediate to high aspect ratios (i.e. $> 80\%$ for subsonic jet transport aircraft, compare ref. [119]). For this reason, the former and more pronounced scale effect that is related to bending dominates over the latter effect related to shear forces.

Consequently, the wing root bending moment correlates favourably with the wing structure mass as far as a population of aircraft models belonging to a particular class is considered. Wing root bending moment has been frequently used for wing configuration trade-offs. Pursuing a top down approach, it therefore appears that the correlation of other parameters such as the relative sectional thickness is low in comparison. One reason for the good correlation of the wing root bending moment with wing mass is that

the aircraft sizes, even in the limited scope of a distinguished group of jet propelled transport aircraft, for example, show a significant spread while the differences of particular wing geometrical properties of realised aircraft such as the relative thickness t/c are rather small. Referring to the example mentioned at the beginning of this section, the increased wing root bending moment in connection with the wing structural mass correlation would, of course, yield an increased wing mass. However, the effect of the reduced structural thickness would remain entirely disregarded although being an effect of first order. Differently, the area moments of inertia of a main wing do not change, if, for example, a tip device is retrofitted leaving the outer geometrical form of the main wing unchanged. The simple wing root bending moment correlation may yield satisfactory results in this case regarding the amount of mass to be added for wing strengthening. These examples were discussed to point out that it really depends on the problem to be tackled whether a simple model is acceptable or whether more sophisticated approaches appear mandatory.

A generic attempt to identify the best wing configuration was presented by Prandtl [19] considering the trade-off between induced drag and structural weight. Incorporation of other aspects such as profile drag was sacrificed to facilitate an analytical treatment, which otherwise would have been impossible. Only unswept planar cantilever wing configurations were considered. Prandtl correlated wing structural mass with the spanwise integrated bending moment, and stated that the thickness of wing sections must remain constant during planform variations, another significant constraint. Although valuable for validation purposes, the many assumptions made have the consequence that Prandtl's solution of optimum wing planforms characterised by increased span and rather pointed tip shapes compared to an elliptical shape must be regarded just as to indicate a basic trend.

2.3 Multiwinglet Systems in Nature - Outer Primaries of Birds

Before turning to the functions of outer primary feathers of birds (short: outer primaries) discussed in the literature, the section will start with a brief review of morphological, physical and anatomical aspects of bird wings. In this context, statistical data will be presented to point out fundamental trends which directly lead to the functional interpretation of outer primaries.

Descriptions of the morphology of bird wings are found in many textbooks, e.g. Herzog [38] or Burton [39]. A concise summary of morphological aspects is contained in the book of Videler [40]. Addressing primarily engineering aspects in this work, trivial names will be preferred to the scientific notion for the description of anatomical aspects.

2.3.1 Wing Morphology

2.3.1.1 Breakdown of Wing Skeleton

Fig. 13 shows the arm skeleton of a bird wing. Just the outer end of the upper arm bone (*humerus*) is shown at the right. The arm continues outwards of the elbow joint with the forearm bone (ell, *ulna*) and the smaller radius up to the two carpal bones (*os carpi radiale*, *ulnare*) forming a double wrist joint about which the main hand bone (carpometacarpus) is articulated. The “thumb” (*alula*) and two fingers (*digitus major*, *digitus minor*) complete the skeleton.

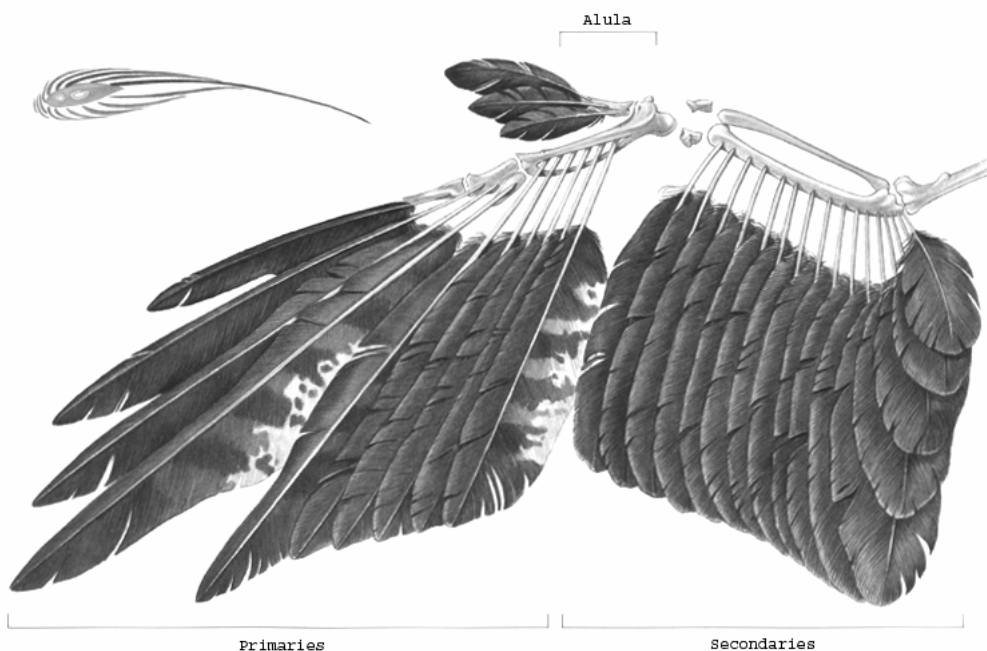


Fig. 13: Wing skeleton and arrangement of flight feathers (adapted from [39]).

2.3.1.2 Feathers

The principal arrangement of flight feathers on the wing and their position with regard to the wing bones is also shown in Fig. 13. Secondary feathers (secondary remiges, secondaries) of the inner wing (arm) are attached to the large forearm bone and the primary feathers (primary remiges, primaries) of the outer wing are attached to the bones of the hand and the fingers. Another functional subdivision is made in inner and outer primaries distinguishing the feathers which tips form a part of the wing trailing edge and those that are often slotted, individually distinguishable and rather exposed. Most bird species have 10 primary feathers, in few cases this number may be 9 or 11 and only grebes have an exceptional number of 12 [40]. The number of the secondaries in contrast is variable and principally increasing with the bird size.

The rounded leading edge shown in the inset of Fig. 13 is formed by contour feathers that cover the front part of the arm wing and the inner part of the hand wing. These contour feathers are further supported by downs. Rows of greater coverts (tertiaries) cover the secondary and primary feathers (not shown in Fig. 13 but schematically indicated in Fig. 15).

Feathers are implanted in and develop out of skin follicles. The outer primaries are comparatively rigidly embedded in the skin and are held in place by ligaments [38]. The finger bones have dents to accommodate the ends of the feather quills although bone and feather quill do not grow together. The outer primaries are by such secured to either resist bending and torsional moments. The wing muscles are able to assist unfolding and folding of the wing as a whole but there is little evidence that incidence, sweep or dihedral of individual outer primaries can be adjusted independently by muscular action. Videler (Videler) mentions feather muscles of chicken and turkey that are successively attached to the calami (roots of feather quills) of neighbored primary feathers. The mutual connection forms 'control chains' having the consequence that the muscles can only act as to collectively increase or decrease feather incidences. The voluntary control is thus rather limited to the incidence of the wing tip and its camber as well as the ability to spread the feathers fore and aft by small amounts as well as to collectively increase incidence of primaries [41].

Functional tasks of the feathers according to Hertel [42] are

- formation of the structural lift carrying wing area
- sealing of the wing surface
- formation of the wing profile section
- fairing around the bones and
- thermal insulation.

Feathers that contribute to the lifting capabilities of the wing possess some unique properties:

- high loadability for a given structural weight
- flexibility
- small mutual friction important for wing folding and configurational changes.

Tension lengths of 31 km were experimentally established for the material of which feathers consist in contrast to conventional aluminium alloys, which achieve only 16 to 20 km. Last but not least to mention is the damage tolerance due to the ability of a single feather or assemblies of feathers to split into individual parts due to punctual forces as well as the ability to return into the initial form when the disturbing object has been removed. In this context it should also be mentioned that bird's moult offers the special opportunity to continuously replace worn out feathers.

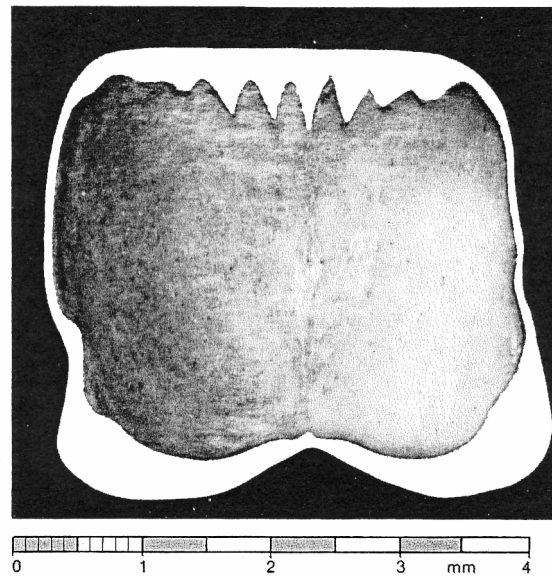


Fig. 14: Cross section through a primary feather quill of a swan at intermediate spanwise location [42].

The structural setup of feathers deserves attention because effects related to structural sizing and mass will be of interest for the present work. The cross section of a primary feather quill of a swan starts elliptically at the root but attains a more rectangular form shortly behind the spanwise location where the vanes start. The enclosed cavity is filled with foam approximately from this location outwards. The foam supports the walls similar to a technical sandwich construction. Fig. 14 shows a cross section at an intermediate location between root and tip. The width is slightly greater than the vertical extent of the quill. The side wall thickness is just 0.04 mm at the thinnest location but about 0.5 mm in the corners of the lower walls. The upper wall is serrated so that the wall thickness varies between 0.23 and 0.6 mm. The serration is supposed to secure the wall against buckling due to compressive stresses which come along with bending moments due to lift. It can be concluded that the quill appears to be an efficient structure to resist bending in the lift as well as drag directions. The described cross section also offers high torsional stiffness. Some differences in details like the central lower panel indent or the strongly variable lower panel wall thickness distribution which both may be significant for the structural behaviour are not found at technical wing boxes. However, a technical wing box construction shares some common design features with the cross section shown, like the fact that principal average wall dimensions (upper and lower panel, two side walls) exhibit similar trends. Shear webs (side walls) are much thinner than the upper and lower panels that carry tension and compression stresses that result from bending moments due to lift.

2.3.1.3 Wing Sections

Bird wing sections have comparatively high degrees of camber compared to technical wing sections used on aircraft (Fig. 15). The sectional camber is larger at the inner wing, becoming less towards the wing tip, a fact that had already been observed by Lilienthal [43]. Not only does the camber reduce towards the slotted wing tip, but the location of maximum camber moves to a farther aft position (Tab. 4).

Tab. 4: Maximum camber values and corresponding chordwise locations.

Section:	(a)	(b)	(c)	(d)
Maximum camber m	11.0 %	9.6 %	8.2 %	5.6 %
Chordwise position of maximum camber p	20.0 %	24.6 %	31.0 %	44.6 %

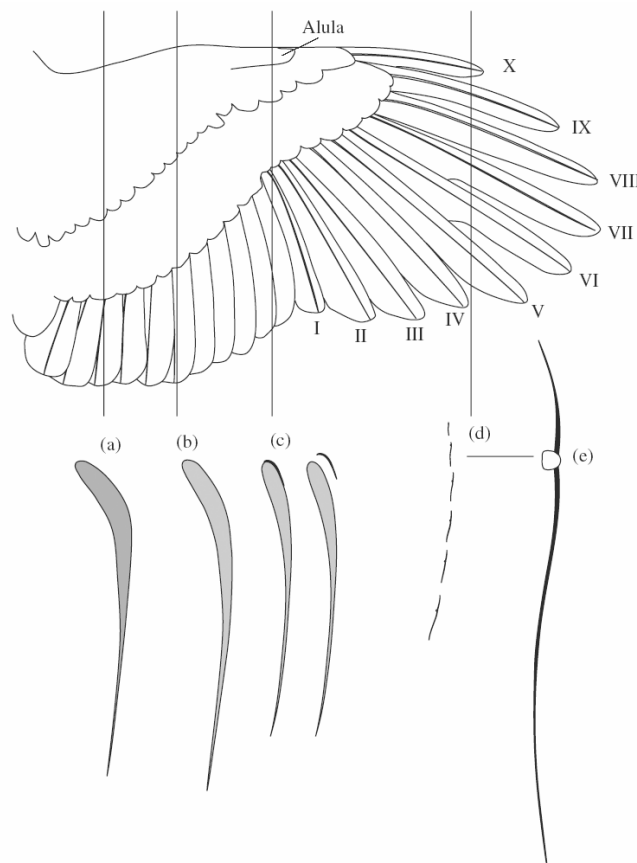


Fig. 15: Wing of a goshawk with cross sectional profiles at four positions ((a)-(d)). The cross section through primary IX in (d) is enlarged to show its actual shape (e) ([40], modified from original sketch by Herzog [38]).

Cross section (c) in Fig. 15, which is located right at the joint of arm and hand wing, shows the alula, which is implanted on the alular digit or “thumb”. The feathers at the alula can be articulated in such ways that two positions are possible, the first where the feathers are embedded in the contour and the second where the feathers are extended so that a slot is formed.

Substantially different from the inner wing sections are the slotted outer primaries (d). In Fig. 15, primary X forms the leading edge. The innermost part of subsequent outer primaries have mutual overhang. The outer part in contrast shows visible gaps when viewed from above due to spreading of the hand feathers and by the emargination of vanes. Emargination is the term for the sudden decrease in chord length of vane outer parts. This may occur at the narrow leading edge vane, at the wide trailing edge vane, or at both vanes simultaneously. Spreading of the hand wing and emargination forms the slots near the wing tip seen in many groups of birds. The enlargement (e) shows that each of the feathers in cross section (d) represents a more or less independent wing section.

2.3.2 Correlation of Wing Loading and Aspect Ratio with Fan-Out

The relative wing loadings of birds have been derived from data given in references [38] and [44] and are plotted versus aspect ratios in Fig. 16. Relative wing loading $(W/S) / (W/S)'$ is a dimensionless quantity which is introduced in order to eliminate the principal scale effect of increasing wing loading with increasing bird weight. Typical mean wing loadings for a given bird weight can be computed by means of the following regression equation that was derived using abovementioned data sets.

$$(W/S)' = k \cdot (W/W_{\text{ref}})^{0.3015} \quad (19)$$

where $k = 28.167 \text{ N/m}^2$ and $W_{\text{ref}} = 1 \text{ N}$. The coefficient of determination R^2 of the regression is 0.820. The data depicted in Fig. 16 is subdivided in a group of birds that have visibly slotted outer primaries and those that have closed or virtually closed wing tips in soaring flight. Species with slotted tips cluster between aspect ratios of about 5 through 8, which is in accordance with the findings of Herzog [38]. The wing loading is clearly below average. Masses of species with closed wing tips span from 0.006 kg for the golden cock up to 9.796 kg for the Albatross. However, the mean aspect ratio of this group is larger and the same is true for the average wing loading. A common factor of all the birds with slotted wing tips is that they soar over land. Bird species such as buzzards and eagles fly independently and use thermals on the lookout for prey. As has been discussed in chapter 2.2.1, low wing loading and also reduced induced drag directly minimise the power required for flight or increase endurance.

Herzog distinguishes these birds of prey with low wing loading from falcons with high wing loading. All seabirds as well as small songbirds belong to the other group.

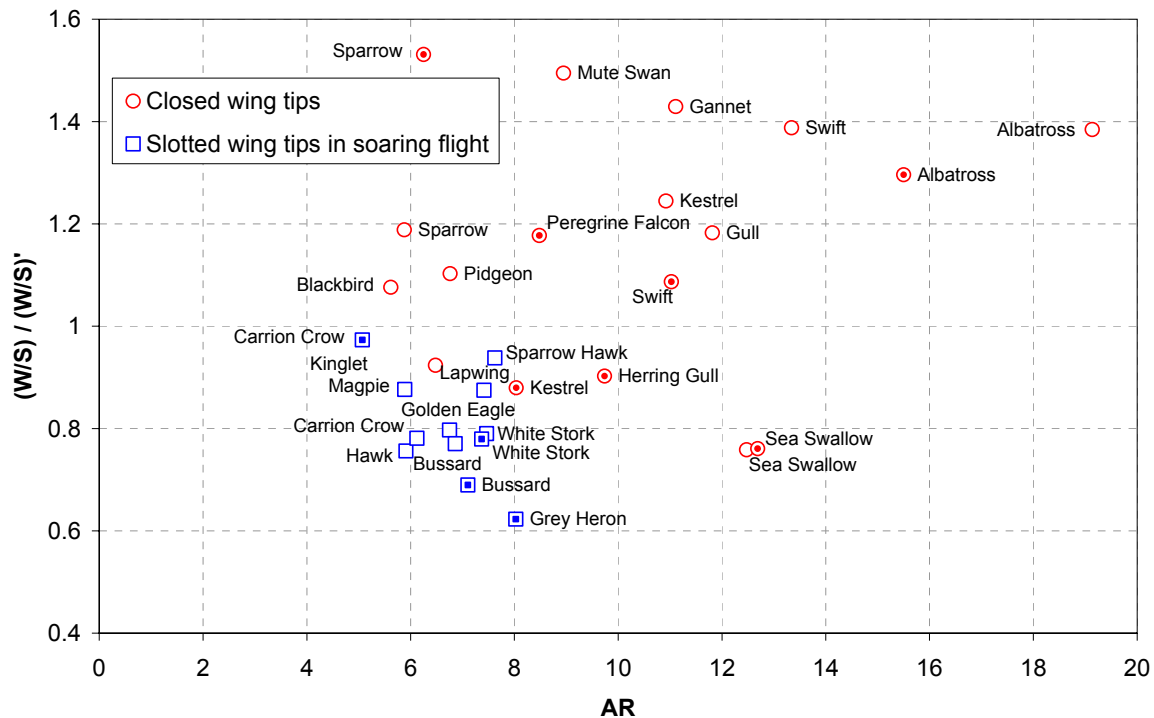


Fig. 16: Relative wing loading versus aspect ratio of bird wings (data indicated by open symbols [38], filled symbols [44]).

2.3.3 Functions of Slotted Outer Primaries in Flight

Among a multitude of attempts to interpret the function of slotted outer primaries are

- thrust production in flapping flight
- increase of maximum lift
- enhancement of low speed manoeuvrability
- induced drag reduction
- increase of static longitudinal stability and
- mitigation of wake vortices.

Fig. 17 is a sketch of a stork [43], a bird that has been extensively studied by Lilienthal, which clearly shows the fan out of 6 outer primaries. During downstroke, the outer half of the wing (outer sections c and d) not only produces lift but also thrust in the flight direction. The larger effective aspect ratio of the slotted wing tips as compared to a single closed tip allows the outer primaries to tilt into the oncoming flow so that the local angles of attack are decreased. The lift with respect to the local wind direction becomes zero in the tip region (section d) during upstroke, while it is slightly negative with respect to the freestream direction. All sections along the span produce drag during upstroke in contrast to the downstroke part of the wing beat cycle where net drag is only generated inboards. It has often been observed that the slots are usually closed during upstroke as

far as the overlap of primary feathers allow. Sweep back of the hand wing, which is frequently seen during the upstroke movement, automatically yields smaller stagger between subsequent outer primaries (compare also planforms in different states of gliding flight Fig. 19). If the outer primaries are collected to form a single wing tip without slots, the effective chord Reynolds number is greater which principally yields boundary layer drag reduction.

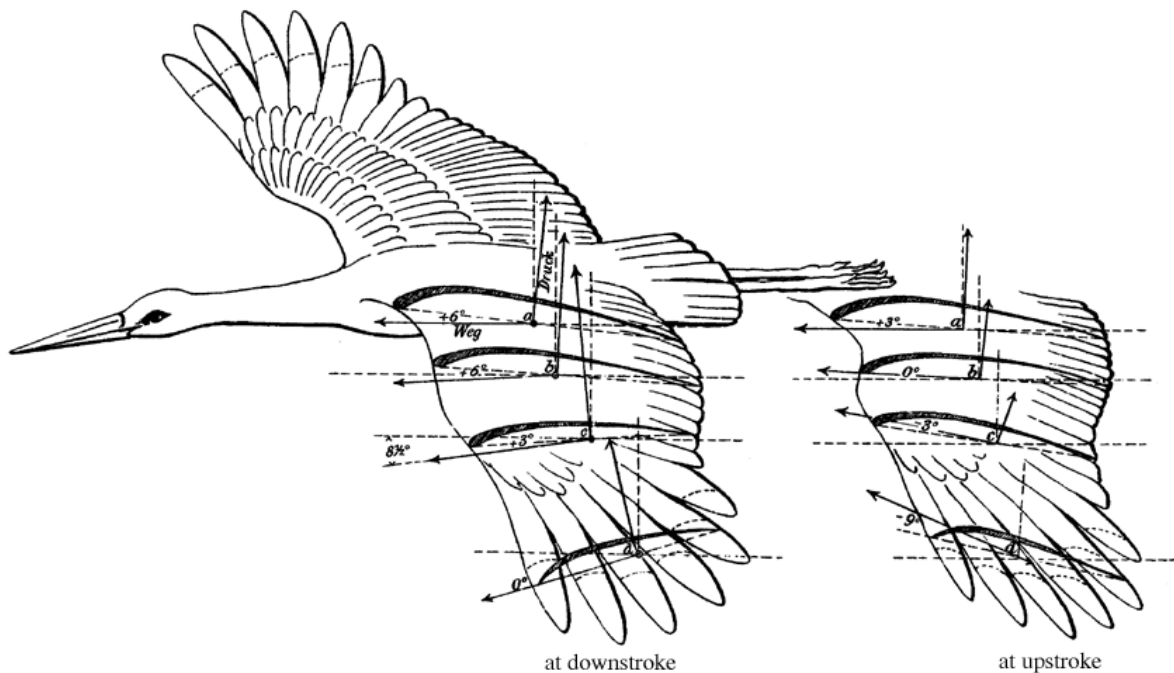


Fig. 17: Wing of a stork at different positions during the flapping cycle [43]. Shown are momentary flow directions (opposite direction of vectors labelled "Weg") and vectors of the resulting forces at sections a-d.

The quill of a primary feather of a condor is located at a distance of 14% of the chord length downstream from the leading edge. The part of the vane ahead of the quill is much smaller than the rear part. The theoretical location of the centre of pressure of a flat plate is at 25% chord given that the full leading edge thrust can be retained. Feathers limit the amount of air which can pass through the vanes, but leakage will always be found to some degree. Patone [45] actually measured the permeability of feathers and found that the leading part of the vane (or outer vane) of an outer primary allows transpiration that is an order of magnitude greater than that through the trailing part of the vane (inner vane). It was brought forward that the transpiration through the leading vane may act as a turbulence generator helping to avoid boundary layer separation being imminent given the small chord based Reynolds numbers found at outer primaries of birds. It can be concluded that large amounts of leading edge suction

are unlikely to be supported by the permeable surface and that in turn makes it likely that the centre of pressure is actually rather aft of the quarter chord location than ahead of it. Whatever the correct functional interpretation may be, it is obvious that aerodynamic loads are not in balance about the quill and thus a torsional nose down moment is produced that more or less decreases the feathers incidence by torsional twist. According to Ahlborn [46], an outer primary feather of a buzzard tilts forward during downstroke so that the effective geometrical sectional angle of attack is indeed reduced.

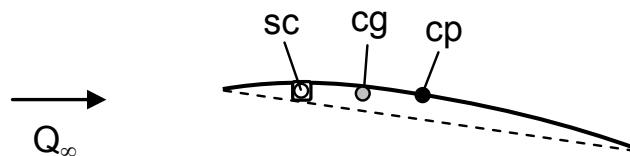


Fig. 18: Characteristic loci: sc - shear centre, cg - centre of gravity, cp - centre of pressure.

The line-up of the shear centre which is also the twist axis followed by the spanwise centre of gravity and finally the centre of pressure as sketched in Fig. 18 is aeroelastically favourable [42]. Loads at the primaries are higher during the downstroke than during upstroke (Fig. 17) so that the local incidences are at least partly adapted to the angle of attack variation during the flapping cycle. Lilienthal surmised that this mechanism may improve the thrust generation in flapping flight and suggested multi-winglet cascades for aircraft propulsion. Lilienthal's interpretation of slotted outer primaries is thus centred on utilisation for flapping flight.

Oehme speculated that the slotted outer primaries might increase the maximum lift capability of bird wings [47]. Spillman [77] supposes that the arrangement of multi-winglets in form of an accelerating cascade gives them the ability to carry high lift coefficients. Hummel questions this interpretation on the ground of two reasons [48]. First, he argues that the distance between the winglets is too large to have a considerable influence on high lift performance. His second argument against the explanation of winglet cascades as high lift devices is that the flow separation usually starts at the highly loaded central part of the wing and that effective high-lift devices should be placed there rather than in the lesser loaded outer parts of the wing.

It has been shown by Patone [45] that the coverts on the upper side of the main wing act like a special type of passive split flap, deflecting automatically at high angles of attack. The extent of boundary layer separation is effectively limited by fixing the separation point to the upper edge of the flap respectively coverts with the consequence that the maximum lift capability is increased. The effectiveness of the covering feathers would be significantly reduced if the outer part of the wing without such devices would not keep pace with the inner part and stall. Hertel argues that the outer slotted primaries

may prevent the bird from stalling. He bases this statement on observations of an osprey during steep approaches [42]. According to Hertel, the slotted outer primaries ensured suitable control and even allowed manoeuvring in this flight condition, even when the inner wing was close or even partly beyond the stalling angle of attack. Thus, it can be speculated that the cascades formed by the outer primaries should be able to generate at least as much lift increase as the central wing does, with its upper side split flaps. It appears that the winglet cascades of birds alone cannot significantly increase the maximum lift capability of a wing, but in connection with the coverts acting as means of separation control, they can. However, it is likely that at least a local high-lift effect of the cascade formed by the slotted outer primaries plays a role in avoiding premature deterioration of flow conditions at the cascade.

Ahlborn acknowledges the function of the separated primaries in supporting gliding flight on the basis of observations of soaring birds. Ahlborn remarkably states that split primary feathers prevent the formation of tip vortices which he refers to as a secondary benefit. However, Ahlborn did not give any detail on what evidence this statement was based.

The ability to adapt the wing planform to the flight regime is shown by Hertel [42] taking a vulture as an example. Hertel uses a sketch for his discussion which was originally put forward by Ahlborn [46]. Hertel states that the outer primaries are most fanned out during climb in a thermal at minimum power speed at which the sink rate becomes minimal. The multi-winglet configuration is obviously detrimental for gliding flight at or above the minimum drag speed since the outer primaries are swept backward so that they overlap and the slots are closed (Fig. 19 d) - f)). Flying at minimum drag speed maximises distance flown for a given difference in altitude. Moreover, the bird decreases wing area the faster it flies, which directly reduces wing profile drag. This adaptation of the wing loading also allows the bird to fly at suitable section lift coefficients which would otherwise be smaller than optimum.

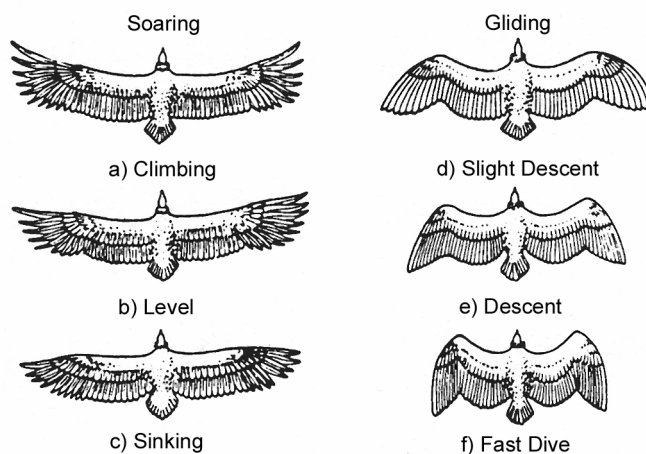


Fig. 19: Variable wing planform of a vulture (schematic illustration reproduced from ref. [46]).

Primaries of birds that soar over land are not only longitudinally separated but they bend upwards and separate vertically under aerodynamic loads, which is thought to reduce induced drag as already discussed on theoretical grounds [49], [48], [50].

Tucker tried to experimentally measure this drag reduction effect [51]. He used a live male Harris' hawk (*Parabuteo unicinctus*) (Fig. 20) of 0.67 kg mass as a test specimen gliding freely in a wind tunnel. The measurement section of the wind tunnel was inclinable by an angle γ so that the bird could fly in different updraft conditions. The drag of the bird obtained from $D = m \cdot g_0 \cdot \sin(\gamma)$ was compensated by a corresponding thrust component. In order to establish the net effect of the wing tip cascade, performance of the original wing was compared to that where the primaries had been clipped (both configurations outlined in Fig. 20).

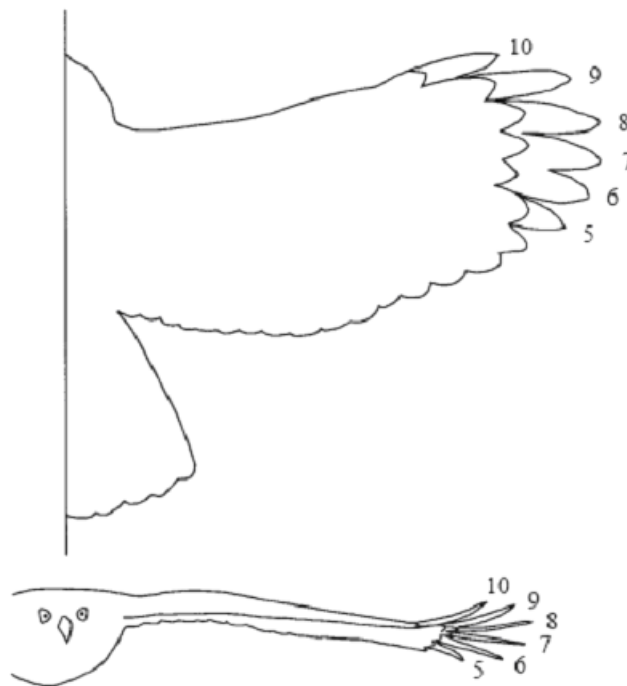


Fig. 20: The Harris' hawk in flight, seen from above (unclipped wing span 1.06 m) and head-on (unclipped wing span 0.92 m) [51]. The lines at the bases of primary feathers 5-10 show the tips of the feathers after clipping.

The Harris' hawk had 10 primary feathers on each half-wing. The bird increased wing span almost linearly as speed decreased for both the unclipped and the clipped configurations. In both cases, span, wing area and aspect ratio varied significantly with speed as can be seen from the data summarised in Tab. 5. Interestingly, the maximum lift coefficient appears not to have been affected by the clipping. Reynolds numbers based on a wing mean chord of 0.205 m varied from $0.90 \cdot 10^5$ through $2.09 \cdot 10^5$.

The drag of the bird was measured before and after removing the slots by clipping the tip feathers by 76 mm (primary feathers 10-6) and 38 mm (5). Maximum lift to drag ratio of the bird before clipping was 29% greater than after. The advantage for the unclipped configuration in endurance parameter was 38%. The larger difference in endurance can be solely attributed to the lower wing loading of the unclipped wing, according to eq. (18).

Attempts of Tucker to identify individual drag components suffered from significant uncertainties due to the fact that profile drag could only be roughly estimated. Tucker assumed the ratio of the actual wing induced drag to that of an elliptically loaded wing of equal span $D_i/D_{i,ell}$ for the clipped wing without slots to be 1.10.

Tab. 5: Geometric and performance parameters of a gliding Harris' hawk [51]. Characteristic figures highlighted in the lower part of the table distinguish both configurations.

Configurations ↓		b [m]	AR	Q_∞ [m/s]	c_L	L/D	$w^{-1} = dt/dH$ [s/m]
a) Unclipped	Max. Lift	1.069	5.22	6.5	1.16	7.90	1.20
	Max. Endurance	1.021	5.12	7.6	0.92	10.02	1.32
	Max. Range	0.938	4.89	9.5	0.67	10.50	1.10
	Fast Glide	0.697	3.72	15	0.37	7.87	0.52
b) Clipped	Max. Lift	0.834	4.07	7.3	1.18	6.72	0.92
	Max. Endurance	0.838	4.08	8.3	0.91	7.97	0.95
	Max. Range	0.796	3.97	10.5	0.61	8.17	0.78
	Fast Glide	0.658	3.49	15	0.39	7.09	0.47
Percentage Deviations (a) - b) / b)	Max. Lift	28%	28%	-11%	-2%	18%	31%
	Max. Endurance	22%	25%	-8%	1%	26%	38%
	Max. Range	18%	23%	-10%	10%	29%	42%
	Fast Glide	6%	7%	0%	-5%	11%	12%

Taking a value for the drag area of the bird body from earlier measurements on frozen hawk bodies, he derived an estimate for the profile drag coefficient of the clipped hawk wing of 0.0359 for speeds of 12.2 m/s and above and applied this value also to the unclipped configuration. It must be mentioned that Pennycuick [52] estimated the minimum profile drag of a living bird of the same species by the momentum loss method to only 0.0207 (empirical standard deviation ± 0.0079). This wing profile drag coefficient was applied to the unclipped wing and at this time, the drag equation was solved for induced drag. Tucker expects the induced drag of the unclipped configuration to be only 62% of an elliptically loaded wing of equal span. Tucker estimated the upper bound of that ratio to be 93% on the basis of an uncertainty analysis. He concluded with his opinion that tip slots in fact reduced induced drag in the experiment and increased span efficiency. It may be speculated that the severe alteration of the aerodynamics of the

bird with the clipped feathers caused the profile drag to extraordinarily increase. This wing profile drag may not have been present at the original unclipped configuration. In this case, the induced drag would turn out higher due to the determination method of just subtracting the profile drag of wing and body from the total drag and the span efficiency would turn out to be smaller.

Theoretical studies on the effects of outer primaries on the flight performance of birds are scarce. Hummel ([50], [48]) conducted numerical as well as experimental studies on the drag reduction capabilities of multi-winglet configurations that resemble cascade arrangements of the outer primaries of birds. The numerical study, for which a panel method was used, predicted significant reductions of induced drag of 15 percent for three winglets that extended over 50% of the half span. The vertical spread of the upper- and lowermost winglets, which had been moved out of the inner wing plane by applying +20 deg dihedral to the upper winglet, 0 deg to the winglet in the mid position and -20 deg to the lower winglet seen from the front or the rear had the most significant influence on induced drag. Adding other winglets between the bracketing upper and lower winglets produced only small additional drag gains.

An experimental study conducted in a low-speed wind tunnel showed that the maximum lift to drag ratio of a configuration with three winglets is slightly inferior compared to a simple rectangular wing of identical span. The endurance parameter, which correlates with the maximum flying time and the minimum power condition, exhibited a maximum advantage of the multi-winglet configuration of 11.7% over the rectangular wing that had the same span.

Oehme [47] studied the aerodynamic performance of wings under steady state gliding conditions with simplified model calculations based on classical results of lifting line theory without regard of extensions for multiple surface configurations such as those proposed by Munk [7]. Oehme inferred from his calculations that a reduction in total drag and a resulting improvement in gliding performance is only likely to occur with birds larger than thrushes since the Reynolds numbers of the flow past the separated primaries of smaller birds might outweigh gains in vortex drag reduction. Oehme stated that reduction of drag by separated primaries will increase with the number of separated outer primaries, with their area relative to the total wing area, with the lift coefficient of the wing, and with decreasing aspect ratio.

Furthermore, Oehme discussed the probable advantages of thin cambered wing sections with sharp leading edges. Such wing sections might help triggering transition such as to produce turbulent boundary layers that may serve as a safeguard against laminar separation with its inevitable drag increase and lift drop. Referring to earlier measurements of Schmitz [53], the critical Reynolds number of such profiles can be reduced down to $1.0 \cdot 10^4$. This Reynolds number is about equal to the average chord

based Reynolds number of the outer primaries of those medium size bird species that occupy the span from the redstart (*Phoenicurus phoenicurus*) with a span of 0.22 m to the black-headed gull (*Iarus ridibundus*) with a span of 0.9 m for which Oehme presents statistical data. The mean chord based Reynolds number of the main inner wing is about an order of magnitude larger and hence generally less critical.

To conclude, it is rather obvious that the arrangement of the outer primaries of different bird species cannot be attributed to one dominating design purpose, instead it appears that evolution came up with a rather complex mixture of functions to simultaneously satisfy a multitude of requirements.

2.4 Non-Planar Aircraft Wing Concepts

In order to achieve reductions in vortex drag without substantial increases in wetted area and profile drag, early low aspect ratio end plates for reduction of induced drag were replaced by smaller and more efficient profiled surfaces of higher aspect ratios. The term winglet was introduced by Whitcomb [55]. Several other terms have been used describing essentially identical concepts. Among those is the classical term end-plate used by Weber [11] to theoretically describe the influence of vertical plates set at an incidence to the oncoming flow, which would nowadays referred to as winglets. Wing tip devices seen on many Airbus aircraft are so called tip fences (Fig. 21, example applications listed in Tab. 6). A concept where the non-planar surface is mounted a short distance behind the wing on a boom that is attached to the wing tip was termed diffusing vane [56]. Nevertheless, in a broader taxonomy, these devices could well be classified as special embodiments of winglets. Configurations where two winglets are arranged at dihedral angles within a range of $\pm 45^\circ$, for example, are referred to as split tip configurations [12]. Spillman [57] called his multi-winglet arrangements wing tip sails.

Tab. 6: Application of tip devices on large commercial transport aircraft.

Tip Device Type	Application Examples
Whitcomb ¹	KC-135, C-17, CRJ-200
Wing Tip Fence	A310, A320
Canted Winglet	A340, B747-400
Blended Winglet	B737-BBJ/800/900

¹ Whitcomb has tested configuration with and without a lower vane, thus the conventional winglet which is attached to the wing tip at right angles will be also referred to as "Whitcomb winglet".

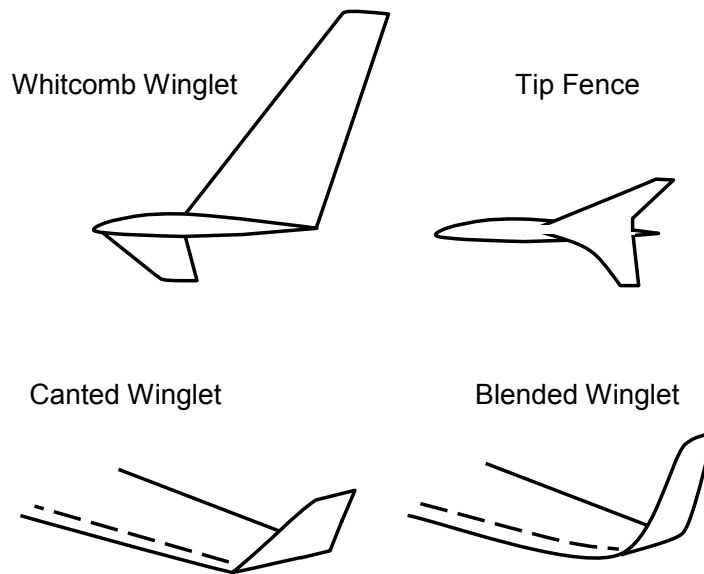


Fig. 21: Winglet and wing tip device geometries.

Synoptic theoretical treatments of various non-planar wing configurations have already been discussed above. The review on induced drag reduction of Kroo [14] itself quotes several earlier reviews on the topic including the role of non-planar configurations and in particular that of winglets. A comprehensive summary on winglet technology and winglet design is provided by Freestone [54].

This section of the present thesis concentrates on concepts that have been intentionally developed for technical implementation on aircraft. Beside practical results from wind tunnel and flight tests, theoretical results will be also discussed as far as they are related to concepts that have been technically realised. Winglet configurations that prevail for practical applications are discussed first before attempts of technical adaptation of multi-winglet concepts are looked at.

2.4.1 Technically Prevailing Winglet Systems

2.4.1.1 Configurations and Performance Implications

It is Whitcomb's merit to have experimentally shown that winglets produce performance gains even under the rather complex conditions of transonic flow. The experimental evidence from wind tunnel tests on half and full models of the military tanker KC135A and the subsequent trials with full size models paved the way for winglets to become accepted as a design feature of large transport aircraft. Reductions in total drag of up to 5.7% due to installation of a rather large vertical winglet with $h/s = 13.5\%$ for a cruising Mach number of 0.79 and a lift coefficient of 0.415 were inferred from wind tunnel tests

compared to 5.9% established in flight tests at the same conditions [58]. Similar percentage values are given for fuel mileage improvements indicating that the added mass for the winglet installation and wing strengthening had only minor impacts. An estimate of an additional 269 kg of added mass was given by Ishimitsu et al., of what only 96 kg were attributed to the two winglets made of an aluminium, honeycomb and glass fibre composite structure [59]. Among the best known winglet configurations is that shown in the upper left corner of Fig. 21, which is commonly referred to as "Whitcomb winglet". Whitcomb also developed practical winglet design guidelines with emphasis on applicability for large subsonic transport aircraft. The rearward mounting of the larger upper winglet was intended to reduce the risk of a premature shock formation caused by superposition of the low pressure regions at the leading edges of wing and winglet that was expected to be of a concern for designs where the winglet root chord extends over the whole length of the planar main wing tip chord. The lower winglet in turn was intended to reduce the loading on the larger winglet. In its original appearance dihedral angles were 72 deg for the upper and -54 deg for the lower winglet.

So-called blended winglets that were developed by Aviation Partners are installed on various members of the B737NG aircraft family (for example on BBJ, -800 and -900 derivatives) [61]. It is claimed that the blending allows for the chord distribution to change smoothly from the wingtip to the winglet, which is claimed to optimise the distribution of the span load lift and to minimise airflow separation due to interference. The buffet onset boundary was not changed by adding winglets according to reference [61] so that the full operational envelope of the aircraft could be retained. The B737NG-family covers a maximum take-off mass span that is ranging from 56,470 through 79,010 kg [68]. All versions basically share the same wing. While the smaller versions -600 and -700 have been initially offered with plain wing tips only, the largest versions -900 could only be ordered with large blended winglets. The variant -800 was offered alternatively with or without winglets but with the option to later retrofit winglets. The percentage improvement in block fuel of the latter version with winglets is up to 4% lower than that of the version without winglets [61], indicating roughly the net benefit that winglets may provide. This is in accordance with a statement by Kreuzer [62] who points out that the induced drag reduction potential of newer jet transport aircraft designs is less than that of the B707 (or KC135) because of smaller tip loadings and smaller spanwise circulation gradients at the tip.

In contrast, the much smaller wing fences do only yield a drag reduction of 1.5% in cruising flight [60].

A large winglet offers a large drag reduction at a high wing lift coefficient, but the wing lift coefficient below which the device increases drag will be higher due to the increased wetted surface area and profile drag. The advantageous effect of virtually increasing span with a non-planar design is evident from a glance at newer sailplane designs that

have a span limitation. Trade-offs are, by and large, dominated by induced and profile drag. Winglets of $h/s = 0.133$ were designed, build and tested on an ASW 19 standard class glider as described by Horstmann [63]. Standard class single seaters are limited to 15 m span. Improvements in lift to drag ratio of up to 7% were obtained at high lift coefficients. Below a lift coefficient of 0.47 corresponding to a speed of 115 km/h at a wing loading of 310 N/m², the added drag components due to retrofitting of the winglets became higher than the induced drag savings. A similar "break-even point" is given by Eppler [15] for a comparable configuration determined by means of numerical analysis. Whitcomb [55] pointed out that the skin friction drag penalties for a full scale application associated with the additions of winglets would be somewhat less than those for Reynolds numbers typical for conventional wind tunnel testing. This means that the break-even condition is a function of Reynolds number. The higher the Reynolds number, the easier it is to obtain performance gains with winglets.

Studies that compared winglet and planar wing layouts with constrained bending moments have been undertaken by Jones and Lasinski [20] who followed the lead of Prandtl [19] regarding the ideal wing planform for minimum vortex drag for a given integrated wing bending moment. Jones and Lasinski established that a winglet configuration with ideal planform shape and twist is not much better regarding induced drag than an ideal planar wing with 10% more span but the same integrated bending moment.

Ewald [65] examined winglets as a retrofit option experimentally. Whitcomb winglets as shown in Fig. 21 with and without lower vanes were compared to a wing tip extension of roughly identical surface area. The winglet configuration with only the upper surface was found to perform significantly better than that with the lower surface added. Beside the lift to drag performance, also the wing root bending moment was measured. Ewald concluded that for equal added wetted surfaces, a winglet offers greater performance gains compared to a wing tip extension. Drag reduction by adding winglets was found to be greater and the wing root bending moment increase significantly smaller than with a wing tip extension.

Tests were also conducted with an extended single slotted trailing edge flap. While the induced drag reduction of 15% was identical for flap deflections of 14° and clean configuration, it was only 6 - 8% for a flap deflection of 40°. Much of the bound vorticity is shed into the wake at the outer end of the flapped section in this case. The fraction of the lift distribution affected by the winglet is smaller than in clean configuration, which may explain the decreased winglet efficiency.

Maximum lift coefficients for the configuration with the single upper winglet surface increased, but they were less than the increments due to the tip extension also tested.

2.4.1.2 Winglets as a Retrofit Option

It has been speculated that significantly greater performance gains due to winglets could be obtained if the tip devices are considered as a design feature from scratch in contrast to winglet retro-fitting. The reason for this expectation is centred on the fact that an integral design allows better tailoring of the lift distribution by optimised chord and wing twist distributions and also a more specific wing structural optimisation [62]. On the contrary, winglets for current aircraft are often optional items and sometimes designed as quasi-retrofits because of the work-sharing of main aircraft developer and winglet supplier [61]. Unlike earlier concerns, there are also indications that winglets are rather particularly suitable as a retrofit measure.

The special suitability for retro-fitting was already shown by NASA's winglet development campaign in the 1970s. Comparison of numerical results obtained from vortex-lattice computations of KC135 configurations [59] with winglets and wing tip extensions, which were later substantiated by wind tunnel test data [67], indicated that the wing root bending moment increment for a given induced drag reduction of 14% compared to the original wing (thus: $\Delta C_{D,i,winglet} / \Delta C_{D,i,Tip\ Ext.} = 1.0$) is smaller for the winglet configuration ($\Delta C_{M,b,Tip\ Ext.} / \Delta C_{M,b,winglet} = 1.31$). The pitching moment difference about the fixed geometric aerodynamic centre was also much smaller compared to the original wing ($\Delta C_{M,25,Tip\ Ext.} / \Delta C_{M,25,winglet} = 1.80$). Since it is not desirable to change the location of the wing fuselage intersection or to alter the fuselage centre of gravity for an aerodynamic performance enhancement measure, the trim drag increase would be significantly greater for the tip extension than that due to the attachment of winglets. This effect is a particular consequence of the swept back wing concept. The example is given to show the difficulty if one is on the lookout for conclusions of general validity.

2.4.1.3 Multidisciplinary Approaches to Winglet Design

A multi-disciplinary numerical parametric study of wing tip devices for large jet transport aircraft has been documented by Büscher et al. [69] considering both high speed cruising and low speed performance. Induced, profile and wave drag, structural mass penalties of the basic wing using a correlation to wing root bending moment, mass increments due to the winglet mass itself and trim drag increments have been considered. Modules for the mentioned items were integrated such as to form a comprehensive analysis tool.

A parametric variation of winglet dihedral and sweep at cruise conditions showed that the sweep had only little influence and favourable dihedral angles were lying between -50 and $+20^\circ$ for program settings modelling a larger impact of mass increments on the overall performance and -50 to $+50^\circ$ for a weighting that caused the mass penalty to be less important. Chord distribution, span data and washout were prescribed. The wing tip

configuration with small anhedral angles thus provided the most favourable predictions. Wing tip extensions where the dihedral angles were identical to the main wing value of 7.6° were almost as good as the optimum configuration. The conclusion drawn by the authors was that wing tip extensions appear preferable compared to the addition of winglets, which is opposing the findings of Ishimitsu et al. [59] and Loptien [67]. Büscher et al. neither allowed pronounced changes of local wing section incidences nor changes of local wing respectively winglet chord lengths in their parametric studies. Since optimum winglet configurations where the additional surfaces are rather perpendicular to the main wing always show sudden changes of these properties in the corner region, it may be argued that the constraints set prevented the identification of more suitable winglet configurations.

2.4.1.4 Wake Vortex Properties

Winglets are devices that reduce induced drag and it can be directly inferred that the energy contained in the wake vortex systems must be reduced. Surveys of the wakes behind wings with simple tips and two-surface Whitcomb winglets installed on a jet transport model (B747-100) showed that the rolling moment of a wing that is positioned behind the vortex generating wing in clean configuration can be lowered by 10-15% ([71], alternatively refer to [22]). An analogous comparison of the vortex generating aircraft model being in landing configuration, on the contrary, did not cause a reduction. This can again be attributed to the optimisation of the winglets for cruise and the fact that the winglets consequently operate under off-design conditions if the high lift configuration is set.

Nockemann [72] experimentally studied the effect of planar parabolic and elliptical tip geometries as well as of various winglet configurations on wake vortices. The largest winglet resembled basically a symmetrical tip fence with an upper and a lower surface with $(h/s)_l = (h/s)_u = 0.104$. Winglets were mounted so that the straight trailing edges were flush with the main wings trailing edge, had taper ratios of 0.25 and possessed dihedral angles of $\pm 60^\circ$. The geometric mean chord of the winglets was just 18.75% of the chord of the rectangular main wing for the test arrangement with an aspect ratio of 5.0. Nockemann observed that a secondary vortex with the same rotational direction evolved from the winglet tip beside the wing tip primary vortex. Both vortices induce opposing velocities between the two cores and thus reduce convection in-between. Experimental evidence shows that this finally resulted in the merger of the cores. The tip vortex remained nevertheless stronger, owing to the fact that the winglet surfaces were rather small and not optimised for the flow conditions. Maximum tangential velocities of the winglet configurations were almost halved compared to the planar wing tip (tip cap identical to those equipped with winglets) while the mean distance from the overall vortex centre where the maximum tangential velocities occurred was doubled. The

influence of the winglet shape however, whether it was just one sided or double sided was found to be negligible.

A recent paper that deals primarily with measurement techniques suitable to assess wake vortex properties shows a similar enlargement of the core region and spreading of vorticity of a vortex system with two cores generated by a wing tip fence [73].

2.4.2 Attempts of Technical Adaptation of Multiwinglet Systems

This section intends to give a review on attempts of technical adaptation of multi-winglet concepts. Emphasis will be put on experimental approaches, i.e. wind tunnel measurements and flight tests. Tables provide concise summaries of publications in this regard.

Lilienthal [43] suggested multi-winglet wingtips for aircraft that resemble the outer primaries of birds. The purpose was to imitate wing flapping of birds for propulsion. His wing-flapping machine was set-up to use either muscle-power or an engine for propulsion (Fig. 22). In 1894 Lilienthal tested the machine powered by a CO₂ engine but the results from the tests were not encouraging.



Fig. 22: Lilienthal's wing-flapping machine [74].

A bigger version was probably completed but had never been tested because Lilienthal died in 1896 after a crash with one of his standard glider designs.

Cayley's paradigm stipulates that the lift production should be decoupled from generation of propulsive forces. Aircraft designed according to this paradigm turned out to perform better than those adapted to the natural example. The idea to propel an aircraft by means of slotted wing tips was hence abandoned but the idea to reduce induced drag was held up. Some publications discuss wind-tunnel and flight test results of rigid multi-winglet configurations aimed at improving aerodynamic characteristics of wings. Appendix A contains a synoptical summary of key experimental data from

references [43], [48], [57], [75], [76], [77], [78], [79], [80], [81], [82] and [84] that will be used to derive fundamental trends associated with multi-winglet configurations.

Statistics show that it was attempted in most cases to exploit the increase in effective aspect ratio by using wings that have particularly low aspect ratios (3.81 - 5.12) ([50], [57], [76], [79]). Some tests were performed with medium aspect ratio wings (6.66 - 8.00) ([80], [75], [82]) and only two references report on multi-winglet cascades tested on high aspect ratio glider [81] and motor glider wings [84]. The largest aspect ratio was that of a Schempp-Hirth Janus Ce with an aspect ratio of 21.2 [81]. Winglet numbers varied from two for split tip configurations, over three up to a maximum of five. Relative spanwise extent of winglets will be expressed by the non-dimensional winglet root coordinate. The largest winglets were those of the split tip configuration of reference [80] with $\eta_0 = 0.67$, the smallest those of the multiwinglet configuration of reference [81] with $\eta_0 = 0.93$. The spread of winglet dihedral angles varied from 0° for references [80] and [79] up to 90° for the so called tip sails of references ([57], [76]). Most configurations had small quarter chord sweep angles with the rear split tip winglet of reference [80] and the forward winglet of the split tip configuration of reference [75] having rather large values of 38° sweepback. Wind tunnel test Reynolds numbers based on the mean geometric chord ranged from $0.29 \cdot 10^6$ through $1.50 \cdot 10^6$ for the main wings and $0.036 \cdot 10^6$ through $0.380 \cdot 10^6$ for the winglets. Corresponding values for the two flight test configurations were $1.75 \cdot 10^6$ and $7.5 \cdot 10^6$ for the main wings and $0.15 \cdot 10^6$ and $0.70 \cdot 10^6$ for the winglets where the higher figures are related to reference [57] and the lower to reference [81]. Only Kravchenko [79] made wind tunnel measurements at transonic freestream Mach numbers of up to 0.85. Maximum flight test Mach number at Spillman's tests with a Morane-Saulnier M.S. 760 jet trainer was 0.33.

Statistics show that the range of configurations and experimental conditions is inhomogeneous, which makes it difficult to draw meaningful conclusions backed up by quantitative data. All experiments for which quantitative results are compiled in Appendix A compare aerodynamic performance of the winglet configurations with the corresponding figures of a basic wing without winglets. Some authors used configuration that guaranteed identical spans and aspect ratios of winglet and basic wing configurations ([80], [81]), others just added the winglet surfaces leaving the basic wing unchanged. Since winglet surfaces are small, the latter had always the consequence of increased aspect ratios. Considering the often limited measurement accuracy, gains in span efficiency could have also been obtained by a planar tip extension adapted to arrive at the same aspect ratio increment as already stated by Zimmer while discussing Spillman's flight test results [83]. However, Kravchenko [79] presents experimental evidence that a multi-winglet configuration has less drag than a straight tapered wing of the same span. Considering the higher profile drag, the induced drag must necessarily be less than that of the planar wing.

Interpretation of the improvements in lift to drag ratios in Appendix A should be exercised with care. Those two references were span and aspect ratio consistency was given obtained maximum gains in lift to drag ratio of 1.8% for the flight tests of Sunkomat [81] and 6.3% for the wind tunnel results of Smith [80] compared to the respective planar wings. Corresponding gains in endurance parameter $c_L^{3/2}/C_D$ for the best points are 1.2% and 2.8% respectively. These gains are rather modest compared to those obtained with single winglets. The fact that the endurance parameter gains are smaller than those in lift to drag ratio is opposing all other experimental results in Appendix A. It has been argued that the difference in configurations excludes the direct comparison of performance figures. Nevertheless, this does not apply for the mutual comparison of the two distinguished performance parameters for maximum range (maximum lift to drag ratio) and maximum endurance (maximum endurance parameter) of the individual configurational couples of winglet and datum configuration. The relative excess gain in endurance parameter over lift to drag ratio of the multi winglet configuration of Sunkomat is thus $1.2\% - 1.8\% = -0.6\%$. Fig. 23 depicts the corresponding figures of Tab. A2 of Appendix A.

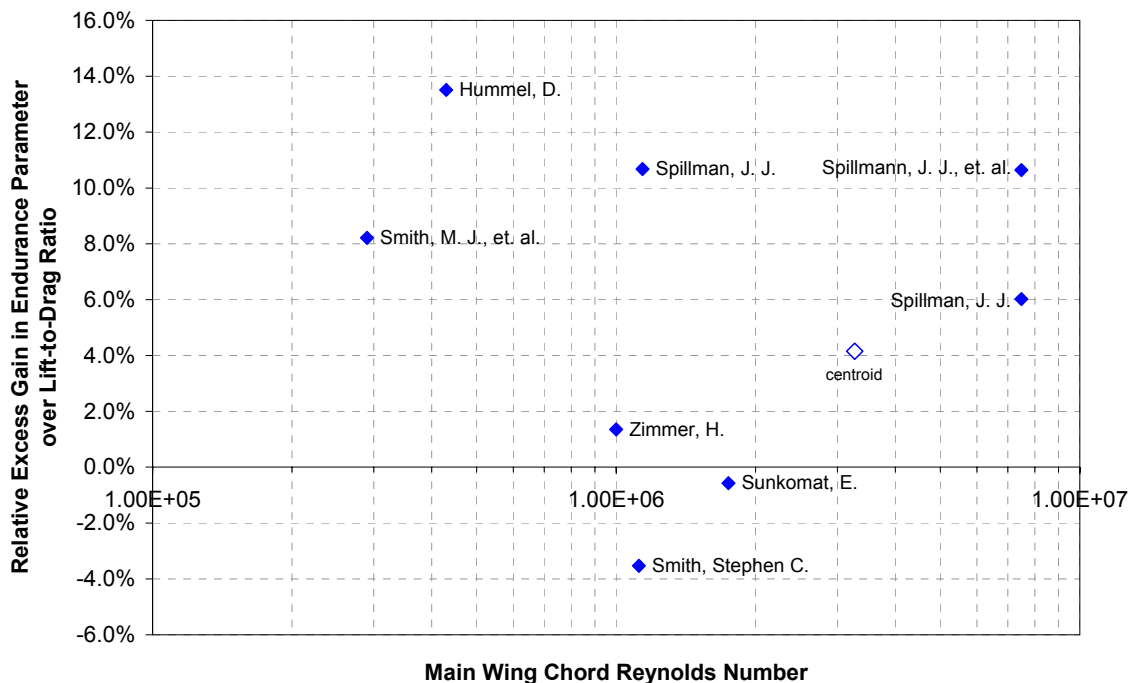


Fig. 23: Relative excess gain in endurance over lift to drag ratio derived from multi-winglet and split-tip experimental data versus chord-based Reynolds number.

As expected, the gains in endurance parameter are higher than those in lift to drag ratio for most experiments. This is in accord with similar findings for single winglet systems because the optimum for the endurance condition is obtained at a higher lift coefficient than the maximum range condition. The relative contribution of vortex drag increases

with lift coefficient while the profile drag contribution decreases. Thus, winglet configurations that decrease vortex drag but increase profile drag are more efficient at conditions where the vortex drag is high than at conditions where it is low. Negative relative excess gains may be obtained not only due to one reason. Firstly, the profile drag polar must be regarded. If the profile drag increases at low lift coefficients due to Reynolds number effects, the maximum endurance of the non-planar design may be slightly higher than expected from simple extrapolation of the datum wing drag polar. Secondly, the interference drag coefficient strongly depends on design details and may not be constant but increase with lift coefficient. Thirdly, the lift coefficient for the maximum endurance condition has been estimated using results obtained from the parabolic drag polar. The real best points may be actually different.

Küppers [78] discusses the effect of wing tip tanks on induced drag such as installed on the M.S. 760 jet trainer used by Spillman [57] for his first flight test programme. Referring to earlier theoretical treatments he concludes that tip tanks indeed yield a small reduction in induced drag but also states that the primary function is to increase fuel capacity.

Conclusions with respect to performance drawn from experiments with multi-winglet configurations can be summarized:

- Gains increase with increasing Reynolds number shown by a decay of lift coefficient where induced drag savings equal drag increments due to other drag components ([57], [76]). Some wind tunnel tests at the lower end of the Reynolds number ranges stated above did not show any improvement in overall drag characteristics [82].
- Comparisons of single winglet and multi-winglet configurations with planar wing configuration at transonic Mach numbers show superior performance for the non-planar configuration with a slight advantage for the single winglet over the multi-winglet configuration [79].
- A split tip configuration yields higher span efficiencies than an elliptical wing if surface area and span remain unchanged [80].
- Multi-winglet systems can increase endurance parameter as well as lift to drag ratio compared to a planar wing tip under the constraint of equal span and equal wing aspect ratio [81].
- Most authors report of flow separation, mostly at the root sections of multi-winglet cascades ([81], [50], [75], [80], [57], [77], [78]). Spillman [57] reports on separation on the lower surface of a highly cambered winglet root section at low angles of attack. This separation disappeared at higher incidences but another separation region appeared on the upper suction side. A different type of separation was identified by Smith [80] ahead of the second winglet of his split tip configuration. The stagnation of fluid ahead of the blunt winglet leading edge produced an adverse pressure gradient over parts of the rounded wing tip surface to which the winglet was attached. The

stagnation effect was obviously strong enough to cause the boundary layer to locally separate, despite sweepback, which usually mitigates this effect. This type of separation is known to produce a so-called necklace vortex. Sunkomat [81] had to adapt winglet incidences because of boundary layer separations at winglets 3 and 4 of a five winglet cascade (index ascending from leading to trailing edge of main wing), while Hummel [50] found boundary layer separation on the highly loaded leading winglet of his wind-tunnel configuration.

Split tip or multi-winglet configurations are usually arranged in form of accelerating cascades. The configuration proposed in the patent of Santos [85] is different in this respect, because the leading winglet is mounted on the main wing tip with anhedral while subsequent winglets are mounted with reduced anhedral respectively increasing dihedral angles so that a decelerating cascade arrangement is formed. Similarly, Pfenninger [102] suggested a wing configuration with three winglets in a cascade setting where the dihedrals of subsequent winglets increase in flow direction.

These setups are in contrast to the natural example of bird outer primaries where the forward winglets point upwards and the rear winglets downwards. Knowledge from turbo-machinery engineering corroborates that loadability expressed in terms of a maximum lift coefficient of a blade section of an accelerating cascade (such as found in turbines) is significantly larger than that of a decelerating cascade (such as found in compressors). Because nature prefers accelerating cascades, it appears that such arrangements allow a greater loadability, whatever the practical extent may be.

The idea of adjustable multi-winglet systems has been put forward by Spillman [41] for gust and manoeuvre load alleviation by means of winglet twisting. The patent of a split tip configuration by Klug [86] suggests a similar functionality.

Adaptation of multi-winglet cascades by means of hinged flaps on the winglets is proposed in the patent of Mederer [87]. Flaps are installed in order to adapt the cascade depending on the particular flight phase requirements. The slots between winglets can be alternatively closed for flight phases where the lift coefficient is low and opened for low speed flight phases where lift coefficient is high.

The fact that the wake vortex core strength is significantly reduced by multi-winglet wing tips has long been known as Zimmer [83] reports based on earlier experiments of Cone [89]. The lower core vorticity also yields a quicker wake vortex dissipation, which makes multi-winglet configurations particularly attractive as a means to reduce separation of aircraft as discussed in 2.1.4. This is at least in principle true. Design of technical high-lift systems and basic wing design paradigms constitute constraining factors that reduce the enhancement potential and make it necessary to analyse in more depth to what degree the basic drag reducing effect can be actually realized.

The effects of non-planar wing tip configurations on wake vortex properties have caused to suggest such configurations for special purposes apart from transport aircraft applications. A common problem with agricultural utility aircraft ("crop dusters") is the inhomogeneous spray distribution on ground because of aerosol concentrations that are due to the wake vortex roll-up. Flight tests of a non-planar multi-winglet configuration mounted on the wing tip of a Piper Pawnee agricultural aircraft showed that the spray measured on a mast downwind of the spraying zone at heights above the flying height of the aircraft was reduced to 40% of the values measured with standard tips [41]. It can be inferred that spray reaches the ground quicker, which in turn implies that the influence of wind drift and vortex roll up on spray distribution is likely to be reduced. Hackett reports on similar experiments [56].

2.5 Synopsis of Trends Affecting Planar and Non-Planar Wing Efficiencies

This section will sum up reasons as to why the multi-winglet configuration deserves attention as a candidate for aircraft efficiency enhancement.

Biplanes achieve almost as high span efficiencies as single sided vertical winglets that fit into the same enclosing box in a plane perpendicular to the freestream, which is characterised by the height-to-semispan ratio h/s . Biplane wings are compact and structurally efficient if a bracing concept is used. However, the monoplane turned out to offer superior performance since many braced biplane wing configurations suffered from excessive profile and interference drag figures due to struts and wires. If a biplane wing were designed with a cantilever wing concept, profile and interference drag would considerably reduce. However, the thin wings would also have a higher structural mass than that what a monoplane wing would have, given that profile section and overall wing area are set equal. The few examples of aircraft with cantilever biplane wings indicate that the mass penalty is so severe that it appears to more than outweigh the benefits in induced drag. Moreover, the average Reynolds number of a biplane wing system having the same planform area and span of a comparable monoplane wing is about halved. In general, reduced Reynolds numbers tend to come along with increased profile drag as discussed in section 2.2.2.

Tab. 7 is a synopsis of performance relevant characteristics of various wing planforms. All lifting systems shown

- produce the same lift
- operate at optimum span efficiency except f)
- have identical local lift coefficients
- have profile sections of the same maximum thickness to chord ratio and
- have the same span.

The geometric mean chord is defined as

$$\text{GMC} / \text{GMC}_{\text{ell}} = \frac{S_{\text{wet}}}{\sum s^*} \frac{S_{\text{ell}}}{S_{\text{wet,ell}}} \quad (20)$$

where s^* - absolute length of the lines produced by the intersections of the inner wing or winglet traces with a Trefftz plane
 S_{wet} - wetted surface area

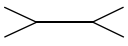
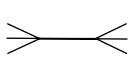
and the average chord Reynolds number ratio is defined as the reciprocal value.

The single winglet c) offers the best span efficiency τ of all configurations. However, the comparatively large winglets come along with a wetted area increase of 21%, which is the highest figure in the table. The average Reynolds number is smaller than that of the planar wing a) but higher than that of the remaining configurations. The wing structure mass is higher than that of the planar wing because of higher local bending moments and reduced structural height due to the decreased inner wing chord lengths, which in turn are a consequence of the constant local lift coefficient constraint. Interference drag can be estimated to be inevitably higher than that of the planar wing, although the absolute magnitude may strongly depend on the particular winglet design and operation conditions. Winglet configuration tailoring for the transonic flow regime can be expected to be more challenging than for purely subsonic flow.

The split tip configuration d) should have less structural mass than the winglet configuration c). This can be inferred from the fact that the mass increments of a split tip configuration with small winglets almost only stem from the higher winglet weights which in itself are due to the decreased structural height of the winglets compared to the single planar wing tip. In contrast, a single winglet configuration c) not only adds structural mass because of the winglets own contributions but also increases wing bending moments which, as a consequence, demand strengthening of the whole wing. The average Reynolds number is less than that of c). This adverse effect may be somewhat compensated by the smaller wetted area. The most significant disadvantage may be seen in the high interference drag [80].

The span efficiency of the optimally loaded multi-winglet configuration e) has been estimated from data of reference [9] for optimally loaded mono-, bi- and tri-planes. Löbert's parametric study results [12] showed that the vertical necking of the central part of a biplane configuration so that a split tip configuration is formed has only a minor influence on the span efficiency. Given the fact that the difference of span efficiency of biplane ($\tau = 1.41$) and split tip configurations ($\tau = 1.38$) is small, it can be expected that the relative difference among mono-, bi- and tri-plane configurations is similar to that of optimally loaded monoplane, split tip and multi-winglet configurations.

Tab. 7: Comparison of fundamental characteristics of non-planar lifting systems. Estimated figures/ratings indicated by shading. Numbers in parentheses indicate ranking.

Configuration		h/s	$S_{wet}/S_{wet,ell}$	GMC/GMC_{ell} ($Re_{c,ell}/Re_c$)	$\tau = D_{i,ell}/D_i$	Wing mass	Interference drag
a) Elliptical Wing [1]		0	1.0 (1)	1.0 (1)	1.0 (5)	0 (1)	0 (1)
b) Cantilever Biplane [8]		0.5	1.0 (1)	0.50 (4)	1.41 (2)	--- (4)	0 (1)
c) Single Winglet [11]		0.5	1.21 (5)	0.81 (2)	1.51 (1)	-- (3)	- (2)
d) Split Tip [12]		0.5	1.05 (4)	0.65 (3)	1.38 (3)	- (2)	-- (3)
e) Multi-Winglet, optimal load [9], [12]		0.5	≈ 1.04 (3)	≈ 0.49 (5)	≈ 1.43 (2)	- (2)	--(3)
f) Multi-Winglet, load as to limit interference drag		0.5	≈ 1.03 (2)	≈ 0.49 (6)	≈ 1.30 (4)	- (2)	- (2)

The optimally loaded multi-winglet configuration e) only offers a small advantage over the split tip configuration d). However, exploitation of cascade effects in order to reduce the risk of boundary layer separation may reduce interference drag and yield better overall performance of the multiwinglet configuration f) where the chordwise loadings are adapted according to the interference drag reduction goal. Whether it will be feasible to reduce interference drag remains a speculation for the time being. However, this design concept is supported by the layout of multi-winglets of some bird species discussed above, which are clearly not optimally loaded according to Munk's necessary condition for minimum induced drag in flight without flapping.

To summarise, it appears that the multi-winglet configuration combines the advantages of a multi-surface configuration like the biplane b) with respect to induced drag with the benefits of the single surface configuration a) regarding profile drag and structural efficiency. Compared to the single winglet configuration c) the advantages are:

- smaller wetted surface area
- larger fraction of the wing surface is employed to produce lift
- greater potential for vortex core diffusion.

Disadvantages stem from the lower average Reynolds numbers, which tend to increase profile drag coefficients. Also, compared to the single winglet configuration, more attention must be paid to the prevention of excessive interference drag.

3 Numerical Model

The state of multi-disciplinary analysis and design methods will be briefly revised at the beginning of the current chapter before the numerical analysis tool VLM++ developed in the frame of the present thesis will be described in detail.

Computational power had increased by the mid 1990s so that solutions for the aerodynamics of full aircraft configurations on the basis of finite volume schemes and the Reynolds Averaged Navier-Stokes equations (RANS) became feasible on desktop PC's (topmost box "4." in Fig. 24). However, the limited assistance to engineers by pre-processors for geometry modelling and discretisation of the computational domain caused the time needed to obtain suitable models to be in the range of weeks. Fortunately progress in this area is clearly visible and turn around times steadily decrease. Simultaneous computation of the aerodynamics with the sophisticated aerodynamic methods as mentioned above on the one hand and structural models based on finite difference modelling on the other also attracted significant research interest (e.g. [88]). Fluid-structure coupling especially extended the opportunities for the assessment of aeroelastic effects.

One objective was to replace some of the costly wind-tunnel and flight tests by cheaper and less time critical numerical computation. This goal was actually achieved and yielded significant efficiency gains in the course of aircraft development. Another proposition of numerics was to put engineers in a situation to analyse a larger number of candidate configurations in advance to the down selection process than was possible with the same resources, model-making and structural respectively wind-tunnel testing before.

Although Euler methods have already been used in multidisciplinary design optimisation at the conceptual design level (refer e.g. to [92]) other recent publications on multidisciplinary non-planar wing optimisation still resort to methods based on potential theory for the prediction of lift, pitching moment and induced drag. Usage of methods based on potential theory offer two advantages:

1. Results can be immediately compared with classical findings on the same or at least closely related methodological basis.
2. For a free flight condition only the wetted surface need to be discretised instead of the whole flow field for field discretising schemes. This leads to superior turn-around times (compare also Fig. 24) and the opportunity to assess more configurations for given computational resources.

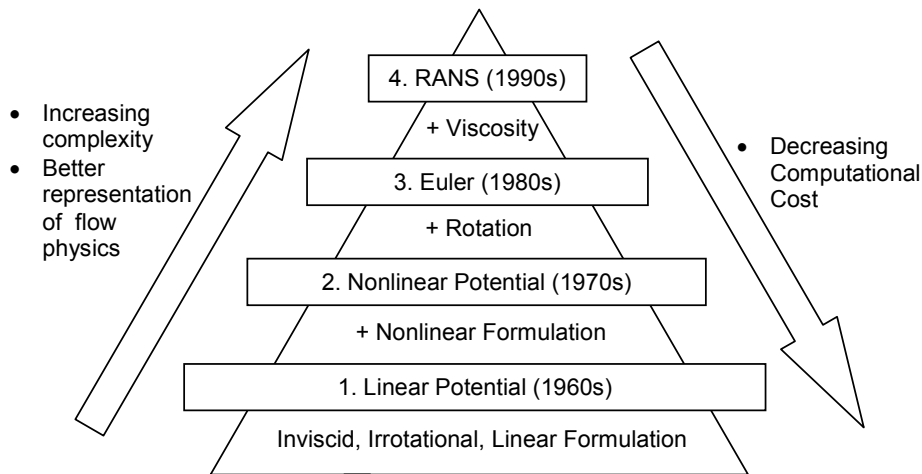


Fig. 24: Hierarchy of fluid flow models.

The numerical tools described in the paper of BÜscher et al. [69] can be seen as representative for the state of multi-disciplinary analysis and design on a conceptual design level with a particular emphasis laid on capabilities for aerodynamic modelling. Three dimensional flow solutions are obtained with the lifting line model of Horstmann [63], which is a popular variant of the vortex lattice method and belongs to box "1." of Fig. 24. Specific characteristics of the method are piecewise parabolic approach functions for the spanwise circulation distribution. Compressibility effects up to the point where the flow locally reaches Mach 1.0 are accounted for by a Göthert transformation of the wing geometry. The results have been complemented by BÜscher et al. by stripwise 2D airfoil computations with MSES [70] providing viscous airfoil and wave drag. The transformation of 2D data to three dimensions is based on infinite swept wing theory. While simple sweep transformations for lift and pitching moments as well as critical Mach number correlate satisfactorily with measurement data if an empirical correction parameter is employed that accounts for the deviation of the real three dimensional wing from the infinite swept wing (refer e. g. to reference [93]), transformation of the wave drag and particularly of drag due to associated flow phenomena such as shock induced boundary layer separation is much more difficult. Since fuselage and nacelles are not explicitly modelled, computations of the respective drag components are performed using handbook methods. Trim drag is accounted for by a simple correction method. Wing structure mass is correlated with wing root bending moment while increments in wing root bending moment are converted into equivalent drag increments using exchange rates. Additional winglet mass is treated in a similar way. Values of the exchange rates are weighted differently in order to reflect different overall design objectives, either minimisation of the direct operating cost DOC at

constant maximum take-off mass $m_{to,max}$ or range maximisation at constant $m_{to,max}$ and constant DOC.

Another example of how to perform multi-disciplinary aircraft optimisation on an advanced conceptual design level is given by Antoine and Kroo [94]. The objective was to study what an environmentally friendly transport aircraft would look like. For that purpose readily available modules for computing

- aerodynamics
- engine performance
- prediction of engine and airframe noise
- structural mass
- stability and control properties
- aircraft performance

and for optimisation were linked to a common database management core module. An immediate necessity to utilize gradient free optimisers originated from the fact that some of the modules used had not been developed with its suitability for numerical optimisation in mind. Hence, some modules produced discontinuous outputs for continuously varying input parameters which were believed to may cause significant difficulties for customary gradient based optimisers. A multi-objective genetic algorithm has been applied to circumvent these problems for the prize of significantly increased numbers of module calls.

Adequate parametric models ease the multi-disciplinary parametric optimisation of wings. Typical requirements are

- design sensitivity
- versatility
- sufficient accuracy.

An alternative means to parametric models based on functional descriptions can be interpolation if a sufficient data base is available. As interpolation routines and efficient structures for data storage are readily available, this option can have significant advantages, especially in cases where the objective function is influenced by a multitude of significant but non-linear and possibly interdependent variables. Advantages of mathematical approximations or curve fitting over interpolation techniques on the other hand can be

- semi-empirical formulation of a physically reasonable approach function
- more confidence in results in regions of the design space where measurement data is rare (extrapolation).

Latter method lends itself to be used in the scope of optimisation problems if

- influencing variables are mutually independent of each other
- normalisation of the data is practical
- variation of the dependent parameter with variation of independent variables allows the fit of common approximation functions

and, hence, curve fitting and regression models, some of which are semi-empirical, will be preferred over data interpolation.

A requirement that had been set for the development of the present numerical model was that extensive multi-variate parametric studies can be made on a conventional desktop PC with turn-around times on the order of one hour. Another principal requirement was to keep the fidelity of individual disciplinary models balanced in order to maintain a consistent level of sophistication.

3.1 Aerodynamics

3.1.1 Vortex Lattice Method

3.1.1.1 Introduction

Vortex lattice or closely related formulations have been successfully employed for design and analysis of non-planar lifting systems (refer e.g. to [16], [59], [63], [69], [64], [83]). Among various approaches that are based on the potential theory, the vortex lattice method is the simplest formulation to compute the lift, induced drag and pitching moment characteristics of non-planar wings. Considering programming and geometry modelling efforts as well as computational time and quality of results, the method has a favourable cost-benefit ratio.

The concept of the vortex lattice method can be traced back to thin airfoil theory for two-dimensional problems or lifting surface formulations for three-dimensional problems, i.e. the analysis of wings with finite span. Thin airfoil theory allows computation of the aerodynamic characteristics of airfoil sections (2D). Because of neglecting the influence of the section thickness, the accuracy of the method increases as airfoil thickness reduces. The systematic error of thin airfoil theory regarding the analysis of technically useful sections is, however, relatively small because the influence of the section thickness on its theoretical aerodynamical characteristics such as lift curve slope and pitching moment is small. This is in turn the reason for the success of models confined to modelling the surface defined by the sectional mean lines only (mean line surface) instead of the exact physical geometry including thickness.

Continuously distributed vortex singularities are located on the mean line according to thin airfoil theory. The strength of the vortex distribution is determined by stipulating the condition of impermeability of the mean line.

A significant simplification of thin airfoil theory with only little compromise with regard to accuracy is the replacement of the distributed vortex sheet by a series of elementary lifting elements consisting of lumped vortices at the quarter chord location of individual elements and collocation points at the 3/4-chord points. Zero normal flow is then stipulated at the collocation points only (Neumann boundary condition) instead of every point on the mean line as for the continuous vortex distribution. A single element produces exactly the same lift compared to a flat plate that has been modelled according to thin airfoil theory with a continuously distributed circulation (theorem of Pistoiesi). Linear potential formulations allow superposition of potentials respectively velocities for assemblies of more than one element. The advantage of the modelling with a limited number of discrete vortices and superposition is that it allows to create a set of simultaneous linear algebraic equations which can be solved for the element circulations.

For the analysis of three-dimensional wings, VLM can also be conceptually traced back to the lifting line theory. Instead of using a single closed mathematical formulation for the spanwise circulation distribution, the geometry and also the circulation distribution is discretised. In the basic "zero-order" form, elementwise constant bound circulations are used. In order to satisfy Helmholtz's theorem, the vortex system is complemented by two free trailing vortices having the same circulations as the bound vortex at the quarter chord line of the element concerned. Theoretically, the vortex system is closed by a starting vortex so that a closed vortex loop is formed. For practical work, the influence of the starting vortex with respect to velocity induction diminishes quickly after it is convected downstream by the flow and can hence be neglected leaving a three-leg horseshoe vortex model. There may be several horseshoe lifting elements not only in spanwise but also in chordwise direction.

3.1.1.2 Numerical Approach

The classical vortex lattice approach is based on elementary horseshoe vortex elements such as shown in Fig. 25. Approaches for the modelling of such elements are presented in many textbooks (e.g. [3], [4]). Following the lead of reference [5], the fundamentals will be just briefly described using the simple form of a horseshoe vortex system that consists of one finite straight bound and two semi-infinite straight trailing vortex filaments. An element consisting of five straight vortex filaments, the two trailing vortices divided into two segments each, can be alternatively chosen in VLM++.

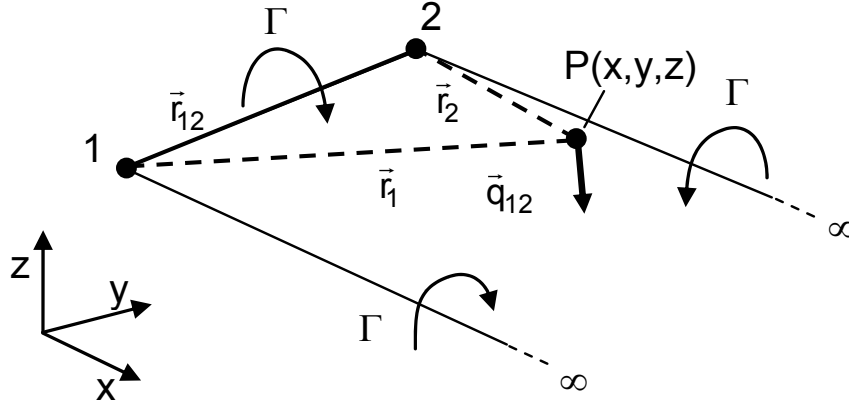


Fig. 25: Velocity induced at an arbitrary point in space P by the bound vortex segment between points '1' and '2' of a three element horseshoe vortex.

The induced velocity of the bound vortex filament \vec{r}_{12} at Point P, which is an arbitrary point in space, is

$$\vec{q}_{12} = \frac{\Gamma}{4\pi} \left(\vec{r}_{12} \cdot \frac{\vec{r}_1}{|\vec{r}_1|} - \vec{r}_{12} \cdot \frac{\vec{r}_2}{|\vec{r}_2|} \right) \frac{\vec{r}_1 \times \vec{r}_2}{|\vec{r}_1 \times \vec{r}_2|^2} \quad (21)$$

The quantity obtained after rearranging equation (21) so that the circulation and the constant factor 4π disappear on the right hand side is the influence coefficient vector - a non-dimensionalised induced velocity.

$$\vec{ic}_{1 \rightarrow 2} = \frac{4\pi}{\Gamma} \cdot \vec{q}_{12} = \Omega \cdot \vec{\Psi} \quad (22)$$

The expression for $\vec{\Psi}$ can be written componentwise in Cartesian coordinates.

$$\begin{aligned} \Psi_x &= [(y - y_1) \cdot (z - z_2) - (y - y_2) \cdot (z - z_1)] / \text{denom} \\ \Psi_y &= -[(x - x_1) \cdot (z - z_2) - (x - x_2) \cdot (z - z_1)] / \text{denom} \\ \Psi_z &= [(x - x_1) \cdot (y - y_2) - (x - x_2) \cdot (y - y_1)] / \text{denom} \end{aligned} \quad (23)$$

where the common denominator is

$$\begin{aligned} \text{denom} &= [(y - y_1) \cdot (z - z_2) - (y - y_2) \cdot (z - z_1)]^2 \\ &+ [(x - x_1) \cdot (z - z_2) - (x - x_2) \cdot (z - z_1)]^2 \\ &+ [(x - x_1) \cdot (y - y_2) - (x - x_2) \cdot (y - y_1)]^2 \end{aligned} \quad (24)$$

The scalar quantity Ω is

$$\Omega = \frac{\left[(x_2 - x_1) \cdot (x - x_1) + (y_2 - y_1) \cdot (y - y_1) + (z_2 - z_1) \cdot (z - z_1) \right]}{\left[(x - x_1)^2 + (y - y_1)^2 + (z - z_1)^2 \right]^{0.5}} - \frac{\left[(x_2 - x_1) \cdot (x - x_2) + (y_2 - y_1) \cdot (y - y_2) + (z_2 - z_1) \cdot (z - z_2) \right]}{\left[(x - x_2)^2 + (y - y_2)^2 + (z - z_2)^2 \right]^{0.5}} \quad (25)$$

Similar expressions can be derived for the trailing vortex legs assuming that they extend in the x direction only

$$lc_{y,1 \rightarrow \infty} = \left\{ \frac{(z - z_1)}{(z - z_1)^2 + (y_1 - y)^2} \right\} \left[1 + \frac{x - x_1}{\sqrt{(x - x_1)^2 + (y - y_1)^2 + (z - z_1)^2}} \right] \quad (26)$$

$$lc_{z,1 \rightarrow \infty} = \left\{ \frac{(y_1 - y)}{(z - z_1)^2 + (y_1 - y)^2} \right\} \left[1 + \frac{x - x_1}{\sqrt{(x - x_1)^2 + (y - y_1)^2 + (z - z_1)^2}} \right]$$

$$lc_{y,2 \rightarrow \infty} = \left\{ \frac{(z - z_2)}{(z - z_2)^2 + (y_2 - y)^2} \right\} \left[1 + \frac{x - x_2}{\sqrt{(x - x_2)^2 + (y - y_2)^2 + (z - z_2)^2}} \right] \quad (27)$$

$$lc_{z,2 \rightarrow \infty} = \left\{ \frac{(y_2 - y)}{(z - z_2)^2 + (y_2 - y)^2} \right\} \left[1 + \frac{x - x_2}{\sqrt{(x - x_2)^2 + (y - y_2)^2 + (z - z_2)^2}} \right]$$

The components of the influence coefficients are collected in vectors

$$\vec{lc}_{1 \rightarrow 2} = \begin{pmatrix} lc_{x,1 \rightarrow 2} \\ lc_{y,1 \rightarrow 2} \\ lc_{z,1 \rightarrow 2} \end{pmatrix}, \quad \vec{lc}_{1 \rightarrow \infty} = \begin{pmatrix} 0 \\ lc_{y,1 \rightarrow \infty} \\ lc_{z,1 \rightarrow \infty} \end{pmatrix}, \quad \vec{lc}_{2 \rightarrow \infty} = \begin{pmatrix} 0 \\ lc_{y,2 \rightarrow \infty} \\ lc_{z,2 \rightarrow \infty} \end{pmatrix}$$

and are subsequently added together so that only one influence coefficient vector remains for the element

$$\vec{lc} = \vec{lc}_{1 \rightarrow 2} + \vec{lc}_{1 \rightarrow \infty} + \vec{lc}_{2 \rightarrow \infty}$$

The bound vortex is placed so that it coincides with the quarter chord line. The collocation point will be placed at the $\frac{3}{4}$ chord location for the time being. The particular advantage is that the basic horseshoe vortex system shown in Fig. 25 has just one unknown parameter. Either the induced velocity is computed if the circulation is specified or the induced velocity is prescribed by the boundary condition and the circulation is computed.

Individual velocities including the freestream velocity can be superposed at arbitrary points in space. In turn, it is possible to compute N unknown circulation values if N boundary conditions are available, i.e. collocation points where the sums of the induced and the normal components of the freestream velocity are zero.

To proceed, the components of induced and freestream velocities normal to the local element surface need to be computed. First, the normal component of the induced velocity in its non-dimensional influence coefficient form is

$$lc_n = \vec{lc} \circ \vec{n}$$

Both vectors must refer to the same coordinate system. The present model uses the body coordinate system for the formulation of the boundary conditions. The free stream velocity vector must thus be transformed into the body coordinate frame of reference (explicit reference neglected for body coordinates):

$$\vec{Q}_\infty = \mathbf{T}_{wb} \cdot \vec{Q}_{w,\infty} \quad (28)$$

where

$$\mathbf{T}_{wb} = \begin{pmatrix} \cos(\alpha) \cdot \cos(\beta) & \cos(\alpha) \cdot \sin(\beta) & -\sin(\alpha) \\ -\sin(\beta) & \cos(\beta) & 0 \\ \sin(\alpha) \cdot \cos(\beta) & \sin(\alpha) \cdot \sin(\beta) & \cos(\alpha) \end{pmatrix} \quad (29)$$

and

$$\vec{Q}_{w,\infty} = \begin{pmatrix} U_\infty \\ 0 \\ 0 \end{pmatrix} \quad (30)$$

Next, the absolute values of the velocities normal to the lattice surfaces are computed using the vector inner product of the free stream velocity (components in body coordinates) and the lattice unit normal vectors:

$$Q_{\infty,n} = \vec{Q}_\infty \circ \vec{n} \quad (31)$$

For more than just one element, a set of linear algebraic equations can be formed and expressed in matrix notation

$$\mathbf{A} \cdot \mathbf{x} = \mathbf{b} \quad (32)$$

where

- A** - matrix of size N^2 (N - number of elements) with influence coefficients lc_n
- x** - vector of the lattice circulations Γ
- b** - right hand side vector of normal velocities $Q_{\infty,n}$.

The coefficient matrix \mathbf{A} is of size N^2 because it contains the incremental velocities that an element is inducing at N collocation points (columns) including that of the actual element but also all $N-1$ incremental velocities that the other elements induce at the collocation point of the element under consideration (rows).

The left hand side $\mathbf{A} \cdot \mathbf{x}$ contains the induced velocity normal to each lattice surface that is required to satisfy the condition of zero normal flow at the collocation points. Equation (32) can now be solved for the solution vector \mathbf{x} using either the product of the matrix inverse of \mathbf{A} with \mathbf{b} or alternatively and more efficiently using the Gaussian elimination which can be expressed as left hand division of \mathbf{A} by \mathbf{b} .

$$\mathbf{x} = \mathbf{A} \setminus \mathbf{b} \quad (33)$$

Following the lead of Horstmann [63] for the other steps, the resulting aerodynamic forces can now be computed using the generalized Kutta-Joukowski theorem

$$d\vec{R} = \rho \cdot \Gamma \cdot (\vec{Q}_{25} \times d\vec{r}) \quad (34)$$

Strengths of vortex filaments are piecewise constant so that equation (34) can also be written for a single horseshoe element (proper indexation is set aside for the sake of a compact representation)

$$\vec{R} = \rho \cdot \Gamma \cdot (\vec{Q}_{25} \times \vec{r}) \quad (35)$$

The velocity vector is the sum of the free stream velocity and the induced velocity component in freestream direction at the quarter chord point

$$\vec{Q}_{25} = \vec{Q}_{\infty} + \vec{q}_{i,25} \quad (36)$$

Equation (36) deserves a comment. First, the vector of induced velocities at the quarter chord points cannot be obtained straight away but need to be computed componentwise using an adapted set of influence coefficients

$$\vec{q}_{i,25} = \begin{pmatrix} u_{i,25} \\ v_{i,25} \\ w_{i,25} \end{pmatrix}, \quad \mathbf{u}_{i,25} = \mathbf{A}_{x,25} \cdot \mathbf{x}, \quad \mathbf{v}_{i,25} = \mathbf{A}_{y,25} \cdot \mathbf{x}, \quad \mathbf{w}_{i,25} = \mathbf{A}_{z,25} \cdot \mathbf{x} \quad (37)$$

where $\mathbf{u}_{i,25}$ - vector containing x-components of induced velocities at quarter chord points

$\mathbf{v}_{i,25}$ - y-components

$\mathbf{w}_{i,25}$ - z-components

\mathbf{x} - Γ 's

The problem with this computation at a location coinciding with the bound vortex filament is that the induced velocity becomes singular. However, similar to the basic lifting line treatment, the singularity can be disregarded on grounds of a boundary value analysis. Hence, the self-induction due to the bound circulation can be explicitly set to zero (refer also to discussion of the problem by Horstmann [63]).

Once the resulting element force \bar{R} has been obtained, a multitude of derived data can be computed in the post-processing-sequence. If the resulting force component is transferred into wind axes, the components are induced drag, side force and lift

$$\begin{aligned}\bar{R}_w &= \mathbf{T}_{wb}^{-1} \cdot \bar{R} \\ &= \begin{pmatrix} D_i \\ S_{frc} \\ L \end{pmatrix}\end{aligned}\quad (38)$$

The non-dimensional aerodynamic loading of one element is

$$\Delta c_p = \frac{|\bar{R}|}{q \cdot S}\quad (39)$$

where $q = \frac{1}{2} \cdot \rho \cdot Q_\infty^2$ - dynamic pressure

S - element surface area

Some authors have claimed that the near-field induced drag as of eq. (38) is accurate enough for conceptual design purposes (e.g. [83]). While this position is acceptable for unswept wings, where near field induced drag figures do not differ from corresponding figures from far-field (Trefftz-plane) analyses, it should be regarded that the near-field values depart significantly from the far-field figures if sweep is added [63] due to the strong influence of bound circulations on the quarter chord point down- respectively upwash velocities. In spite of the inevitable systematic error, the near field induced drag distribution offers additional insight into the process of induced drag generation, which the Trefftz-plane analyses cannot provide. Taking a canard and wing configuration as an example, the near field analysis shows the drag distribution between the two surfaces where the canard may experience a thrust component. The Trefftz-plane analysis on the other hand is only able to provide the total induced drag of a configuration as its only meaningful result. Though, in order to eliminate the abovementioned error source, all incremental near-field induced drag force components are linearly corrected by multiplying each with the ratio of the total induced drag computed in the Trefftz plane to the total near field value.

Because the influence of the bound vortices decays quickly with distance from the wing, only the trailing vortices remain effective in governing the flowfield far behind the wing. A Trefftz plane is set perpendicular to the trailing vortex filaments, hence, the vectors of induced velocities coincide with the plane producing a quasi-two-dimensional flowfield. It is worth to note that the trailing vortex filaments of the five filament element, as usual, extend downstream in the direction defined by the freestream. The induced drag of a single elementary surface in the Trefftz plane is

$$D_i = \rho \cdot \Gamma \cdot \left[\left(\frac{1}{2} \bar{q}_{i,T} \times d\bar{s} \right) \circ \bar{e}_x \right] \quad (40)$$

where \bar{e}_x is the unit vector perpendicular to the plane. Individual drag contributions of all elementary surfaces must be subsequently summed up in order to obtain the configuration total value.

3.1.1.3 Wing Geometry

Fig. 26 illustrates schematically the build up of the wing geometry. Each individual lattice element can be addressed by its index. The index consists of four integers. The first index n is the designation of the wing, the second index k is the number for the wing part, the third index j indicates the spanwise strip and the fourth index i stands for the chordwise location. A particular syntax is used for the setup of arbitrary lifting surface geometries defined in dedicated input files. The connectivity relations of wing parts, which essentially define the topology of a lifting surface configuration, are translated into a connectivity matrix. The basic built up is limited to the chord line surfaces and starts with a root point which serves as a basis for the quarter chord line as indicated by the unfilled bullet in Fig. 26. The incidence ι gives the angular setting of the root chord line against the body ('b') x-y plane for fundamentally horizontal wings (designation 'h') and against the body x-z plane for upright surfaces such as vertical tailplanes (designation 'v'). Local coordinate systems, an example for such a system in Fig. 26 is designated with an 'l', eases the handling of geometrical data. The x_l -axis is parallel to the x_b -axis but y_l and z_l axes are tilted by the dihedral angle Υ against the body coordinate system. The spanwise construction is based on the wing parts quarter chord line which stretches by an amount of semi-span s out towards the tip section. The total length of the semispan is the length of its projection into the body or local y-z planes. The quarter chord location of the tip section is found after accounting for the influence of the sweep angle Λ_{25} that alters the x_b - or x_l -positions. Deviating from the quarter chord based scheme, the sweep angle can alternatively be specified for other chord locations if this appears necessary or convenient. The tip section of each wing part is defined in the y-z plane of the local coordinate system.

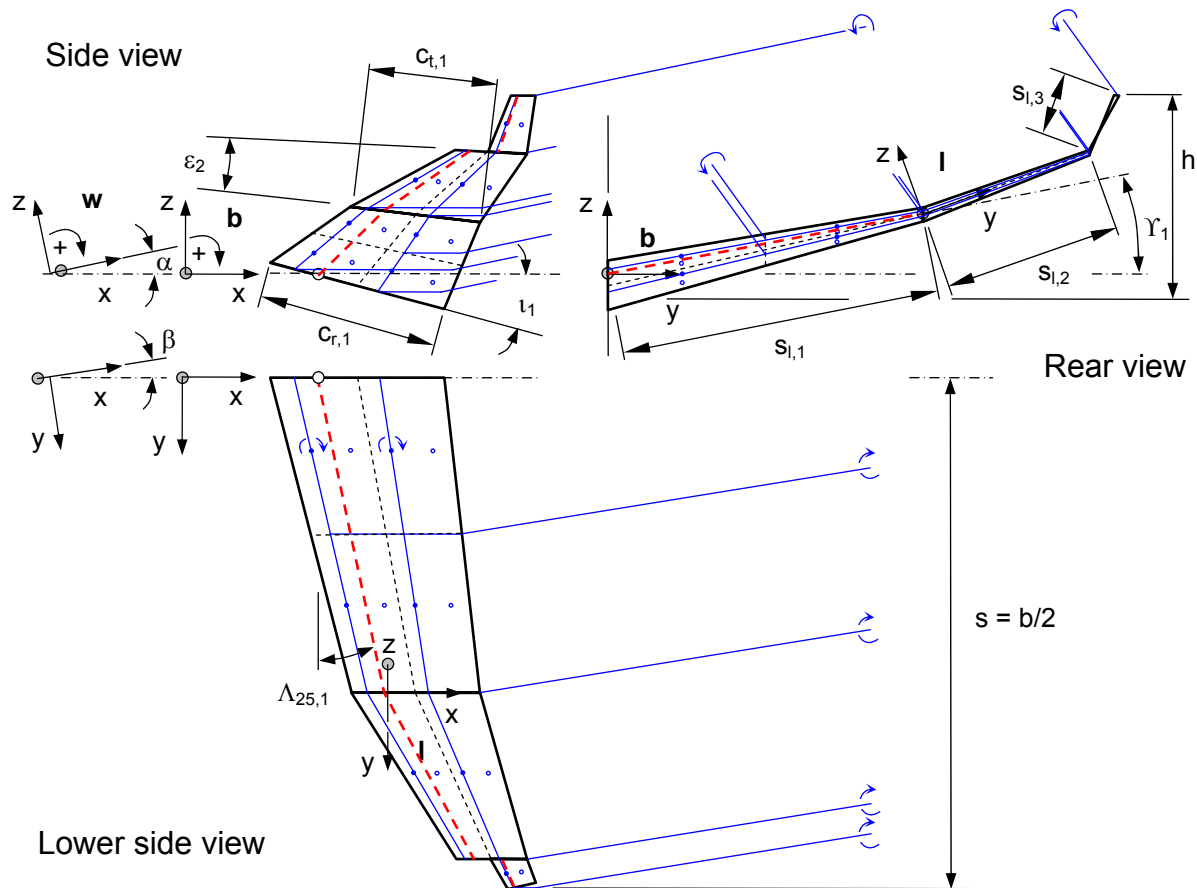


Fig. 26: Schematic illustration of geometry build-up of right hand side wing half. Coordinate systems: wind axes (w), body axes (b) and local axes for wing part 2 (l) (not shown in side view for clarity). Shown are fundamental planform parameters and vortex arrangement (five vortex filaments per lattice element option). Sideview shows only projection of washout angle ϵ_2 into body x - z plane.

If the wing sections have camber as shown in Fig. 27, the mean line ordinates are added perpendicular to the chord lines in the plane where the incidence was specified (body x - z plane for wing root section, local coordinate system for tip sections).

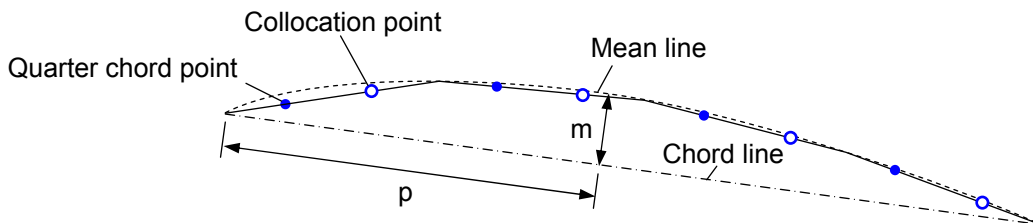


Fig. 27: Discretisation of mean line.

The lattice data which comprise

- the four surface element corner point coordinates
- the coordinates of the two corners that delimit the bound vortex filaments and
- the collocation point and the quarter chord point coordinates

can now be computed by means of linear interpolation. Optionally a cos-distribution of the above mentioned points can be used in the spanwise direction, which produces strips of continuously decreasing widths towards the wing tip.

Another option allows catering for bend wing parts. After the piecewise linear wing elements and lattice geometries are defined a spanwise circular arc curvature can be introduced by specifying the angular difference ΔY between tip and root of the lines that are tangent to the projection of the quarter chord line into the y-z plane. In other words the wing is wrapped around a cylinder of radius $R = s / \Delta Y$ whose principal axis of symmetry is parallel to the x_b -axes.

The last free vortex at the wing tip can be indented, which is frequently used with low order vortex lattice methods to improve the accuracy of induced drag results. While the outer wing geometry and the elementary surfaces at the tip are unchanged, the vortex system is indented by $\frac{1}{4}$ of the lattice width in the local spanwise direction. Alternatively a spanwise cos-distribution can be used, which also allows accurate predictions of induced drag. For this geometrical setup the lifting line solution for elliptical lift distribution is closely approached for wings with elliptical planform and without twist.

Two different models for the rigid free vortex sheets are available:

1. A wake vortex model with two trailing vortex filaments.
2. An arrangement with four trailing vortex filaments.

The first option utilises simple horse-shoe vortices where the free vortices emanate from the ends of a bound vortex filament in the x_b -direction towards infinity. This definition holds under the assumption of small perturbations and hence small angles of attack only. The computational effort to compute the aerodynamic influence coefficient matrix is on the order of the number of elementary surfaces squared. A particular advantage of the wake being rigidly coupled to the body is that the influence coefficient matrix does not change for variations in angle of attack. Since only the right hand side of the equation system needs to be changed, the time needed to compute the lift characteristic as influenced by angle of attack is significantly reduced.

However, this simple definition is not suitable for computations with sideslip and thus the second option should be preferred where the free vortex filaments only run in the x_b -direction until the trailing vortex filaments intersect with a plane that is essentially perpendicular to the body x-axis and running through the rearmost trailing edges of a

wing assembly and then turn to continue in the freestream or x_w -direction (compare also Fig. 26). The initial leg in the x_b -direction is necessary in order to prevent free vortex filaments running across collocation points of lattices that are located farther aft in the chordwise direction. The five-filament vortex system appears to be physically better justified. Nevertheless, this definition is computationally more expensive since the influence coefficient matrix needs to be recomputed not only for changes in geometry but also for changes in angle of attack and sideslip.

3.1.2 Profile Drag Estimation

3.1.2.1 Flat Plate Analogy

A common technique for modelling the profile drag in the conceptual aircraft design phase is the flat plate analogy. Since the largest profile drag component of streamlined bodies is skin friction, the friction force of a flat plate is computed that has the same streamwise length as the chord line of the actual body. The integral skin friction drag coefficient of a flat plate in incompressible flow at zero incidence is suitably described as a function of the Reynolds number Re_c and the state of the boundary layer. If the boundary layer flow is laminar over a fraction of the contour and another part is turbulent after transition, the transition location x_t/c is another important parameter. The usual approach is to replace the turbulent skin friction coefficient by the appropriate laminar skin friction coefficient up to the transition point [91].

$$c_F = c_{F,c,tu} + \frac{x_t}{c} \cdot (c_{F,t,tu} - c_{F,t,la}) \quad (41)$$

with
$$c_{F,x,tu} = \frac{0.455}{\log(Re_x)^{2.58}} \quad (42)$$

$$c_{F,x,la} = \frac{1.328}{\sqrt{Re_x}} \quad (43)$$

The upper case index F distinguishes the integral skin friction coefficients from local coefficients. The integral coefficients have been obtained by integration of the local coefficients (eqs. (42) and (43)).

The Reynolds numbers for varying reference lengths is defined as

$$Re_x = \frac{Q_\infty \cdot x}{\nu} \quad (44)$$

where x is the length on which the Reynolds number is based which is either the chord length or the distance between leading edge and transition location x_t .

The non-zero thickness of the actual body is accounted for by a zero lift drag correction function according to Hoerner [97] with the maximum thickness to chord ratio (t/c) as parameter (the index 'max' is neglected since presently only the maximum thickness to chord ratio is of interest). Because of thickness, the average velocity around a symmetrical airfoil section is higher than that of the flow past a flat plate, even at zero lift. The potential flow solution for a circular cylinder with $(t/c) = 1$ placed in a uniform flow yields $Q_{\max}/Q_{\infty} = 2$, thus $(Q_{\max}/Q_{\infty} - 1) = (t/c)$ in this particular case. This indicates that the maximum supervelocity ratio $(Q_{\max}/Q_{\infty} - 1)$ roughly increases with thickness to chord ratio. For moderate thickness to chord ratios the maximum dynamic pressure is also directly proportional to the thickness to chord ratio so that $(Q_{\max}/Q_{\infty} - 1) = [(Q_{\infty} + \Delta Q_{\max})/Q_{\infty} - 1] = \Delta Q_{\max}/Q_{\infty} = t/c \approx \frac{1}{2} \cdot \Delta q_{\max}/q_{\infty}$. As a first order approximation it can be concluded that the average chordwise dynamic pressure increment is half the maximum pressure increment $\Delta q/q_{\infty} \approx \frac{1}{2} \cdot \Delta q_{\max}/q_{\infty} \approx t/c$. Since the friction drag increases with dynamic pressure if the Reynolds number effect has been considered separately, the zero lift profile drag coefficient is

$$c_{d,p,0} = 2 \cdot c_F \cdot \left(1 + a_{sv} \cdot (t/c) + a_{pd} \cdot (t/c) + b_{pd} \cdot (t/c)^4 \right) \quad (45)$$

with $a_{sv} = 1$ - coefficient accounting for increased skin friction due to supervelocity

$a_{pd} = 1$ - linear pressure drag coefficient

$b_{pd} = 60$ - non-linear pressure drag coefficient.

The coefficients are suitable for NACA 4-digit sections up to maximum thicknesses of 30% of the chord length.

3.1.2.2 Leading Edge Thrust Concept

The 'leading edge suction' or 'leading edge thrust' method suggested in [98] and used for conceptual aircraft design purposes in reference [99] gives an upper bound for lift dependent profile drag and will therefore be used as a basis for the following derivation. A symmetrical airfoil with a rounded leading edge at incidence will produce lift in low speed airflow but ideally experience no drag (d'Alembert paradox) because the drag component acting on the rear of the airfoil is cancelled by a thrust component at the leading edge. Such an airfoil is schematically depicted in Fig. 28 a).

In the case of a flat plate, where the leading edge radius approaches zero with decreasing plate thickness, a strong suction peak will start to develop near the leading edge of the airfoil's low pressure side, followed by a strong adverse pressure gradient towards the trailing edge. As the boundary layer is initially laminar, it will separate under the influence of the adverse pressure gradient already at a very small angle of attack.

Laminar-turbulent transition above the small separation bubble at the leading edge is to be expected with turbulent re-attachment behind. Whatever boundary layer effect will influence the aerodynamics, the flat plate at incidence is lagging any wall with a positive contour gradient dz/dx (wind axes) as can be seen in Fig. 28 b) and hence there cannot be any thrust component as for the profile a) with the rounded leading edge.

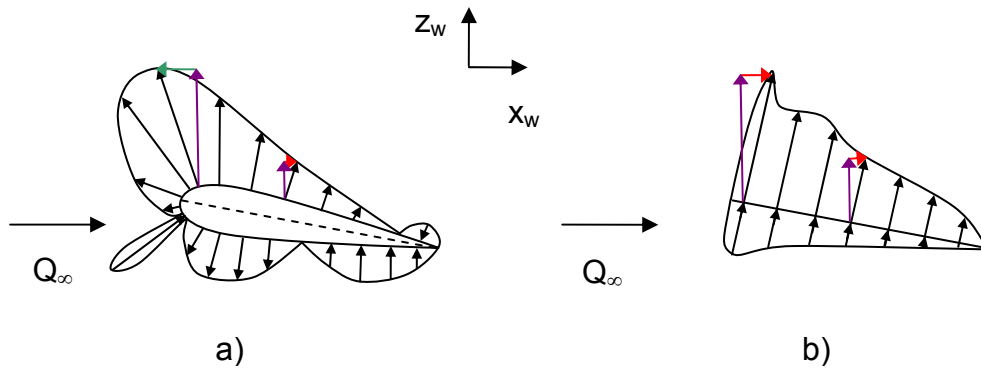


Fig. 28: Aerodynamic load distributions: a) Profile with rounded leading edge and leading edge suction. b) Flat plate with sharp leading edge without leading edge suction.

3.1.2.3 Lift Dependent Profile Drag

Under the assumption of small angles of attack and disregarding friction drag, the drag of the flat plate is directly proportional to lift and angle of attack

$$\Delta c_{d,p} = c_l \cdot \alpha$$

The lift coefficient of a symmetrical airfoil can be expressed as a function of α and the linear lift is

$$c_l = \left(\frac{dc_l}{d\alpha} \right) \cdot \alpha$$

Rearranging this equation and inserting into the latter yields

$$\Delta c_{d,p} = \frac{c_l^2}{(dc_l/d\alpha)}$$

or in the style of a parabolic drag polar

$$\Delta c_{d,p} = k_p \cdot c_l^2 \quad (46)$$

The theoretical lift curve slope $dc_l/d\alpha$ of a flat plate in incompressible flow is $2\cdot\pi$ according to potential theory with real values for usable profiles differing only little from this value. For this reason the coefficient for the 'worst case' with respect to pressure drag is

$$k_{p,\max} \approx \frac{1}{2 \cdot \pi} = 0.159 \quad (47)$$

There will always be a leading edge radius greater than zero for airfoils of practical use and values of just 1-5% of $k_{p,\max}$ are to be expected.

For cambered airfoils it is convenient to extend above approach for the lift dependent profile drag eq. (46), which is modelled as a pressure drag component, in so far as to allow the minimum drag condition to be obtained at a finite 'design lift coefficient' $c_{l,i}$ (term according to Abbott & von Doenhoff [100], 'i' stands for ideal):

$$\Delta C_{d,p} = k_p \cdot \left(c_l - \left(\frac{c_{l,\text{ref}}}{c_{l,i}} \right) \cdot c_{l,i} \right)^2 \quad (48)$$

The best fit for several NACA 4-digit sections was obtained for $(c_{l,\text{ref}} / c_{l,i}) = 0.23$. A load distribution where this condition is present is sketched in Fig. 29. If the design lift coefficient is not explicitly known it can be roughly approximated as ten times the camber m . The camber is the maximum elevation of the mean line above the chord line divided by the chord length (for example NACA 2412: $m = 0.02$ camber $\rightarrow c_{l,i} \approx 0.2$).

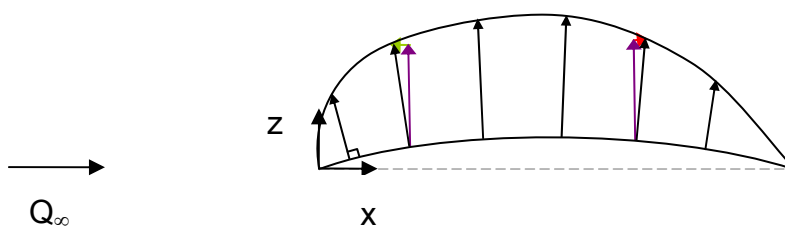


Fig. 29: Possibility of vanishing pressure drag for cambered airfoil at non-zero lift coefficient.

The simple quadratic eqs. (46), (48) are not sufficient to match the lift dependent profile drag closely. In the case of a thick airfoil with trailing edge stall, the pressure drag increases strongly for lift coefficients greater than about 70% of $c_{l,\max}$ and the lift curve slope decreases because the region of separated flow starts to grow. To model this increase in drag, the coefficient k_p will be similarly modelled as a quadratic of the lift

coefficient but with an empirically estimated reference lift coefficient $c_{l,ref,k}$. Equation (48) will hence be a quartic of c_l .

$$k_p = k_{const} + k_{cl}$$

$$k_{cl} = a \cdot \left(c_l - \left(\frac{c_{l,ref,k}}{c_{l,i}} \right) \cdot c_{l,i} \right)^4$$

A curve fit over all NACA 4-digit wind tunnel data reproduced by Abbott & von Doenhoff [100] for $Re_c = 6 \cdot 10^6$ (NACA 0006, 0009, 1408, 1410, 1412, 2412, 2415, 2418, 2421, 2424, 4412, 4415, 4418, 4421, 4424) by means of a least-squares technique and non-linear optimization produced a value $(c_{l,ref,k}/c_{l,i}) = 1.85$.

It is important to mention that the prediction of the lift dependent profile drag does not only comprise pressure drag but also all other lift dependent drag components as well.

Another underlying assumption is that the k -values are expected to be identical at $c_{l,max}$ and $c_{l,min}$ when the wing section stalls. The k -factor model must be subdivided into two branches in order to accommodate the parabolic approach function as well as the constraints for k_{cl} . Since the lift dependent pressure drag as well as the stall of the airfoil at the maximum lift coefficient are due to boundary layer separation, latter will be used as a correlation parameter

$$a = \frac{k_{min,max}}{\left(c_{l,extr} - \left(\frac{c_{l,ref,k}}{c_{l,i}} \right) \cdot c_{l,i} \right)^4} \quad \left\{ \begin{array}{l} c_l \geq \left(\frac{c_{l,ref,k}}{c_{l,i}} \right) \cdot c_{l,i} : c_{l,extr} = c_{l,max} \\ c_l < \left(\frac{c_{l,ref,k}}{c_{l,i}} \right) \cdot c_{l,i} : c_{l,extr} = c_{l,min} \end{array} \right. \quad (49)$$

Values for the k 's have been derived from abovementioned measurement data. The values given below are with respect to the theoretical maximum pressure drag coefficient $k_{p,max}$ (eq. (47)):

$$k_{const} / k_{p,max} = 1.52\%$$

$$k_{min,max} / k_{p,max} = 2.15\%$$

These values are applicable if the trailing edge stall type is to be expected. If the stall type changes, limit lift coefficients may significantly change. Also, the pressure distribution as well as the boundary layer states change if another stall type is encountered. This has the consequence that the lift dependent sectional drag characteristics significantly change and hence it proved not to be possible to derive a satisfactory model for all types of stalls. However, it is suggested just to adapt the parameters of the approach described above. Among various stall types as categorised

by Gault [129], it is assumed that it is sufficient to distinguish between just two characteristics for the present purpose, namely the

- a) thin airfoil type and the
- b) trailing edge type.

Clearly, emphasis is laid on the trailing edge stall, which is most relevant for wings of subsonic aircraft. Without presenting details, a satisfactory fit for the NACA 0006 airfoil where thin airfoil stall has to be expected could finally be obtained by just doubling the coefficients k_{const} and k_{minmax} .

The measured and the predicted lift dependent profile drag of the unsymmetrical NACA 2412 airfoil section is depicted in Fig. 30 and the agreement of both curves is satisfactory. The approximation suggested by Torenbeek [101]

$$\Delta C_{d,p} = 0.75 \cdot (\Delta_l C_{d,p})_{\text{ref}} \cdot \left(\frac{C_l - C_{l,i}}{C_{l,\text{max}} - C_{l,i}} \right)^2$$

where for $Re_c \leq 10^7$: $(\Delta_l C_{d,p})_{\text{ref}} = \frac{67 \cdot C_{l,\text{max}}}{(\log(Re_c))^{4.5}} - 0.0046 \cdot \left(1 + 2.75 \cdot \frac{t}{c} \right)$

is not as close to the data as the curve obtained from the present regression approach, especially for high lift coefficients.

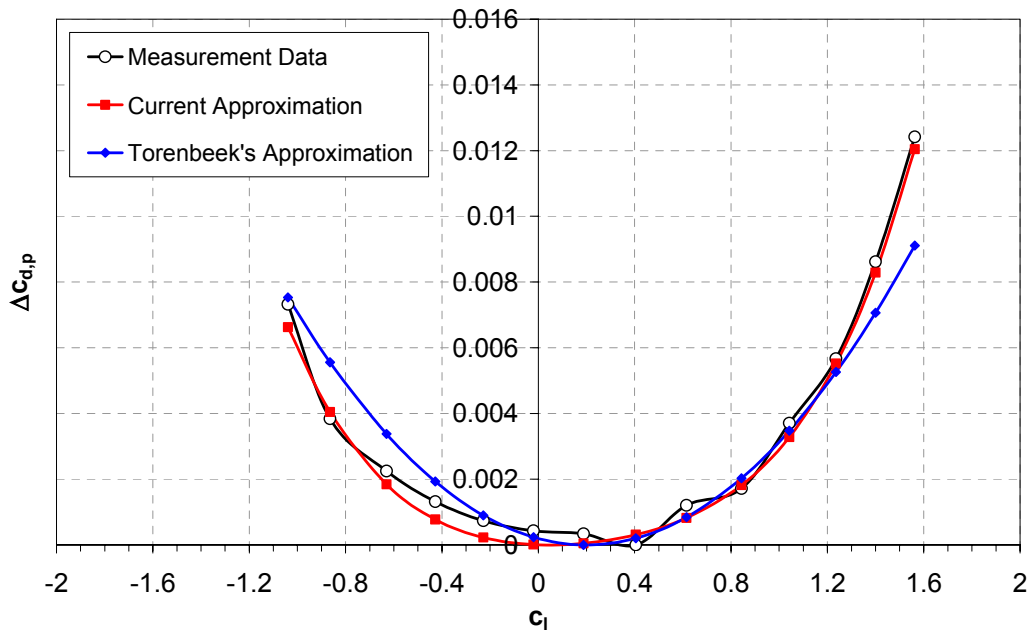


Fig. 30: Lift dependent profile drag of NACA 2412 airfoil in incompressible flow ($Re_c = 6 \cdot 10^6$, measurement data from reference [100]).

The maximum total error of the predicted lift dependent profile drag coefficient compared to the referenced measurement data samples for the profile sections listed above is $54.2 \cdot 10^{-4}$ and the standard error (or RMS error) is $7.43 \cdot 10^{-4}$.

3.1.2.4 Lift Dependent Profile Drag Assessment in the Course of Parametric Studies and Optimisation

The concept for calculating the lift dependent profile drag fraction is based on maximum and minimum lift coefficients (compare eq. (49)). If it is expected that interference between two or more lift producing surfaces affect surfaces maximum loadability limits, it is possible to estimate the possibly altered maximum and minimum lift coefficients by means of the cascade and non-linear lift models as will be later shown in chapter 4.1 (details on the methods are contained in chapters 3.1.6 and 3.1.5). However, it is necessary in this case to evaluate whole polars, which renders the method inefficient for parametric studies and optimisation where many configurations need to be evaluated.

A method is suggested to avoid this effort but which holds on to the consideration of influences that multiple surface arrangements exert on the maximum loadability of sections. This will be done by replacing the correlation of the lift dependent profile drag with the actual lift coefficient in relation to maximum and minimum lift coefficients with an alternative correlation on the basis of the ratio of supervelocities at the section minimum pressure locations to the respective trailing edge values (computation of pressure distributions is discussed in chapter 3.1.6.3). The maximum and minimum lift coefficients are replaced by critical supervelocity ratios as determinants for boundary layer separation and finally stall. The critical supervelocity ratios correspond to the critical canonical pressure coefficients which themselves are derived from loadability data of the profile sections. The concept makes use of the fact that the velocity ratios develop approximately linear with angle of attack respectively lift coefficients (see velocity ratios that are plotted against section lift coefficients in lower part of Fig. 31).

The suggested equation for lift dependent section profile drag using alternative loadability metrics is

$$\Delta c_{d,p} = \left(\frac{t}{c} \right)_{\max} \cdot \left[k_{\sigma,2} \left(\frac{\sigma_u}{\sigma_{u,crit}} - \frac{\sigma_l}{\sigma_{l,crit}} \right)^2 + k_{\sigma,4} \left(\frac{\sigma_u}{\sigma_{u,crit}} - \frac{\sigma_l}{\sigma_{l,crit}} \right)^4 + k_{cl,2} \cdot c_l^2 + k_{cl,4} \cdot c_l^4 \right] \quad (50)$$

where

$$\sigma_{u,l} = \left(\frac{Q_{\max}}{Q_{te}} \right)_{u,l} - 1 \quad \text{- normalised velocity differences for upper (u) respectively lower (l) sides}$$

$$\sigma_{u,l,crit} = \left(\frac{Q_{\max}}{Q_{te}} \right)_{u,l,crit} - 1 \quad \text{- normalised velocity difference at maximum respectively minimum lift conditions derived from section data}$$

$$\left. \begin{array}{l} k_{\sigma,2} = 0.032 \\ k_{\sigma,4} = 0.018 \\ k_{cl,2} = 0.009 \\ k_{cl,4} = 0.007 \end{array} \right\} \text{ - calibration coefficients NACA 4-digit sections } Re_c = 6 \cdot 10^6$$

The lift coefficients had to be included as an additional influence parameter because the lift dependent profile drag curve would otherwise not have acceptably matched the measurement data. The model would have produced lower drag figures for high lift coefficients and on the contrary higher drag figures for lift coefficients lower than that at the condition of minimum drag. With the calibration coefficients stated, about half of the drag is covered by the lift coefficient influence, the other half by the supervelocity correlation.

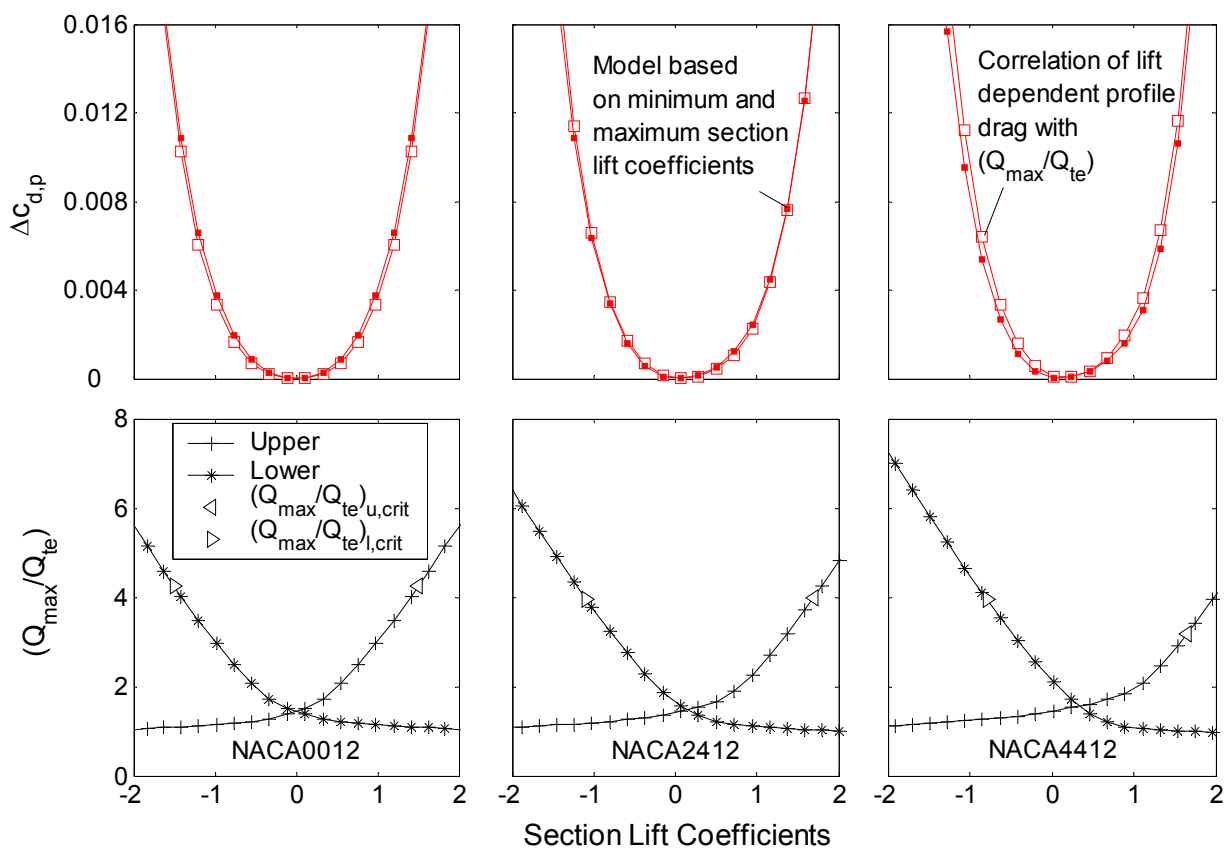


Fig. 31: Comparison of two different correlatives with lift dependent profile drag of three NACA 4-digit airfoil sections in incompressible flow (maximum and minimum lift coefficients for $Re_c = 6 \cdot 10^6$ [130], [100]).

The agreement of the supervelocity-based model with that based on maximum and minimum lift coefficients can be seen in the upper part of Fig. 31 presenting the data for three NACA 4-digit airfoil sections with 12% relative thickness. Increasing section

camber shifts the velocity ratio curves to the right, when, at the same time, the drag polars also experience such a shift. The agreement of the supervelocity-based model with that based on maximum and minimum lift coefficients is satisfactory. Although this feature based modelling approach leaves room for improvement and demands a more rigorous justification, it is believed that it nevertheless sufficiently reflects the actual trends.

3.1.3 Interference Drag Estimation

For a subsonic transport aircraft, interference may make up 5% of the total drag in the cruise configuration. Interference drag is not a physical drag source but rather an engineering workaround, which accounts for the difference of the drag forces of component assemblies that constitute of two or more parts compared to the sum of the drag forces measured or computed individually for each of the components. Interference drag is thus a concept to be applied in connection with handbook type methods. Interference drag can be positive but under certain conditions also negative (refer to Hoerner [97], pp. 8-1 through 8-3).

Interference drag will lose significance, as handbook analysis methods are getting replaced by modern CFD techniques simulating flow physics on the basis of first principles. However, for the time being, the concept is valuable if predictions of aircraft total drag shall be accurate. Motivation to pay attention to interference drag effects also arises from the fact that the figure of merit for numerical optimisation should be able to distinguish roughly between configurations that are undesirable with respect to interference drag and those that perhaps feature only a minimum of additional drag penalties in this respect. The lack of suitable models for winglet configurations necessitated the derivation of a method tailored for being applied in connection with the vortex lattice method. Hence, a design sensitive empirical model for the prediction of interference drag with emphasis on consideration of viscous effects in incompressible flow was developed. Refer to Appendix B for a detailed description. Note that induced drag due to mutual interference is automatically accounted for by the vortex lattice method and, hence, did not require explicit attention.

The empirical approach functions and the regression parameters of the model are based on published experimental data, most of which were taken from the compilation of Hoerner [97]. Most of the data were obtained for configurations of technical relevance considering wing-fuselage, wing-wall or strut intersections. Hence, strictly speaking, the developed model is applicable to technical configurations only, characterised by impermeable and relatively thick wing sections ($t/c = 0.1 \dots 0.4$) with rounded leading and pointed trailing edges. Some of the data sets accounted for varying intersection angles. Lift dependent measurement data was only available for wing-wall intersections. For wing-multiwinglet intersections a rather tentative extrapolation based on the small

amount of experimental data available and the models for the other types of configurations mentioned above was attempted.

Empirical equations for the interference drag prediction of

- wing-wall intersections $f(c_i, (t/c), \Lambda, \Upsilon)$
- T-junctions $f(c_i, (t/c), \Upsilon, k_{int,det})$
- wing-winglet intersections $f(c_i, (t/c), \Upsilon, k_{int,det})$ and
- wing-multiwinglet intersections $f(c_i, (t/c), \Upsilon, k_{int,det}, C_{d,p}(i))$

have been derived. Equation (B.8) of Appendix B allows to compute the interference drag with respect to the winglet root chord squared for a single winglet being part of a wing-multiwinglet assembly:

$$C_{D,int,wmwl,cr^2}(i) = \left[\underbrace{a_{cl} \cdot c_{i,r}(i)^2}_{\text{Influence of local aerodynamic loading}} \cdot \underbrace{\left(\frac{t}{c}\right)_i^3}_{\text{Thickness effect}} + \underbrace{b \cdot \left(\frac{t}{c}\right)_i^\lambda}_{\text{Correction depending on type of configuration}} + \underbrace{d_{tc0}}_{\text{Dihedral effect}} \right] \cdot \underbrace{k_{int,dih}(i)}_{\text{Dihedral effect}} \cdot \underbrace{k_{int,det}(i)}_{\text{Design quality (adapted fillets?)}} \cdot \frac{C_{t,0}}{C_r(i)} + \underbrace{\Delta C_{D,int,ts,cr^2}(i)}_{\text{Correction in case of consecutive intersections lined up in streamwise direction}}$$

Where applicable, the lift coefficients or geometric parameters such as (t/c) are based on the surface with the smaller chord. From the data available it was not possible to find a direct and empirically significant correlation with Reynolds number so that this parameter was finally discarded for the current model. Nevertheless, a small Reynolds number influence is included in case of a multiwinglet cascade due to the dependency on profile drag. The model has been adapted to measurement data in the Reynolds number range of $3 \cdot 10^5 - 3 \cdot 10^6$, which can also be seen as the limits of model applicability.

The model computes an interference drag fraction with respect to total aircraft drag of 1.25% for a configuration where a full-chord winglet is set at a dihedral angle of 45° . The aircraft wing for the verification had a rectangular planform with an aspect ratio of 10, a thickness to chord ratio of 12% and was untapered. The wing Reynolds number was set to $6.6 \cdot 10^6$ and the lift coefficient was 0.51, which was also taken as the local lift coefficient at the junctions. Average transition location was set to 30% of the chord length. The drag fraction increased to 1.69% for a configuration with three winglets set at $+45^\circ, 0^\circ, -45^\circ$.

Due to the limited experimental evidence, the model encompasses a large amount of engineering judgement. Particularly the lift dependency as well as the tentative

approach for additional interference in the case of multiple winglets (or winglet cascades) should be considered with care.

3.1.4 Minimum and Maximum Section Lift Coefficients

The lift dependent profile drag model described in chapter 3.1.2 uses maximum and minimum lift coefficients as input parameters. For parametric studies and optimisation of multi-winglet configurations it is desirable to base the operational limits of airfoil sections on geometric parameters. If a parameter changes, for example the camber, also the maximum and minimum lift coefficients change. The following brief section suggests a basic procedure how aerodynamic limits can be determined for small variations from a datum condition.

Fig. 32 depicts the regions where various stall characteristics of wing sections are to be expected. Laminar-turbulent transition was free in the experiments that produced the data that Gault used to derive the diagram and transition location unknown [129]. Therefore, the state of the boundary layer as another important factor influencing the stall characteristics could not be explicitly regarded in Gault's empirical work.

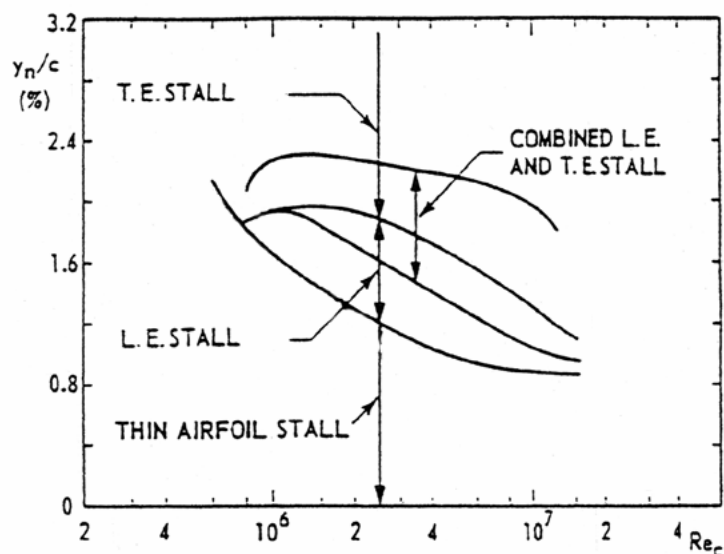


Fig. 32: Types of airfoil stall according to (reproduced from [129]).

The importance of knowing the stalling characteristics can be proven by taking a look at Fig. 33 where the $c_{l,max}$ of the NACA 0012 airfoil increases from 0.82 at $Re_c = 1.2 \cdot 10^5$ up to 1.58 at $8.3 \cdot 10^6$. With $y_n/c = 1.89\%$ the airfoil is in the thin airfoil stall region at the lower Re_c (refer to Fig. 32), then passing through the leading edge stall region and finally entering the combined leading edge and trailing edge stall region at the higher Re_c . Although the diagram of Gault (Fig. 32) is a reliable source for classifying the stall

type it proved to be problematical to find a universal but simple model for the $c_{l,max}$ and $c_{l,min}$ characteristics of NACA 4-digit airfoils.

Referring to Fig. 33 (b) it appears that at a chord Reynolds number of $5.0 \cdot 10^5$ camber increases the maximum lift coefficient in as much as $c_{l,i}$ is increased, whereas thickness (a) has only little influence. The situation changes over at Reynolds numbers one order of magnitude greater. The effectiveness of camber in increasing maximum lift coefficient reduces to just about a quarter of that at the aforementioned Reynolds number while the effectiveness of the thickness to chord ratio becomes more pronounced.

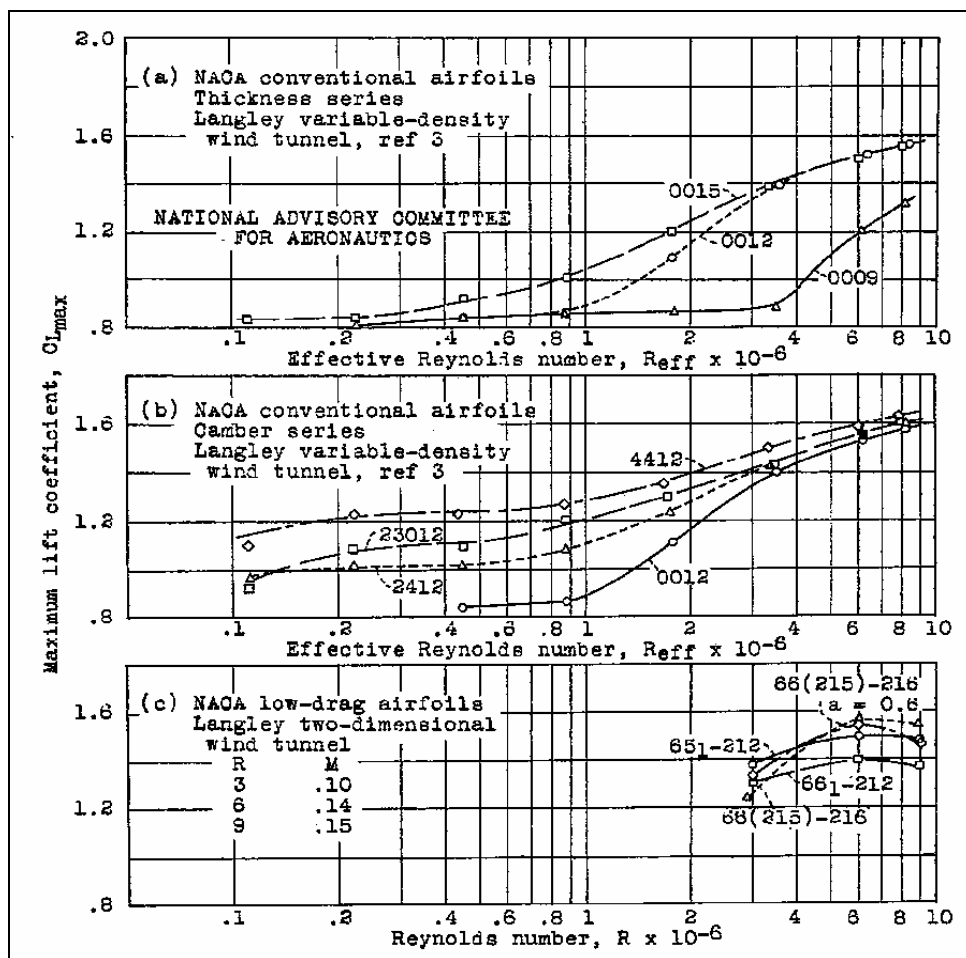


Fig. 33: Variation of maximum lift coefficients of several NACA airfoils with Reynolds numbers (Fig. 15 reproduced from [130]).

In order to guarantee some parametric freedom for the wing optimiser, the influence of camber will be automatically accounted for. Hence, $c_{l,max}$ of a symmetrical section with maximum thickness to chord ratio (t/c) has to be provided as well as the gradient by which $c_{l,max}$ is increasing with camber, both depending on Re_c .

Given a $C_{l,max}$ as a function of chord-based Reynolds number and relative thickness for zero camber, values for maximum and minimum lift coefficient can be estimated as follows:

$$C_{l,max} = C_{l,max,uncambered} + \left(\frac{dc_{l,max}}{dc_{l,i}} \right) \cdot C_{l,i}$$

For thin airfoil stall, the coefficient ($dc_{l,max} / dc_{l,i}$) can be set to 1.0. For regions where trailing edge stall can be expected a value of 0.3 ... 0.5 is more realistic.

For the minimum lift coefficient no significant influence of the type of stall can be observed. A rough estimate is

$$C_{l,min} = -C_{l,max} + C_{l,i}$$

3.1.5 Non-Linear Lift Effects

Aircraft are usually designed to operate with fully attached flow because of the rapid loss of performance in case of flow separations. It is common practice in the conceptual design phase of transport aircraft to guarantee this condition by specifying that the local spanwise lift coefficients must be lower than the sectional maximum lift coefficients, which in turn are specified by the type of airfoil section, Reynolds and Mach number. Aircraft wings of moderate to high aspect ratios in this respect benefit from the fact that the local lift coefficients do not differ much from the wing mean value.

A review of the relatively small number of documented experiments of wings equipped with multiple winglets (representative references are [50], [57], [78]) reveals that the designs were made rather intuitively. Some configurations were optimised iteratively with the aim of enhancing performance. Most authors report of problems with flow separations at winglet roots. A review of the abovementioned documents suggests that the condition of fully attached flow has hardly been achieved for the bulk of experiments. It was an objective of the programme development process to allow validations with experimental data. For this purpose it was required to leave the field of linear aerodynamics and add a module for the non-linear effects encountered at the maximum and minimum lift regions of operation.

The discussion will be initially restricted to 2D airfoil sections. The boundary layer of a symmetrical airfoil section of moderate thickness well above the critical Reynolds number with free transition will separate on the suction side starting at the trailing edge. With increasing angle of attack, the suction on the forward part of the section intensifies and the adverse pressure gradient between the minimum and the trailing edge pressure increases. The point where the critical pressure recovery is reached (compare Stratford's criterion as discussed by Smith [131]) moves forward against the flow

direction while the angle of attack becomes larger. At the same time, the local lift curve slope is reducing until it becomes zero when maximum lift is reached. The underlying physical process is not influenced by this technically important condition and the lift curve slope as well as the lift will continue to decrease. This sketchy description of the trailing edge stall mechanism for time averaged conditions comprises three main differences to linear aerodynamics being of concern so far which are to be tackled:

1. The lift curve slope varies in the non linear region of the lift polar.
2. The lift does not increase unlimitedly with angle of attack as assumed in lifting line approaches or up to $\alpha = \pi/2$ for the vlm approach but has a lower and an upper boundary.
3. The profile drag increases in case of partly or fully separated flow.

There are several methods at hand to implement variable lift curve slopes in vortex lattice programmes. The basic lift curve slope of a lumped vortex element of infinite span with the collocation point located at the three-quarter-chord position and assuming incompressible flow is 2π . This value can be altered by allowing for a virtual permeability of the element by changing the Neumann boundary condition (refer e.g. to Katz and Plotkin [4]). An alternative method is to move the collocation points from their basic three-quarter-chord locations fore or aft and thus decrease respectively increase the lift curve slope as suggested by Truckenbrodt [95].

Based on the second approach, the relation between lift curve slope and collocation point offset is defined as follows

$$\Delta\xi = \frac{(dc_l/d\alpha)_{\text{pst}}}{2 \cdot \pi} = \frac{c_{l,\text{pst}}}{c_{l,\text{lin}}} \quad (51)$$

where $\Delta\xi$ is the relative distance between the quarter chord and collocation points. The lift coefficients are with respect to sectional chord lengths. The equality of the lift coefficient ratio with the lift gradient ratio stems from the fact that both the actual angles of attack as well as the zero lift angles of attack are identical for the linear and the non-linear case (for an example at the maximum lift point refer to Fig. 34, right). In order to realise a lift curve slope of π , for example, the collocation point must be moved $\Delta\xi = 0.5 = 50\%$ of the original distance between quarter chord and three-quarter chord points forward (i.e. to the mid chord position). It is important to note that the reduction of the lift curve slope is unaffected by the number of chordwise lattice elements as long as subsequent surface elements have identical chord lengths.

The maximum sectional lift coefficients have to be specified as a programme input as well as the shape of the lift characteristics close to the maximum lift condition. The present post-stall model follows the lead of Montgomerie [96]. The shape of the lift

curve up to the maximum lift point is schematically shown on the left hand side of Fig. 34. For compactness of the presentation, only the part with positive lift coefficients is shown.

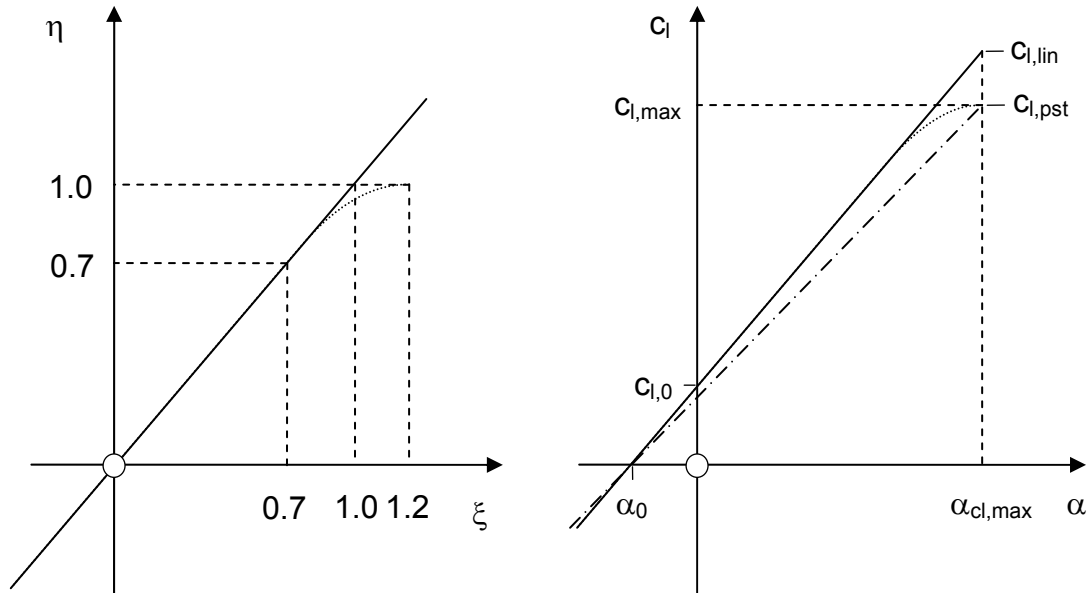


Fig. 34: Left: Generalised lift curve. Stated values applicable to trailing edge stall characteristics. Right: Sectional lift-polar up to $c_{l,max}$. Dash dot line represents VLM lift curve after collocation point adaptation.

The actual non-linear lift-curve with respect to the angle of attack is obtained by the following transformation. The lift coefficients are computed from the shape parameter η

$$c_{l,pst} = \eta \cdot c_{l,max} + \Delta c_{l,sym} \cdot (1 - \eta) \quad (52)$$

where

$$\Delta c_{l,sym} = \frac{c_{l,max} + c_{l,min}}{2}$$

Correspondingly, the angles of attack are derived from the parameter ξ

$$\alpha_{pst} = \frac{c_{l,\xi} - c_{l,0}}{dc_l/d\alpha} \quad (53)$$

where

$$c_{l,\xi} = \xi \cdot c_{l,max} + \Delta c_{l,sym} \cdot (1 - \xi)$$

Parameters defining shapes of the lift curve at maximum respectively minimum lift are available for three different stall types (see Tab. 8). The first shape describes the rather gentle trailing edge stall (see also left hand side of Fig. 34), the second the rather abrupt leading edge stall and the third shape stands for a typical thin airfoil stall.

Tab. 8: Parameters used to compute non-linear lift curves for three different stall types.

Trailing edge stall	ξ	-1.2	-0.7	0.7	1.2
	η	-1.0	-0.7	0.7	1.0
Leading edge stall	ξ	-1.15	-0.8	0.8	1.15
	η	-1.0	-0.8	0.8	1.0
Thin airfoil stall	ξ	-1.25	-0.7	0.7	1.25
	η	-1.0	-0.7	0.7	1.0

Referring to Hoerner [104], Montgomerie [96] suggests to use lift characteristics of a fully separated thin airfoil for angles beyond the maximum lift angle of attack with some modifications for camber and thickness. Since the lift produced by such a surface is usually significantly lower than that predicted by linear aerodynamics, a transition from the maximum lift coefficient to the curve for fully separated flow is required. The shape of the transition curve depends strongly on the type of stall. The mathematical modelling of the transition curve will be based on piecewise cubic splines with prescribed gradients at the start and endpoints.

An equation for the lift of a thin flat plate according to Hoerner [104] is

$$c_{l,fp} = c_{d,90} \cdot \sin \alpha \cdot \cos \alpha \quad (54)$$

Modifications are required since sections with rounded noses will produce lift even at an angle of attack of 90 deg. Furthermore, the lift of a cambered plate is not exactly zero at $\alpha = 0$ deg. Montgomerie suggests to replace α by an correlation angle β

$$\beta = \alpha - \delta_1 - \delta_2 \quad (55)$$

where $\delta_1 = c_{l,90} \cdot \sin \alpha$, $c_{l,90} = 2/3 \cdot \left(\frac{t}{c} \right)_{\max}$

and $\delta_2 = \alpha_0 \cdot \cos \alpha$

Another camber correction is suggested in [96] which is a multiplier 'A' that increases the lift at incidences around 45 deg for positive camber and decreases lift for angles around -45 deg:

$$A = 1 + \frac{c_{l,0}}{\sin(\pi/4)} \cdot \sin \alpha \quad (56)$$

The following equation is the final outcome describing the lift characteristics of a cambered section of zero to moderate relative thickness in case of fully separated flow:

$$C_{l,sep} = A \cdot C_{d,90} \cdot \sin\beta \cdot \cos\beta \quad (57)$$

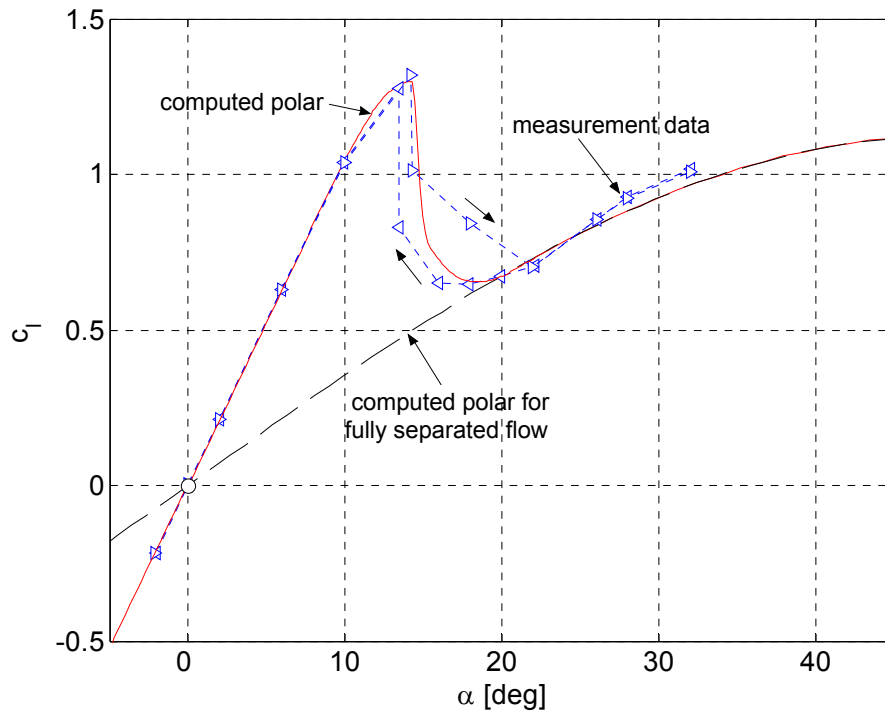


Fig. 35: Section lift polar of NACA 0012 airfoil: $Re_c = 1.8 \cdot 10^6$, $(dc_l/d\alpha)_{lin} = 6.0$, Leading edge stall, $C_{l,max} = 1.30 = -C_{l,min}$, $C_{d,90} = 2.3$, Measurement data from reference [110].

Fig. 35 compares the resulting lift polar of the NACA 0012 airfoil section with experimental data of Critzos et al. [110]. Measurements were taken at Mach numbers below 0.15 using a wind tunnel model spanning from wall to wall so that the results can be regarded to represent two-dimensional conditions. The measurements show a pronounced hysteresis in the post-stall region. At angles of attack between 14 and 22 deg the lift is higher when the incidence is increased to greater values and vice versa. It is neither the purpose of the current modelling nor necessary for the assessment of configurational performance to reproduce this effect closely so that the fit of the computational model in the transition region from the steeper linear lift curve slope to the polar applicable to fully separated flow is acceptable. The difference between the angle of attack for maximum lift and the intersection with the polar for fully separated flow is 8.5 deg in the present case. The correspondence of the polar for fully separated flow with the measurement data were found to be better for an increased $C_{d,90}$ of 2.3 instead of the measured value of 2.08 according to [110]. This deviation from the actual value is acceptable since the lift characteristics in the post-stall region below

angles of attack of 45 deg are of concern. Therefore, the following computations are based on the adapted value.

Another modification to the vortex lattice code for suitable post-stall computations is with regard to the profile drag. Measured drag coefficients for the NACA 0012 airfoil section of reference [110] are plotted in Fig. 36. The sudden drop of lift after exceeding the maximum lift coefficient is accompanied by an increase in profile drag. The profile drag model so far expresses this quantity as a function of local lift coefficient. The actual loss of lift would thus result in decreasing drag which does not make sense. The following equation is devised for the additional profile drag increment and has been integrated into the lift dependent profile drag module of VLM++

$$\Delta c_{d,pst} = 0.16 \cdot \Delta c_l^{1.5} \quad (58)$$

where

$$\Delta c_l = |c_{l,lin} - c_{l,pst}|$$

With such simple corrections, the lift, drag and pitching moment characteristics can be computed with a satisfactory quality for angles of attack that do not exceed the corresponding stall value by more than a factor of two (Fig. 36). No further corrections have been applied to the pitching moment computation. Whilst the collocation points are moved forward, the centre of the chordwise load distribution automatically moves aft, which, for positive lift coefficients, generates a negative pitching moment (nose down) about the quarter chord point.

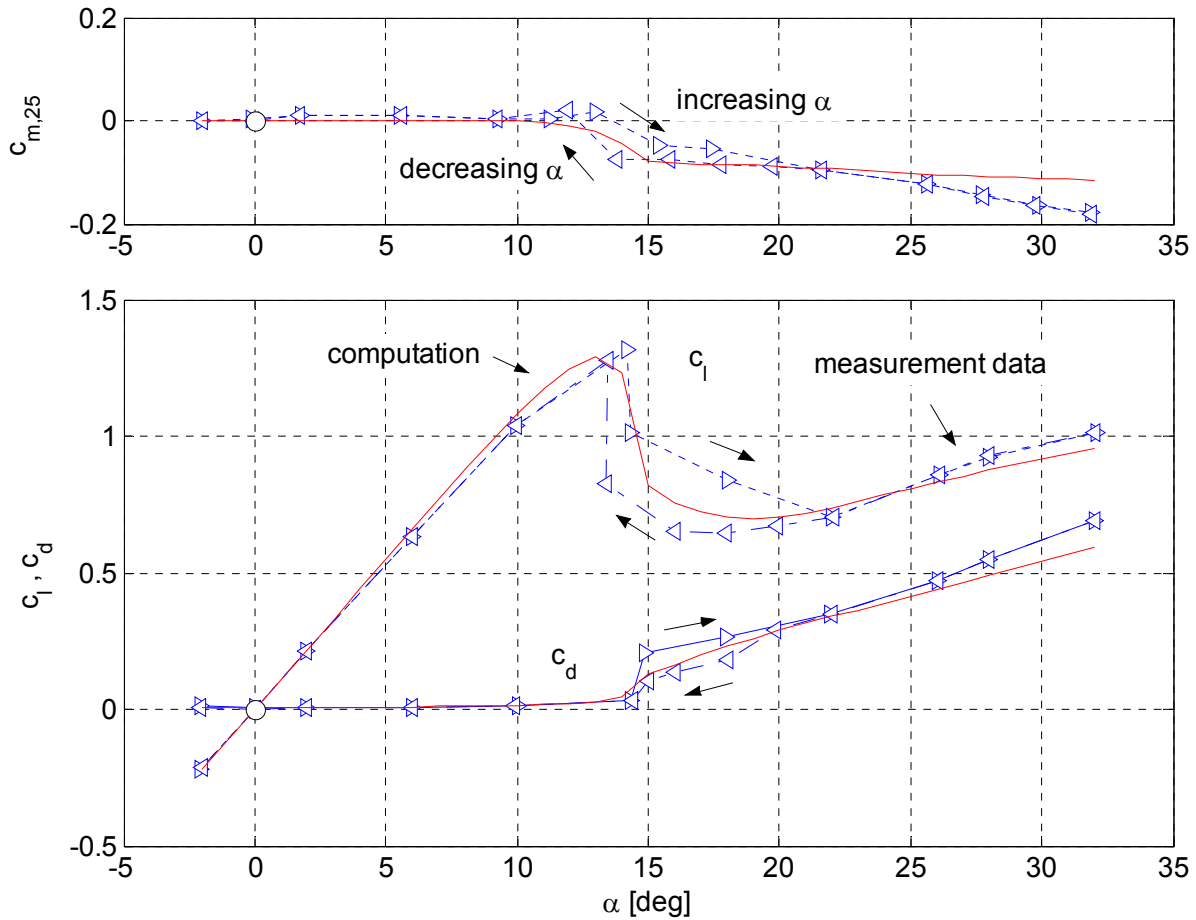


Fig. 36: Computed section lift, drag and pitching moment polars of NACA 0012 airfoil in comparison to measurement data [110]: $Re_c = 1.8 \cdot 10^6$, $(dc_l/d\alpha)_{lin} = 2 \cdot \pi$, Leading edge stall, $c_{l,max} = 1.30 = -c_{l,min}$, $C_{d,90} = 2.3$.

There are differences in the post-stall behaviour of two- and three-dimensional surfaces which deserve attention. Critzos et al. refer to earlier measurements where a drag coefficient of 1.48 was measured for a flat plate with an aspect ratio of 20 at 90 deg incidence, which is significantly lower than the two-dimensional value of about 2. The following tentative approach is suggested to represent 3D conditions using the linear lift curve slopes of the wing sections as a basis

$$\begin{aligned}
 C_{d,90} &= C_{d,90,2D} \cdot \frac{1}{2} \cdot \left(1 + \frac{(dc_l/d\alpha)_{lin}}{2 \cdot \pi} \right) & (dc_l/d\alpha)_{lin} < 2 \cdot \pi \\
 C_{d,90} &= C_{d,90,2D} & (dc_l/d\alpha)_{lin} \geq 2 \cdot \pi
 \end{aligned} \tag{59}$$

The maximum drag of a surface in a setting perpendicular to the flow direction is thus lowered if the wing has a finite span and hence a lift curve slope that is less than 2π .

The corrected lift curve of a cambered NACA 4415 airfoil section is depicted in Fig. 37 together with an example illustrating the practical use of the model. The lift curve slope is only 3.0, which is a typical value for outboard wing sections. For a linear lift coefficient of 1.90, a correspondent post-stall value of 1.165 is found. In order to guarantee similar sectional characteristics in the vortex lattice code, the collocation point is moved forward towards the quarter chord point by $(1 - c_{l,pst}/c_{l,lin}) = (1 - 0,613) = 38.7\%$ of the original distance in order to implement the required lower lift curve slope of 1.839.

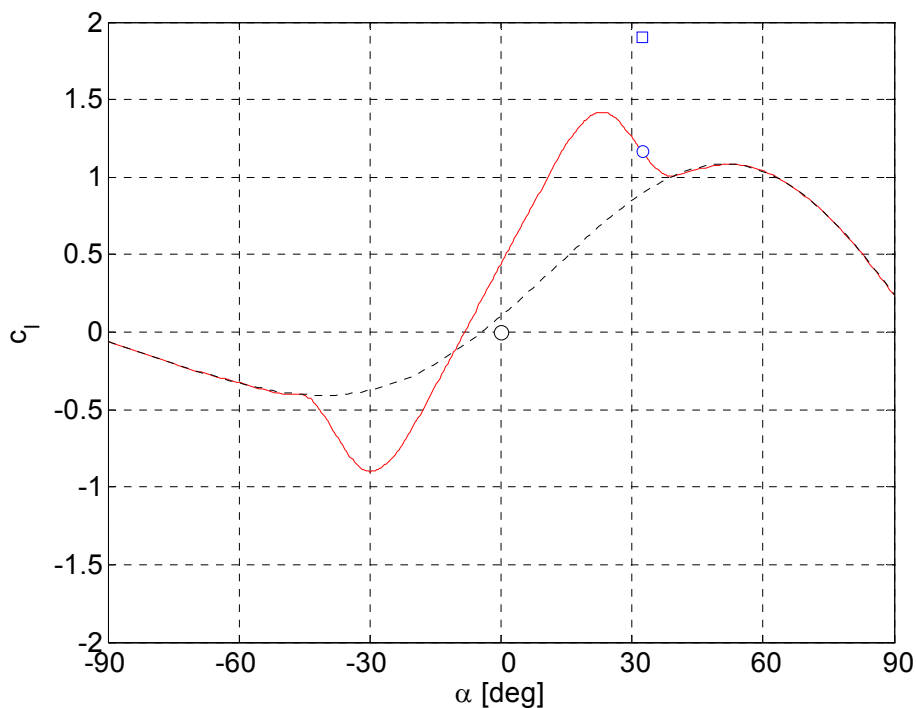


Fig. 37: Section lift polar of NACA 4415 airfoil: $Re_c = 3.0 \cdot 10^6$, $(dc_l/d\alpha)_{lin} = 3.0$, Trailing edge stall, $c_{l,max} = 1.42$, $c_{l,min} = -0.9$, $c_{d,90} = 2.3$, $c_{l,lin} = 1.90$ (square symbol), $c_{l,pst} = 1.165$ (bullet).

In connection with cascade computations, it became necessary to use the post-stall model in an iterative way. Given a cascade arrangement of three airfoils, the problem arises that usually one surface stalls first. It has been previously discussed that the lift loss may be rather abrupt. If the leading surface of the cascade stalls, the load on the subsequent two airfoil sections suddenly rises and can eventually cause these sections to stall as well. Considering three-dimensional problems, multiple iterative calls of the post-stall subroutine tend to relocate only certain collocation points but others not, producing non-homogeneous spanwise distributions of the collocation points. More precisely, the collocation point offsets after the first call are smoothly distributed due to the original smooth lift distributions of the basic linear solution with all collocation points at the same relative position. Supposedly, because of the degree of freedom increases with the number of spanwise strips, the distribution of collocation point offsets attains a

rather rectangular shape. Starting from the second call, the sections outward of a particular spanwise station are unloaded so that the linear lift range is recovered but the linear load increases inboards instead, pushing the respective stations deeper into the stalled condition. The unloading of the outboard sections is thus at the cost of higher loads at the inboard stations.

By nature, boundary layer separation cannot be restricted to a sharp bounded local area as suggested by the cycle described above because it is an unsteady process. It was possible to achieve more realistic results by adding a certain spanwise stiffness. Neighbouring collocation point offsets were averaged so that the fundamental shape of the load distribution was retained but the transitions from stalled sections to those still in the linear range of the polar were smoothed.

The maximum iteration number has been set to six in order to limit above effects. Even for multiple surfaces, the convergence criterion defined by the rate of change of the sum of relative collocation point offsets is met before the maximum iteration number is reached, in most cases.

3.1.6 Cascade Effects

3.1.6.1 Overview of Effects for High-Lift Generation

The fact that cascade arrangements of airfoil sections may be suited to increase maximum lift has already been recognized in the early days of aeronautics. Smith [131] cites a paper of Handley Page dating back to 1921 that documented the development of airfoils with slots. Starting with a maximum lift coefficient of 1.65 for the basic RAF 19 airfoil section a maximum lift coefficient of 3.92 was reached for a cascade arrangement of 7 elements. Smith presents a summary of the primary effects that cause airfoil cascades to develop higher maximum lift than independent airfoil sections:

1. slat effect
2. circulation effect
3. dumping effect
4. off-the-surface pressure recovery
5. fresh boundary layer effect.

In an arrangement where a small lift producing surface is placed forward and above a following one like a combination of slat and main element, the circulation of the forward slat is such as to reduce velocities on its lower (pressure) side but also to reduce flow velocity at the upper side of the main element. Thus pressure peaks at the leading edge of the main element are reduced. This is referred to by Smith as slat effect.

The circulation effect describes the increased load of an upstream surface (e. g. a slat) due to the presence of the second one which is best illustrated by an increase in local lift curve slope $dc_l/d\alpha$ (c_l with respect to the forward surface chord) which can easily double the flat plate lift curve slope even in incompressible flow.

Smith first introduced the term "dumping effect" for the pressure recovery relief regarding the suction side of a forward airfoil section if the trailing edge is positioned in the low pressure region of a following section. Since pressure and velocity are connected by the Bernoulli equation, the discharge velocity of the air leaving the trailing edge is higher than it would be in an unbounded flow. The relief of the pressure rise has the effect that the boundary layer separation is delayed which permits to attain higher lift coefficients.

Once the boundary layer from a forward element is dumped, it inevitably undergoes a pressure recovery process. If the boundary layer does not have contact to the wall it cannot separate. Off-the-surface pressure recovery is thus very efficient on condition that the wall distance is sufficiently large.

If an airfoil section of given chord length is broken down into three individual lifting elements so that the streamwise extent remains unchanged the average boundary layer thickness of the three elements will be lower than the corresponding figure of the single airfoil. Each new element starts out with a fresh boundary layer at its leading edge and that is the reason for thinner boundary layers. Thin boundary layers can withstand stronger pressure gradients than thick ones.

The circulation effect (2) is automatically represented in common tools for the assessment of multi-element configurations such as panel or vortex-lattice codes. The part of the dumping velocity (3) that is induced by other cascade elements can be computed even with a vortex lattice programme on condition that the trailing edge of a forward surface is in the far field of elements belonging to a rear element. At least a panel code has to be utilised to cover all items that refer to pressure distributions or contour velocities as it is required to simulate the slat effect (1). Standard vortex-lattice programmes only represent the mean line surface. Contour velocities can be computed with higher order lifting surface approaches but are only valid for surfaces of zero thickness. Nevertheless, the slat effect described above would be of little benefit since the computational contour velocity at the leading edge becomes singular with only few exceptions. A leading edge singularity is physically impossible and will not be encountered in real flow. In the simple case of a flat plate, the boundary layer already separates at an angle of attack of just a few degrees. A separation bubble develops that alters the effective shape so that a finite effective thickness is generated. This mechanism prevents the development of extreme super-velocities. It is clear that potential based methods cannot compute this complex effect and hence care must be

placed upon the interpretation of computational results from schemes that utilise the airfoil section mean line. A leading edge velocity singularity will be directly evident from lifting surface or vortex lattice schemes that use a higher order approach for the chordwise circulation distribution (compare e.g. Lan [103]). At a first glance, it is less apparent from the results of simpler schemes such as used here but it can be shown that the circulation of the leading lattice element strengthens without bounds as the number of chordwise elements is increased. The amount of pressure recovery is thus also singular and the reduction of the infinite leading edge peak velocity by a finite amount would computationally not make any difference. Representation of the effective thickness is thus a necessary prerequisite for incorporating the slat effect into an aerodynamic prediction tool intended to represent high lift effects of arbitrary surface arrangements.

The discussion so far assumed that effects with regard to boundary layer flow can be tackled with implicit computations without explicit boundary layer computations. For conceptual design purposes this implicit approach appears promising and the concept will be outlined as follows.

It appears that Smith favoured the "dumping effect" (3) as the pivot point for explaining the high-lift effect of airfoil cascades. His train of thought is centred on kinetic energy contained in boundary layer flows. He argues that a 2-inch airfoil model at 100 mph will have very high values of velocity gradients, but a similar 200-inch airfoil at 1 mph will have extremely low values. Nevertheless, both airfoils are exactly similar with regard to their flow separation characteristics and high-lift properties because of identical Reynolds numbers. Distributions of the pressure coefficients are different in magnitude and Smith suggests to normalise the contour velocities in a different way. Instead of using the free stream velocity he suggests to take the velocity at the beginning of the pressure rise for normalisation.

This leads to a new quantity which is referred to as canonical pressure coefficient

$$\bar{c}_p = 1 - (Q_t/Q_0)^2 \quad (60)$$

where Q_t - local velocity tangent to the contour
 Q_0 - initial velocity at start of deceleration (point of minimum pressure).

In the canonical system $\bar{c}_p = 0$ represents the start of pressure rise (minimum static pressure) and $\bar{c}_p = 1$ the maximum static pressure possible if $Q_t = 0$. Smith states that if two pressure distributions can be made congruent by proper scaling, a flow experiencing a deceleration of $(Q_t/Q_\infty)^2$ from 20 to 10 is no more and no less likely to separate than one decelerating from 1.5 to 0.75.

The canonical pressure coefficient can be expressed in terms of the conventional pressure coefficient definition:

$$\bar{c}_p = 1 + (c_p - 1) \cdot \left(\frac{Q_\infty}{Q_0} \right)^2 \quad (61)$$

where

$$c_p = 1 - \left(\frac{Q_t}{Q_\infty} \right)^2 \quad (62)$$

Smith illustrates the dumping mechanism as a way to delay separation and to increase loadability by means of a rough calculation. The basis is a prescribed contour velocity distribution for an airfoil section in unbounded flow at a given angle of attack. He assumes that the basic pressure distribution does not change in shape if three sections of the same profile shape are organised in a cascade configuration. The second assumption is that subsequent sections induce a dumping velocity ratio of $(Q_t/Q_\infty)^2 = 1.5$ on the forward element due to the position of the trailing edge of the forward element in the low pressure region of the following one. The higher trailing edge velocity of the upstream element makes a higher maximum contour velocity possible while holding the critical canonical pressure coefficient at the trailing edge constant. The critical trailing edge canonical pressure coefficient is assumed to be predominantly a characteristic of the profile section (for $Re, M = \text{const}$). The lift coefficient for the dominating upper (suction) side of the airfoil $c_{l,u}$ can be directly correlated to the increased dumping velocity because it is computed by means of chordwise integration of the c_p -distribution which in turn is directly dependent on the local airspeed squared. The lift of the ensemble could be estimated with the following equation

$$c_{l,u} = f_1 \cdot c_{l,u,0} + f_2 \cdot m_2^2 \cdot c_{l,u,0} + f_3 \cdot (m_2 \cdot m_3)^2 \cdot c_{l,u,0} \quad (63)$$

where $m_2 = m_3 = (1.5)^{1/2}$ - magnification ratio for velocities
 $f_1 = f_2 = f_3 = 1/3$ - chord length divided by sum of chord lengths.

Division by $c_{l,u,0}$ yields an equation for the magnification factor of the loadability of the cascade above that of the basic section

$$(c_{l,u}/c_{l,u,0}) = f_1 + f_2 \cdot m_2^2 + f_3 \cdot (m_2 \cdot m_3)^2 \quad (64)$$

which, in the present example, assumes a value of 1.583. The loadability gain is thus 58.3%. Smith admits that this simple assessment is as much hypothesis as it is a statement of fact but he expressed confidence that the dumping effect plays an important role for high-lift generation with passive high lift devices and that at least the tendency of the prediction is correct.

3.1.6.2 Outline of a Method for Implicit Estimation of High-Lift Effects due to Cascade Arrangements

For the present purpose, a similar but refined approach compared to the rough outline of the idea above will be pursued. The objective is not to compute maximum and minimum lift coefficients from scratch, a task that has not yet been satisfactorily solved even with help of modern CFD methods, but rather to derive these characteristics on the basis of well established sectional data (i.e. from experiments), which will then be incrementally altered depending on the mutual interference of airfoil section or wing pressure distributions. Even this task is of considerable complexity and some of the prerequisites stated further below may not exactly hold in real flows.

The approach is to compute the critical canonical trailing edge pressure coefficient $\bar{c}_{p,te,crit}$ for a given 2D airfoil section. Values for the upper and lower sides are established according to the given maximum and minimum lift coefficients. The loadability limits are taken from measurement data and hence effects of Reynolds number, surface condition, transition location and flow quality on the loadability are already regarded from the outset. The 3D pressure distributions of sections in cascade settings are then computed for a sequence of incidences from which the canonical pressure coefficients $\bar{c}_{p,te}$ are derived. The condition where $\bar{c}_{p,te,crit}$ is reached is interpolated from the results and the corresponding lift coefficient is established and saved as the maximum respectively minimum lift coefficient for the section as part of the airfoil cascade. By so doing, the scheme regards slat effect (1), circulation effect (2) and dumping effect (3) according to [131]. Preconditions are that the following properties do not change

- the type of stall of the airfoil section and
- the boundary layer flow conditions, i.e. the transition location.

It appears that the method is best suited for cases where the loadability is limited by the trailing edge stall type. Nevertheless, it is expected that at least the resulting trends are also applicable to other types of stall such as leading edge or thin airfoil stall. All stall types are interrelated with boundary layer separation and this process is inevitably connected to the pressure distribution, particularly the adverse pressure gradients in the deceleration region of the suction side. Thus, any means of pressure recovery relief should be effective with regard to stall delay.

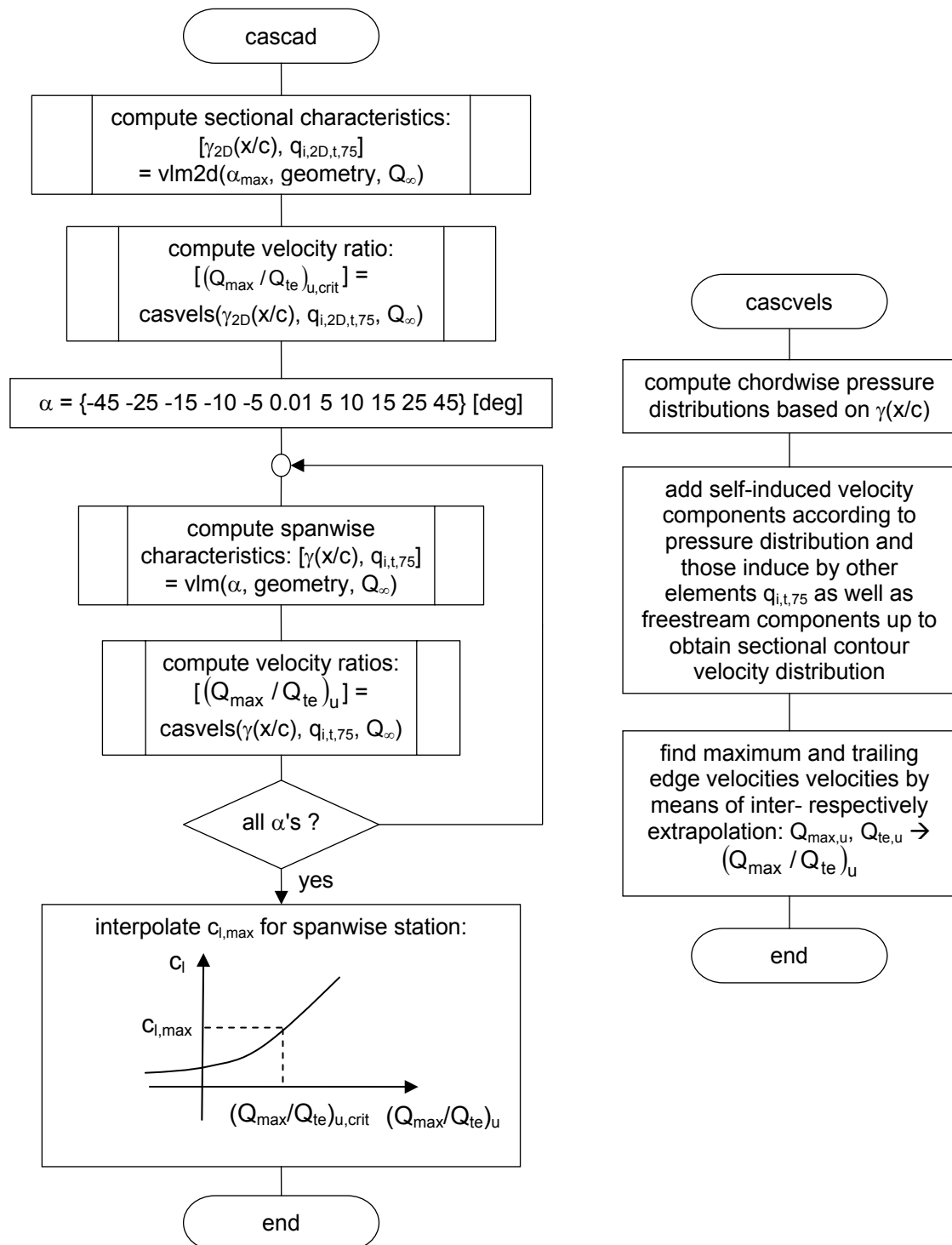


Fig. 38: Simplified program structure for cascade effects computations. Example for maximum lift only. All quantities with respect to section coordinates.

Fig. 38 illustrates the procedural sequence of subroutines for the cascade computation. The figure shows the series of calculations for the maximum lift only. The subroutine "cascad" starts with the computation of the velocity ratio $(Q_{max}/Q_{te})_{u,crit}$ on the critical

upper (suction) side of the airfoil section under two dimensional conditions and for the maximum lift angle of attack.

The problem of finding the trailing edge velocity ratio in three dimensional flow must be tackled in a different way, because of the fact that the maximum angle of attack depends on the individual spanwise sections. The velocity ratios are hence computed for a sequence of α 's and the local maximum lift coefficient is found by interpolating the three dimensional lift coefficient for which the critical velocity ratio is reached.

Note, that the contour velocities induced by other lifting elements $q_{i,t,75}$ are computed at the three-quarter chord points of the lattice elements by the VLM program. This location is advantageous, since the tangential self-induced velocities are usually small (zero for uncambered sections) and the contributions of other lift producing interfering surfaces are greater. The induced tangential velocities are then computed at all chordwise nodes that were chosen for the section pressure distribution computation (description in section 3.1.6.3, number of nodes on the order of 10^2) by means of interpolation of the VLM data ($q_{i,t,75}$), respectively extrapolation aft and in front of the three-quarter chord points of the rearmost or foremost lattice elements. These velocities are superposed with the freestream velocity and the section contour velocity obtained from the chordwise pressure distribution computation. Confining the discussion to the maximum lift coefficient, the velocity peak Q_{\max} ($= Q_0$) at the suction side and the velocity at the trailing edge Q_{te} are computed in subroutine "cascvels" and handed over to the calling subroutine "cascad".

3.1.6.3 Chordwise Pressure Distributions

The vortex lattice method makes use of concentrated vortex filaments. Induced velocities tangent to the surface of a single lifting element become singular at the quarter chord location and are zero at the others (2D case for exemplification). This makes the direct computation of the chordwise pressure distribution impossible.

However, pressure distributions can be obtained by exploiting family relations among the various methods based on potential theory, namely VLM and thin airfoil theory including extensions for the present case. Fig. 39 illustrates the concept of the suggested hybrid method. First, continuous quasi-two-dimensional chordwise circulation distributions are adapted to the discrete VLM results, thus effectively inverting the derivation of the lumped vortex concept from thin airfoil theory. Second, following the approach of Riegels [114], a model accounting for the displacement effect due to section thickness is added that effectively removes possible leading edge velocity singularities. Third, the velocities tangent to the mean line that are predominantly induced by adjacent lifting surfaces are added. Corrections of the resulting chordwise pressure distributions according to simple sweep theory are applied if the wing is swept back or forward. Appendix C contains a detailed description of the method.

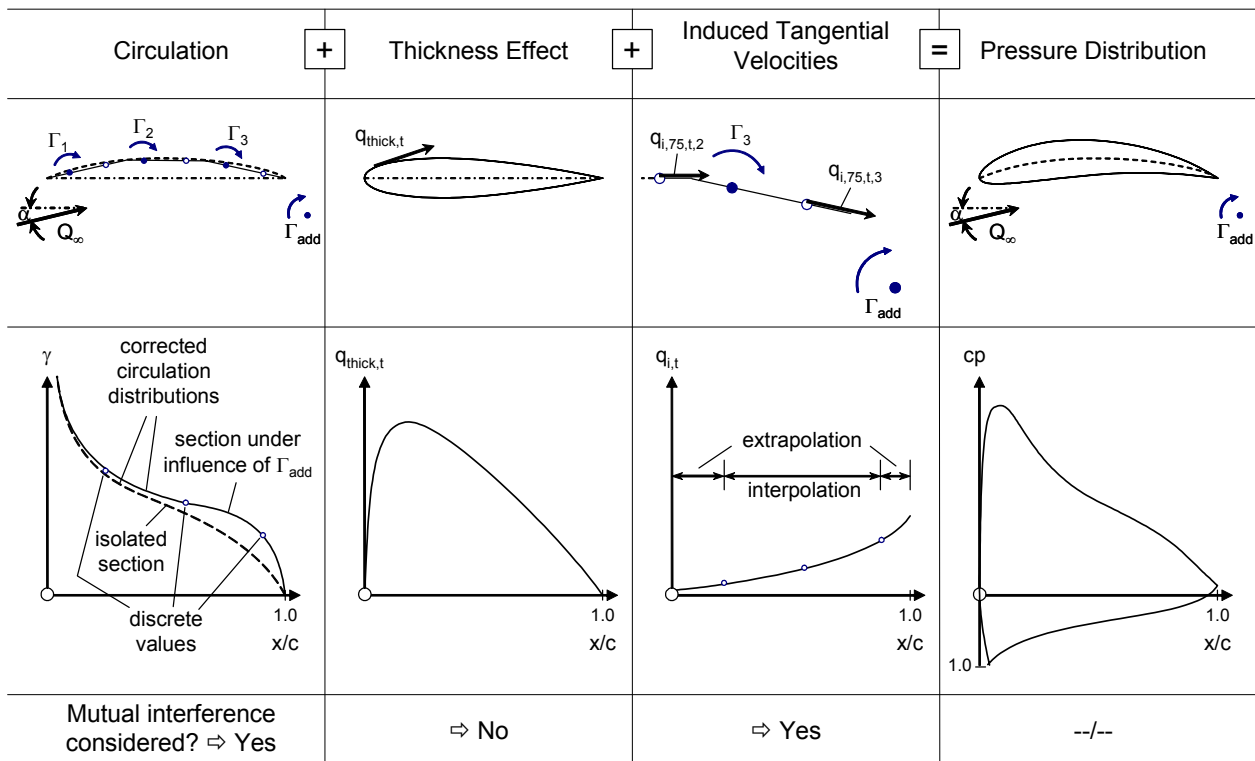


Fig. 39: Concept of hybrid method to estimate pressure distributions based on VLM.

The method produces reasonably accurate pressure distributions of single surfaces as well as of multiple surface assemblies having arbitrary wing sections. For the present purpose, however, only NACA-4-digit sections were used. Due to the fact that the method neglects the mutual interference due to thickness, the reliability of the method reduces with decreasing distance between adjacent interfering lifting elements (i.e. settings where the gap between two sections is significantly influenced by the section thicknesses). This disadvantage of the suggested hybrid method as compared to panel methods, where the thickness effects and interferences are inherently incorporated, is compensated by the fact that the VLM geometry set-up is much simpler and versatile than a panelling scheme for thick bodies with enclosed volumes. Moreover, the present method may offer advantages with respect to turn-around times compared to panel methods because of the significantly smaller number of elementary surfaces and the smaller coefficient matrices. It is expected that these advantages are not outweighed by the additional computational steps of the hybrid method outlined above.

3.1.6.4 Verification of Maximum Aerodynamic Loadability Changes of Two Interfering Wing Sections due to Varying Cascade Arrangements

Having the opportunity to obtain pressure distributions, the loadings of airfoil sections and combinations thereof can be compared with well established sectional data in terms

of the contour velocity ratio between the location of minimum pressure and the trailing edge or, equivalently, the corresponding canonical pressure coefficient. Fig. 40 summarises the results of a parametric study where the gap between two NACA 0015 airfoil sections without stagger was systematically changed. The trailing surface (2) was moved from a location of -4 chord lengths below the leading section (1) to a position of 4 chord lengths above. For each location, the maximum and minimum lift coefficients were computed. The maximum sectional lift coefficient of the airfoil section was assumed to be 1.55 in unbounded flow. The post-stall model was switched off for this computation.

In the course of the trailing surface moving upwards so that the vertical gap decreases, the maximum lift coefficient of the leading surface rises while the value for the trailing surface drops. The effect of gap variation on minimum lift coefficient is less pronounced, the leading surface having greater values than the trailing surface up to $\Delta h / c = -0.235$. The forward section attains its greatest value for the maximum lift coefficient of 2.18 at $\Delta h / c = -0.15$. The rear and lower section reaches a minimum in maximum lift coefficient of 1.10 at $\Delta h / c = -0.05$.

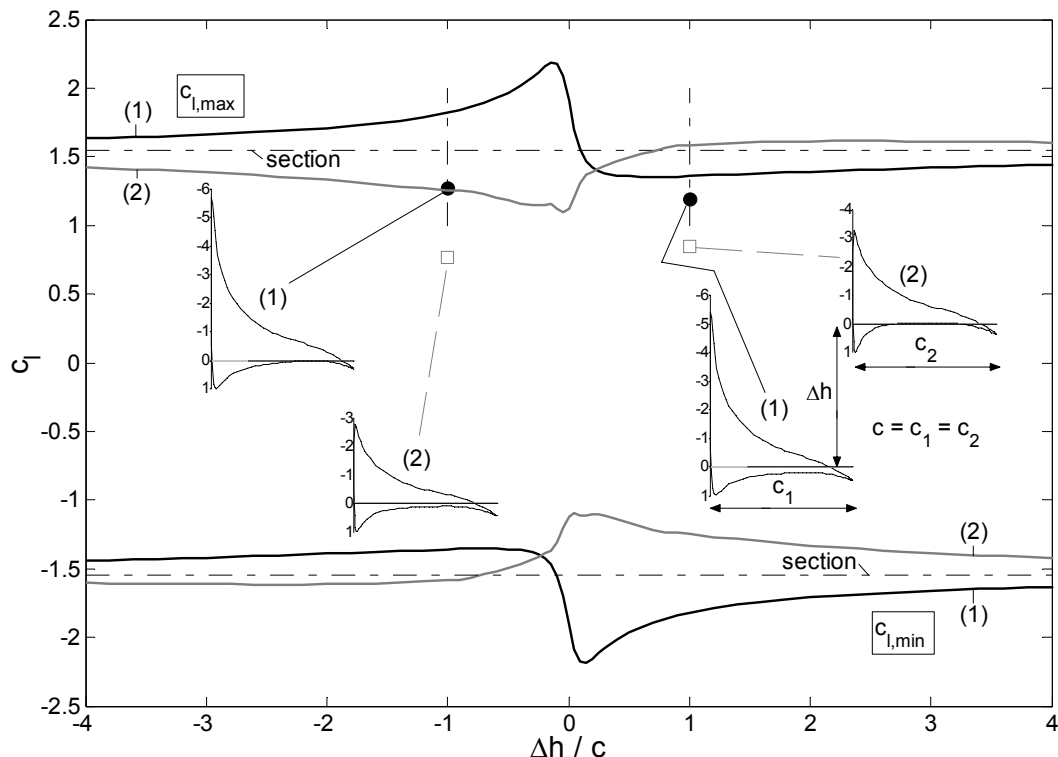


Fig. 40: Effect of gap variation between two NACA 0015 airfoil sections on maximum and minimum section lift coefficients ($n_{i1} = n_{i2} = 4$, $\Delta h = z_2 - z_1$). Insets show chordwise c_p -distributions for $\alpha = 10^\circ$.

If the rear surface comes to pass the co-linear configuration, the maximum lift coefficient of the forward wing drops and the value for the rear and now higher surface starts to increase. The resulting trend when increasing the gap to positive values is analogous to the development of the minimum lift coefficient when the gap was negative as discussed above. This is because of the symmetry of the configuration.

Chordwise distributions of the pressure coefficients for an angle of attack of 10° have been added to Fig. 40 to illustrate the effect of the gap. It can be observed that the trailing edge pressure of the forward section is greater for the positive gap (compressor cascade configuration) and smaller for the negative gap (turbine cascade configuration). The velocity ratio of the leading section between the location of minimum pressure and the trailing edge is 3.07 for the negative gap set-up, implying a greater margin to the critical velocity recovery of 3.95 compared to a value of 3.50 for the positive gap (see also data summary in Tab. 9).

Tab. 9: Key data of Fig. 40. Lift coefficients derived from VLM-results. Data index * for $\alpha = 10^\circ$.
Section values: $c_l^* = 1.097$, $c_{l,max,prof} = 1.55 = -c_{l,min,prof}$, $(Q_{max}/Q_{te})_{u,crit} = (Q_{max}/Q_{te})_{l,crit} = 3.95$.

$\Delta h / c$	-1		1	
Section	1	2	1	2
c_l^*	1.271	0.765	1.190	0.846
$(Q_{max}/Q_{te})_u^*$	3.07	2.56	3.50	2.56
$(Q_{max}/Q_{te})_l^*$	1.39	1.25	1.24	1.26
$c_{l,max}$	1.822	1.256	$-c_{l,min,1} (\Delta h/c=-1)$	$-c_{l,min,2} (\Delta h/c=-1)$
$c_{l,min}$	-1.357	-1.586	$-c_{l,max,1} (\Delta h/c=-1)$	$-c_{l,max,2} (\Delta h/c=-1)$
c_l^*	1.018		1.018	
Critical section (high α)	<input checked="" type="checkbox"/>	<input type="checkbox"/>	<input checked="" type="checkbox"/>	<input type="checkbox"/>
$\Rightarrow c_{l,max}$	1.459		$-c_{l,min} (\Delta h/c = -1)$	
Critical section (low α)	<input checked="" type="checkbox"/>	<input type="checkbox"/>	<input checked="" type="checkbox"/>	<input type="checkbox"/>
$\Rightarrow c_{l,min}$	-1.161		$-c_{l,max} (\Delta h/c = -1)$	

As a consequence, the overall maximum lift coefficient is significantly higher for the turbine cascade compared to the compressor cascade arrangement. Overall maximum lift coefficient is limited by the surface that first attains its ultimate value. This commonly used aircraft pre-design assumption is accurate enough for verification purposes. The leading winglet reaches the maximum respectively minimum lift conditions first, for positive as well as negative gap settings. Despite the fact that the overall maximum lift coefficient is smaller than that of the airfoil section, the value of 1.459 is 17.5 % higher than the corresponding figure of 1.242 without regarding cascade effects.

The total maximum lift coefficient of the configuration with a gap of $\Delta h/c = -1$ increases if the rear surface is set at an incidence of 1.5° . The lift coefficients for $\alpha = 10^\circ$ are 1.305, 0.908 and 1.11 (section (1), (2) and total with respect to $c_{\text{tot}} = c_1 + c_2$). The maximum lift coefficients are analogously 1.860, 1.273 and 1.556. For this configuration the overall maximum lift coefficient is thus slightly higher than that of the airfoil section.

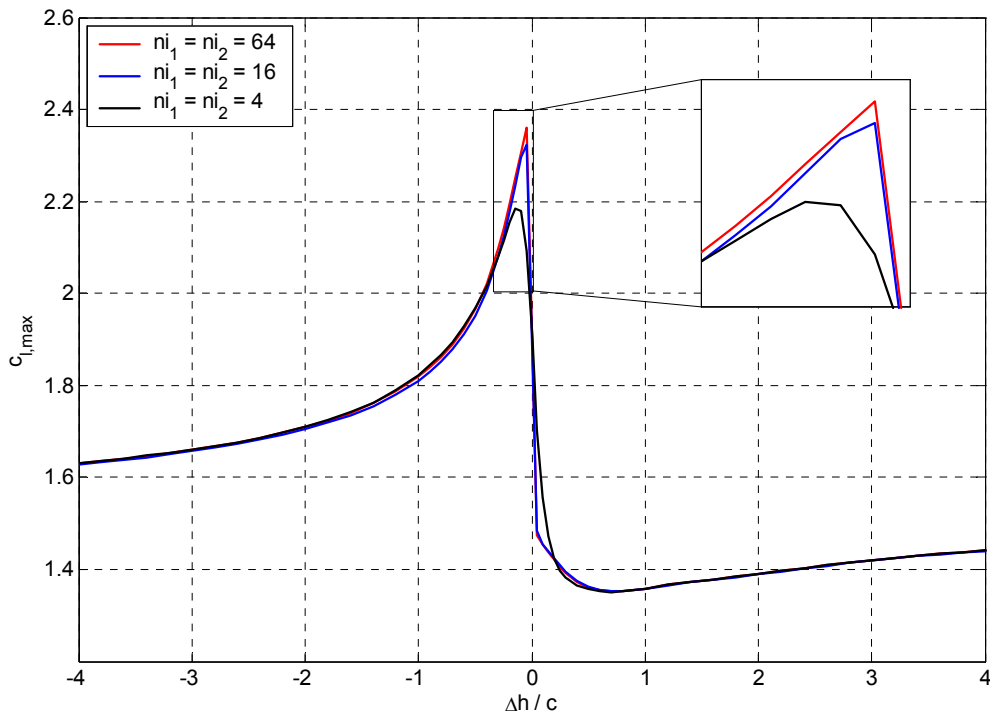


Fig. 41: Effect of the number of chordwise elementary surfaces on the maximum lift coefficient of the leading airfoil section of a two-surface configuration ($\Delta h/c = -1$).

Fig. 41 finally indicates the influence of the chordwise number of lattice elements on maximum lift interference for the leading surface of the original setup with zero incidences. For small negative gaps, the maximum lift coefficient increment becomes greater the more chordwise elements are used. This is because the tangential velocity at the three-quarter chord location of the rearmost lattice element attains its maximum value at a smaller gap in the case of the fine resolution. The velocity induced by the leading edge circulation of the rear surface is mostly greater because of the smaller gap. Comparing the increments in $c_{l,\max}$, it will be noted that the development is convergent because the relative difference decreases with increasing number of elements. However, the range where this discretisation effect is substantial is relatively small. For many practical cases and in particular for multi-winglet configurations with its usually wide gaps, the smallest chordwise resolution is expected to be sufficient for statements on performance trends.

3.1.6.5 Three-dimensional Validation of Maximum Lift Effects due to Cascade Arrangements

This section is intended to demonstrate how the maximum lift adaptation method actually works. An experiment on a generic wing-canard configuration documented in reference [125] has been taken as validation basis. A two-view sketch of the model is shown in Fig. 42.

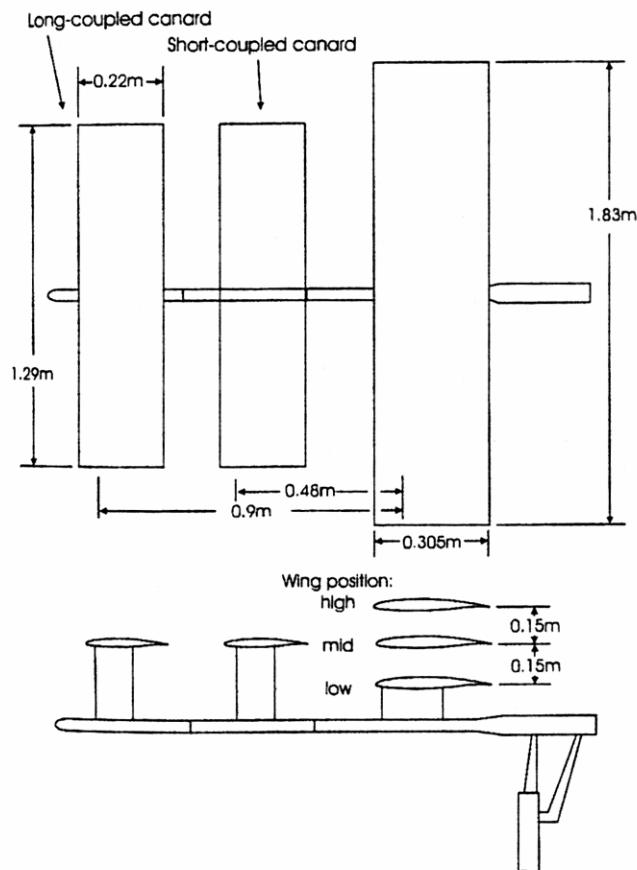


Fig. 42: Two-view sketch of wing-canard interference model (according to reference [125], sketch reproduced from reference [126]).

Both, long- and short-coupled configurations had been tested. Variations of the relative vertical position of wing and canard showed a pronounced maximum lift gain at the canard for the configuration where the canard was positioned close to and above the wing. A maximum lift coefficient loss occurred for canard positions vertically below the wing as can be seen in Tab. 10.

The computed lift decrement for the transition of the canard from the mid to the low position is significantly underpredicted by the present computational method if compared to the experimental data. Differently, the corresponding decrement for the transition from the high to the mid position is predicted more accurately. It can be

concluded that the computational model at least reproduces the trend of the maximum lift coefficient of the canard surface under the influence of the main wing correctly, despite the discrepancy for the low canard position.

Tab. 10: Influence of vertical position of a short-coupled canard-type horizontal stabiliser surface with respect to the main wing on its maximum lift coefficient (reference surface is that of the main wing).

Vertical Canard location	Experimental data	Computational data
high	0.700	0.705
Δ mid - high	-0.039	-0.044
mid	0.661	0.661
Δ low - mid	-0.041	-0.010
low	0.610	0.651

A detailed description of the computations with the extended vortex lattice model and comparisons with experimental lift polars are summarised in Appendix D.

3.1.6.6 Interaction of the Cascade Model with the Post-Stall Model

A principle weakness of the cascade model is that it does not consider the altered flow conditions due to partly separated flow predicted by the post-stall model. The adaptation of the maximum and minimum lift coefficients is computed with the VLM model, which, without further measures, implies attached flow. Taking the experimental results of Feistel et al. [125] as an example, the stall of the canard with the subsequent lift loss alters the flow conditions or more precisely the span- and chordwise pressure distribution at the main wing. Confining the discussion to the canard high case, the decreased downwash due to the stalled canard results in a less "curved" flow field so that the conditions on the main wing come closer to those of an isolated wing. This, for example, means more pronounced suction peaks and an increase of canonical pressure coefficients $\bar{c}_{p,te}$, which, in turn, results in decreased maximum lift coefficients.

The goal must be an adaptation of the maximum lift coefficient of the wing depending on the actual flow conditions. If the conditions depart from "linear" aerodynamics, not only the actual loads need to be checked but also the loadability. If, for example, the canonical pressure coefficient $\bar{c}_{p,te}$ is greater than it should be according to the linear solution and approaching the critical section value, the loadability is corrected. Corrections on surfaces where the collocation points have already been moved to alter the local lift-curve-slope afford a special treatment since the pressure distributions are fundamentally changed. For configurations with more than just one chordwise lattice

element, moving collocation points towards the quarter chord points equalises the chordwise loading. A possible suction peak would be reduced in magnitude and the loadability would be consequently increased. This does not make physical sense. To circumvent this problem, the critical canonical pressure coefficients for the two-dimensional sections are computed for various collocation point locations (compare block diagram, Fig. 43). This modification makes it possible to implicitly determine the distance from the maximum lift condition in terms of canonical pressure coefficients even if the collocation points are at offset positions.

The correction method has been tailored for the computation of c_L - α -polars. Examples of the effectiveness of the method are discussed in chapter 4.1.

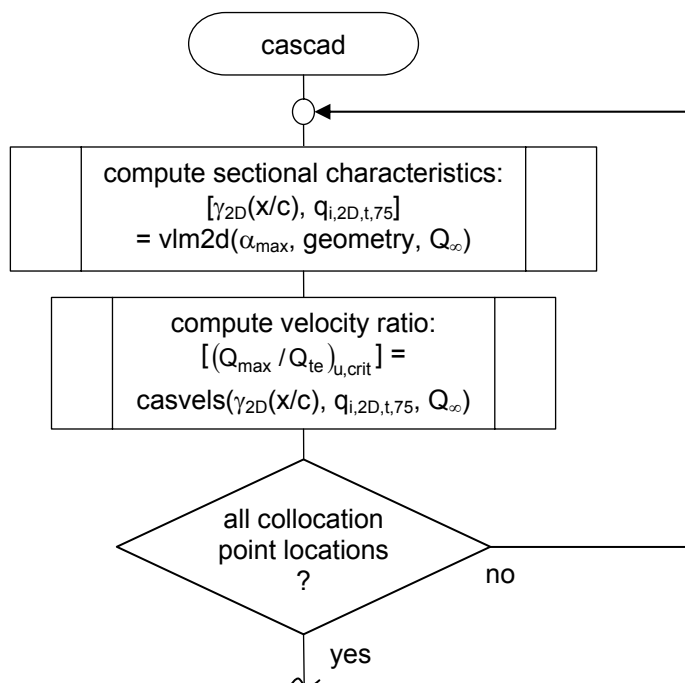


Fig. 43: Simplified structure of subroutines for computation of cascade effects modified for collocation point offsets (compare Fig. 38).

The following list summarizes the range of capability of the cascade model

- The model allows to compute the effect of cascade arrangements of multiple lifting surfaces on the maximum respectively minimum lift.
- The model also works when the collocation points have been moved to a different location than the basic three-quarter point. Either the sectional lift curve slope may have been changed or the post-stall model requires that the collocation point is moved fore or aft of the normal location at three-quarters of the elements chord.

There are also limitations to the model. Clearly, it is not possible to simulate and account for convection effects like the deterioration of flow quality if low-energy fluid due to flow separation impinges on a subsequent lifting surface.

3.1.7 Aggregation of Integral Forces and Moments

An essential element of the post-processing is the integration of forces and moments. The integration is performed following the geometrical topology:

① Elementary Surface \Rightarrow ② Wing Section \Rightarrow ③ Wing Part \Rightarrow ④ Wing \Rightarrow ⑤ Total Configuration

The numbers indicate the hierarchical rank of the elements. The structure is similar to that of the geometrical model. First, characteristics of the elemental surfaces ① are computed and stored in a way already described in chapter 3.1.1.2. Characteristics of chordwise rows of elemental surfaces are then aggregated to section characteristics ②. Profile drag is added at this step in the process. Spanwise integration of the sectional characteristics yields corresponding properties of the wing part ③. In the course of lift, side force, drag and moment cumulation of wing part values into wing values ④, viscous interference drag is added. Rolling, pitching and yawing moments cannot just be arbitrarily added such as force components because the lever arms must be explicitly regarded. Moments are integrated from the wing tips towards the wing reference point at the quarter chord location of the wing root. Total values ⑤ deviate from wing values if the configuration consists of more than one wing or if an additional drag component such as for a fuselage is added.

Once the total forces and moments are established, normalised figures can be computed. Coefficients of lift, side and drag forces are computed by dividing the dimensional forces by appropriate reference surfaces and the freestream dynamic pressure.

Sectional pitching moment coefficients are additionally divided by the local chord length. The pitching moments of the wings are referred to the geometrically defined mean aerodynamic chord of the wing. Unlike the absolute moment, the pitching moment coefficient is integrated with respect to the quarter chord location of the mean aerodynamic chord. The aggregation of sectional data to wing values is performed according to the standard procedure as, for example, outlined in reference [101].

Three alternative definitions of reference surface areas can be selected for wing parts ③, wings ④ and total configurations ⑤:

- Classical definition: This definition is based on the integration of the chord lengths along the spanwise body-y-coordinate for essentially horizontal surfaces and along the body-z-coordinate for essentially vertical surfaces (vertical tailplanes)

- Projection: Instead of using the chord lengths, this definition uses the projections of the surfaces on the body XOY plane for horizontal respectively the body XOZ plane for vertical surfaces
- Chord line surface: The local chord lengths are integrated along the curved spanwise coordinate defined by the line that connects the quarter chord locations from the root towards the tip.
- Mean line surface: Similar to chord line surface definition above but based on mean line lengths instead of chord lengths.

The choice of the wing reference surface definition does not have any effect on the net aerodynamic characteristics of the configuration. Nevertheless, because various definitions are used in the literature, the choice to switch from one to another definition may be convenient for mutual comparison of data.

It is possible to specify fixed reference areas for normalisation purposes that replace computed areas of individual wings or that of the complete configuration. Fixed reference areas have been used in published parametric studies where profile drag was not of concern. Utilisation of constant reference surface areas, again, may ease the comparison of results.

Similarly, the wing spans can be optionally specified at fixed values. This option is useful in the case of aeroelastic computations where the actual span of a wing along the body y-axis changes due to different degrees of bending.

3.2 Structures

3.2.1 Simplified Dimensioning of Wing Box

3.2.1.1 Introduction

Generic results regarding the optimum planform of wings have been obtained in the past by parallel assessment of aerodynamic and structural properties. Lifting line or Trefftz plane analyses have been used to model aerodynamics. Rough estimates of the relative impact of structural weight respectively mass on performance have been made using the spanwise integrated bending moments that solely result from aerodynamic loads (Prandtl [19], Jones and Lasinski [20]). The referenced authors were aware that this modelling would only provide a satisfactory correlation with wing structure mass if the height of the shear webs would be invariant in the spanwise direction. This is hardly realistic considering the resulting elliptic to triangular wing planforms being optimal with respect to induced drag or a combined figure of merit incorporating wing weight given that a lift coefficient constraint is obeyed. Nevertheless, since the inner part of the wing contributes most significantly to the wing mass of high aspect ratio wings and regarding

that the inner part does not change much, the results will at least give the correct trend. However, the method becomes unacceptable for the following cases. The first case is where the spar height cannot be kept constant across the span. The second case is where the integrated bending moment is not small enough as to ignore errors arising from violating the condition of equal spar heights. A wing equipped with multiple winglets is such a configuration. Unless the relative thickness at the tip of the main wing is extremely small, the spar height at the root sections of the winglets must be smaller than that of the main wing in order to allow realistic thickness to chord ratios that in turn prevent early flow separation at supercritical Reynolds numbers. The relative span of the winglets is about a fourth to a third of the semi-span of the wing, and hence the contribution of the winglets to the wing mass will be significant enough to justify a more detailed analysis.

3.2.1.2 Wing Mass Estimation Approach

The simplified dimensioning of a wing box allows a design-sensitive assessment of the wing mass. The approach is principally based on beam theory. It is a compromise between empirical methods that are primarily based on the weights of existing aircraft (e.g. Torenbeek [119]) and methods usually employed in detail design such as finite-element analysis. Empirical methods give reliable results if the new design evolves from the population of older ones on which the method is based. The advantages of empirical and semi-empirical methods are simplicity and accuracy. These benefits are pros but a con is the lack in universality. Finite-element analyses are somewhat closer to the underlying governing physics and offer advantages for generic problems. However, further complexity is added especially for mesh generation and computations are rather expensive.

The present approach follows the lead for a preliminary wing box sizing by Wiedemann [120]. The calculation sequence is as follows:

1. Generation of wing box geometry.
2. Computation of aerodynamic loads at the ultimate load condition and calculation of cut loads.
3. Computation of tension flows due to bending, local side forces and shear flows due to normal and tangential forces and torsion.
4. Sizing of wall thicknesses of shear webs and skin panels according to maximum allowable stress levels.
5. Computation of material volume and structural mass.

The list below contains a summary of simplifying assumptions:

- The structure is a statically determined equivalent system.
- All loads on the wing will be ultimately concentrated in the primary box structure consisting of upper and lower skin panels, a front and a rear spar web.
- The position of the shear centre is predefined at the centre of the wing box.
- Structural members that guarantee sufficient structural stiffness and stability such as stringers and ribs are neglected. All structural items other than the basic wing box are accounted for by a factor. The factor thus constitutes of aforementioned supplementary items of the primary structure plus any items belonging to the secondary structure that might be present.
- The load case used for the wing mass analysis is the quasi-static pull-up manoeuvre condition at the ultimate load factor n_{ult} .
- Sizing is performed on the basis of strength requirements. Stiffness requirements can have an influence on aircraft wing sizing but will be neglected here for the sake of simplicity and traceability of basic effects.
- The computation is performed for the left hand wing part only. The mass is doubled to obtain the total wing mass. Thus, only symmetrical configurations with respect to the body XOZ plane can be assessed.

The assumed structural principles are as follows:

- Bending about local x_b -axis (due to 'lift') is absorbed only by the skin panels. Contributions of the spars are neglected.
- Bending about local z_b -axis (due to 'drag') is absorbed only by the spars. Contributions of the skin panels are neglected.
- Tension due to side forces is absorbed by the skin panels.
- Shear force loads due to normal ('lift') and tangential forces ('drag') are transmitted by the spar webs.
- Shear force loads due to torsion are transmitted by spars and skin panels.

Especially the assumption that tension due to bending is transmitted by the skin panels only yields a rather conservative sizing.

3.2.1.3 Geometry

Fig. 44 illustrates the relation of the physical wing box contour to an equivalent simplified rectangular wing box.

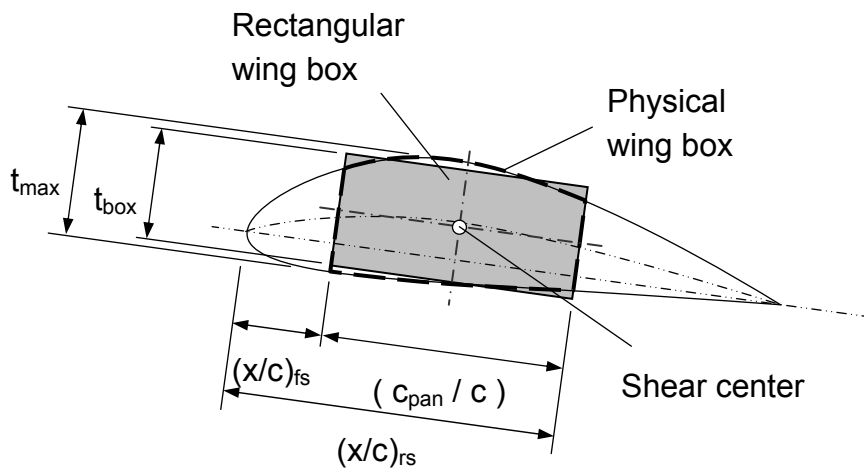


Fig. 44: Geometry of equivalent rectangular wing box.

The tangent to the mean line at $[(x/c)_{fs} + (x/c)_{rs}] / 2$ defines the chordwise orientation of the skin panels. The height of the wing box is a weighted average of the thickness ordinates of the profile section at the front spar, the shear centre location and the rear spar: $t_{box} = (t_{fs} + 2*t_{sc} + t_{rs}) / 4$.

3.2.1.4 Cut Loads

The forces and moments due to aerodynamic loads are integrated at the root section of each spanwise wing box element j (Fig. 45). The integration is performed in body coordinates. However, the calculation of shear and tension flows in the skin panels and spar webs is more conveniently performed in the local wing box coordinate systems wb_j and thus the loads are transformed accordingly.

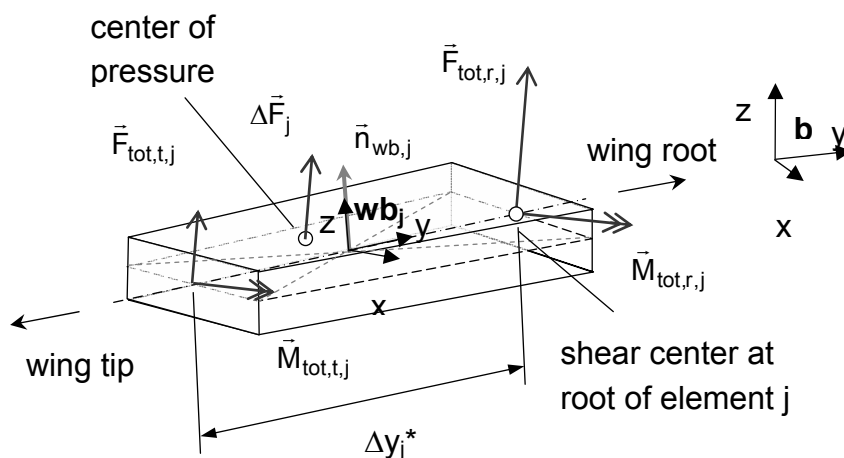


Fig. 45: Forces and Moments at wing box element.

The local z-axis coincides with the surface normal of the central wing box plane. The y-axis is aligned with the locus of the shear centres and the x-axis results from the condition that it must be perpendicular to the other two axes.

3.2.1.5 Tension and Shear Flows

The tension and shear flows can be computed from the given geometrical data and the cut loads (compare ref. [120], pp. 34-35). The tension flow of the upper and lower skin panels neglecting the contribution of the shear webs are

$$p_{up,M,x} = -M_{wb,x} / t c_{pan} \quad \text{and} \quad p_{lp,M,x} = M_{wb,x} / t c_{pan}$$

where the minus sign guarantees that a compression of the upper skin panel corresponds to a positive tension flow.

The tension flows due to bending in the spars are computed accordingly

$$p_{fs,M,z} = -M_{wb,z} / t c_{pan} \quad \text{and} \quad p_{rs,M,z} = M_{wb,z} / t c_{pan}$$

Tensions due to side forces are transmitted by the skin panels only

$$p_{up,F,y} = p_{lp,F,y} = F_{wb,y} / 2 c_{pan}$$

The shear flow in the skin panels is

$$q_{up,F,x} = q_{lp,F,x} = F_{wb,x} / 2 c_{pan}$$

and the more significant component in the spars equates to

$$q_{fs,F,z} = q_{rs,F,z} = F_{wb,z} / 2 t$$

Finally, the shear flow due to torsion needs to be computed

$$q_{up,M,y} = q_{fs,M,y} = -q_{lp,M,y} = -q_{rs,M,y} = M_{wb,y} / 2 t c_{pan}$$

In another step, the tension flows and shear loads are separately added up for each structural part. As an example, the tension flow in the upper skin panel is

$$p_{up} = p_{up,M,x} + p_{up,F,y}$$

whereas the shear flow has only one component such that $q_{up} = q_{up,M,y}$.

3.2.1.6 Sizing of Wall Thickness

The next step is to compute the equivalent stress levels due to tension and shear by means of a comparison stress hypothesis. It is then possible to determine the appropriate wall thicknesses if the maximum stress level of the material to be used is known. Most straight-forward for isotropic material is to use the maximum distortion

energy criterion of v. Mises-Henky (also referred to as von Mises Yield Criterion). Since the tension flows for the wall panels are assumed to underlie a uniaxial tensile stress condition, the von Mises equation simplifies to the following expression

$$\sigma_{eq} \cdot t = p_{eq} = \sqrt{p^2 + 3q^2} \leq \sigma_{max} \cdot t$$

The equivalent stress levels σ_{eq} must be lower than the maximum tensile stress σ_{max} of the material to guarantee that it withstands the ultimate load condition as well as usual working loads for the expected service life. For the sake of simplicity a fatigue analysis is out of scope, and the present analysis will concentrate on the ultimate load condition only, similarly to the approach of reference [121].

The optimum wall thicknesses for skin panels and spars are

$$t = p_{eq} / \sigma_{max} \cdot k_{saf}$$

where σ_{max} is the maximum tensile strength of the material and k_{saf} is the safety factor which is usually 1.5. According to [119] the maximum useful tensile strength of Al2024 is approximately $3.4 \cdot 10^8$ N/m² for large aircraft. For small general aviation aircraft wings made of aluminium alloy the value significantly reduces to about half that value (eq. AD4.1d, p. 343 of reference [93]).

3.2.1.7 Mass of Structure

The next measure is to compute the material volume. The volume can easily be multiplied by the material density to obtain the mass. Conventional aluminium alloys used for aircraft construction possess a density of about $2.8 \cdot 10^3$ kg/m³. To obtain values that are easier to compare with real wing mass data, the masses of the neglected items are accounted for by simple approximations

$$m_w = m_{w,prim,box} \cdot (1 + k_{prim}) + m_{w,scal} + m_{w,sec} \quad (65)$$

Values of the factor k_{prim} , which accounts for wing ribs, stiffeners and non-optimum effects reduce with increasing aircraft size. Calibration of the current model to that of Howe [93] for a small general aviation aircraft with 1000 kg maximum take-off mass yields a value of 1.042. Following the lead of Howe, additional contributions to the primary wing structure comprises additions for wing folds, cutouts in primary structure for landing gear and scale effects for light aircraft to mention but a few. Without going in too much detail, only the scale effect is considered which can be expressed by following relation

$$\left(\frac{m_{w, \text{scale}}}{m_{\text{to}}}\right) = 0.006 \cdot e^{-\left(\frac{m_{\text{to}}}{m_{\text{to,ref}}}\right)} \quad (66)$$

where $m_{\text{to,ref}} = 5,700 \text{ kg}$

Secondary structure items such as for control surfaces or flaps make up about 25% to 40% of the wing mass with only little influence of the wing and overall aircraft size (compare [93], [119]). Tab. 11 lists typical values for secondary structure items made of aluminium given as a ratio of take-off mass.

Tab. 11: Incremental mass ratios for estimation of secondary wing structure mass [93].

No.	Item	Mass ratio with respect to maximum take-off mass
1	Fixed leading and trailing edge with ailerons only	0.02
2.1	Plain or single slotted trailing edge flaps	0.003
2.2	Fowler or double slotted trailing edge flaps	0.006
2.3	Triple slotted trailing edge flaps	0.012
3	Leading edge flaps	0.007
4	Spoilers / air brakes	0.0015
5	Tips, fairings, etc.	0.002

Again, an additional penalty of up to 0.5% of the take-off mass is suggested for aircraft with a take-off mass that is less than 140.000 kg. A smooth blending is provided by

$$\left(\frac{m_{w, \text{sec, pen}}}{m_{\text{to}}}\right) = 0.005 \cdot e^{-0.25 \left(\frac{m_{\text{to}}}{m_{\text{to,ref}}}\right)} \quad (67)$$

and the relative mass of the secondary structure is finally

$$\left(\frac{m_{w, \text{sec}}}{m_{\text{to}}}\right) = \sum \left(\frac{m_{w, \text{sec}}}{m_{\text{to}}}\right)_i + \left(\frac{m_{w, \text{sec, pen}}}{m_{\text{to}}}\right) \quad (68)$$

Effects that are not considered are the load alleviation due to fuel stored in the wing box as well as due to wing-mounted engines. Also neglected is the self-alleviating effect due to the wings own structural mass. Because of the fact that the wing structure mass is to be computed, but the result is also needed as an input of the computation, the full sizing process is iterative by nature. The distributed forces due to the wing structure weight and further items as mentioned above subtract from the integral lift force that the wing is required to provide at its centre to carry items like the fuselage, fuselage mounted engines, the payload, the empennage, fuselage mounted parts of the undercarriage and

most of the aircraft systems weight. The inner wing bending moments due to the wing lift are also reduced. Neglect of these alleviating effects generally becomes more critical the greater the size of the aircraft category considered, which can be deduced from mass statistics. The wing group mass fraction with respect to the maximum takeoff mass of a general aviation aircraft having 1000 kg maximum takeoff-mass and a single fuselage mounted engine is on the order of 0.2 while it can be up to 0.6 for large subsonic long range aircraft equipped with wing mounted turbofan engines. The systematic error due to neglecting load alleviating effects is clearly prohibitive in the latter case but it appears acceptable in the former as far as one is on the lookout for fundamental trends in the stage of aircraft conceptual design.

3.2.2 Aeroelastic Deformation of Wing

Jupp discussed a special root bending moment relief mechanism due to winglets [122]. Fig. 46 shows a winglet which is vertically oriented in straight level flight ($n = 1.0$). The resulting aerodynamic load can be represented by a force vector which points inboard. Under $n = 2.5$ manoeuvre loads the wing may bend upwards so that the load vector of the winglet passes below the wing root, giving some bending moment relief at the inner wing compared to the design static loads. This may result in some structure mass reduction. However, increased bending moments at the outer wing remain almost unchanged.

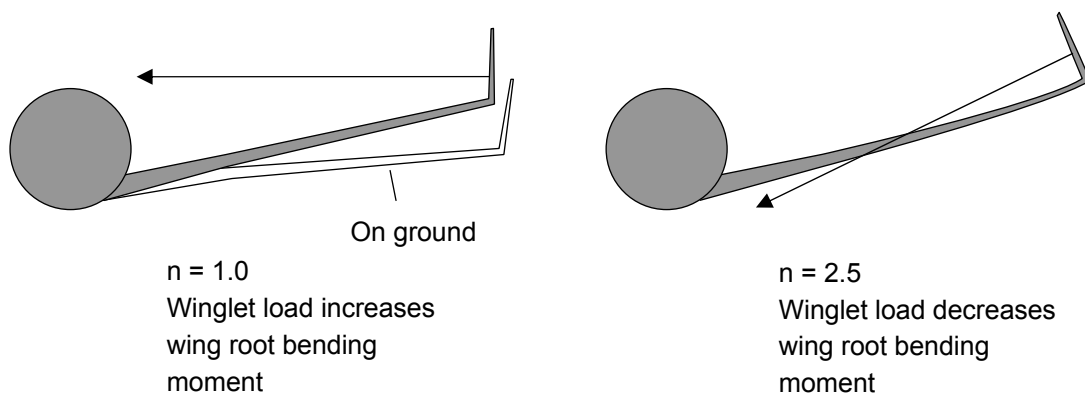
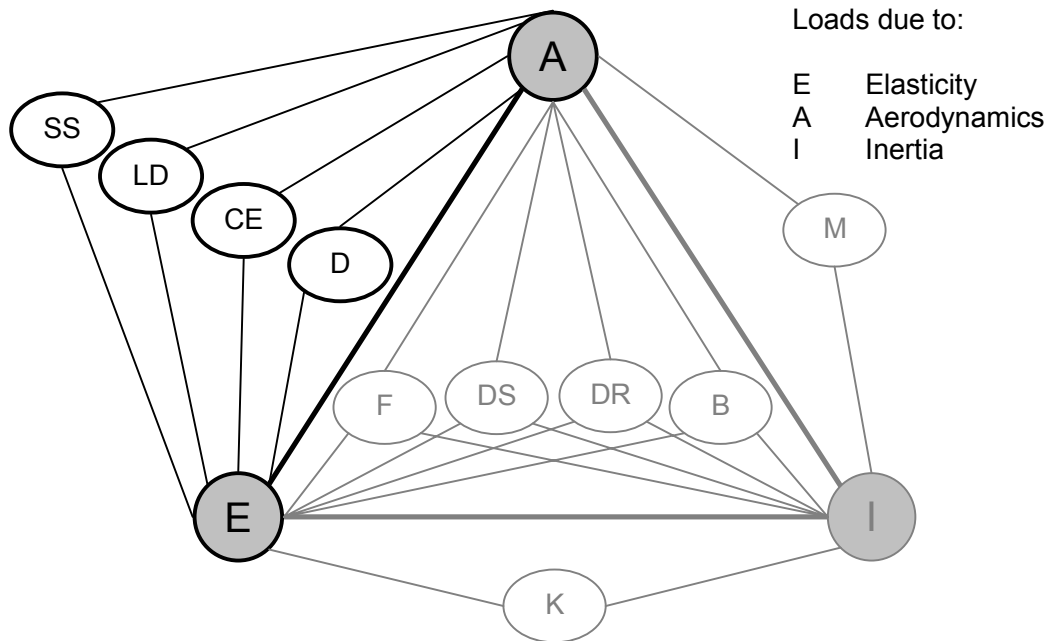


Fig. 46: Effect of wing bending on canted winglet load vector (adapted from figure in [122]).

It is this effect which is supposedly of first order with respect to the overall performance gain when adding a winglet and which prompts to distinguish quasi-static deformations of the wing under normal flight and ultimate design loads in the process of wing sizing.



Static aeroelastic problems: Dynamic aeroelastic problems: Related Disciplines:

D	Divergence	F	Flutter	M	Flight Mechanics
CE	Control effectiveness	DS	Dynamic flight stability	K	Kinematics
LD	Lift distribution	DR	Dynamic response		
SS	Static flight stability	B	Buffeting		

Fig. 47: Aeroelastic Load Triangle [123].

The scope of looking at aeroelasticity is limited to static effects, which have a greater potential of altering aircraft performance than dynamic effects. Only the quasi static structural elastic loads 'E' of Fig. 47 and the aerodynamic loads 'A' are concerned here excluding inertial loads 'I'. Inertia plays an important role in the analysis of dynamic effects. Dynamic behaviour of aircraft parts is equally important but affects the handling qualities of aircraft rather than performance.

The present numerical model basically allows tackling the problems that are highlighted in Fig. 47. Divergence is concerned with the critical flight speed above which a small disturbance causes the lifting system to suddenly deflect beyond critical boundaries with subsequent structural failure. Control effectiveness can be impaired if the loads due to a deflected aerodynamic control surface alter the wing setting against the free stream due to elastic structural deformation so that the effect of the control deflection is neutralised or even negative. The best known phenomenon of this type is aileron reversal, which can be a problem especially for large aircraft operating in the transonic Mach-number range. The static elastic deformation not only alters the wing shape compared to a rigid

wing but also its aerodynamic properties. This has to be particularly regarded in the preliminary design stage of large aircraft because of the generally decreasing wing stiffness with size. An incorrect estimation of the aeroelastic deformation in the pre-design stage bears the risk of the wing performance falling significantly short of design expectations. The aerodynamic centre of an elastically deformed wing may be at a different location compared to an equivalent rigid wing at the same load condition. Moreover, structural elasticity can change the lift curve slope of a wing. Both effects directly alter the neutral point location and thus directly affect static stability.

Static aeroelastic effects are involved in a considerable range of wing design problems. In order to prevent the scope of the present works getting out of hand, only the effects of modified lift distributions due to elastic deformation that affect structural sizing will be considered.

The static deflections of the structure due to bending and torsion can be computed by means of beam theory. The following equations for deflections and twist at the tip locations of spanwise elements j are solutions of the bending and torsion differential equations under the condition of small linear strains and purely elastic deformation.

Deflection in local z_{wb} -direction:
$$\Delta w_{wb,t} = \frac{M_{wb,t,x}}{E \cdot I_x} \cdot \Delta y^*$$

Deflection in local x_{wb} -direction:
$$\Delta u_{wb,t} = \frac{M_{wb,t,z}}{E \cdot I_z} \cdot \Delta y^*$$

Twist about local y_{wb} -axis:
$$\Delta \vartheta_{wb,t} = \frac{M_{wb,t,y}}{G \cdot I_{d,y}} \cdot \Delta y^*$$

A transformation yields the corresponding deflections of the quarter chord axis, once deflections and twist angles of the shear centre axis have been determined. This data is used to adapt the curvature parameter ΔY and the washout angle ε of the basic wing geometric model for each wing part k in order to allow the generation of a lattice consistent with the wing box deflection for further aerodynamic computations. The deflections in the x_{wb} -direction are neglected in this respect since the wing geometry model does not provide for this type of deformation. This should normally not be a problem because the deflections in this direction, which is principally aligned with the flow direction, are usually small.

3.2.3 Structure Model Performance

3.2.3.1 Example of Wing Box Sizing and Computation of its Static Aeroelastic Deformation

A method for estimating the wing mass based on fundamental structural principles has been programmed. Fig. 48 shows the resulting geometry of an arbitrary multi-winglet configuration with a span of $b = 18.7$ m and a required lift of $2.0 \cdot 10^4$ N. In their jig shapes, the left and right inner wing parts are already curved and have initial dihedral angles of 20° at root location. The upmost and leading winglets A feature a discontinuity in chord lengths at winglet semi-span locations. The configuration does not by any means represent a necessarily useful design. It is intended to give an impression of the geometric versatility offered by the computational model and its capabilities for structural analysis and sizing.

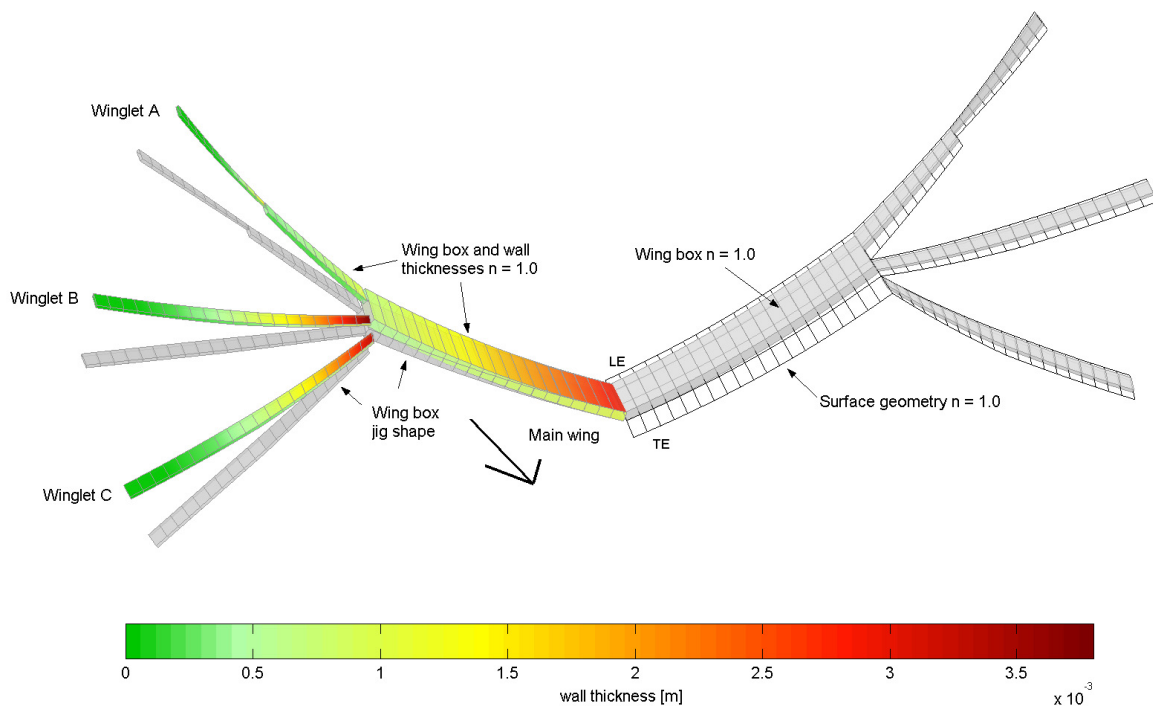


Fig. 48: Wall thicknesses of skin panels and spars of multi-winglet configuration sized to 2.5 g manoeuvre loads (left hand side of wing). Right hand side of wing shows geometric relation of paneled mean line surface and wing box.

The cut loads with respect to the individual local coordinate systems to which the wing box was sized are depicted in Fig. 49. Beside the main wing, only the data for the first

leading winglet characterised by the discontinuity in the chord distribution is shown for clarity.

No attempt has been made for an assessment of the flange masses, which inevitably increase the primary structure mass for connecting multi-winglets to the main wing box.

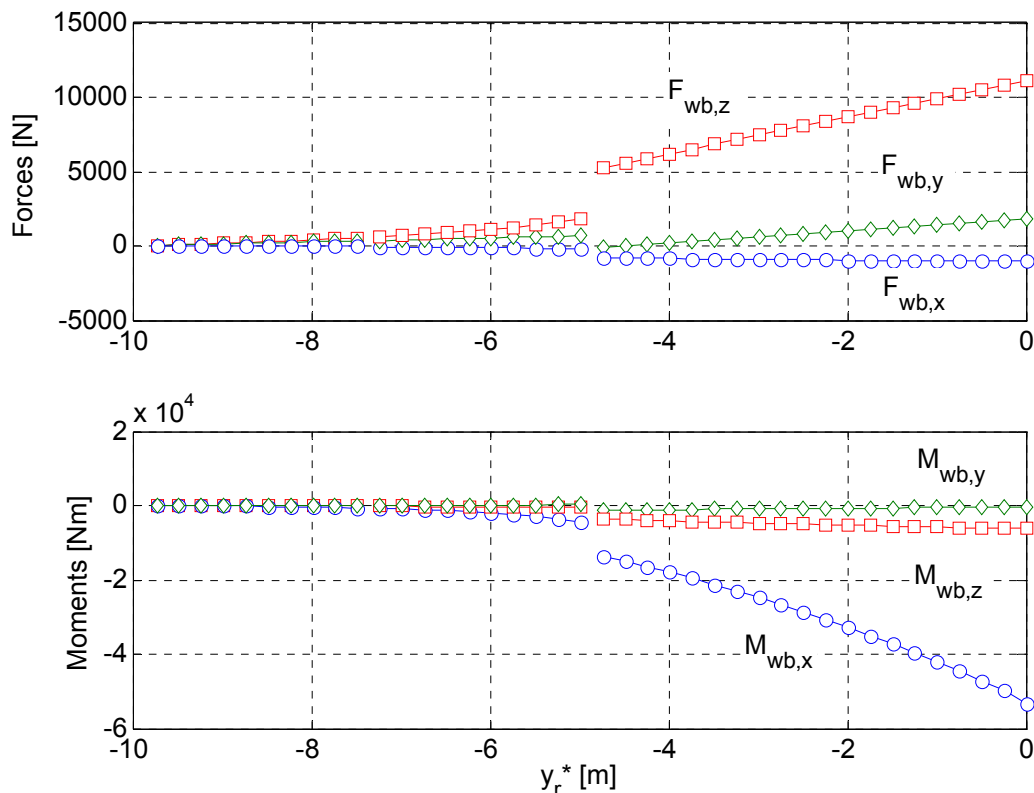


Fig. 49: Cut loads at root locations of wing box elements with reference to curvilinear wing box coordinate systems. Plotted data for main wing and leading winglet A only.

3.2.3.2 Comparison of Various Figures for Wing Mass Correlation

Finally, Fig. 50 presents a comparison of the root bending moment about the local wing box x-axis, the bending moment that is integrated across the span and the wing mass for various slitting ratios $\eta_0 = y_0 / s$ of an untwisted, untapered and non-optimised multi-winglet configuration with three winglets attached at dihedral angles of $+20^\circ / 0^\circ / -20^\circ$. Root bending moments (as used in references [64] and [65]) and spanwise integrated bending moments (as used in [19] and [20]) have been used as alternatives to detailed structural wing sizing procedures for the assessment of wing mass implications due to configurational changes.

Confining the discussion to multi-winglet configurations the figure clearly shows that the integrated bending moment is in fact a suitable substitute for wing structure mass as

long as the winglets are small. Both parameters which are non-dimensionalised by dividing through the respective rectangular wing values are almost congruent between $\eta_0 = 0.85$ and 1.0. The trends of these metrics start to deviate progressively for smaller values of η_0 and the error of the integrated bending moment in representing wing structure mass assumes a value of more than 50% for a slitting ratio of 0.6.

The wing root bending moment takes up the same trend as the integrated bending moment but at only about half the level. Using this metric as substitute for wing structure mass tends to underpredict the effect of geometrical changes even for slitting ratios close to unity. The figure shows that putting up with the effort of wing box sizing is not only justified but needed in order to arrive at realistic trends for the mass of wings equipped with multiple winglets.

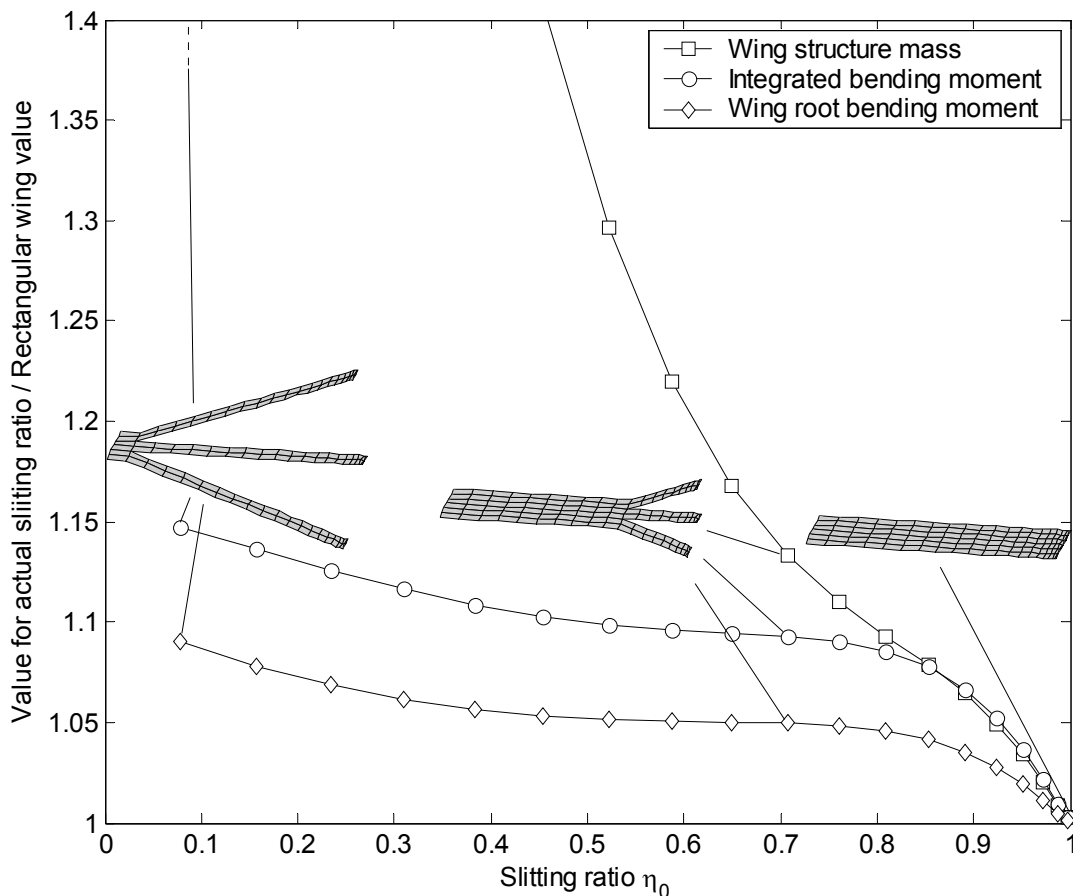


Fig. 50: Variation of wing structure mass, integrated and wing root bending moments with slitting ratio. Inset sketches show only right hand side of otherwise symmetrical wings. The value for the wing structure mass at $\eta_0 = 0.079$ is $m_w / m_{w,rect} = 2.81$.

3.3 VLM⁺⁺ - Suite for Multidisciplinary Analysis of Wing Configurations

3.3.1 Programme Modules

Fig. 51 summarises the capabilities of the MATLAB-based programme suite VLM⁺⁺. The sketch only shows the principal arrangement for the single point computation option (1) and names core modules explicitly. The sketch also shows that the programme has been built around the vortex lattice method as its nucleus. Top level option (4) is based on option (1) but comprises an additional module for wing structural sizing. The optimisation mode (3) makes use of modes (1) and (4). The parametric study mode (5) calls modes (1), (4) or mode (3) as its submodes. The polar mode (2) is similar to the parametric study mode (5) but the sole independent parameter is the angle of attack. Main difference to mode (5) is the production of data tailored for creating standard polar plots.

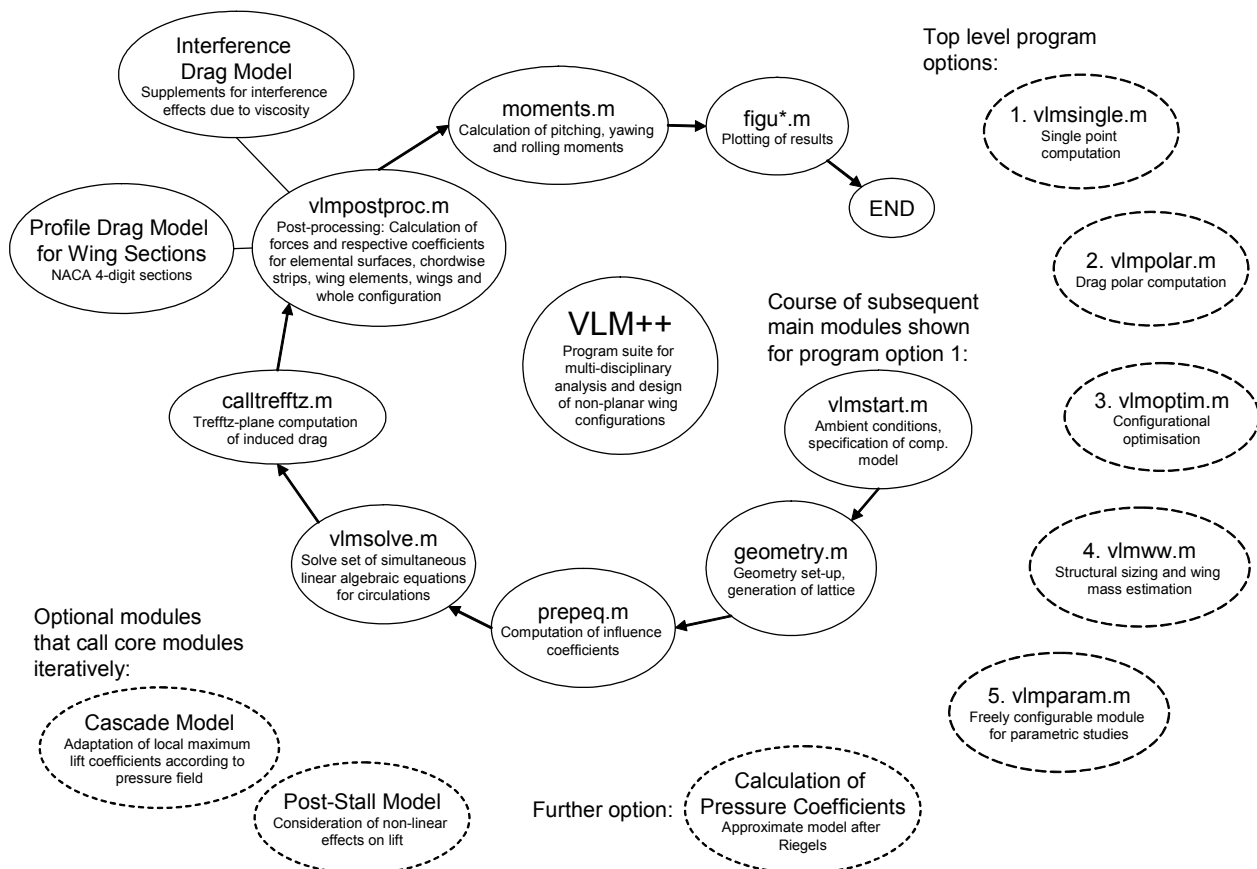


Fig. 51: Outline of MATLAB-based programme suite VLM⁺⁺.

3.3.2 Numerical Optimisation Mode

Optimisations are performed with the optimiser *fmincon* of the MATLAB-Optimisation Toolbox. The function optimises constrained nonlinear multivariable objective functions. The method is based on sequential quadratic programming, which is a gradient based method. Gradients of the objective function with respect to independent variables (partial derivatives) are computed numerically via finite differences because analytical gradient information is not available. This involves perturbing each of the design variables in turn and calculating the rate of change in the objective function. Second partial derivatives are provided in form of an approximate Hessian matrix derived from gradient information of successive iteration steps in the course of searching for the optimum of the objective function. The derivation of the Hessian matrix from gradient information is preferred because it is significantly less computationally expensive than explicit computation of the Hessian matrix.

An example for an objective function, which is relevant for the present work is the fuel efficiency of an aircraft measured as fuel required per payload and distance or alternatively time. Independent variables are geometric parameters of the wing to be optimised.

The gradients are used to estimate a new solution. The process is repeated at the new point in the parametric space until convergence is obtained.

Explicit equality or inequality constraints are specified as fixed-value boundaries for independent variables. Constraints on dependent parameters that are not directly involved in the optimisation problem because of a lack of repercussions on the objective function are considered in form of penalty functions. These penalties are placed as additional expressions to make the objective function less optimal if the constraint boundaries are approached.

If there are clues that the objective function may have more than one optimum, the optimiser *fmincon* may converge only to a local optimum. A straight-forward approach to increase likeliness of finding global optima is to start computations at different initial conditions. The probability of having found the global optimum increases with the number of optimisation runs from different starting points if the different runs all find the same solution. Parameter combinations should, however, be suitably chosen. Disadvantage of this procedure is that the computational efficiency quickly decreases. However, if the topology of the problem gives rise to the assumption that there is only one optimum, no special provisions are necessary. The latter condition applies to some of the problems encountered with multi-disciplinary wing optimisation at the conceptual design level.

3.3.3 Parametric Study Mode

In the parametric study mode, the user has to specify one or more independent variables and one or more dependent variables. Arrays containing values for the independent variables must be provided. The product of the lengths of the arrays determines the number of variations and also the number of calls of the core function. The results are saved in a data file. In the post processing step, the data can be plotted in various forms. A standard contour plot plots a dependent variable with respect to four independent variables. Two variables constitute ordinate and abscissa of a standard plot, variations of two further variables are accounted for by arranging diagrams in a matrix of size $n_3 \times n_4$, where the n's are the lengths of the independent parameter arrays. It is possible to swap the arrangement of independent parameters. For more than just one dependent parameters, plots are generated analogously.

4 Validation of Numerical Model

The purpose of this chapter is the validation of the numerical model. A particular focus is placed on checking the interplay of various modules of VLM++ and another one on comparison of computational results produced by VLM++ with published multi-winglet data. Tab. 12 is a summary of test cases and the modules of VLM++ used to reproduce the reference data.

Tab. 12: Test cases and modules used for validation of VLM++.

Chapter ⇒	4.1 Comparison with Multi-Winglet Low Speed Experimental Results	4.2 Comparison with Published Numerical Results	4.3 Planform Optimisation with Wing Mass Constraint and Comparison with Analytical Results
Multi-Winglet Example ?	✓	✓	-
Comparison with:	Experimental Data	Panel Method	Analytical Model
Module ↓			
VLM Core	✓	✓	✓
Profile Drag	✓	-	-
Interference Drag	✓	-	-
Non-Linear Effects	✓	-	-
Cascade Effects	✓	-	-
Structure Model	-	-	✓
Optimiser	-	-	✓

4.1 Comparison with Multi-Winglet Low Speed Experimental Results

Experimental investigations of multi-winglet systems have been performed by Hummel [50], [48] in the 1970s. Four configurations were tested in a closed circuit wind tunnel with a square cross section of 1.3x1.3 m. The basic configuration was a wing of rectangular planform with a span of 0.7 m and an aspect ratio of four. Both, wing and winglets had symmetrical NACA 0015 airfoil sections. The Reynolds number based on the chord of the main wing was about $0.43 \cdot 10^6$. The slitting ratio was 0.714 which corresponds to a span of 0.10 m for a single winglet. Each of the three winglets was pointed from $2 \cdot c_{\text{main}} / 7$ at the winglet root to $c_{\text{main}} / 7$ at the winglet tip. The average winglet Reynolds number was thus about $0.092 \cdot 10^6$.

4.1.1 Adaptation of Section Characteristics to Reynolds Numbers

It was necessary to adapt several parameters of the computational model that influence the lift and drag characteristics in order to meet the measured performance. In order to avoid pure curve fitting it was attempted to back up the parameters set by comparison with well established aerodynamic characteristics, particularly regarding sectional characteristics. The characteristics of the NACA 0015 airfoil section as given in reference [127] are shown in Fig. 52 for three selected Reynolds numbers. According to the stall type classification of Gault [129], given an upper surface ordinate of 2.37% chord at $x/c = 0.0125$, the thin-airfoil stall characteristic had to be expected for the lower two Reynolds numbers and trailing edge stall for the greater one. Contrary to the classification of Gault, it can be supposed that the sudden drop of lift for the large Reynolds number $Re_c = 3.18 \cdot 10^6$ is associated with the leading edge stall mechanism. A value of only 1.07 for the adapted model parameter ξ_{\max} in Fig. 52 representing the deviation of the maximum lift condition from the linear lift trend also gives evidence for a leading edge stall. The fact that the measurements of reference [129] had been made using a wing of rectangular planform but finite span with an aspect ratio of 6 renders it difficult to draw a convincing conclusion with regard to the lift curve shape in the $c_{l,\max}$ region.

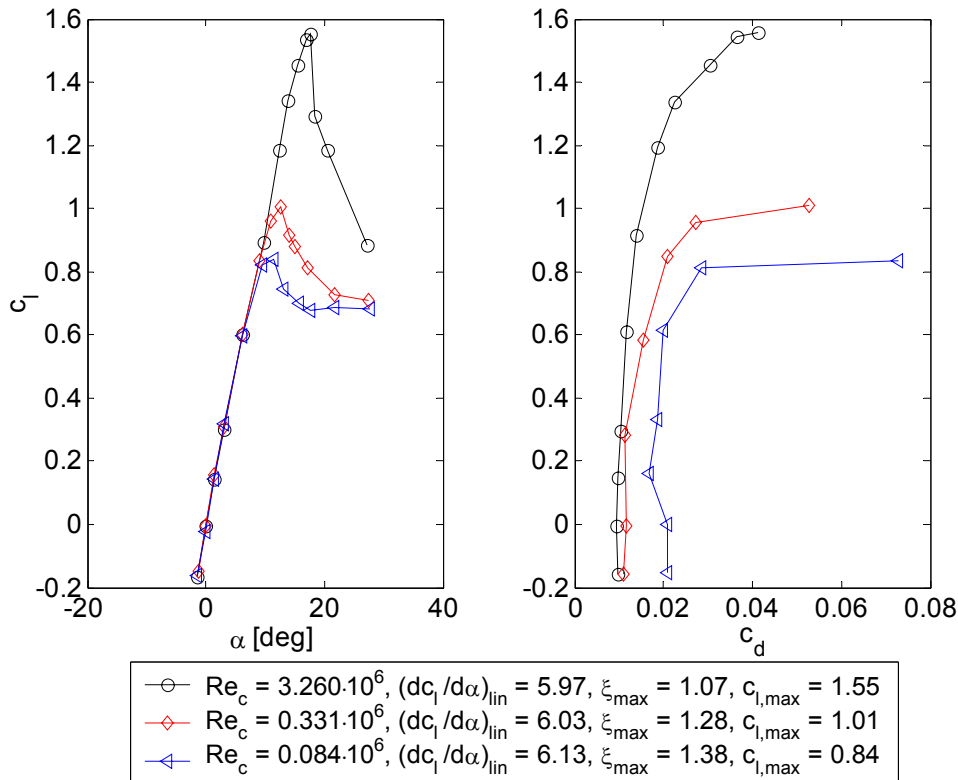


Fig. 52: Lift and drag characteristics of NACA 0015 airfoil section [127].

Considering the correction method as outlined in [127], the maximum lift coefficient values can be seen as reliable figures but more doubt should be placed regarding the shape of the c_l - α -curve. In case of a trailing edge stall, the inner wing sections stall first and the separated flow region then starts to spread both in the spanwise direction towards the tips as well as in the chordwise direction towards the leading edge. This behaviour leads to a less pronounced stall compared to real 2D data such as more closely approached with a wing spanning from wall to wall in a closed test section wind tunnel. The lift curve slope $(dc_l/d\alpha)_{lin}$ in the nearly linear region is close to the theoretical value of the flat plate $2 \cdot \pi$ for all Reynolds numbers.

It was possible to approximate the measured polars of Hummel's rectangular wing as well as the wing configuration equipped with three canted and twisted multi-winglets [50], [48] after setting the maximum section lift coefficients to the values of Tab. 13. The values agree approximately with those interpolated from the maximum lift coefficients of Fig. 52.

Tab. 13: Maximum airfoil section lift coefficients.

	Reynolds number Re_c	Maximum section lift coefficient $c_{l,max}$
Main Wing	$0.433 \cdot 10^6$	1.03
Winglets	$0.093 \cdot 10^6$	0.86

Apart from the lift, it was found that the drag characteristics at Hummel's test Reynolds numbers also not only deviate from high Reynolds number cases but also differ beyond amounts, which can be accounted for by simple Reynolds number corrections. First, the zero lift drag at $Re_c = 0.084 \cdot 10^6$ in Fig. 52 is significantly higher than the minimum drag, which can be attributed to the fact that the boundary layer is laminar and separates from the rear before transition to the turbulent state (subcritical boundary layer). The curve for $Re_c = 0.331 \cdot 10^6$ does not show such a bucket at low lift coefficients so that the Reynolds number probably has exceeded the critical one. It was only possible to meet the minimum drag of the rectangular wing of Hummel's measurements by setting the transition location as far back as $x_t/c = 0.5$. The lift dependent part of the profile drag is also different such that the respective coefficients had been adapted: $k_{const} = 0.05$ (quadratic parameter, high Re figure for comparison: 0.0152), $k_{minmax} = 0.01$ (quartic parameter, high Re figure: 0.0215).

4.1.2 Comparison of Lift and Drag Characteristics

The unconnected open symbols in Fig. 53 show the experimentally evaluated lift-drag-characteristics given in references [50] and [48] for the rectangular wing (1), the configuration with planar winglets (2), the configuration with planar winglets set at

different incidences against the main wing (3) and a winglet configuration (4) that has individual winglet dihedral and incidence angles. Configuration details are summarised in Tab. 14.

Tab. 14: Tested winglet dihedral and incidence settings according to reference [50] and [48].

Configuration	Winglet dihedral $\Upsilon_{A,B,C}$ [deg]	Winglet incidence $i_{A,B,C}$ [deg]	Reference area S [m ²]
(1)	-/-	-/-	0.1225
(2)	0 / 0 / 0	0 / 0 / 0	0.1100
(3)	0 / 0 / 0	-10 / -5 / 0	0.1100
(4)	20 / 0 / -20	-10 / -5 / 0	0.1100

In the scope of the vortex lattice method, the mean line surfaces are modelled only. This brings up the problem of how to attach the winglets to the main wing properly if they feature individual setting angles. It was decided to twist the innermost chordwise strips by an amount of washout ε identical to the respective original incidence angles i . The discretisation of each winglet is 8×4 (spanwise \times chordwise) elements without spanwise clustering but the outermost free vortex filament indented. A main wing half of configurations (2) - (4) consists of 6×14 elements with decreasing element widths according to a cos-distribution towards the location where the winglets are attached (geometrical details are shown in Fig. 55 and Fig. 61). A half of the rectangular wing (1) had only 7×7 elements and an indented outer free vortex without spanwise clustering. The winglet configurations thus consisted of 360 elements while the rectangular wing was made up of 98 elementary surfaces.

The drag coefficients are plotted against the lift coefficients on the left hand side of Fig. 53. Both coefficients are with respect to the actual planform areas as given in Tab. 14. The lift coefficient is plotted against the reciprocal of the endurance parameter on the right hand side of the figure.

Tab. 15: Measured aerodynamic performance of rectangular wing and of wing with canted and twisted multi-winglets ([50], [48]).

	$C_{L,max}$	$C_{D,min}$	$(C_L/C_D)_{max}$	at C_L	$(C_D/C_L^{3/2})_{opt}$	at C_L
(1) Rectangular wing	0.865	0.0094	16.98	0.324	0.0951	0.648
(4) Wing with canted and twisted winglets	0.896	0.0146	16.93	0.337	0.0840	0.677
Change %	+ 3.58	+ 55.3	- 0.30	+ 4.01	- 11.7	+ 4.48

While the maximum lift to drag ratio of the rectangular wing is 0.3% higher than that of the winglet configuration according to Tab. 15, the minimum sinking velocity of the winglet configuration would be 11.7% less (if both configurations had identical wing loadings).

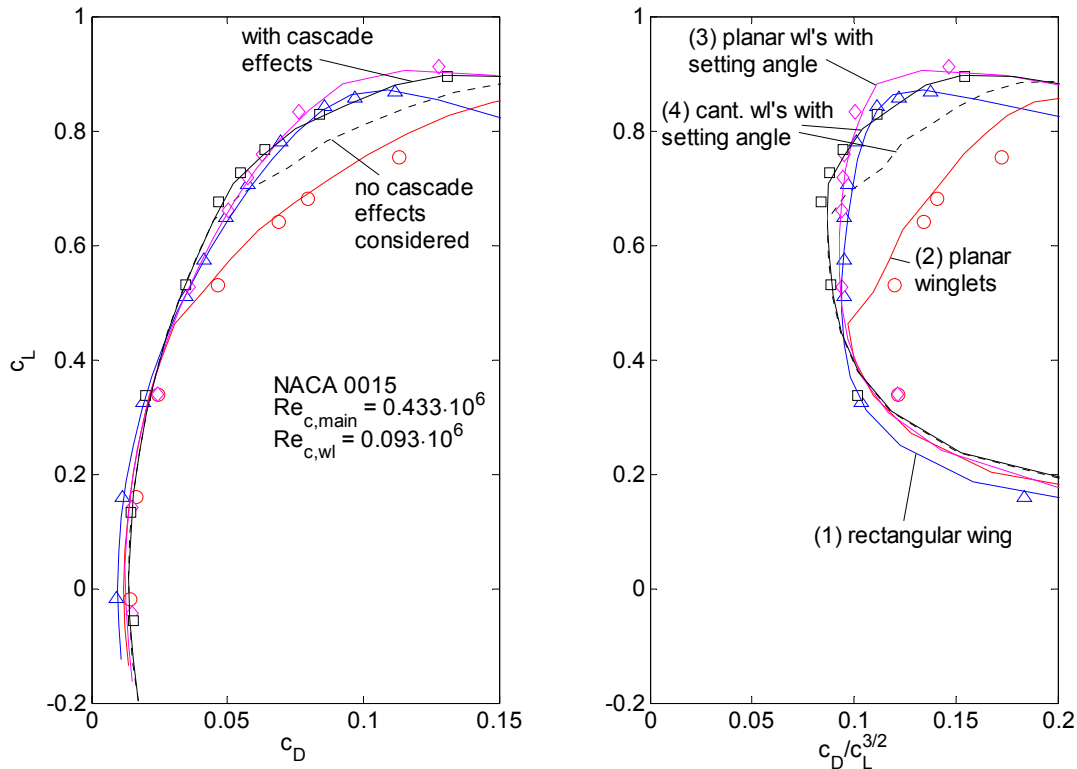


Fig. 53: Comparison of experimental (symbols) and computational (lines) lift to drag characteristics. Numbers in parentheses distinguish configurations according to reference [50] respectively [48]. Indicated Reynolds numbers are with respect to geometric mean chords of the respective wing parts.

Computations have been performed with the post-stall model switched on. The fit of the computational results to the measured data for the rectangular wing (Fig. 53, configuration 1) is excellent.

The configuration with planar winglets (2) has a higher minimum drag coefficient of 0.0121 compared to $c_{D,min} = 0.0097$ for the rectangular wing (1). Considering that the reference surface areas of the winglet configurations are 10.2% lower, the absolute minimum drag of the planar winglet configuration is still higher than that of the rectangular wing. The computed minimum drag coefficient is the sum of profile drag ($c_{D,p} = 0.0110$, 90,9%) and interference drag ($c_{D,int} = 0.00011$, 9.1%). The root section of the leading winglet 'A' reaches its maximum lift coefficient already at an angle of attack of 7 deg. The local maximum lift coefficient is 0.8474, a value that is approximately

identical to the basic section value of 0.86 (Tab. 13). Incipient separation and the subsequent drag rise can clearly be seen on the right hand side axes of Fig. 53 respectively Fig. 54. Less downwash by the stalled sections yields higher loads on the downstream winglet 'B', which starts to stall at its root section at $\alpha = 10$ deg. The stalled region spreads outwards with increasing angle of attack. At $\alpha = 15$ deg all winglets are almost completely stalled as indicated on the left hand side of Fig. 55 (a). Maximum lift is not reached until the greater part of the main wing is stalled at $\alpha = 17$ deg (refer to c_L - α -polar on the left hand side of Fig. 54).

Reduction of the winglet incidences reduces the loading on the center and front winglets of configuration (3), which effectively delays boundary layer separation. Despite the higher profile drag coefficients and additional interference drag, the lift to drag ratio of this configuration is slightly higher than that of the rectangular wing for lift coefficients greater than 0.4. One reason for this is the effectively tapered planform of the winglet configuration. This yields a more homogeneous spanwise lift coefficient distribution and a reduction in lift dependent profile drag compared to a configuration with a rather uneven lift coefficient distribution but with the same total lift coefficient. Another reason is the reduced induced drag because the slotted tips form an effective non-planar configuration if set at angle of attack. A consequence of this non-planarity is that lift curve slopes of all slotted configurations are higher than that of the rectangular wing (left hand side of Fig. 54). The computed drag coefficients of configuration (3) are smallest of all configurations for lift coefficients greater than 0.78.

The agreement of the computational results with the measured data for the canted winglets with individual incidence angles (configuration 4, without cascade effects) is satisfactory up to $c_L = 0.72$ above which the computational drag starts to increase more than the experimental data suggest because of flow separations at the root section of the upstream winglet 'A'. Moreover, compared to the measured value of 0.896 the lift coefficient reaches a value of 0.860 (-4.0%) only.

With the cascade correction model for the maximum lift coefficient switched on, the agreement of the computational result with the measured data is good. The lift to drag curve in Fig. 53 shows a better agreement with the experimental data than the one without cascade effects. The higher overall maximum lift is obtained due to an increase of section maximum lift coefficients at the winglets which yield less flow separation as can be seen by comparison of Fig. 55 (b) and (c). It is due to the rather rectangular shape (Fig. 55 (c), left) of the spanwise load distribution that the overall maximum lift coefficient of 0.896 comes closer to the sectional maximum lift coefficient of the main wing compared to the rectangular wing. Again, as derived from the experimental data, the plot of the lift to drag ratios in Fig. 54 shows that even the best winglet configuration is inferior to the rectangular wing (configuration (1)). However, the minimum sinking velocity of configuration (4) in free flight would be less than that of the rectangular wing.

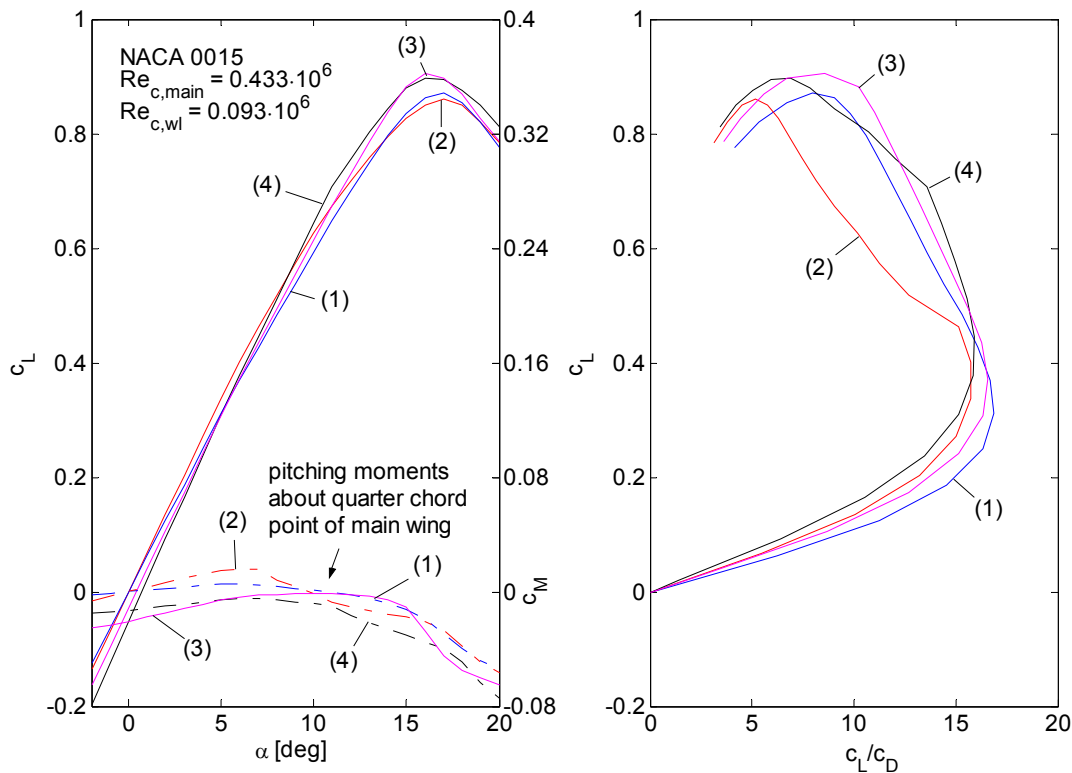
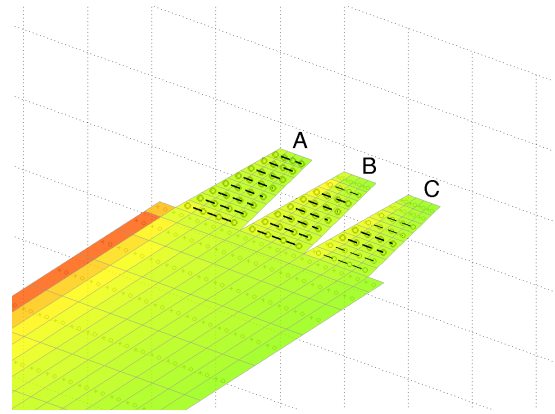
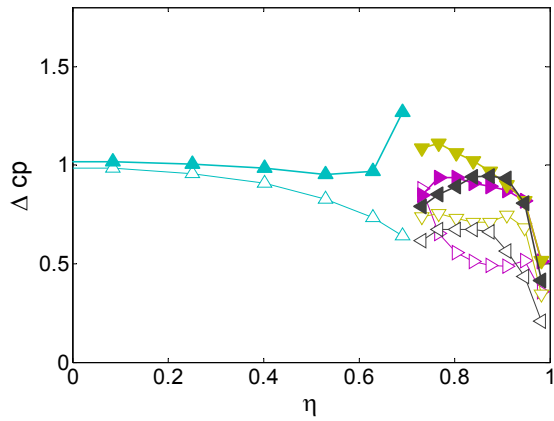


Fig. 54: Computed polars: c_L - α -polar and c_M - α -polar (left). Lift to drag ratio vs c_L (right).

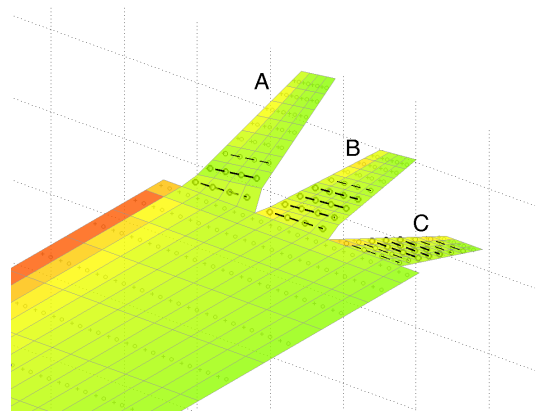
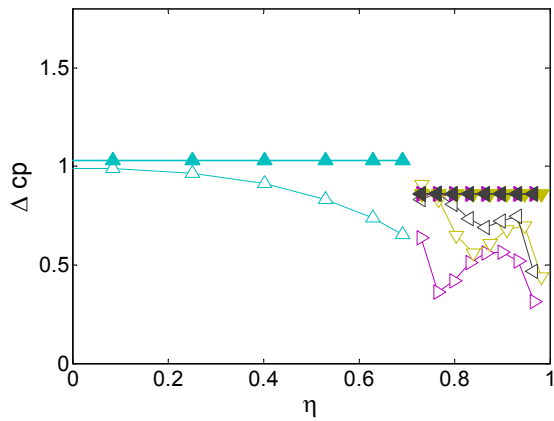
The gradient of the pitching moment coefficient of the planar winglet configuration (2) with angle of attack is slightly positive and greater than that of the rectangular wing (1) for low lift coefficients (right hand side of Fig. 54). As soon as the upstream winglet 'A' starts to separate, the lift loss ahead of the quarter chord point causes the trend to swap. Reduction of the incidences of winglets 'A' and 'B' increases the loads of the rear winglet 'C'. This produces nose down pitching moments, particularly at low angles of attack before the chordwise load distribution changes due to incipient boundary layer separation. The moment coefficients for the canted and twisted winglet case (4) are approximately $\Delta c_M = 0.01$ lower than those of the rectangular wing.

Fig. 55 summarises the spanwise load coefficients Δc_p along with the load limits. Parts of the winglets are already stalled at $\alpha = 15$ deg which are indicated by dashed lines in the perspective views on the right hand side. The higher loadability of configuration (4) with the cascade model switched on can clearly be seen by comparison of (b) and (c).

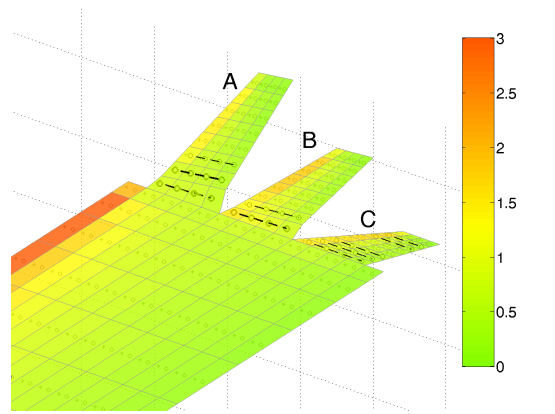
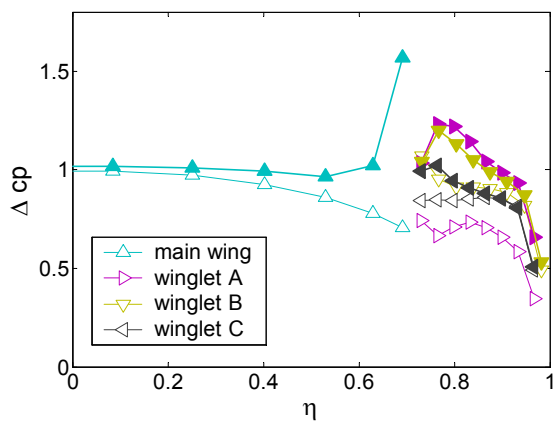
It must be noted that the satisfactory agreement of the computation with the experimental data has only been obtained after a tuning process of geometrical and other model parameters. However, it has been shown that it was possible to adapt the VLM++ numerical model to experimental data for a series of aerodynamically complex configurations in a Reynolds number range that is also rather demanding to model theoretically.



(a) Configuration (2), with cascade effects



(b) Configuration (4), without cascade effects



(c) Configuration (4), with cascade effects

Fig. 55: Local wing loading Δc_p at $\alpha = 15$ deg. Left hand side: Limits are represented by solid symbols, open symbols indicate actual loading. Right hand side: Element loadings are indicated by color shading, dashed lines show separated wing sections and line thickness indicates how much aerodynamic loading is lost compared to the linear result.

4.2 Comparison with Published Numerical Results

Hummel [50] presents results of a parametric study on multi-winglet configurations performed utilising a numerical panel method. Fig. 56 shows a comparison of Hummel's results for induced drag with those obtained with the present numerical model.

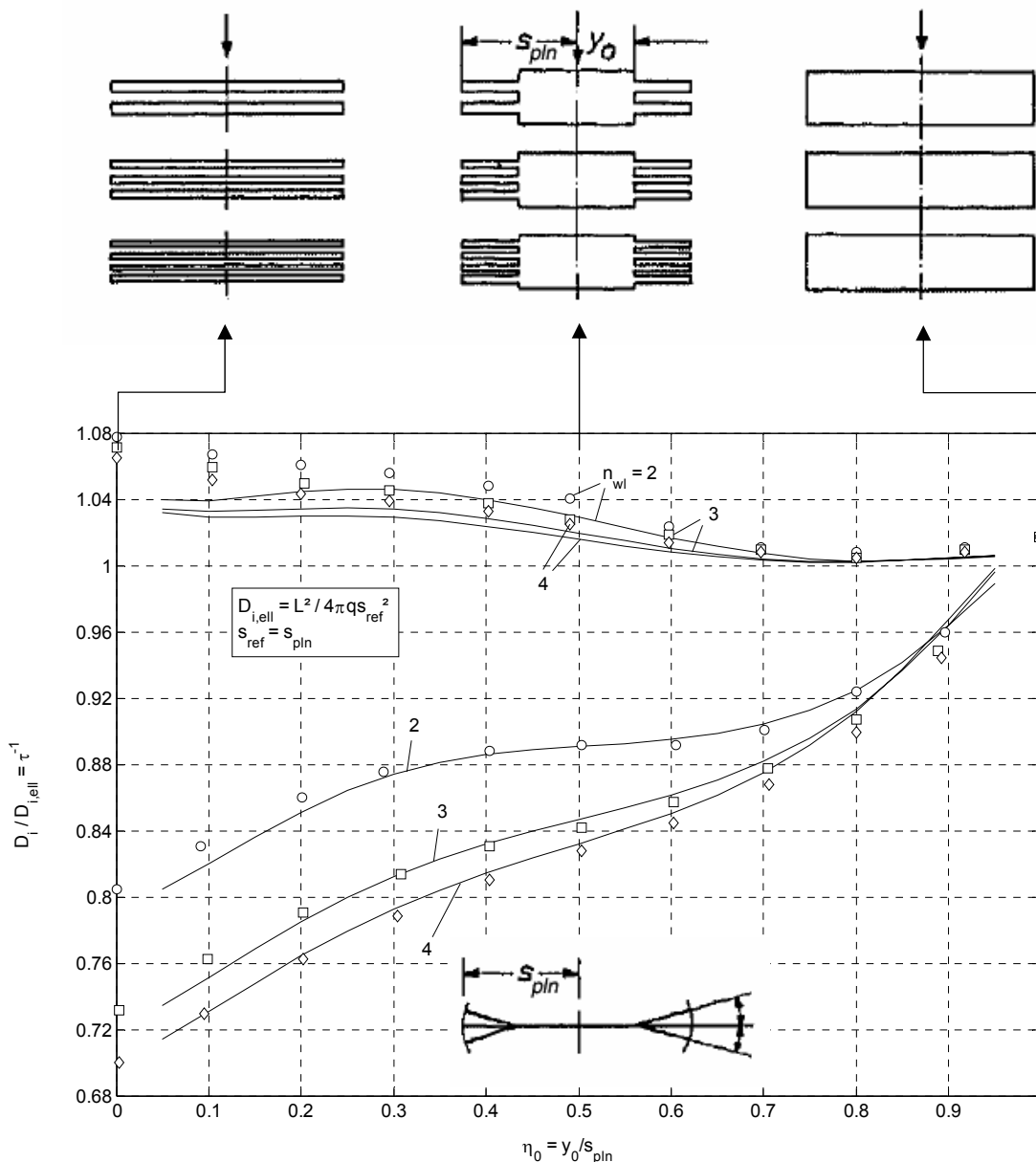


Fig. 56: Comparison of theoretical induced drag characteristics of planar and non-planar wings with slotted wing-tips: Bullets and sketches from ref. [50], solid lines calculated with present model. Upper data bullets and lines for zero dihedral $\Upsilon_{wl,i} = 0^\circ$, lower data bullets and lines for $\Upsilon_{wl,i} = \Upsilon_l - (\Upsilon_l - \Upsilon_t) \cdot (i - 1) / (n_{wl} - 1)$, $i = 2 \dots n_{wl}$. Leading winglet dihedral $\Upsilon_l = +20^\circ$, trailing winglet dihedral $\Upsilon_t = -20^\circ$.

The basic rectangular wing without slots (i.e. $\eta_0 = 1.0$) has an aspect ratio of four. The slitting ratio, the spanwise coordinate of the body-fixed coordinate system with respect to the planar semi-span $\eta_0 = y_0/s_{pln}$ determines the relative lateral dimensions of main wing and winglets. Indenting of the last free vortex has been used for induced drag accuracy improvement. The lattice consists of $n_j = 20$ chordwise strips per wing half. Chordwise discretisation has been adapted according to the sketches shown in Fig. 56 such that $n_i = 5$ for $n_{wl} = 2$, $n_i = 7$ for $n_{wl} = 3$ and $n_i = 9$ for $n_{wl} = 4$, leaving gaps of one element between subsequent winglets.

As to be expected, the induced drag ratio of the rectangular wing, which is obtained by dividing the induced drag through the optimum value of an elliptically loaded wing having the same span is slightly larger than 1.0. Dividing the outer part of the planar wing into two to four individual surfaces produces tandem-like configurations. Induced drag increases slightly while the penalties computed with the panel method are larger than those obtained with the present vortex lattice programme. Adding dihedral to the winglets in the range between $+20^\circ$ and -20° results in moderate induced drag reductions. The results presented are equally valid for all lift coefficients in the scope of potential theory since the configurations do not have washout. It should be noticed that the geometries are not optimised for minimum induced drag.

The gains obtained by adding additional winglets reduce quickly. This result is in accordance with 2D Trefftz-plane analyses (compare [14], [13], [18]) and Prandtl's stream tube analogy [9], since vertical spread of upper and lower surfaces is governing the potential for induced drag reduction. Both surfaces must be comparatively highly loaded for minimum induced drag. Adding winglets that are located between the two bracketing high and low surfaces does not improve span efficiency significantly.

Returning to Fig. 56, it can be concluded that the agreement of the present computations with Hummel's data is satisfactory.

4.3 Planform Optimisation with Wing Mass Constraint and Comparison with Analytical Results

4.3.1 Wing Planform of Minimum Induced Drag with Wing Mass Constraint

The following section will start with a recalculation of a classical optimisation problem aimed at finding the best planform for a planar wing in terms of induced drag with a constraint placed upon the wing structural mass is. A solution to this problem was published by Prandtl in 1933 [19]. The primary purpose of the present effort is to validate the interdisciplinary interplay of the structural sizing module with the vortex lattice core module of VLM++.

For a wing with prescribed total lift and span, the lift should be distributed elliptically in the spanwise direction in order to obtain minimum induced drag. The induced drag can be generally lowered by increasing the span. It approaches zero in the limit of the span becoming infinite. Since wing span is not explicitly limited in most practical design cases - gliders belonging to the Standard or FAI competition classes are a prominent exception - the question arises what the best span and planform shape for a given lift requirement would be. However, arbitrary wing span extensions of cantilever wings are practically limited because of the quickly increasing wing structural weight.

Prandtl's approach is based on the idea to prescribe the integrated bending moment of a cantilever wing. The integrated bending moment figure is obtained by integration of the local bending moments due to lift from the wing tip to the root. Stresses due to bending mainly determine the structural sizing of a high aspect ratio cantilever wing, and thus, the integrated bending moment is a suitable, though not exactly sufficient correlation parameter for the wing weight. Prandtl devised a variational problem to solve for the optimum lift distribution and span of a planar wing with prescribed integrated bending moment analytically. The aerodynamical aspects were treated with the lifting line approach, which holds for planar and unswept wing concepts.

A parabolical downwash distribution turned out to be the necessary condition for a wing with least induced drag at its design point with prescribed integrated bending moment. The corresponding circulation distribution is

$$\Gamma = (\Gamma_0 + \Gamma_2 \eta^2) \sqrt{1 - \eta^2} \quad (69)$$

where Γ_0 - circulation at root where $\eta = 0$

Γ_2 - additional circulation.

Prandtl defined a shape parameter

$$\mu = -\Gamma_2 / \Gamma_0 \quad (70)$$

that is used to compute the downwash at the lifting line

$$w_{25} = \frac{\Gamma_0}{2b} \left(1 + \frac{\mu}{2} - 3\mu \eta^2 \right) \quad (71)$$

The equation for the induced drag is

$$D_i = \frac{\pi \rho \Gamma_0}{8} \left(1 - \frac{\mu}{2} + \frac{\mu^2}{4} \right) \quad (72a)$$

or

$$D_i = \frac{L^2}{8\pi\rho Q_\infty^2 r^2} \frac{\left(1 - \frac{\mu}{2}\right)\left(1 - \frac{\mu}{2} + \frac{\mu^2}{4}\right)}{\left(1 - \frac{\mu}{4}\right)^3} \quad (72b)$$

where r is the "radius of inertia" representing the bending moment constraint

or

$$D_i = \frac{2L^2}{\pi\rho Q_\infty^2 b^2} \frac{\left(1 - \frac{\mu}{2} + \frac{\mu^2}{4}\right)}{\left(1 - \frac{\mu}{4}\right)^2} \quad (72c)$$

For $\mu = 0$, the conditions for an elliptically loaded wing are attained. The induced drag decreases for increasing values of the shape parameter μ with a value of 1.0 as an upper limit. Beyond that value the circulation and the lift at the wing tip become negative, and thus the integral of the bending moment for the outer wing part also becomes negative. Nonetheless, even negative loads will require a wing box to support the loads and thus the simplified analysis would lose its validity. The span compared to that of an elliptical wing that has the same integrated bending moment is

$$\frac{b}{b_{\text{ell}}} = \sqrt{\frac{\left(1 - \frac{\mu}{4}\right)}{\left(1 - \frac{\mu}{2}\right)}} \quad (73)$$

such that a value of $\sqrt{3/2}$ is attained for the practical maximum value of the shape parameter ($\mu = 1.0$). Similarly the induced drag ratio from eq. (72b) is

$$\frac{D_i}{D_{i,\text{ell}}} = \frac{\left(1 - \frac{\mu}{2}\right)\left(1 - \frac{\mu}{2} + \frac{\mu^2}{4}\right)}{\left(1 - \frac{\mu}{4}\right)^3} \quad (74)$$

and the value for $\mu = 1.0$ is 8/9. Hence, the induced drag can theoretically be reduced by 11.1% if the span is increased by 22.5% without changing the integrated bending moments. The span efficiency factor is given by the bracketed expression of eq. (72c) and attains a value of $\tau = 3/4$.

If it is prescribed that each section of the wing shall operate at the same lift coefficient [20], the chord distribution becomes equal to the load distribution according to equation (69). However, for wings with $\mu > 0$ the spanwise varying downwash according to equation (71) implies that the wing must be geometrically or aerodynamically twisted.

4.3.2 Numerically Optimised Wing Planforms

Now, the capabilities of the present programme in connection with the MATLAB optimisation routine *fmincon* will be looked at. The analytical results discussed above serve as a benchmark for the present numerical tool.

Three numerical optimisation runs will be performed starting with a simple rectangular wing of 10.92 m span. In a first run, the optimiser is assigned to optimise the planform for maximum span efficiency which is equal to the task of minimising induced drag for a given span. In a second run the task is identical to that discussed at the outset of this chapter in that the induced drag is to be minimised for a given integrated bending moment. The third run is comparable to the second but this time the constraint is placed on the wing structure mass. The end point of the first run serves as the starting point for runs 2 and 3. Tab. 16 gives an overview of the settings.

Tab. 16: Schedule of planar wing optimisation runs and constraints.

Run	Start Configuration	End Configuration	Figure of Merit → max	Optimisation Variables	Constraints Penalty Function Settings (refer to Tab. 17)
1	Rectangular wing	Wing of minimum induced drag for fixed span	Span efficiency factor τ	- chord length [m]: $c_i, i = 1, \dots, 5$ (index from root to tip)	1. $0.0 < c < 5.0$ 2. $c_{i+1} < c_i$ 3. $L = 12.500 \text{ N}$ 4. $c_i = 0.5$ 1.2 5. $c_L = 0.5$ 1.1 6. $s = 10.92 \text{ m}$
2	End configuration of run 1	Wing of minimum induced drag with fixed integrated bending moment	Lift to induced drag ratio L/D_i	- chord [m]: $c_i, i = 1, \dots, 5$ - washout [deg]: $\varepsilon_j, j = 1, \dots, 4$ - semi-span [m]: s	1. $0.0 < c \leq 5.0$ 2. $c_{i+1} < c_i$ 3. $L = 12.500 \text{ N}$ 4. $c_i = 0.5$ 1.2 5. $c_L = 0.5$ 1.1 6. $0.5 \cdot s_{\text{start}} \leq s \leq 2 \cdot s_{\text{start}}$ 7. $-10.0 \leq \varepsilon_j \leq 0.0$ 8. $\int M_b dy = \int M_{b,ell} dy$ 1.1
3	End configuration of run 1	Wing of minimum induced drag with fixed wing structure mass	Lift to induced drag ratio L/D_i	- chord [m]: $c_i, i = 1, \dots, 5$ - washout [deg]: $\varepsilon_j, j = 1, \dots, 4$ - semi-span [m]: s	1. $0.0 < c \leq 5.0$ 2. $c_{i+1} < c_i$ 3. $L = 12.500 \text{ N}$ 4. $c_i = 0.5$ 1.2 5. $c_L = 0.5$ 1.1 6. $0.5 \cdot s_{\text{start}} \leq s \leq 2 \cdot s_{\text{start}}$ 7. $-10.0 \leq \varepsilon_j \leq 0.0$ 8. $m_w = m_{w,ell}$ 1.1

Apart from these premises, it is worth noting that induced drag is the only drag component considered. Stipulating total lift and wing overall lift coefficient and assuming constant dynamic pressure means that the reference surface is invariable throughout the computations.

The constraints of Tab. 16 deserve some comments. In the first run, the optimisation routine is responsible for the compliance with the inequality constraints 1 and 2 only. A subroutine of the user defined optimisation function ensures that the lift constraint is obeyed by iterative adaptation of the angle of attack. The semi span (constraint 6) is just a constant. It is not possible to specify a goal value to a variable with *fmincon*. Instead one has to resort to work with penalty functions that are used for constraints 4 and 5. The formulation of the figure of merit under the influence of penalty functions is

$$pobjf = objf \cdot \left(1 - \sum_i pf_i\right) \quad (75)$$

where

objf	- objective function value
pf _i	- i'th penalty function
pobjf	- corrected objective function.

Penalty functions are normalised such that they produce a percentage penalty for the objective function.

$$pf = k_{pf} \cdot \left(\frac{cf}{cf_{req}} - 1\right)^{n_{pf}} \quad (76)$$

where

cf	- function that computes value of implicit constraint
cf _{req}	- required value to be observed in the course of optimisation
k _{pf}	- constant
n _{pf}	- exponent

Two standardised sets of values for the parameters k_{pf} and n_{pf} as listed in Tab. 17 have been used.

Tab. 17: Penalty function settings.

No.	Objective function penalty of 1% for 1% deviation of the constrained function from the limit value		Objective function penalty of 10% for 10% deviation of the constrained function from the limit value	
	1.1	1.2	2.1	2.2
n _{pf}	2	4	2	4
k _{pf}	1.0·10 ²	1.0·10 ⁶	1.0·10 ³	1.0·10 ⁷

The higher exponents offer the advantage of greater tolerance against small deviations from the goal value because of the flat base of the penalty function. However, the penalty rises sharply beyond a deviation in the constraint function (cf) of 1% (1.2) respectively 10% (2.2) from the value to be obeyed (cf_{req}).

4.3.3 Numerical Results

Tab. 18 is a summary of the optimisation results. The rectangular wing values, configuration (0), are included in the table for reference. Fig. 57 depicts the corresponding final wing planform shapes. The objective of the first optimisation run was to find a planform of minimum induced drag without changing span. The starting point was a rectangular wing, configuration (0), having a span efficiency of $\tau = 0.9710$. After 250 function evaluations the relative objective function value change between optimiser steps decayed below $1 \cdot 10^{-6}$ for which convergence was assumed (this convergence criterion has been used throughout this chapter). The resulting function value at the solution was $\tau = 0.9932$, a value just 0.68% below the value to be expected from lifting line theory. The wing mass of the resulting elliptical surface (1) turned out to be 22.7% lower than that of the rectangular wing due to the increased chord lengths at the inner wing increasing the wing box geometrical moments of inertia. Interestingly, the integrated bending moment figure has just decreased by 9.6%.

In the next run (2), it was attempted to reproduce the result of Prandtl [19]. Starting with the elliptical wing, the constraint on span was cancelled but a new one was placed upon the integrated wing bending moment. The rate of convergence decayed during the optimisation and the run was aborted upon reaching the maximum number of 1500 function evaluations. The span increased by 17.17%, which is somewhat less than the theoretically expected value of 22.48%. The induced drag decreased by 10.14%, just about 1.0% less of the analytical reduction for the same shape parameter value μ . The root chord of the wing increased but the tip became extremely pointed, instead.

Tab. 18: Optimisation results (configuration (0) is the starting point for optimisation run (1)).

Run/ Config.	Designation	$n_{\text{iter}} /$ conv.	μ	b/b_{ell}	$D_i/D_{i,\text{ell}}$	τ	$M_{\text{int}}/$ $M_{\text{int,ell}}$	S/ S_{ell}	$m_w/$ $m_{w,\text{ell}}$
0	rect	n/a	n/a	1	1.0229	0.9710	1.1065	1.0029	1.2931
1	1.1 ell	250 / yes	0	1	1	0.9932	1	1	1
	1.2 ell - analyt.	n/a	0	1	1	1	1	1	n/a
	$\Delta (1-2)/2$ (%)	n/a	0	0	0	-0.68	0	0	n/a
2	2.1 M_{int}	1500 / no	0.8544	1.1717	0.8986	0.8074	1.0001	0.9999	0.9649
	2.2 M_{int} analyt.	n/a	dito	dito	0.8896	0.8188	1	1	n/a
	$\Delta (1-2)/2$ (%)	n/a	0	0	1.012	-1.39	0.01	-0.01	n/a
3	Wing mass	1500 / no	n/a	1.1939	0.8655	0.8071	1.0438	1.0000	1.0000

The last optimisation run (3) again took the elliptical wing as starting point. This time, the computed wing mass had to be maintained by the optimiser instead of the integrated bending moment. Again, the maximum number of function evaluations terminated the optimisation. As the relative wing mass $m_w/m_{w,\text{ell}}$ of run (2) already allowed to anticipate, the span increased to a greater value than before. Following the original trend of the optimisation where the integrated bending moment was kept constant, the induced drag reduced further but the same is true for the span efficiency. The differences in the results of runs (2) and (3) are small, however, it can be seen that there is no real alternative to considering the explicit structural sizing of the wing for assessing the effects of the wing mass upon configuration performance.

It has been shown that the penalty function approach works effectively. Nevertheless, it also turned out that the introduction of penalty functions came along with an obvious reduction in optimiser performance. The satisfactory reproduction of the analytical results showed that the structure module appears to represent structural sizing trends correctly. Moreover, it has been shown that the interplay of the vortex lattice core module and the structure model functions appropriately.

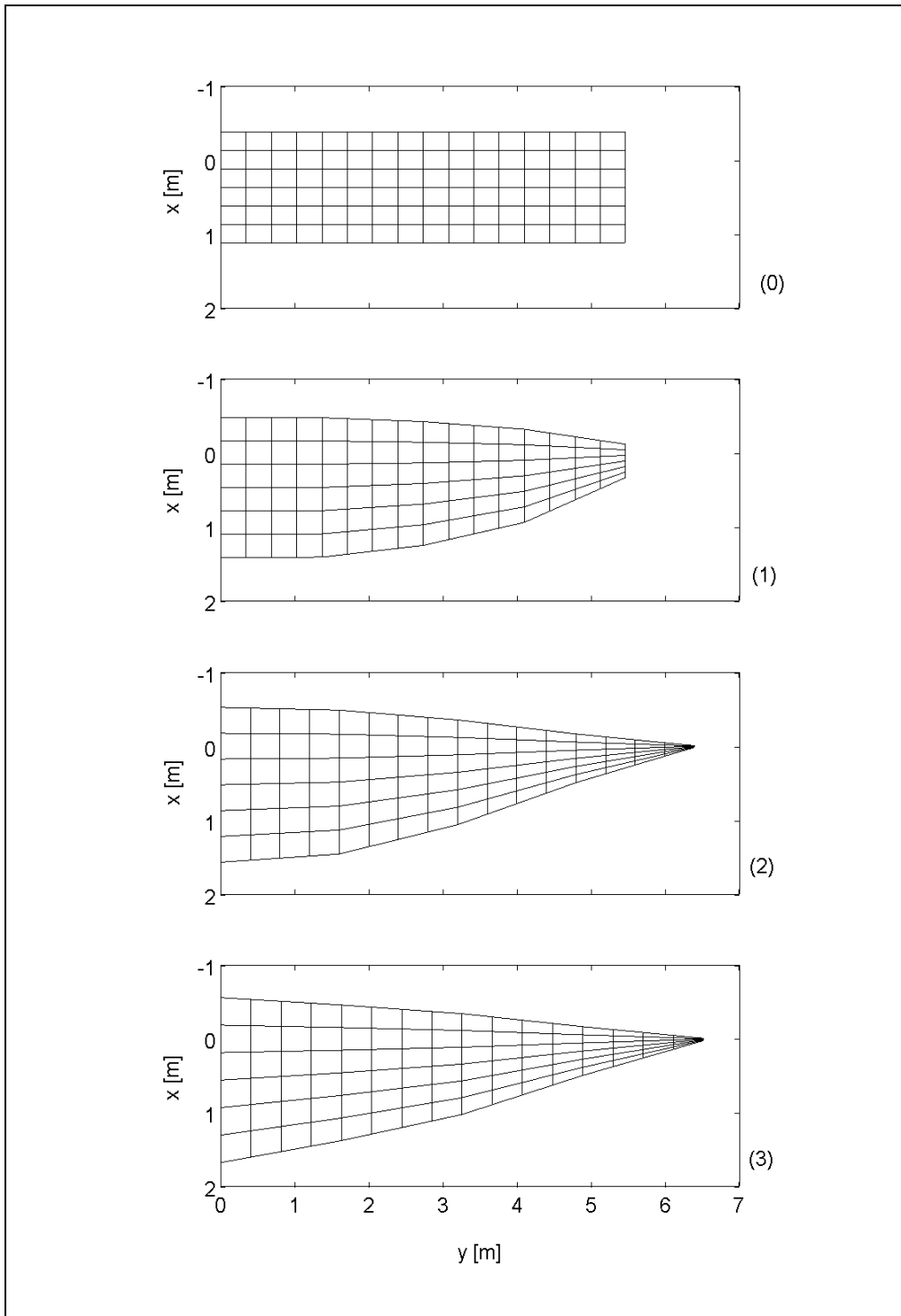


Fig. 57: Comparison of wing planform shapes of equal area and lift according to Tab. 18.

5 Multi-Winglet Parametric Studies and Optimisation

Parametric studies and optimisations of various multi-winglet configurations are the subject of the present chapter. After an introductory note in chapter 5.1, chapter 5.2 intends to identify characteristic trends in aerodynamic performance by analysing sensitivities of a low speed multi-winglet configuration that has already been introduced in chapter 4.1. While chapter 5.2 focuses on the influence of configuration parameters as well as Reynolds number on the aerodynamic efficiencies, Chapter 5.3 carries on with analysing the influence of the fidelity of the computational model on the optimum slitting ratio including the consideration of wing structure mass.

Tab. 19: VLM++ modules and model settings used for computations in chapter 5. VLM++ core module of is used in all cases.

Chapter	Profile Drag			Interference Drag	Additional Drag Area for Aircraft Parts Other than Wing	Cascade Model		Non-Linear Effects	Wing Structure Sizing		
	Flat Plate and Zero Lift Profile Drag Due to Thickness (Section, x/c)	Lift Dependent Profile Drag				a) Adaptation of Maximum Loadability	b) Evaluation of Canonical Pressure Coefficients		Mass Model		Consideration of Static Aeroelastic Deformation
		a) Based on Maximum Loadability	b) Based on Supercritical Ratios						1: Scaling According to Primary Mass Only	2: Different Secondary Structure Mass Scaling	
5.2.1	✓ (0015, 0.3)	✓	-	✓	-	✓	-	✓	-	-	-
5.2.2	✓ (4412, 0.5)	✓ ¹⁾	-	✓	-	✓	-	✓	-	-	-
5.2.3	✓ (0015, 0.5)	✓ ¹⁾	-	✓	-	✓ ²⁾	-	✓	-	-	-
5.2.4	✓ (4412, 0.5) ³⁾	✓ ¹⁾	-	✓	✓	✓	-	✓	-	-	-
5.3.1	✓ (0012, 0.3) ⁴⁾	-	-	-	✓	-	-	-	✓	✓	-
5.3.2	✓ (0012, 0.3)	-	✓	✓	✓	-	✓	-	✓	✓	-
5.3.3	✓ (0012, 0.3)	-	✓	✓	✓	-	✓	-	✓	-	✓
5.4.1	✓ (XX12, 0.3)	-	✓	✓	✓	-	✓	-	-	✓	-
5.4.2	✓ (XX12, 0.3)	-	✓	✓	✓	-	✓	-	-	✓	-
5.4.3	✓ (XX12, 0.3)	-	✓	✓	✓	-	✓	-	-	✓	-

1) Model coefficients adapted to small Reynolds numbers.

2) Also computations without cascade model.

3) Computation of additional polar of wing with NACA 0015 airfoil section.

4) In addition to fixed transition location also computations with fixed profile drag.

The configuration for this analysis is set-up according to a general aviation aircraft scenario which constitutes a second datum and which is used for the remainder of chapter 5. Set-up and results of comprehensive multi-variable parametric studies and an example of how to optimise multi-winglet configurations by means of non-linear multi-variable numerical optimisation are discussed in chapter 5.4. Tab. 19 gives an overview about the models of VLM++ and specific settings used.

5.1 Introductory Note - Sensitivity of Results to Planform Parameter Definition

Engineers and to an even greater extent scientists try to identify and work with generalised principles that describe physical problems. In aerodynamics this is often done by normalisation of forces and moments by means of the dynamic pressure, reference surfaces and characteristic lengths, in order to obtain dimensionless coefficients. As long as the reference figures are known, the corresponding dimensional values can always be regained. While normalisation is of tremendous value to engineers, it can also be misleading if the reference values are ambiguous. This ambiguity often occurs in cases without a certain commonly accepted way of normalisation as precedence or, where the definition of a normalisation quantity itself is not unequivocally defined. In the end of the day, experimental or theoretical results may be perfectly documented, but, the mere way of normalisation may favour the one or the other interpretation. This frequently happens in cases where one gets down to multidisciplinary aircraft design. Examples, which may be a source of inconsistency, are wing areas and the definition of characteristic lengths used to compute moment coefficients. This introductory note attempts to illustrate such a problem in the current context of non-planar wing configurations by example of wing span definitions in parametric studies. The present section is thus also intended as a cautionary note, anticipating the discussions that accompany the parametric studies to follow.

The data of reference [50] shown in Fig. 56 always referred to the semispan of a basic rectangular wing. The span of main wing and winglets obtained by summing up along local curvilinear y-coordinates was kept at a fixed value. Fig. 58 compares the reciprocal span efficiencies for two and four winglets with those where the span is defined as the maximum spanwise extent in the body-coordinate system y-direction. Adding dihedral to the winglets in the present fashion has a similar span reducing effect as the folding wing mechanism of some aircraft used for saving parking space on ground.

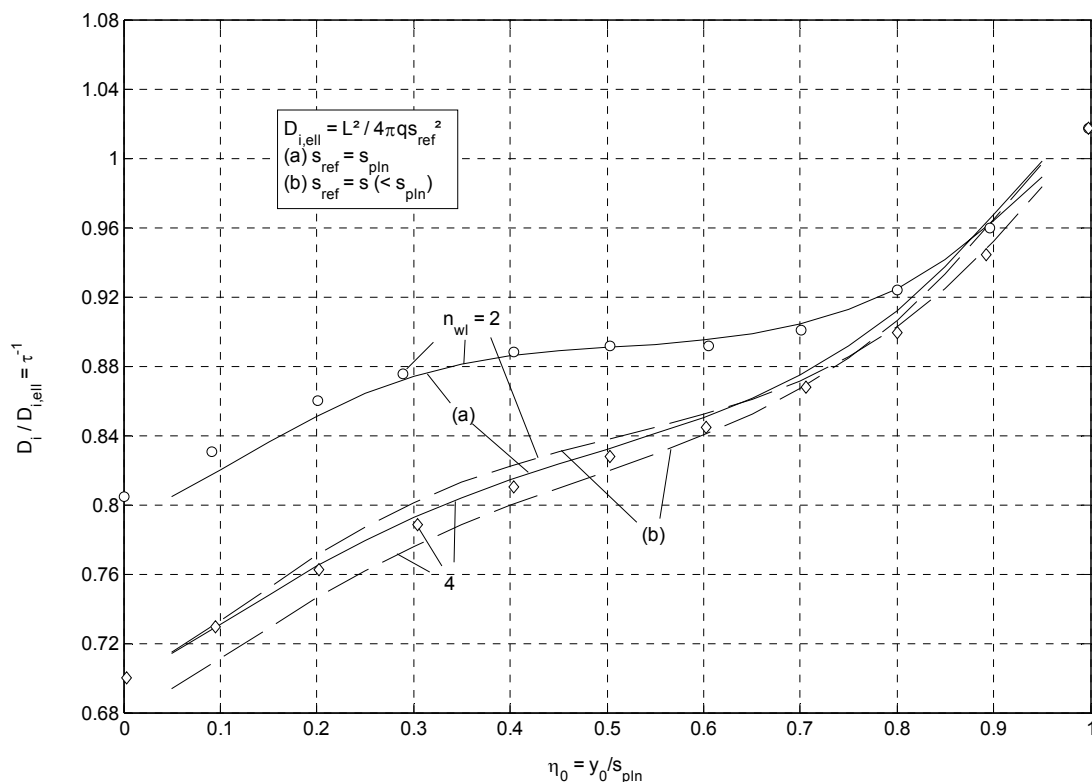


Fig. 58: Comparison of theoretical induced drag characteristics of non-planar wings with slotted wing-tips. Bullets and sketches from ref. [50], solid lines obtained with present model.

Physically, only the cosine of the dihedral times the winglet span plus the semi-span of the main wing part add up to the semispan of the wing such that

$$S_{nwl} = 2 < S_{nwl} = 4 < S_{pln}$$

It can be seen that the span efficiency of the configuration with four winglets is in fact not much better than that with only two winglets if the latter and more common span definition is used, instead of the curvilinear span sum-up.

It appears that the mere choice of simple planform parameter definitions significantly alters the appearance of the underlying physical effects of non-planar wings. The encounter of substantial trouble by tackling the relatively straightforward task of comparing different planform configurations with respect to induced drag points out that considerably more emphasis must be put on planform shape definitions than is required for studies involving planar surfaces only.

5.2 Sensitivity of Aerodynamic Performance to Parameter Changes

The model that has been adapted to the experimental data of Hummel ([50], [48]) as described in chapter 4.1 will serve as a basis for an extended parametric study intended to give additional insight as to what physical trends change with altered influence parameters and to what degree the overall performance balance changes. This will allow to identify trends and ease to identify "sweet spots" in the design space.

5.2.1 Variation of Reynolds Number

In many experimental attempts to reproduce the significant performance gains that have been computationally predicted, it was found that the experimental performance was in fact much less than expected. In some cases a small performance gain was established, in others the performance was even less than that of a planar reference configuration without winglets. It is supposed that a significant portion of these discrepancies can be attributed to specific problems associated with low Reynolds number testing. Single as well as multi-winglets reduce the lift induced drag of the configuration. They thus become most efficient at higher lift coefficients. The maximum lift coefficient is strongly dependent on the Reynolds number Re_c (compare Fig. 52). It can thus be expected that just an increase in the Reynolds number may yield a performance gain. Spillman [57] proved this by comparing flight-test with wind-tunnel test results of his wing tip sails.

To theoretically study the effect with VLM++, the settings originally adapted to reproduce the experimental results of Hummel have been adjusted to a case where the Reynolds number has increased by a factor of 20. First, the parameters for the lift dependent part of the profile drag have been set back to their original values according to the calibration of the model to the data of reference [100]: $k_{const} = 0.0152$, $k_{minmax} = 0.0215$. Second, the relative transition location x_t/c (applicable to both sides of the wing) has been moved forward from 0.50 to 0.30, thus coinciding with the location of the maximum thickness.

Tab. 20: Maximum NACA 0015 airfoil section lift coefficients for several Reynolds numbers.

	Reynolds number Re_c	NACA 0015 $C_{l,max}$ (adapted to [50], [48])	Reynolds number Re_c	NACA 0015 $C_{l,max}$ ([130])	Change $\Delta C_{l,max}$
Main Wing	$0.433 \cdot 10^6$	1.03	$8.65 \cdot 10^6$	1.57	+0,54
Winglets	$0.093 \cdot 10^6$	0.86	$1.85 \cdot 10^6$	1.20	+0,34
Main Wing / Winglets	$4 \frac{2}{3}$	1.198	$4 \frac{2}{3}$	1.308	- / -

Third, the sectional maximum lift coefficients have been adapted for the increased Reynolds numbers as outlined in Tab. 20. Fourth, the type of stall has been altered from the adapted form to a generic trailing edge stall for the main wing and a short bubble or leading edge stall for the winglets.

Fig. 59 and Fig. 60 compare the lift and drag characteristics of the rectangular wing (1) and the configuration with canted and twisted winglets (4) for the two different Reynolds numbers. The maximum lift coefficient of the rectangular wing attains a much higher value than the corresponding one of the winglet configuration as the Reynolds number is increased. Two reasons can be put forward. First, the main wing gains much more loadability than the winglets which can be seen from the maximum lift coefficient ratios in Tab. 20. Second, the lift loss is much more pronounced due to the leading edge stall characteristics of the winglets when separation starts at winglet 'A'. The stalling sequence is virtually identical to that at the lower Reynolds numbers.

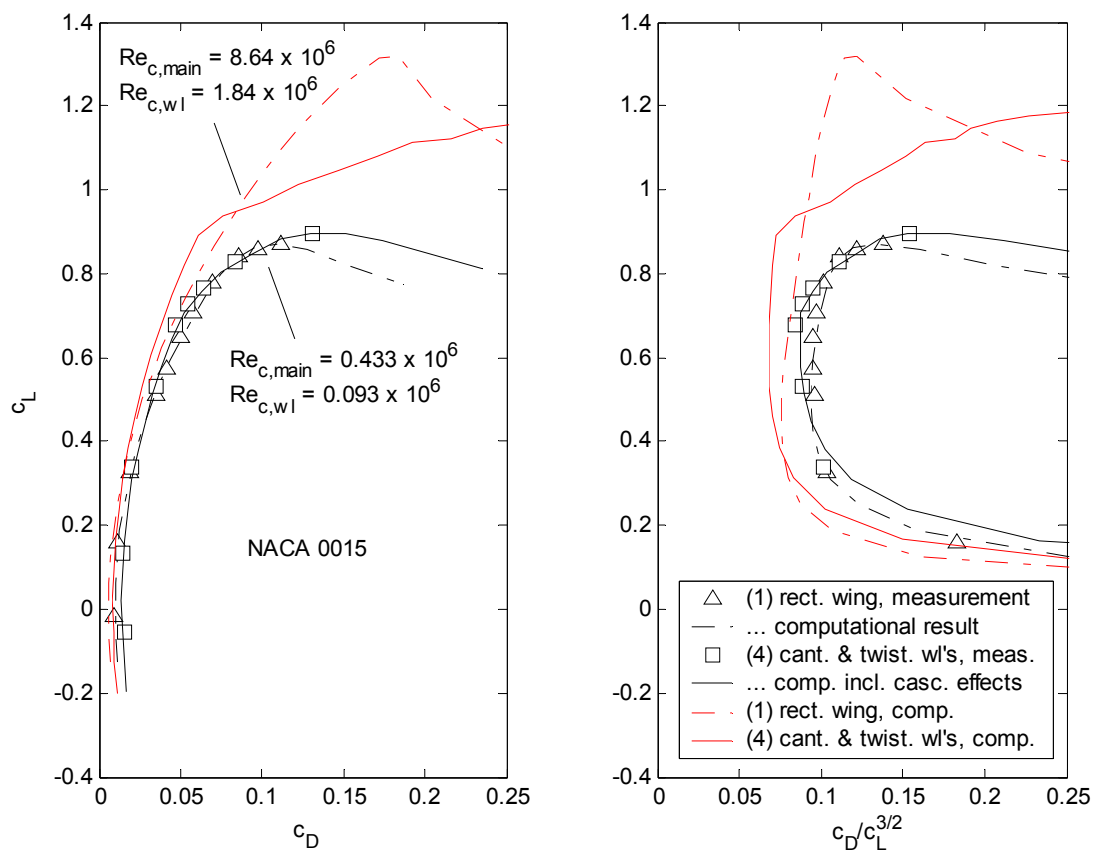


Fig. 59: Computed lift to drag characteristics for two different Reynolds numbers.

Despite the larger fraction of turbulent flow, the zero lift drag coefficients are significantly smaller due to the higher Reynolds numbers.

On the right hand side of Fig. 59, the reciprocal endurance parameter $c_D/c_L^{3/2}$ for the high Reynolds number is 10.2% less for the winglet configuration compared to that of the rectangular wing, which is approximately the same relative difference as established for the low Reynolds number case (see Tab. 15). Confining the discussion to the winglet configuration, the lift coefficient for maximum endurance for the high Reynolds number is 0.605. This figure is smaller than the original experimental value of 0.677 for the low Reynolds number, which is mainly caused by the reduction in profile drag.

Obviously, the rectangular wing profits as much from the higher Reynolds numbers as the multi-winglet configuration does. The maximum lift coefficient of the rectangular wing is in contrast to the low Reynolds number case significantly higher than that of the multi-winglet configuration.

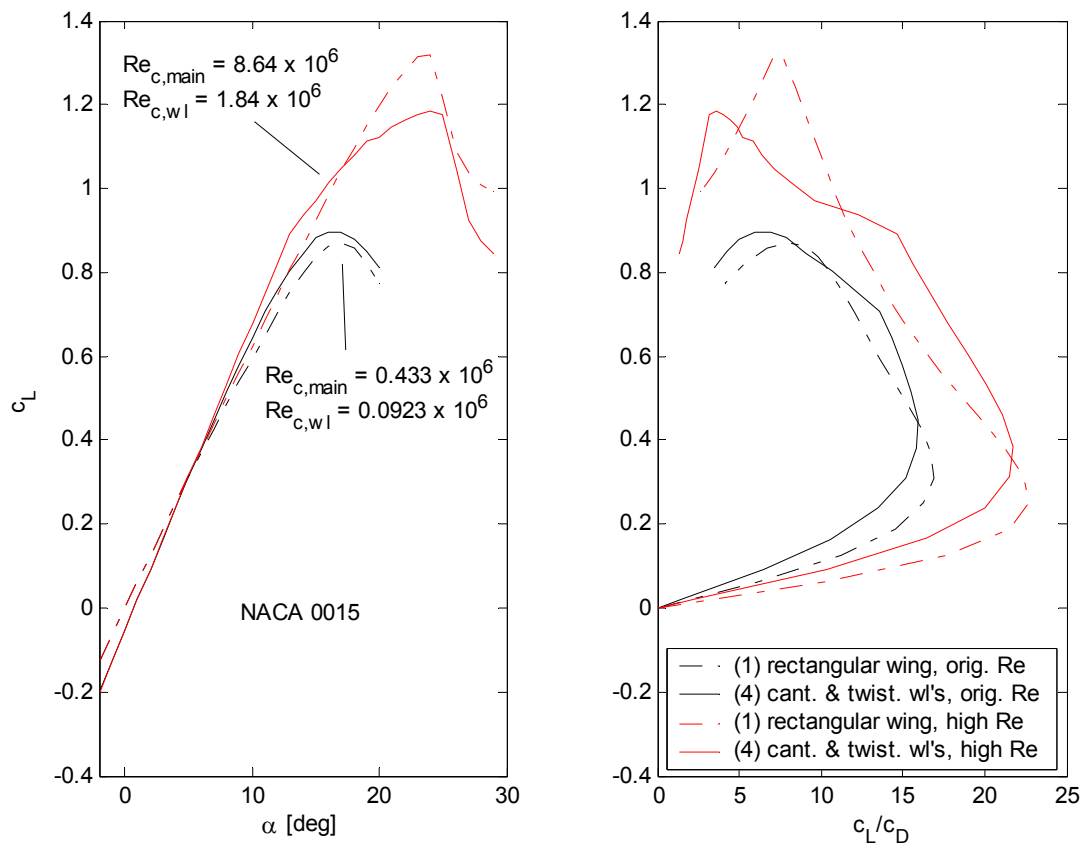


Fig. 60: Computed lift-vs- α and lift to drag polars for two different Reynolds numbers.

5.2.2 Variation of Camber

Early publications on bird flight and its technical adaptation, among which Lilienthal's investigations are the best known [43], already emphasised the obvious significance of wing camber. Wing camber proved to be an effective means for increasing sectional lift

to drag ratios especially at low Reynolds numbers. Hence, it can be expected that the shift from symmetrical sections to cambered sections would significantly increase the performance of multi-winglet configurations. However, Spillman and Fell [77] found the performance of cambered tip sails with 12% relative thickness at chord based Reynolds numbers of about 46,500, inferior to that of uncambered sections. With regard to this unexpected behaviour, it should be noted that the authors mention in their conclusion that more time could have been spent on transition fixing on the model.

In the present investigation, the NACA 4412 airfoil section is used as a basis because its significantly larger maximum lift capability compared to the respective figures of the NACA 0015 section (Tab. 21) for the Reynolds numbers under consideration.

Tab. 21: Maximum lift coefficients of NACA 0015 and NACA 4412 sections.

	Reynolds number Re_c	NACA 0015 $c_{l,max}$ (adapted to results of [50], [48])	NACA 4412 $c_{l,max}$ ([130])	Change $\Delta c_{l,max}$
Main Wing	$0.433 \cdot 10^6$	1.03	1.23	+0,20
Winglets	$0.093 \cdot 10^6$	0.86	1.06	+0,20

The higher sectional loadability results in an overall higher maximum lift coefficient as shown in Fig. 62. The lift to drag polar of configuration 4 with the NACA 4412 section does not exhibit a kink at about 80% of the maximum lift in contrast to the same configuration using the NACA 0015 section. An inspection of the stall behaviour reveals incipient separation at the outer part of the trailing winglet 'C' not before an angle of attack of 12 deg for the modified configuration with the cambered sections. This behaviour is different to the initial root separation at the leading winglet 'A' in case of symmetrical sections. Fig. 61 compares the pressure distributions of both configurations at $\alpha = 10$ deg for the ideal situation of fully attached flow (this assumption is justified for the current purpose since all sections of both configurations operate below $c_{l,max}$). It can be noticed on the right hand side of the figure for the symmetrical sections that the suction peak at the root of winglet A is lower than the corresponding value close to the centre of the wing despite the lower incidence.

In contrast, it can be observed that winglet 'C' bears higher loads than winglets 'A' and 'B' in case of the cambered configuration. Winglet 'B' stalls at its centre together with the root section of winglet 'A' not before an angle of attack of 15 deg which is also the maximum lift angle of attack of the wing.

An indicator of lift effectiveness of a wing configuration is the ratio of a characteristic local sectional lift coefficient to the total one. For the NACA 0015 configuration the overall maximum lift coefficient of 0.896 divided by the maximum local value of 1.03 of

the main wing that occurs at the section next to the wing geometric centre yields a ratio of 0.870. This indicates that some parts of the wing already have passed the local maximum lift conditions with the consequence that some lift at the outer wing has already been lost.

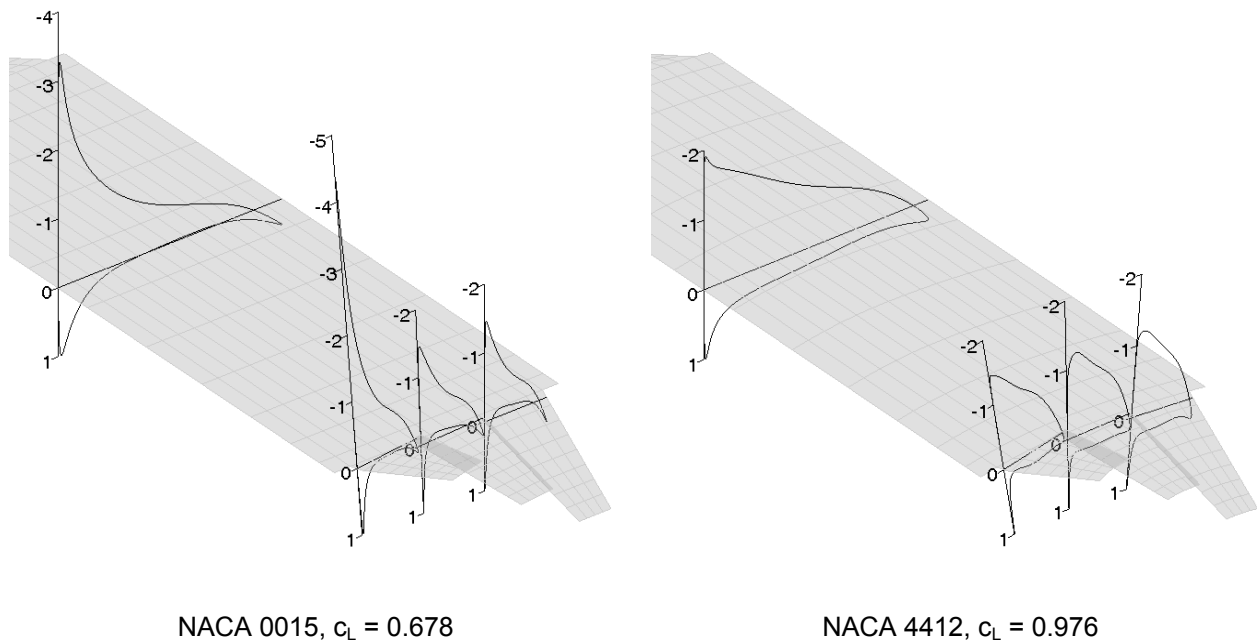


Fig. 61: Comparison of c_p distributions at $\alpha = 10$ deg. Left: Basic configuration with NACA 0015 sections according to reference [50] and [48]. Right: Same configuration but with NACA 4412 sections.

The values for the NACA 4412 case are $1.122 / 1.23 = 0.912$. It is due to the fact that maximum lift conditions of the individual surfaces are attained rather simultaneously what brings about a better exploitation of the lift capabilities compared to the configuration with symmetrical sections.

Inspection of the reciprocal endurance parameter on the left hand side of Fig. 62 shows a favourable result for the cambered sections. Comparing the computational results for the winglet configurations reveals that the variant with camber has a small benefit over the uncambered one with regard to the maximum endurance capabilities. The lift coefficient range of reasonable aerodynamic performance increased significantly due to cambering the airfoil sections, both for the rectangular as well as the multiwinglet configuration with a somewhat larger advantage for the latter, as expected. A fact that could be of importance is that the lift coefficient for maximum endurance is higher for the cambered configuration. Referring to the soaring flight of birds, a higher lift coefficient allows reduced flying speed and smaller curve radii while thermalling. This further improves climbing performance because the vertical velocity profile of convective thermal updrafts increases towards the thermal centre (compare [133], [134] and [90]).

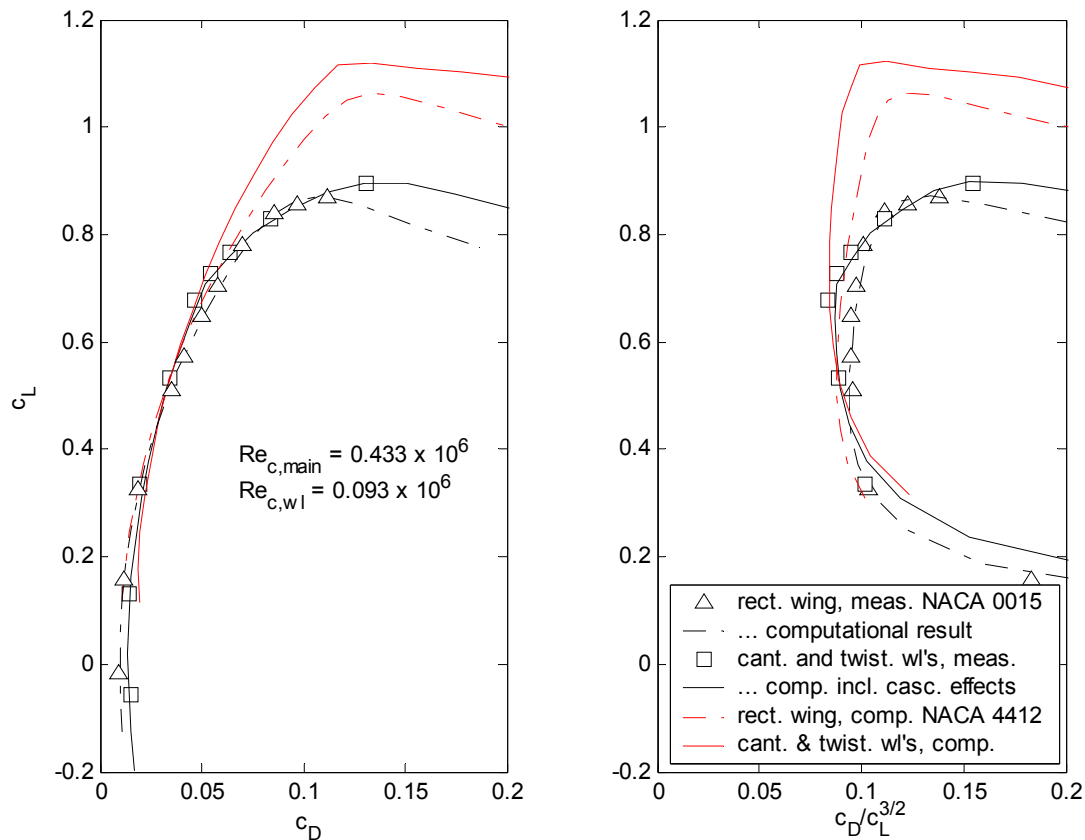


Fig. 62: Lift to drag characteristics of basic configuration with NACA 0015 section according to reference [50] and [48] compared to computational results for the same configuration but using NACA 4412 sections.

Finally, it is worth mentioning that the performance gain of the winglet configuration in comparison to the rectangular wing has increased significantly over that of the experimental configuration of Hummel.

5.2.3 Variation of Winglet Number

Flight test results of Spillman [57] showed that the lift to drag performance of three winglets is superior to a configuration with only one. Zimmer [83] compared two configurations with only two winglets both computationally and experimentally. The first configuration could be referred to as a split tip configuration. The leading winglet pointed upwards with a dihedral of +25 deg and was set at an incidence of -4.5 deg whereas the trailing winglet had a dihedral of -20 deg pointing down and 0 deg incidence. Incidences of the second configuration were identical but dihedrals were +10 deg and +5 deg in order to closely approach the so called optimal biplane configuration of [128]. Winglets had taper ratios of 0.2, a leading edge sweep of 42.0 deg for the leading respectively 25.2 deg for the trailing winglets for both configurations. The numerically predicted

induced drag of the first configuration was lower compared to that of the second configuration despite the smaller span due to dihedral. It appeared from the VLM computations of Zimmer that the effect of the vertical spreading of the wing vortex system exceeded the span effect. Nevertheless, the measurements at a Reynolds number of $0.10 \cdot 10^6$ based on the chord of the rectangular main wing ($Re_{c,wl,root} = 0.05 \cdot 10^6$) showed a small advantage of the second configuration from $c_L = 0.52$ upwards. Below, the drag coefficients of both configurations were virtually identical. Zimmer attributed the better performance of the second configuration to positive interference effects of the optimal biplane configuration, which appeared to have prevented early separation on the leading winglet. This experimental evidence again indicates that cascade effects obviously play an important role for the aerodynamic performance of multi-winglet systems. Multi-slotted high-lift devices of aircraft and turbomachinery cascades substantiate the expectation that the lift producing capabilities of winglets may increase with their number.

The effects of varying the winglet number has been analysed with VLM++, taking once again Hummel's measurements ([48], [50]) as a basis. The planform shapes and the results are listed in Tab. 22. The rectangular wing and the configuration with only one winglet have neither dihedral nor twist. For all the other cases, the values of Hummel's leading and trailing winglets of configuration (4) have been applied to the leading and trailing winglets with linear interpolation for the evenly distributed winglets in between. Sectional maximum lift coefficients have been set to the values of Tab. 13.

At first glance, the lift curve slope of the linear part of the lift polar $(dc_L/d\alpha)_{lin}$ continuously increases with number of winglets. The transition from the configuration with no winglets to the one with only one planar winglet is effectively a change from the rectangular planform to a tapered planform which is closer to an elliptical shape. The aspect ratio increases from 4.0 to 4.9. The planform effect as well as the aspect ratio tend to increase the lift curve slope. The vertical spreading of the two winglets ("split tip" configuration) yields another step up in the lift curve slope. Adding winglets in between the leading and trailing winglets with +20 and -20 deg dihedral yields rather small further increments. So far, the results are in excellent agreement with other numerical results ([13], [14], [18]).

The wing maximum lift coefficients have been computed first without cascade effects and second with cascade corrections switched on. The difference of the maximum lift coefficients between the two cases is small. Again, changing the planform from the rectangular to the rather elliptical planform results in a marked increase in maximum lift coefficient. One reason of the better lift capability is the more homogeneous spanwise distribution of the lift coefficients. The maximum lift condition for an elliptical wing, for example, will be reached at all spanwise sections simultaneously if the sectional maximum lift capability is a constant.

Tab. 22: Change of aerodynamic performance with winglet number ($c_{l,max}$ with respect to section coordinates).

Configuration	n_{wl}	S_{ref} [m ²]	$\left(\frac{dc_L}{d\alpha}\right)_{lin}$ [rad ⁻¹]	$c_{L,max}$	$c_{l,max}$ at leading winglet root	$c_{l,max}$ at second winglet root	$c_{l,max}$ at second winglet root for otherw. attached flow	$c_{L,max}$	$(L/D)_{max}$
Cascade effects:	n/a	n/a	n/a	no	yes	yes	yes	yes	yes
	0	0.1225	3.58	0.869	-/-	-/-	-/-	0.854	16.9
	1	0.1100	3.86	0.919	0.839	-/-	-/-	0.921	17.6
	2	0.1100	4.08	0.893	0.989	0.813	1.026	0.894	15.6
	3	0.1100	4.15	0.888	1.041	1.064	1.726	0.899	15.9
	4	0.1100	4.18	0.887	1.005	1.064	1.587	0.909	15.9
	6	0.1100	4.20	0.889	1.169	1.273	1.944	0.909	15.7

The tapered wing (single winglet configuration) has the best lift to drag ratio, the split tip the lowest. So far, the hypothesis of performance improvements by adding winglets must be rejected.

Reference to the lift and drag characteristics in Fig. 63 allows to deepen the discussion as it offers a more comprehensive view compared to the characteristic corner values of Tab. 22 only. Neglecting cascade effects and using just sectional maximum loadability values causes the performance to quickly deteriorate with number of winglets. With the cascade corrections applied, the deterioration is less severe. The problem with the winglets is that the drag coefficients start to break away already at moderate lift coefficients caused by the high loads and subsequent boundary layer separation at the leading winglet root. Tab. 22 also contains the sectional maximum lift coefficients for the root sections of the leading winglet. By and large, the loadability of this particular wing section grows with the number of winglets. Nevertheless, the growth of the loadability is not large enough to counter the effect of the actually increased root loading at a given angle of attack. Nevertheless, the drag rise is postponed to larger lift coefficients. An inspection of the root section loadability of the second winglet reveals that it would be much higher if the leading winglet did not stall. With the leading winglet in the stalled condition, the positive interference effect of the first onto the second winglet is no longer present and, finally, the maximum lift value of the second winglet will not be much greater than that of the leading winglet.

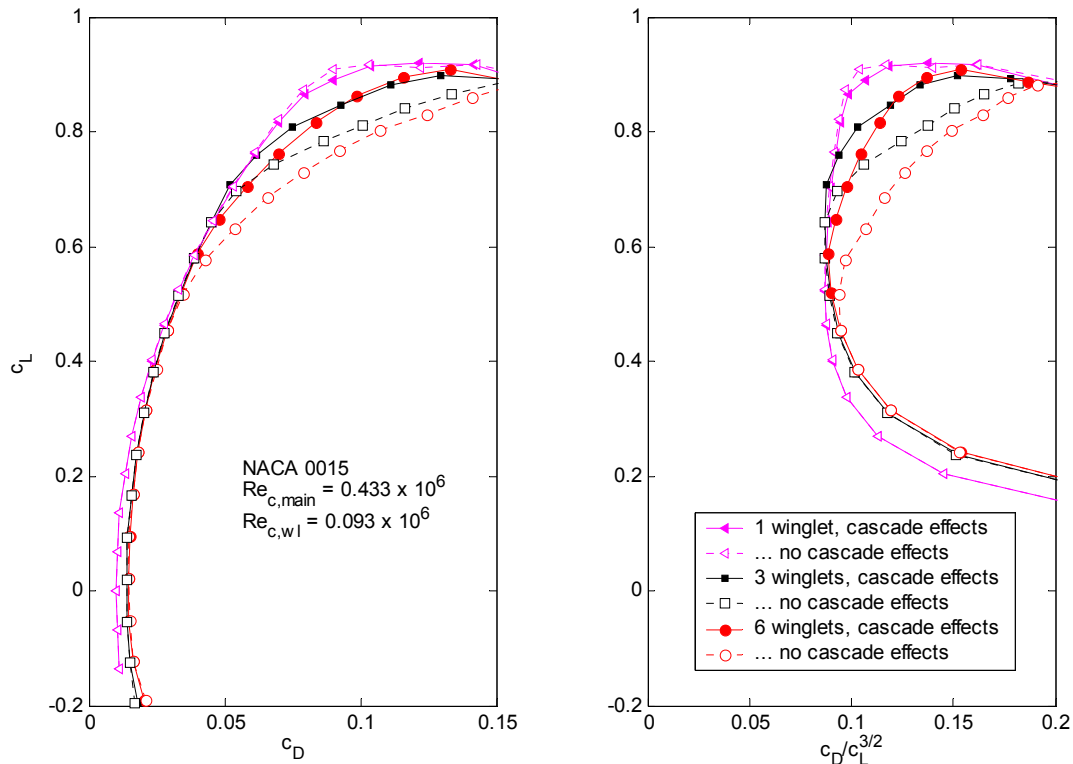


Fig. 63: Lift to drag characteristics with varying numbers of winglets.

However, this leads to the conclusion that a successful winglet cascade must tackle the problem of the high loads at the leading winglet root either

1. by improving the cascade arrangement so that the loadability is significantly increased or
2. by decreasing the actual load by means of choosing appropriate profile section, incidence and twist or a combination thereof.

5.2.4 Configuration Enhancements

Section 5.2.2 showed that proper sectional camber effectively improves the performance of a wing equipped with multi-winglets. The current section is dedicated to analysing what goal-oriented changes of planform and further fundamental configuration design parameters are able to contribute towards improving performance. The aim must be to shift fundamental planform parameters so that the already manifested favourable performance gains better coincide with the optimum conditions from a performance point of view.

Considering the basic parabolic drag polar model, eq. (14), a greater aspect ratio increases the slope of the c_L^2 -versus- c_D -curve k^{-1} and also the lift coefficient where the

maximum lift to drag ratio will be attained. The lift coefficient for best lift to drag ratio also rises if the lift independent drag component increases. This is the case if, for example, a non lift-producing body or fuselage is added to the configuration. These relations are illustrated in Fig. 64. All polars are normalised by the optimum lift to drag condition of the reference polar 1.

Tab. 23: Normalised zero lift coefficients and induced drag factors k for polars shown in Fig. 64.

Polar	1	2	3	4
$c_{D,0} / c_{D,0,1}$	1	1.5	3	3.5
k / k_1	1	0.66	1	0.66

Polar 2 is computed by increasing wing zero lift drag by 50% of the original zero lift drag of polar 1 while reducing the k -factor by 1/3 (corresponds to an increase in span efficiency or aspect ratio of 50%). Tab. 23 contains further parameters specific to the polars of Fig. 64. The transition from polar 1 to polar 2 exemplarily illustrates the basic trend to be expected if multi-winglets are added to that wing. The profile drag increases (in the simplified case this is the zero lift drag increment of 50%) but at the same time the induced drag decreases. The best lift to drag ratio does not change at all, but the minimum sink speed will reduce by 18.4%. The lift coefficients for optimum conditions rise in both cases.

The same measures yield a gain in maximum lift to drag ratio of 13.4% of polar 3 over polar 4 if a further drag component such as caused by a fuselage or other drag producing non-lifting body is considered. The reduction of the minimum sink speed would be 23.3%. While these effects are accounted for by the simple parabolic drag polar, the consequences are outlined here because the effects become easily blurred if the field of simple aerodynamic models is left. Despite the fact that the simple parabolic drag model is not applicable for the present multi-winglet computations with its distinct non-linear effects, the trends are nevertheless similar. The example of Fig. 64 shows that the performance findings for a wing alone may appear entirely different in contrast to the findings when a whole configuration of a bird or an aircraft is considered. For this reason, conditions that are closer related to aircraft configurations are introduced and used henceforth.

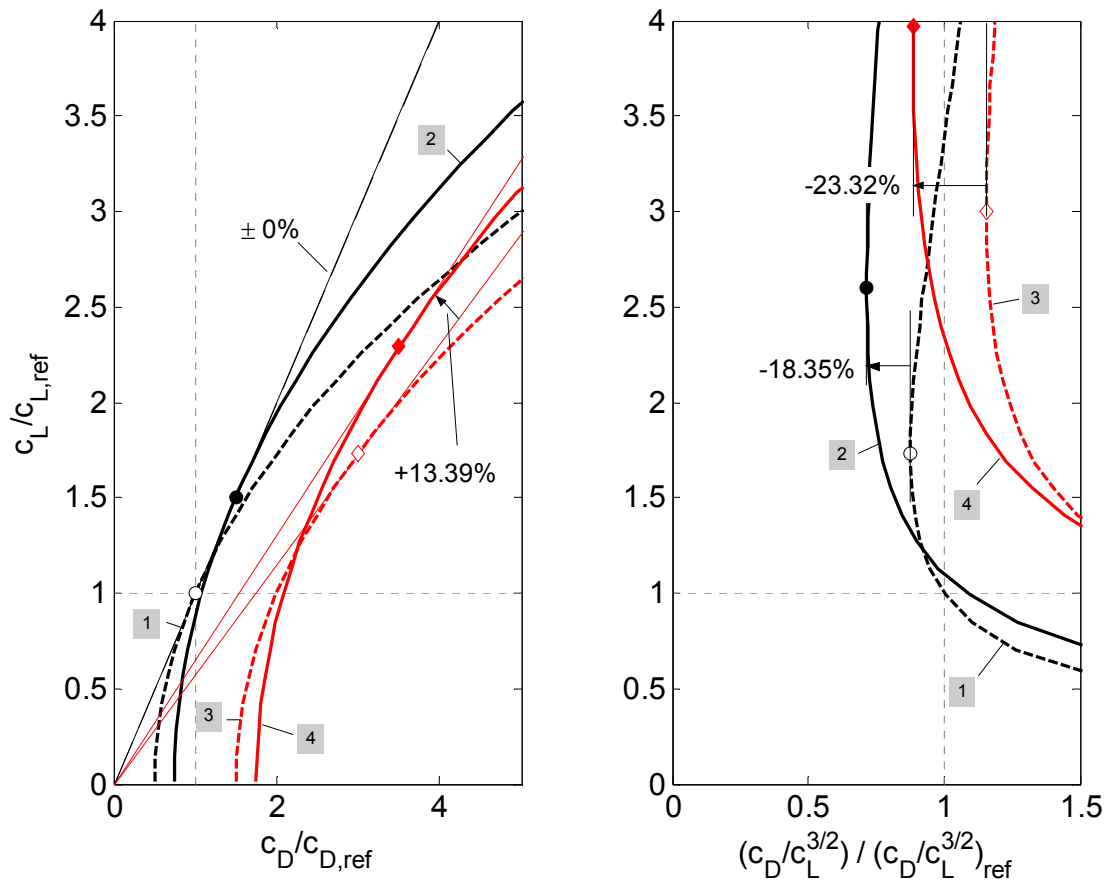


Fig. 64: Generic polars to illustrate the effect of additional lift independent drag components on lift to drag ratio and reciprocal endurance factor.

The zero lift drag increment to be added to the wing model, which is again based on Hummel's wind-tunnel test configuration, is based on the model of a streamlined body with a length to diameter ratio l_f / D_f of 3.0. The length of the body is three times the root chord of 0.175 m. The Reynolds number based on the body length is $1.298 \cdot 10^6$. According to the data compiled by Hoerner [97], the drag coefficient of the body can be expected to be about 0.0038 based on the wetted surface area. Torenbeek suggests a quick method for estimating the wetted area of streamline bodies [101]. Application to the current problem yields 0.2069 m^2 . Multiplication of the drag coefficient with the respective reference area yields the drag area of the body which is the basis for the incorporation of additional drag components in VLM++. Although a geometric conception of the drag producing body has been pictured, the additional drag has been introduced merely for studying its effects on flight performance. Hence, no attempt has been made to subtract the profile drag of the wing parts that would be masked by the body, neither attempt was made to account for wing-body interference.

The altered planform shapes are derived on the basis of the cambered configurations of section 5.2.2. Only the span was doubled for the rectangular wing (originally this was Hummel's configuration (1)) increasing the aspect ratio from 4 to 8. Scaling up the span by a factor of two was also applied to the configuration with canted and twisted winglets (4).

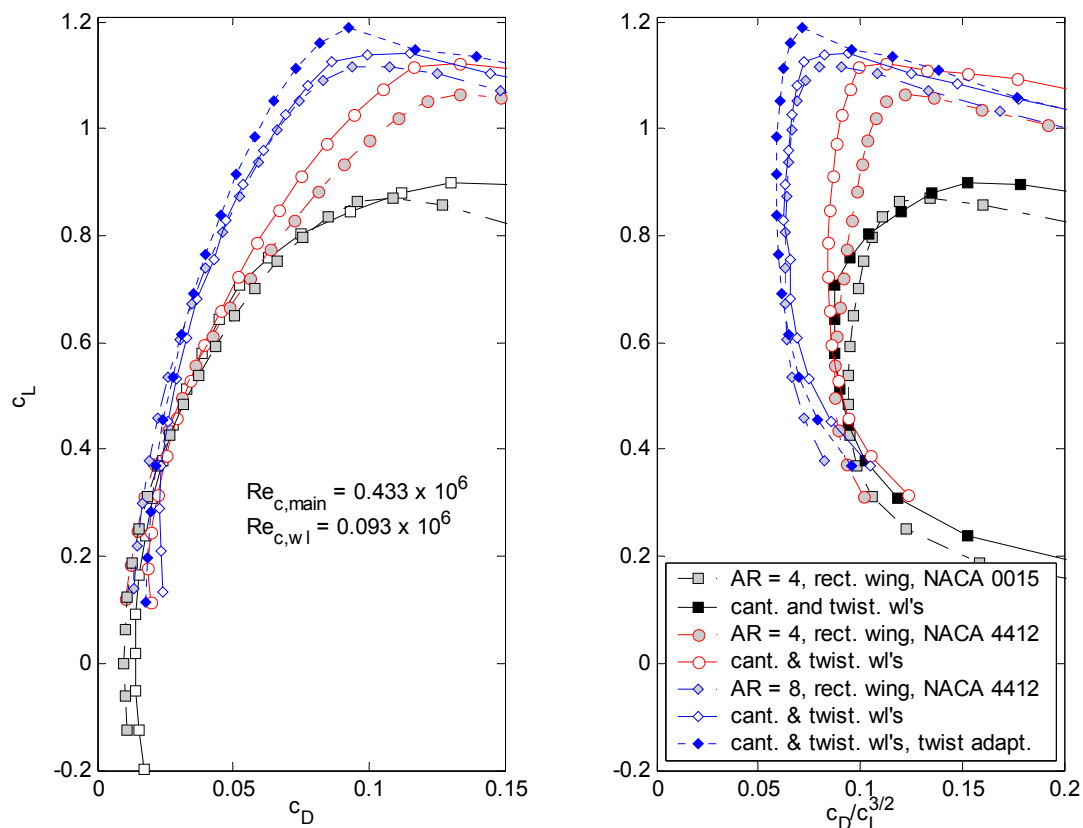


Fig. 65: Effect of camber, aspect ratio and zero lift drag on lift to drag performance.

The computational results are depicted in Fig. 65. As expected, the performance gain is significant, mainly due to increasing the wing span. Lift coefficients for the maximum endurance condition increase from about 0.60 to 0.74 for the cambered rectangular wings and from 0.72 to 0.83 for the cambered wings with winglets. With regard to the maximum lift to drag ratio, the simple rectangular wing with camber maintains its superior performance compared to the winglet configuration (refer to Tab. 24 for numerical data). Unexpectedly, the winning margin of the multi-winglet configuration for the inverse of the endurance parameter becomes very small. During the computations, the stalled regions grew from back to front with increasing angle of attack. This results in the prediction of a rather benign stalling characteristic. Nevertheless, the partly

separated flow leads to additional profile drag, which compensated some of the favourable effects of the winglets with respect to induced drag.

Tab. 24: Key performance parameters of high aspect ratio configurations.

Configuration	n_{wl}	$(L/D)_{max}$	@ c_L	$(c_D/c_L)_{min}^{3/2}$	@ c_L	$c_{L,max}$
Rectangular wing	0	20.5	0.534	0.0629	0.741	1.117
Canted and twisted winglets	3	18.6	0.609	0.0626	0.829	1.141
Cant. & twist. wl's, modified washout	3	19.8	0.616	0.0588	0.914	1.190

The spanwise distributions of the lift coefficients and the spanloads are plotted versus the non-dimensional spanwise coordinate η^* for a lift coefficient of 0.8 and attached flow (Fig. 66). The rectangular wing shows the well known trend of increasing lift coefficients when moving towards the tip for wings of increased aspect ratios. The opposite trend can be observed for the multi-winglet wing. Particularly the changes in the lift coefficient distribution are remarkable. The difference in the outer third of the wings is mainly due to lower loads on winglet 'A' at the higher span configuration.

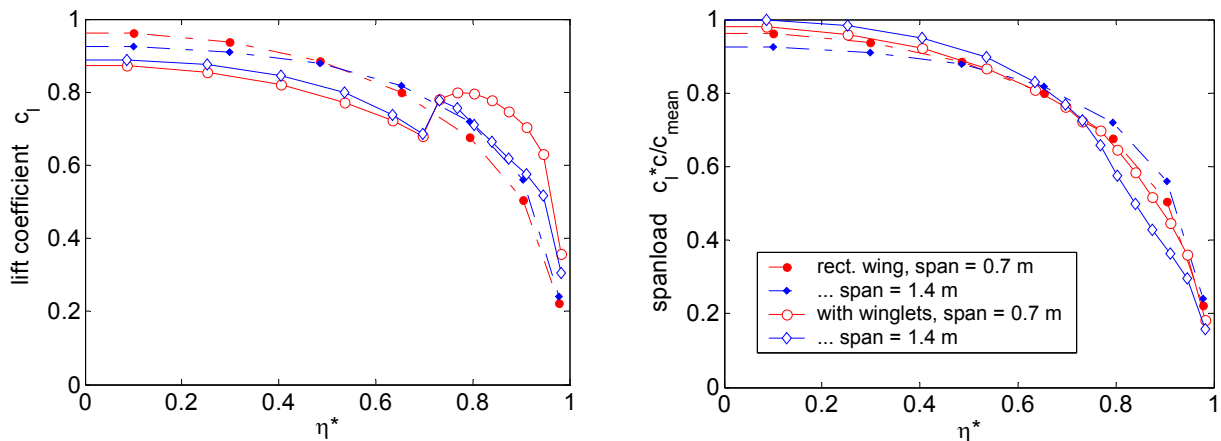


Fig. 66: Distribution of lift coefficients and spanwise loading for two different wing spans at $c_L = 0.8$. Lift coefficients for the winglet cascade are mean values for particular common spanwise stations as measured in local winglet coordinate systems.

Finally, the winglet twists were adapted on the lookout to improve the stalling characteristics. A washout of 10 deg was assigned to the outer part of the trailing winglet 'C' to unload this critical surface. Contrarily an inwash of 15 deg was applied to the outer part of the leading winglet 'A'. Fig. 67 illustrates the modified configuration.

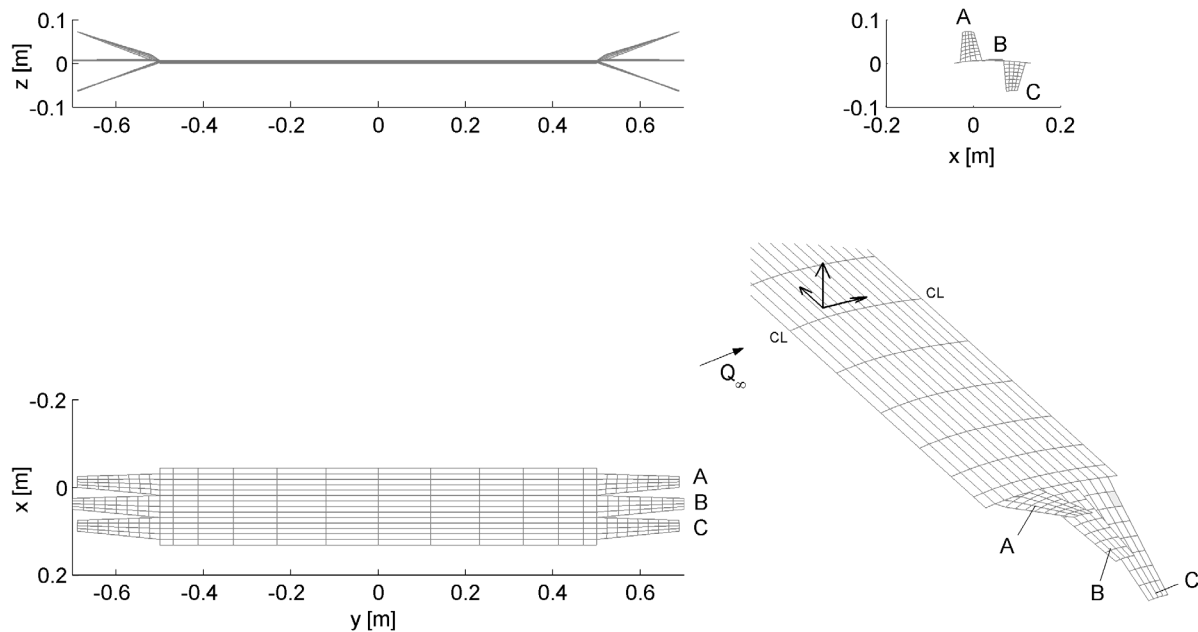


Fig. 67: Modified configuration (4) with NACA 4412 sections, doubled span and modified linear twist: Winglet 'A': root $\varepsilon = -10$ deg, outer wing $\varepsilon = 15$ deg, Winglet 'B': root $\varepsilon = -5$ deg, outer wing $\varepsilon = 0$ deg, Winglet 'C': root $\varepsilon = 0$ deg, outer wing $\varepsilon = -10$ deg.

The adaptation improves the stalling behaviour of the high aspect ratio configuration which is also reflected by the enhanced performance (Fig. 65).

5.3 Change of Optimum Slitting Ratio with Stepwise Refinement of Computational Model

5.3.1 Effect on Profile Drag, Wing Mass and Aircraft Performance Parameters

This chapter is dedicated to the performance implications of varying the slitting ratio of a simple multi-winglet configuration. In addition to the aerodynamic characteristics, the implications of the wing structural mass will be also considered. First, a quality parameter has to be identified that jointly takes effects of both disciplines into account.

A multitude of figures of merit have been used in studies regarding the efficiency of non-planar wing configurations. The number of different figures particularly increased if it was intended to reflect the efficiency from a multi-disciplinary point of view. While particular figures of merit such as the increment in lift to drag ratio divided by the wing root bending moment $\Delta(L/D) / \Delta M_{b,root}$ may have been sufficient for the respective study

purposes in reference [65], they are not generally applicability. Löbert [12] probably progressed furthest in this respect as he amalgamated induced drag, wing structural mass and the wetted surface area as a substitute for profile drag into one parameter, termed "effective induced drag". Löbert's approach for wing structural mass estimation is more convincing than the root bending moment correlation, because it was not only based on spanwise integration of the bending moments due to the actual loading but it also simultaneously regarded the effect of local wing thickness on structural sizing. It is because different authors used different figures of merit that makes it difficult to mutually compare findings. This however, would be of great interest given the often contradictory conclusions of studies pursuing similar objectives.

If ever possible some difficulties with interpretation of results might be prevented if figures of merit of general scope are used. A common quality indicator used for aircraft assessment in the conceptual design phase are airline direct operating costs DOC (as for example used in [69]). DOC can be broken down into cash operating costs COC on the one side and capital costs for the purchase of the aircraft on the other. Of the two main elements the COC proportion dominates the life cycle costs of civil aircraft. Fuel costs in turn account for a significant part of the COC, which is particularly true for general aviation aircraft. Moreover, it is often difficult to assess the development and production costs of a candidate design innovation that would effect the capital costs. Hence, it is frequently preferred to reduce the uncertainty in trade-offs between alternative technologies by consideration of COC only.

For the following conception it is assumed that the maximum take-off mass of an aircraft design concept is fixed at a specified value. This assumption is not unreasonable given the fact that the maximum take-off weights of general aviation aircraft are frequently limited by regulations (e. g. increasing certification requirements depending on design weights in steps of 5000 lb, 12,500 lb and 19,000 lb in CS-23 [135]). If it is possible to reduce drag by some artifice on the one side but increase structure mass on the other while holding the all-up mass constant, the fuel required for a given mission and also the fuel costs may sink but the payload capacity may reduce at the same time. Therefore, a reasonable measure of efficiency that is suitable for a fundamental technology assessment should relate the payload capacity to the fuel consumption for a given mission defined in terms of distance or time.

The following computations are hence performed for

1. maximum range and
2. maximum endurance conditions.

Flight strategies with constant angle of attack (respectively constant wing lift coefficient) and speed (true airspeed) are assumed for computations of integrated performance figures for both conditions. Because of the requirement that the lift has to compensate

the weight, the lift demand continuously decreases with decreasing aircraft weight due to the fuel consumption. The only way to practically satisfy all these constraints is to adopt a cruise-climb strategy. The agreement onto a specific scenario - a general aviation scenario in the present case - is a necessity for a meaningful interpretation of the parametric study results and encompasses an agreement on

- Unit Reynolds number
- typical mass fractions for the calibration of the wing mass model
- typical mass fractions for aircraft parts that are not affected by the computation such as fuselage, landing gear, engine and tail
- "power producing" engines.

5.3.1.1 Maximum Range Condition

The Breguet range equation

$$dR = -\frac{\eta_{prop} \cdot L/D}{psfc \cdot g_0 \cdot m} dm \quad (77)$$

implies that the lift to drag ratio must be maximised to achieve maximum range for constant power specific fuel consumption and a constant propulsive efficiency (in the present study $\eta_{prop} = 0.9$), which are acceptable approximations for propeller aircraft in the climb or cruise flight phases. In other words the aircraft ought to operate at the minimum drag condition. The power specific fuel consumption can be computed from the engine thermodynamic and mechanic efficiencies as well as the lower heating value of the fuel used

$$psfc = \frac{1}{\eta_{th} \cdot \eta_{mech} \cdot LHV} \quad (78)$$

where, in the present study, $\eta_{th} \cdot \eta_{mech} = 0.25$ and $LHV = 4.27 \cdot 10^7$ J/kg.

Integration of equation (77) under the condition that η_{prop} , L/D and $psfc$ are constants yields range as a function of start to end mass ratio of a flight segment

$$R = \frac{\eta_{prop} \cdot L/D}{psfc \cdot g_0} \ln \left(\frac{m_{to}}{m_{ldg}} \right) \quad (79)$$

Rearranging eq. (79) and using the basic mass balance $m_f = m_{to} - m_{ldg}$ yields the corresponding fuel fraction with respect to the take-off mass

$$\frac{m_f}{m_{to}} = 1 - \frac{1}{e^{\left(\frac{psfc \cdot g_0 \cdot R}{\eta_{prop} \cdot L/D} \right)}} \quad (80)$$

Because of the assumption of a single aerodynamic operating point, the whole flight is supposed to be conducted in a single segment.

The aircraft mass is broken down into four fractions for the present purpose. The payload fraction is

$$\left(\frac{m_{pl}}{m_{to}}\right) = 1 - \left(\frac{m_{fix}}{m_{to}}\right) - \left(\frac{m_w}{m_{to}}\right) - \left(\frac{m_f}{m_{to}}\right) \quad (81)$$

where $(m_{fix}/m_{to}) = 0.45$ - fixed mass items
 (m_w/m_{to}) - wing mass fraction
 (m_{pl}/m_{to}) - payload mass fraction.

The wing mass fractions of single engine propeller driven general aviation aircraft certified according to CS-23 [135] airworthiness requirements constitute about 10% of the maximum take-off mass (Tab. 25).

Tab. 25: Mass break down of single engine propeller driven aircraft [116].

Aircraft type	Wing structural concept		Wing group m_w^* (only structure)	Remaining structure, powerplant, systems m_{fix}	Fuel m_f^{**}	Payload m_{pl}^{**}	Totals m_{to}
Cessna 172 Skyhawk	Strut-braced	Mass [kg]	102.5	484.0	114.3	318.4	1019.2
		Mass fraction (%)	10.1	47.5	11.2	31.2	100.0
Cessna 210J Centurion	Canti-lever	Mass [kg]	152.0	739.4	174.3	476.5	1542.2
		Mass fraction (%)	9.9	47.9	11.3	30.9	100.0

* Without wing-fuselage carry-through spars

** Typical values

Maximum structural loads of the wing are likely to be defined by the design gust condition. However, the current sizing is based on a maximum manoeuvre load factor $n_{lim} = +4.4$ that produces an ultimate load factor of 6.6. The results of the present study are always related to a basic rectangular wing configuration designed to the same load scenario. No matter what design load scenario, the impact on the final result will cancel out at least to first order of accuracy such that the simplified computation seems acceptable. However, using the manoeuvre load condition only will yield a very low wing mass. Non-optimum effects particularly influence the design of small aircraft and give way for the actual wing mass being often far from ideal figures [101]. Two mass models accounting for scale effects, secondary wing structure and non-optimum masses will be

used both required to provide realistic overall mass figures. In the first model (mass model 1), the primary wing mass is just scaled up to a realistic figure by means of a factor. However, a more realistic differentiation of scale effects, non-optimum and secondary mass items is provided by the second model (mass model 2).

Tab. 26: Parameter settings of two wing mass models based on different scaling concepts.

	Mass Model 1	Mass Model 2
k_{prim}	2.231	1.042
$(m_{\text{w, scale}}/m_{\text{to}})$	0.0 %	0.50 %
$(m_{\text{w, sec}}/m_{\text{to}})$	0.0 %	3.28 %

The factors for non-optimum wing primary structure mass k_{prim} have been calibrated to the abovementioned wing mass fraction of 10.1% of the take-off mass for the Cessna 172. This aircraft model was selected as a reference because it is equipped with a NACA 2412 wing section, which has the same thickness distribution as the symmetrical NACA 0012 airfoil used for the current calibration. Because the numerical model assumes a cantilever wing concept it is important to mention that the actual mass of the Cessna 172 wing, which is a strut braced wing, is not much different to that of comparable aircraft with cantilever wings such as that of the Cessna 210J, for example (compare Tab. 25). The mass fraction is thus just taken as a representative figure.

The low value for the maximum strength of the material $\sigma_{\text{max}} = 2.0 \cdot 10^8 \text{ N/m}^2$ as well as the factor k_{prim} being far greater than zero for model 1 as well as model 2 (see Tab. 26) indicates that the sizing of the Cessna 172 wing is conservative even if it would have been designed as a cantilever wing. The factors for scale effects and secondary structure mass of model 2 have been estimated by means of the data given by Howe [93] and are used henceforth. The dimensional values for $m_{\text{w, scale}}$ and $m_{\text{w, sec}}$ are constants throughout the parametric study because of the constant maximum take-off mass.

The figure of merit mentioned at the outset of the present section is found after rearranging eq. (81)

$$\left(\frac{m_f}{m_{pl}}\right) = \frac{1}{1 - \left(\frac{m_{fix}}{m_{to}}\right) - \left(\frac{m_w}{m_{to}}\right) - 1} \quad (82)$$

$$\left(\frac{m_f}{m_{to}}\right)$$

The aerodynamic calculation is performed at a single operating point. Implications of adopting a cruise climb technique on performance (variation of energy height) in order to hold the wing lift coefficient at its initial optimal or near-optimal value are neglected. Further premises for the time being are:

- geometry of outer rectangular wing: $S = 13.5 \text{ m}^2$, $AR = 6$
- no wing twist, camber or incidence
- profile drag independent of lift
- lift equals weight $L = W$
- $W_{to} = 9.807 \cdot 10^3 \text{ N}$, i.e. wing loading W_{to}/S with respect to chord line surface area is constant
- cos-distribution of lattices in the spanwise direction
- three winglets having the same spans (measured along local curvilinear y-coordinates), dihedral angles $\Upsilon = +20^\circ/0^\circ/-20^\circ$ (dihedrals descending in streamwise direction)
- constant Reynolds number based on the chord of the main inner wing $Re_{c,\text{main}} = 5.135 \cdot 10^6$
- ISA conditions
- performance computations start at sea level.

Furthermore, the drag area for aircraft parts other than the wing has been set equal to the initial wing profile drag of the basic rectangular wing which serves as reference. This assumption is reasonable for aerodynamically well designed configurations that are perhaps equipped with a retractable undercarriage. The sum of both drag contributions is set equal to the lift dependent induced drag. Under the assumption of a parabolic drag polar, the lift to drag ratio becomes a maximum for this condition.

A setting that is specific to the maximum range task is a freestream velocity of $Q_\infty = 50 \text{ m/s}$. Fig. 68 shows perspective views of selected configurations.

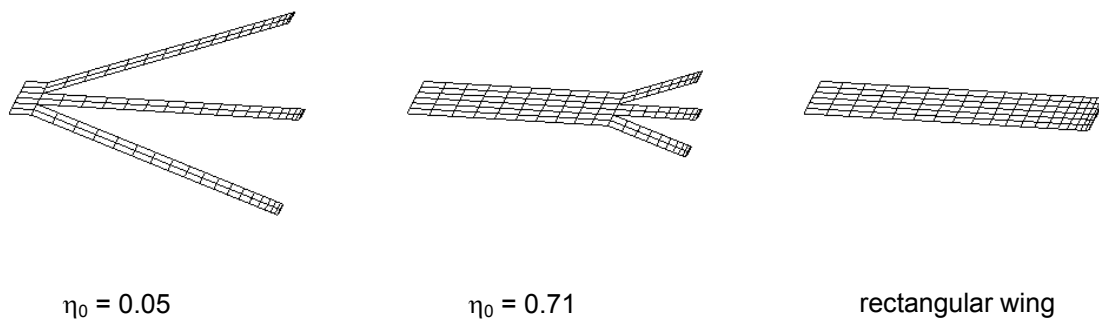


Fig. 68: Fully fanned, intermediate and rectangular wing configurations of different slitting ratios (wings are symmetric, sketch shows right hand sides of wings only from a rear and elevated position).

While the results of the slitting ratio variation are presented in Fig. 69, the reference values for the rectangular wing are listed in Tab. 27.

Tab. 27: Reference values for rectangular wing ($\eta_0 = 1$), additional information in parentheses. The numbers refer to subplots of Fig. 69 (row index / column index).

1/1 - Induced drag $D_i = 251.8 \text{ N}$, $\tau = 0.9782$	1/2 -/-
2/1 - Wing profile drag $D_{\text{prof}} = 125.9 \text{ N}$	2/2 -/-
3/1 - Lift to drag ratio $L/D = 19.45$	3/2 -/-
4/1 -/- ($c_L = 0.4739$)	4/2 - Fuel per payload unit R = 1500 km: $(m_f / m_{pl}) = 0.2033 (= 1.355 \text{ kg} / (\text{Pax} \cdot 100 \text{ km}))$ R = 3000 km: $(m_f / m_{pl}) = 0.4835 (= 1.612 \text{ kg} / (\text{Pax} \cdot 100 \text{ km}))$

As the winglets are fanned out, the induced drag decreases. It is interesting to see that the curve has an s-shape. Starting with the rectangular wing, the initial decrement is smaller than at $\eta_0 = 0.75$ where the gradient is steepest.

Two profile drag settings have been used. First, the profile drag was computed using a boundary layer transition location of 30% on both the upper and the lower surfaces, which is a realistic value for a conventional NACA 4-digit airfoil section. Wing profile drag increases by 24.7% for $\eta_0 = 0.05$ compared to the rectangular wing. Second, the profile drag coefficient has been kept constant at the level found for the rectangular wing. The influence of the smaller Reynolds numbers at the winglets is thus disregarded. The constant profile drag condition is considered because it will ease the theoretical treatment of systematic errors later on.

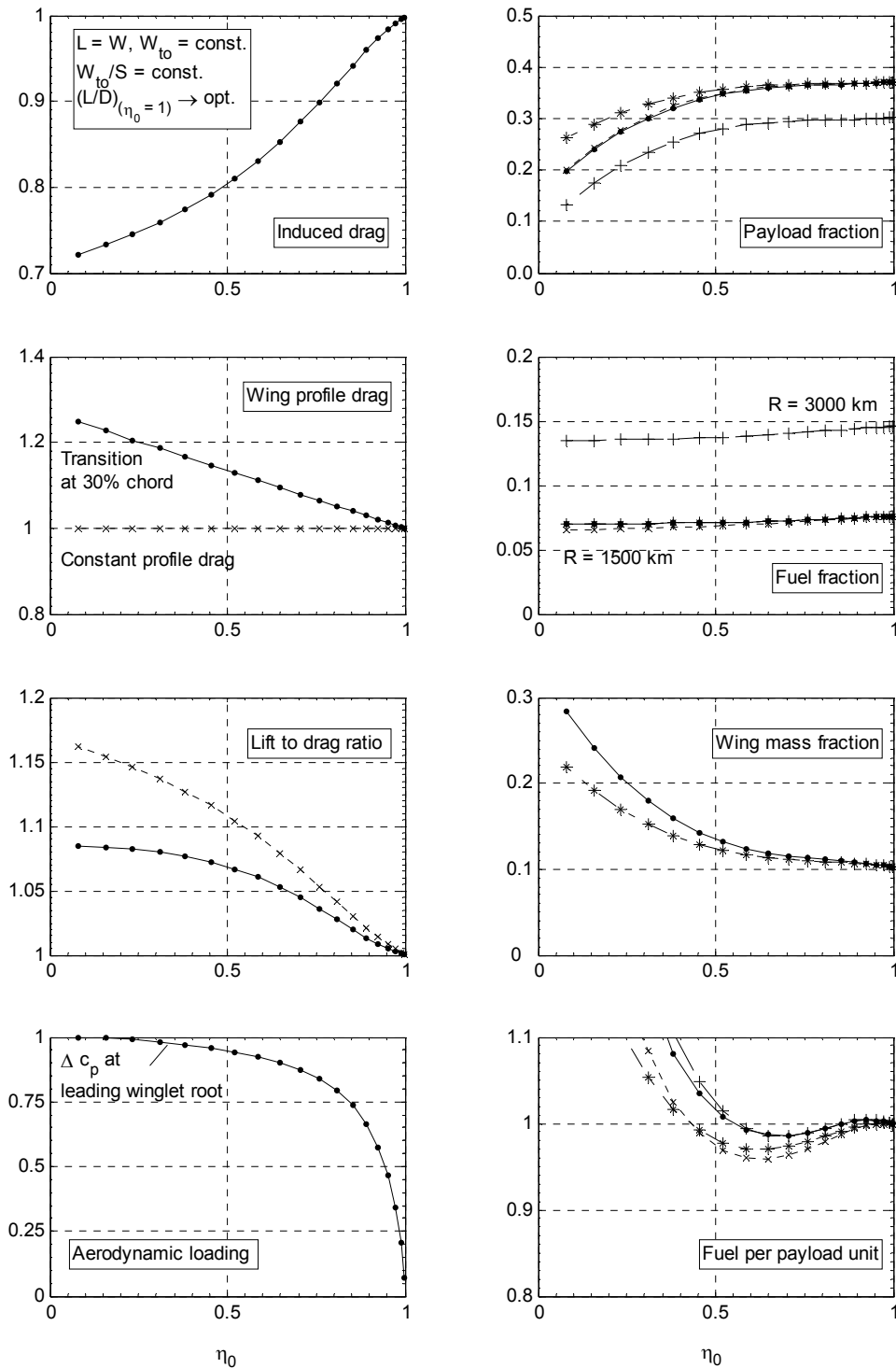


Fig. 69: Effect of slitting ratio on range (all values with reference to rect. wing ($\eta_0 = 1$) except mass fractions and aerodynamic loading). Legend (reference cond. and differences):

- Ref. condition: $(x_t/c)_{u,l} = 30\%$, scaled primary structure mass (mod. 1), $R = 1500 \text{ km}$
- x Constant profile drag
- * Wing mass with constant contributions for secondary structure (mass model 2)
- + $R = 3000 \text{ km}$

The maximum lift to drag ratio improvement for constant profile drag is about twice the gain obtained with Reynolds number influence. Again, the initial improvements are smaller at $\eta_0 = 1.0$ than at stations about three quarters of the total semi-span. The curve with fixed transition location flattens out for small slitting ratios because the induced drag improvements become successively smaller while the profile drag continues to rise linearly.

The local loading at the leading winglet root crosses the mean loading already at $\eta_0 = 0.94$ where the winglets are still small and reaches a value of approximately 1.0 at the innermost slitting station, which is approximately twice the mean loading.

On the right hand side stacked upon each other are the wing mass (3/2), above the fuel (2/2) and, topmost, the payload fractions (1/2). The wing mass also exhibits an s-shaped development with decreasing slitting ratio. The initial gradient is steeper than at $\eta_0 = 0.8$. The wing mass steeply increases not before passing a value of 0.6 coming from larger values. Fuel fractions decrease because the only non-constant influence is the lift to drag ratio. The payload fraction for the reference condition is only slightly decreasing down to $\eta_0 \approx 0.6$ when it starts to drop because of the wing mass build up.

All this culminates in the mission fuel per payload plot in the lower right hand corner of Fig. 69 (4/2). The maximum gain in payload specific fuel consumption for the reference condition is 1.47% at $\eta_0 = 0.71$. Improved fuel efficiency is only to be expected for slitting ratios between 0.56 and 0.85. For very small winglets, the penalties are larger than the advantages, rendering these configurations inferior compared to the slitting ratio range stated above as well as the rectangular wing.

Constant profile drag would yield a maximum enhancement of 4.15%. This explicitly shows that the performance of a multi-winglet configuration is particularly sensitive to profile drag increments.

Fig. 69 also compares the wing mass development for the scaling based on the primary wing box structure mass (mass model 1, reference condition) and that obtained with mass model 2 allowing for different scaling principles regarding primary and secondary wing structure mass fractions. Since the secondary wing structure mass is a constant, the mass increase due to larger winglets is less than that for the simple scaling of the primary mass only.

Increasing the range requirement from 1500 to 3000 km and thus increasing the fuel fraction makes almost no difference compared to the reference condition. On the one hand, the absolute fuel savings become greater, but on the other hand, the influence of the wing mass build-up on the payload fraction is more severe.

5.3.1.2 Systematic Errors in Parametric Study for Maximum Range Condition

The drag characteristics of lifting surfaces where the incidences of all local sections become zero at the zero lift condition can be modelled by a second order parabola, eq. (14).

Higher order terms come into play for configurations with geometric and/or aerodynamic washout such that the drag polar is no longer a quadratic parabola. However, terms that comprise other powers of the lift coefficient than two are usually small enough that the quadratic approximation is an acceptable model. It is its mathematical simplicity that lends the parabolic drag polar to tackle performance problems analytically. The optimum lift to drag condition that allows maximising the range of an aircraft equipped with engines where the fuel consumption is proportional to power has already been introduced in chapters 2.2.1 and 5.2.4. From eq. (14), the lift at the maximum range condition can be derived, which is

$$L_{\text{opt}} = \sqrt{\pi \cdot b^2 \cdot \tau \cdot q \cdot D_0} \quad (83)$$

If altitude and speed are constants, the dynamic pressure q as well as the zero lift drag D_0 (reference surface S is also invariant) also become constants and the optimum lift is only dependent on the span b and the span efficiency τ . The square root must be a constant in order to guarantee that different configurations that produce the same lift are at their best points. This prerequisite can hardly be assured in practice. Improving the span efficiency would require to either reduce span or to reduce zero lift drag.

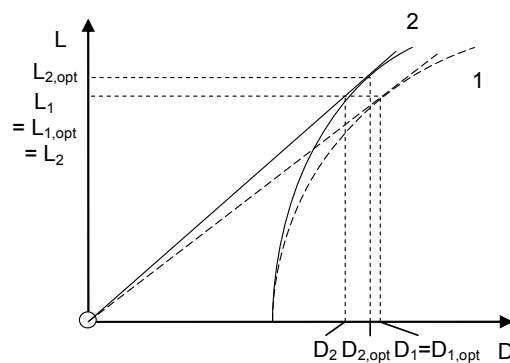


Fig. 70: Change of optimum lift to drag ratio condition if span efficiency is changed (schematic sketch).

The following discussion is confined to the example where zero lift drag as well as span and dynamic pressure are constants and only span efficiency τ is altered (corresponding to curves with x-symbols in Fig. 69). Hence, the departure from the optimum condition set for the rectangular wing is inevitable. Fig. 70 illustrates the

departure from the originally optimum situation of configuration 1 to the improved but non-optimum configuration 2. It will be attempted to estimate the systematic error associated with the constraints set. An equation has been derived based on the parabolic drag polar eq. (14) and on the condition that the sectional zero lift drag coefficient is a constant.

$$\frac{(L/D)_2 - (L/D)_{2,opt}}{(L/D)_{2,opt}} = \frac{\Delta(L/D)_2}{(L/D)_{2,opt}} = \frac{2x}{x^2 + 1} - 1$$

where $x = \frac{1}{\left(1 + \frac{\Delta b}{b_1}\right) \cdot \left(1 + \frac{\Delta q}{q_1}\right) \cdot \sqrt{\left(1 + \frac{\Delta \tau}{\tau_1}\right)} \cdot \sqrt{\frac{(c_D S)_{misc}}{c_{d,0} \cdot S_1} + \left(1 + \frac{\Delta S}{S_1}\right)}$ (84)

and $(c_D S)_{misc}$ - drag area of miscellaneous aircraft parts

The equation relates the difference in lift to drag ratio between optimum and current conditions of the altered configuration 2 to the magnitude of deviation of independent parameters from the reference condition 1, which, by definition, must also be a local optimum. The drag area for other aircraft parts except the wing is assumed to be a constant and the ratio $(c_D \cdot S)_{misc} / (c_{d,0} \cdot S_1)$ is presently 1.0 because the denominator is also a constant.

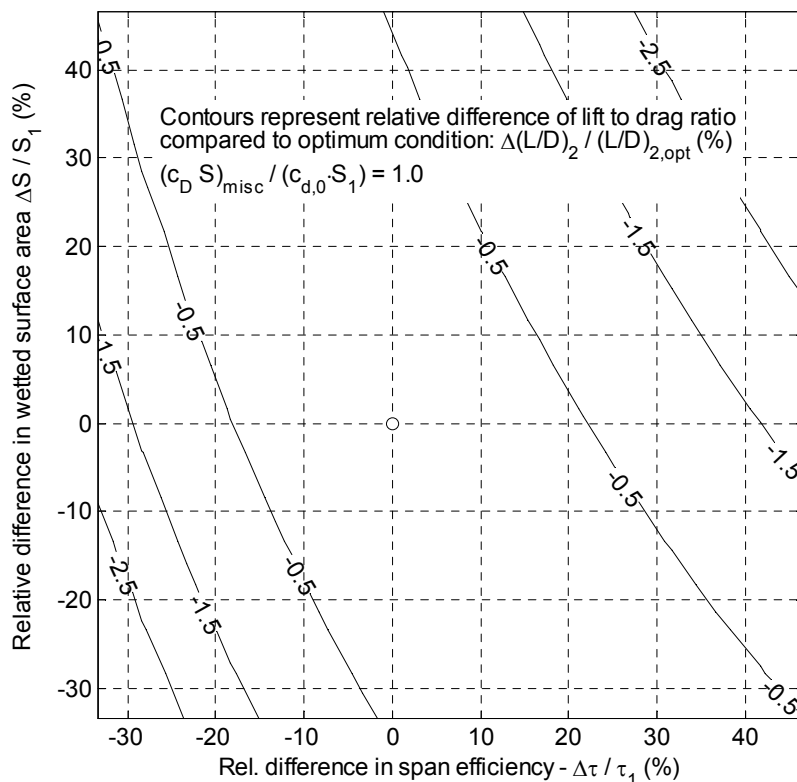


Fig. 71: Relative deviations from optimum lift to drag ratio.

Fig. 71 shows the relative deviations from the optimum lift to drag ratio if the parameters surface area and span efficiency are altered due to configuration changes while the other influence parameters remain at datum values. The best fuel efficiency for constant profile drag was obtained at $\eta_0 = 0.65$ (Fig. 69) where the induced drag ratio was 0.84 and the gain in lift to drag ratio was 11% with respect to the rectangular wing. The span efficiency ratio is the reciprocal value of the induced drag ratio such that $\Delta\tau / \tau_1 = 19\%$. Eq. (84) or Fig. 71 reveals that the lift to drag ratio is 0.4% lower than the optimum value due to the fixed lift and fixed reference area conditions compared to a situation where the lift would have been adapted appropriately.

Optimum conditions for the changed configuration could be established by lowering the dynamic pressure. This could either be achieved by lowering the air density i.e. increasing flight altitude or alternatively by lowering the flight speed. Both measures do not affect the range performance of a propeller aircraft. However, the measure would require to increase the lift coefficient. The improved lift to drag ratio converts into a fuel saving of 0.4% if the equation for the fuel fraction is linearised on the ground of a small perturbation treatment. For fixed lift (not lift coefficient) the payload fraction increases accordingly and the error from considering a non-optimum point amounts to a factor of $0.996/1.004 = 0.992$. The payload specific fuel consumption for optimum lift to drag conditions would be 0.8% lower, i. e. the improvement in specific fuel consumption would not only be 1.47 but 2.27%.

As a conclusion it can be put on record that the present parametric study becomes the more conservative the more the winglets are fanned out because of increasing deviations from optimum conditions in the design space.

5.3.1.3 Maximum Endurance Condition

Winglets as a means of reducing induced drag are most effective at high lift conditions. The infinitesimal time for level flight per infinitesimal reduction of aircraft mass due to the consumed fuel of a propeller aircraft is

$$dT = -\frac{\eta_{\text{prop}} \cdot L/D}{\text{psfc} \cdot Q_{\infty} \cdot g_0 \cdot m} dm \quad (85)$$

The only difference to the Breguet range equation (77) is the flight speed Q_{∞} as an additional parameter in the denominator. The best specific endurance dT/dm is obtained if the ratio $(L/D)/Q_{\infty}$ is maximised. The optimum must be obviously at a lower flight speed than that for maximum range. The operating point for maximum endurance of an aircraft with power-producing engines is frequently referred to as the minimum power condition. Introducing aerodynamic coefficients and integrating eq. (85) assuming that angle of attack (or equivalently c_L) and the flight speed (true airspeed) are constants yields

$$T = \frac{\eta_{\text{prop}}}{\text{psfc} \cdot g_0} \cdot \sqrt{\frac{S}{2} \cdot \left(\frac{\rho}{m}\right)} \cdot \frac{c_L^{3/2}}{c_D} \cdot \ln\left(\frac{m_{\text{to}}}{m_{\text{ldg}}}\right) \quad (86)$$

Contained in equation (86) is the endurance parameter $c_L^{3/2} / c_D$. The ratio (ρ/m) is a constant, which is actually set to $(\rho_{0,\text{ISA}}/m_{\text{to}})$. Configurations can only be mutually compared in terms of the endurance parameter if the expressions $(0.5 \rho S / m)^{0.5}$ are identical. This can be achieved, for example, by stipulating that reference surface areas, take-off masses and initial altitudes (air density) are all the same.

The classical performance optima derived from eqs. (79) and (86) are used to establish the appropriate speed offset of the maximum endurance condition from the maximum range condition $Q_{\infty,\text{opt},T} = Q_{\infty,\text{opt},R} / 3^{1/4}$. The kinematic viscosity was adjusted in order to keep the Reynolds number at the same level as used for the maximum range study. Reynolds number effects are hence confined to the varying slitting ratios only. The fuel fraction equation for endurance is

$$\frac{m_f}{m_{\text{to}}} = 1 - \frac{1}{e^{\left(\frac{\text{psfc} \cdot Q_{\infty} \cdot g_0 \cdot T}{\eta_{\text{prop}} \cdot L/D}\right)}} \quad (87)$$

Equating the fuel fraction equations (80) and (87) allows the computation of the endurance T that requires the same fuel as needed for flying a distance R at the maximum range condition. For the basic rectangular wing and the settings used for studying range performance a corresponding maximum endurance of $T \approx 9.5$ h is found for $R = 1500$ km and $T \approx 19.0$ h for $R = 3000$ km, accordingly.

Results for maximum endurance are presented in Fig. 72 in the same fashion as already shown in Fig. 69 for maximum range. Tab. 28 presents reference values for the rectangular wing. The ratio of the optimum lift to drag ratios is $(L/D)_{\text{opt},T} / (L/D)_{\text{opt},R} = 16.70 / 19.45 = 0.859$, which is only 0.9% less than the theoretical value of $(3/4)^{1/2} \approx 0.867$. It is worth mentioning that the absolute profile drag is smaller due to the lower flying speed while the absolute induced drag increased compared to the maximum range operating point.

Tab. 28: Reference values for rectangular wing configuration ($\eta_0 = 1$) at the maximum endurance condition, additional information in parentheses (row/column as in Fig. 72).

1/1 - Induced drag $D_i = 441.3 \text{ N}$, $\tau = 0.9667$	1/2 -/-
2/1 - Wing profile drag $D_{\text{prof}} = 72.7 \text{ N}$	2/2 -/-
3/1 - Lift to drag ratio, endurance parameter $L/D = 16.70$, $c_L^{3/2} / c_D = 15.13$	3/2 -/-
4/1 -/- ($c_L = 0.8209$)	4/2 - Fuel per payload unit $T = 9.5 \text{ h}$: (m_f / m_{pl}) = 0.2060 (= 2.168 kg / (Pax · h)) $T = 19 \text{ h}$: (m_f / m_{pl}) = 0.4900 (= 2.579 kg / (Pax · h))

The curves of relative induced drag (1/1) and profile drag (2/1) (which have been made dimensionless by dividing by the values for the rectangular wing) are identical to the corresponding figures for maximum range. Relative gains in lift to drag ratio which are identical to the gains in endurance parameter excel those found for the maximum range condition (3/1). The influences of profile drag and hence implicitly also of the Reynolds number are much smaller for the same reason.

The aerodynamic loading at the leading winglet root is merely linearly scaled up compared to the maximum range condition (4/1).

The wing mass fraction is identical to the maximum range condition since the aerodynamic design loads are identical (3/2).

The impact of the reduced induced drag for the fanned configuration has a profound effect on the fuel fraction (2/2).

Shown in the lower right hand corner is the mission average fuel consumption per payload and time (4/2) relative to the rectangular wing. The optimum slitting ratio for the reference configuration $\eta_{0,\text{opt},T} = 0.60$ is inboard of the corresponding location for maximum range $\eta_{0,\text{opt},R} = 0.71$. The endurance gain of 7.86% is significantly larger than the gain of 1.47% in range. Again, the performance would benefit if the profile drag could be kept constant although the difference to the reference condition is much less than it was for the maximum range study. Contrarily, the relative performance improvement for the lighter wing structure design is as great as for the maximum range condition. It was originally surmised that the fanned configurations would benefit from longer range requirements because of the greater fuel fractions. While this speculation had to be rejected for the maximum range condition, it is true for the maximum endurance condition. Inspection of Fig. 72 renders the fanned configuration with the high endurance requirement superior to the short endurance requirement.

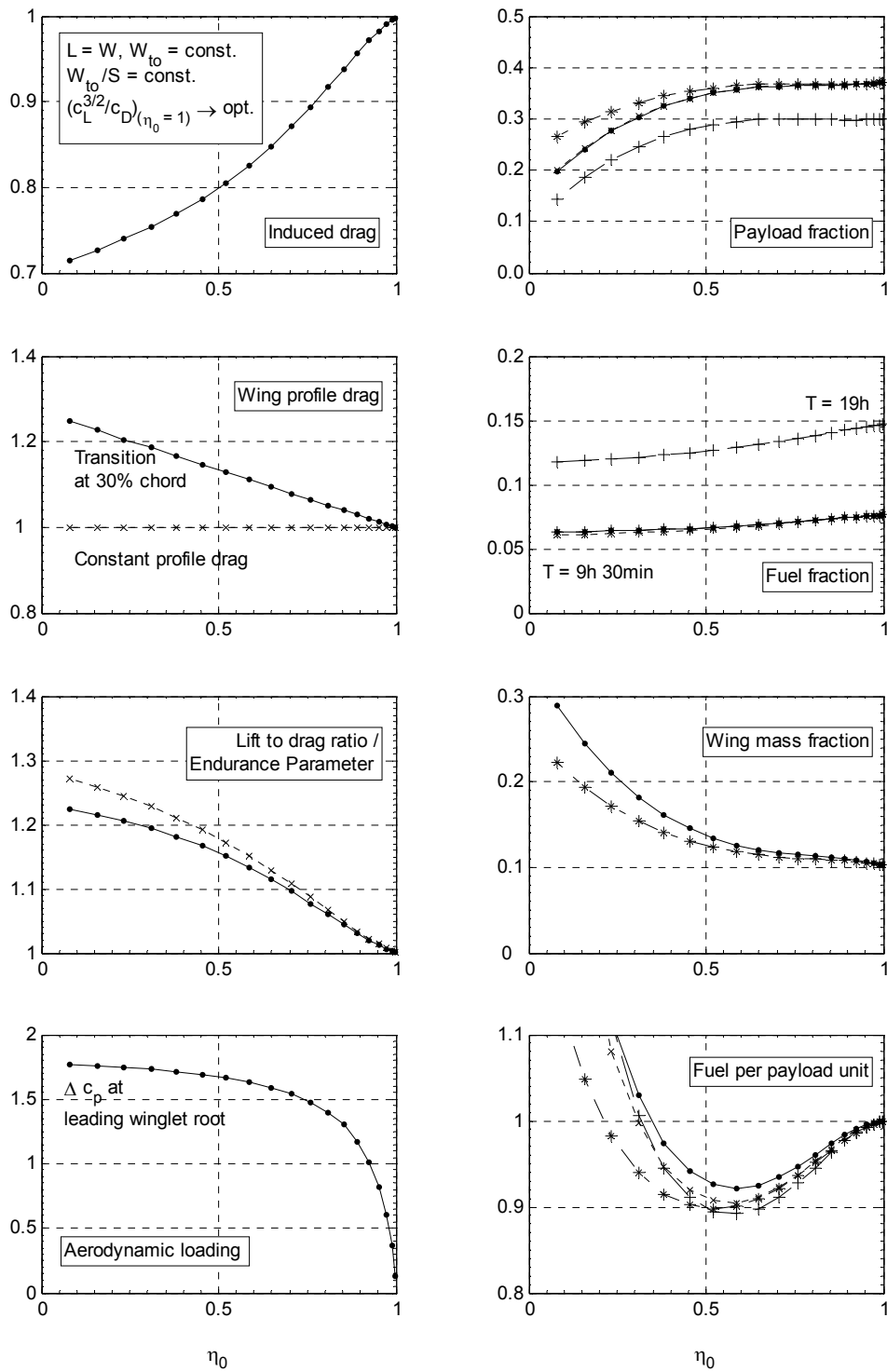


Fig. 72: Effect of slitting ratio on endurance (all values with reference to rect. wing ($\eta_0 = 1$) except mass fract. and aerod. loading). Legend (reference cond. and differences):

- Ref. condition: $(x_t/c)_{u,l} = 30\%$, scaled prim. struct. mass (model 1), $T = 9\text{ h } 30\text{ min}$
- x Constant profile drag
- * Wing mass with constant contributions for secondary structure (mass model 2)
- + $T = 19\text{ h}$

5.3.2 Incorporation of Refined Aerodynamic Models

This section will show to what extent the incorporation of higher order aerodynamic effects is going to change the findings obtained with the simple model discussed in chapter 5.3.1. In a first step

- lift dependent profile and
- interference drag contributions are added.

In a second step additional allowance is made for

- cascade effects that influence lift dependent profile drag.

Both conditions for maximum range and for maximum endurance are considered. Since the lift dependent profile drag is usually only a small fraction of the overall drag, no attempt has been made to adapt the operating point of the reference rectangular wing configuration such as to make it an optimal point. Instead, the same starting points as in chapter 5.3.1 are used. The drag area of other aircraft parts except the wing remains at its original value. The rectangular wing as well as the multi-winglet configurations thus operate in conditions that are slightly off-design.

Tab. 29 shows the maximum and minimum section lift coefficients for the NACA 0012 airfoil section required for the lift dependent profile drag computation.

Tab. 29: NACA 0012 maximum and minimum section lift coefficients of main wing and winglets (data taken from reference [100]).

	$Re_c \times 10^{-6}$	$C_{l,max} = -C_{l,min}$
Main wing	5.135	1.57
Winglet	1.712	1.50

The factor $k_{int,det,fillet}$ has been set to 0.25 which assumes the presence of corner fillets or other appropriate means to guarantee a smooth and aerodynamically favourable blending of the main wing - winglet intersections.

Cascade effects are computed with the optimisation mode algorithm. Instead of computing adapted local maximum and minimum lift coefficients, the correlation of lift dependent profile drag with the velocity ratios Q_{max}/Q_{te} is exploited in this mode. The critical velocity ratios $(Q_{max}/Q_{te})_{crit}$ for the upper and lower sides indicating attainment of maximum or minimum lift conditions are derived from a sectional analysis and the maximum loadability data of Tab. 29.

Results are depicted in Fig. 73 where the left hand side subplots show the data for the maximum range while the right hand side subplots show the data for the maximum endurance condition. The drag increases due to the additional drag contributions while the lift is constant. Hence, lift to drag ratio and endurance parameters decrease while the fuel quantity required per payload and distance or time increases.

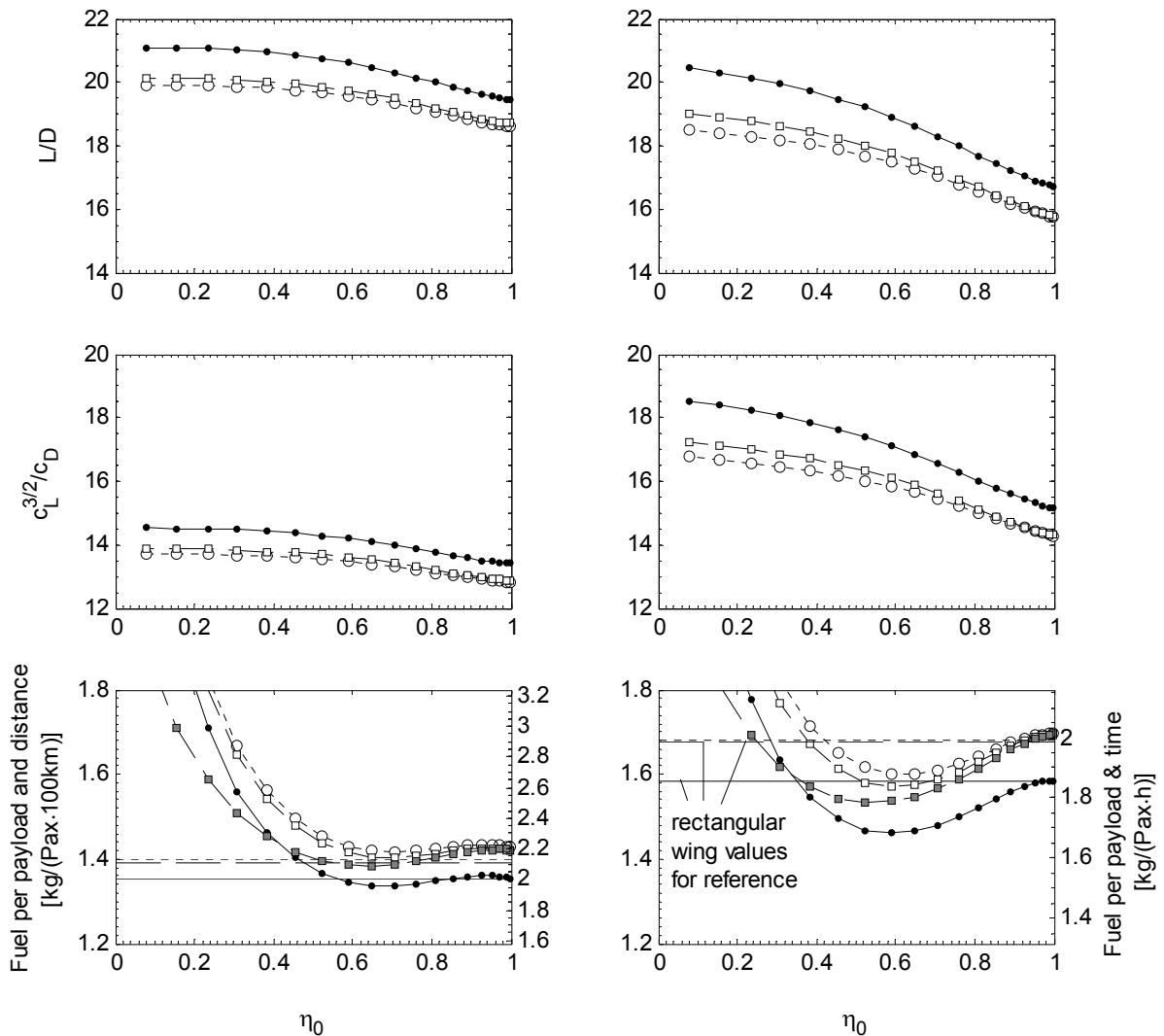


Fig. 73: Effect of slitting ratio on range (left hand side, $c_L = 0.4739$) and endurance (right hand side, $c_L = 0.8209$). Legend (reference condition and differences):

- Ref. condition: Mean boundary layer transition at 30% chord, scaled primary structure mass (mass model 1), R = 1500 km (left), T = 9 h 30 min (right)
- + lift dependent profile drag, + interference drag
- + lift dependent profile drag, + interference drag, + cascade effects
- + lift dep. prof. drag, + interf. drag, + casc. effects, constant contributions for secondary wing structure mass (mass model 2)

The horizontal lines in the fuel consumption axes indicate the corresponding values for the rectangular wing for reference. The step increment of fuel required per payload when changing from the rectangular wing to the wing with smallest winglets is caused by the interference drag model. However, the basic trend does not change compared to the reference condition and computations in the preceding chapter.

The fuel consumption for maximum endurance also increases due to higher drag but leaves a maximum advantage for the model with lift dependent profile and interference drag of 4.75%. The figures are more favourable if the cascade model is utilised where the fuel efficiency of the best winglet configuration is 6.31% better than that of the rectangular wing. This improvement is only little less than the 7.86% predicted with the simple reference model in chapter 5.3.1.3. Again, performance figures obtained from computations with mass model 2 are better.

The lift to drag and endurance parameter plots show that the drag penalty due to higher local aerodynamic loading and the lift dependent profile drag model grows as the slitting ratio becomes smaller. The drag increase is not so serious because of the high loadability of the profile section at present Reynolds numbers. Incorporating cascade effects yields a smaller drag penalty especially at the maximum endurance condition.

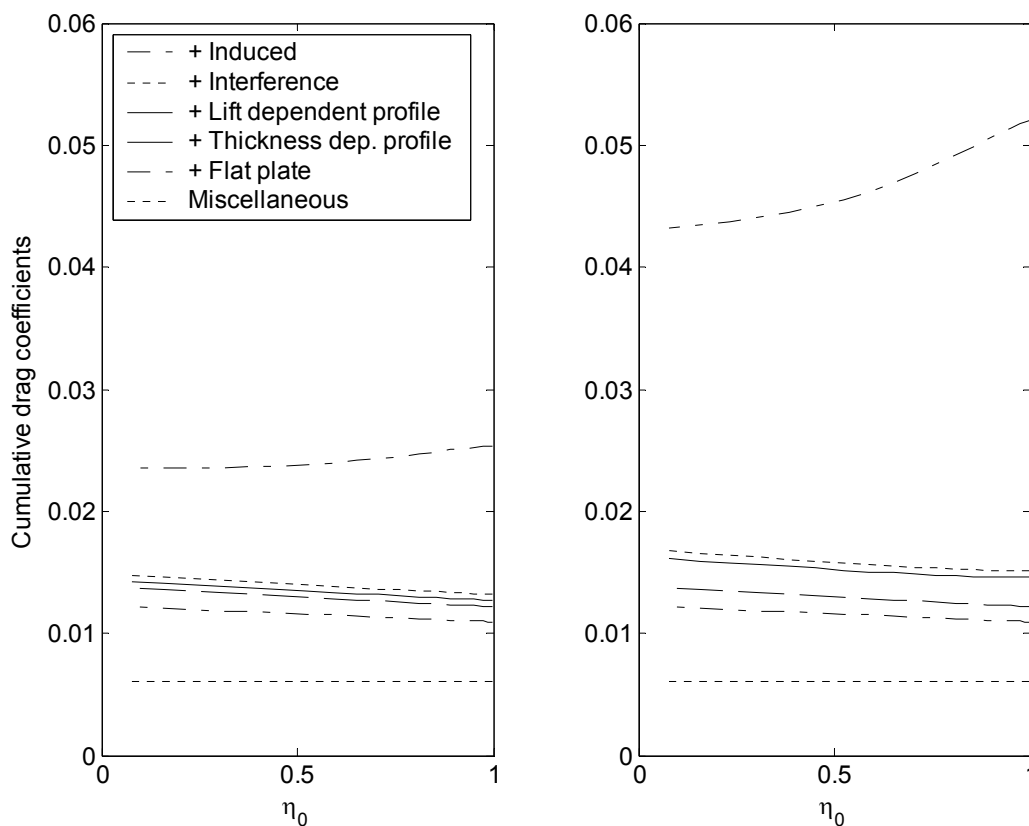


Fig. 74: Effect of slitting ratio on drag build-up; model with cascade effects. Left: Maximum range condition. Right: Maximum endurance condition.

Fig. 74 illustrates the drag build-up. Induced drag is always the largest drag component. The lift dependent profile drag contribution is relatively small for the maximum range condition on the left hand side, just a fourth of that for the maximum endurance condition. Interference contributes about 2% to the overall drag. The interference drag increases with decreasing slitting ratio and aerodynamic loading but the dependency is only moderate.

Fig. 75 compares computations that made use of the sectional loadability limits as listed in Tab. 29 on the one hand, and the adapted figures by means of the cascade model on the other. A value of $k_{cl,max} = 1.0$ indicates that the section has already attained the condition of maximum aerodynamic loading in terms of the sectional maximum lift coefficient. Similarly $k_{cl,max} = 1.0$ indicates the maximum lift condition of the wing. The latter figure is calculated by a spanwise integration of the sectional values weighted by the areas of the corresponding spanwise strips.

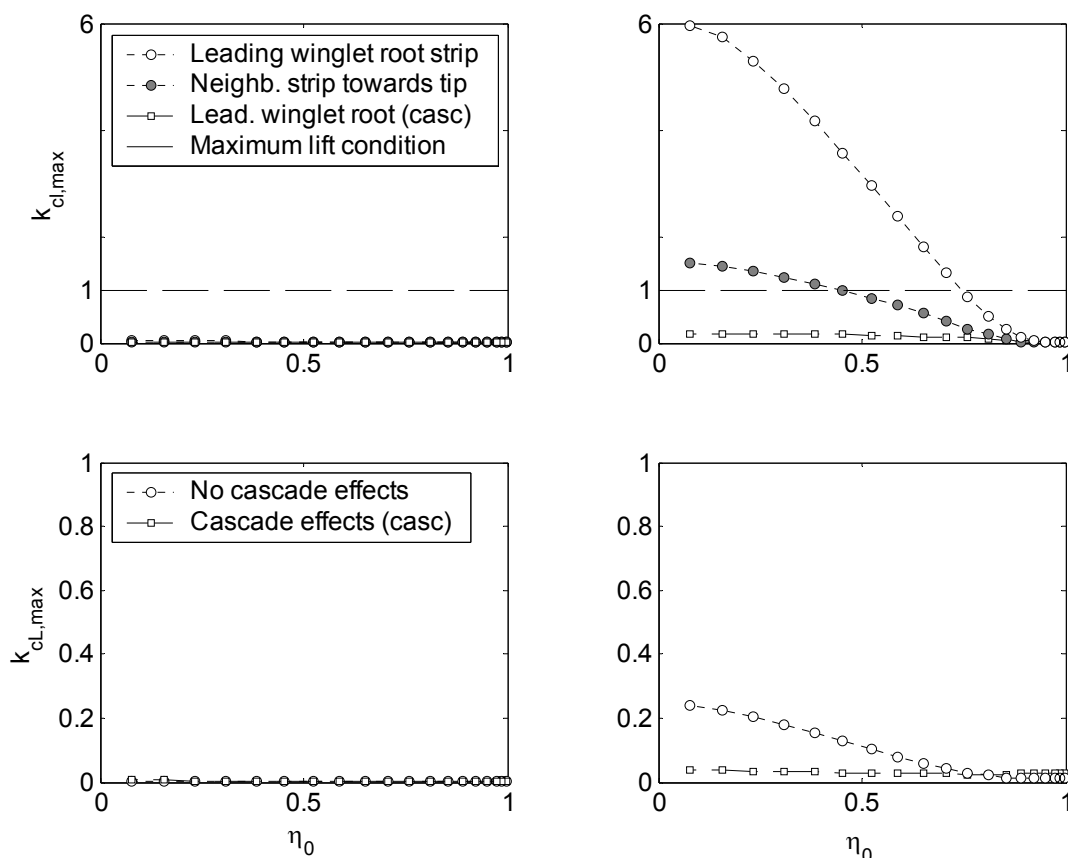


Fig. 75: Effect of slitting ratio on maximum lift parameters ($a_{cl,max} = 10$). Left: Maximum range condition. Right: Maximum endurance condition.

The lift coefficient of the leading winglet root is greater than the upper bound (compare Fig. 72) for slitting ratios less than 0.75 considering the maximum endurance case

without regarding cascade effects (upper right axes in Fig. 75). The line with the filled bullets is the load parameter of the neighbouring chordwise strip towards the winglet tip which illustrates the rapid decay of the loading away from the junction of the winglet with the main wing. The wing has a still-positive lift curve slope at the maximum endurance condition even with partly separated flow. This is indicated by the global wing load parameter being less than unity. Nevertheless, flow separation would increase drag as has been shown in Fig. 73.

Considering cascade effects, computations predict that the root section will actually fall below the maximum lift condition. Any risk of reaching loadability limits is not visible for the maximum range condition irrespective of the model used.

5.3.3 Consideration of Aeroelastic Effects on Wing Sizing

The structural model of VLM++ allows computing the static aeroelastic bending and torsion of the wing. So far the wing has been regarded as a rigid body according to the specified geometrical parameters. The wing mass builds up as the slitting ratio of the multi-winglet wing is reduced and the winglets are increasingly fanned out. Several factors can be identified that bring about the need to increase wing strength by adding material and thus mass among the two most straightforward items are:

1. increase of effective cantilever ratio by an outward movement of the wing half center of pressure
2. reduction of the ability to resist bending due to decreased wing thickness and thus smaller area moments of inertia.

Both effects can be clearly identified from the results of the present parametric study. The lift is set to a constant value but the aerodynamic load per unit span changes such that the centre of pressure of a wing half moves slightly outwards to the wing tip. However, taking a rectangular wing as an example, it will be observed that the structural sizing does only change little if the span load would be adjusted as to resemble the spanload of the multi-winglet wing. The adjustment could be performed by geometric twist ("washin" in order to increase the tip loading). The fact that the impact of the spanload distribution on the wing structural sizing is small is commonly acknowledged (refer e.g. to [119]). For that reason, the mass increase of multi-winglet configurations due to reducing slitting ratios η_0 is almost only due to the decreasing wing box area moments of inertia.

At the same time the wing stiffness reduces and bending deflection as well as torsional twist increase. Putting torsion aside for the moment, it can easily be imagined that the lift effective wing area reduces if an uncambered and untwisted wing that is originally planar bends upwards under aerodynamic loads. The lift effective area shall be defined

as the projection of the wing surface onto the body x-y-plane. The angle of attack and hence the root loading must increase in order to produce a specified amount of lift at a given dynamic pressure. The local load reduces in the extreme case of the wing local curvilinear y-coordinate pointing in the z-direction of the body-fixed reference coordinate system, which is possible at stations close to the wing tip.

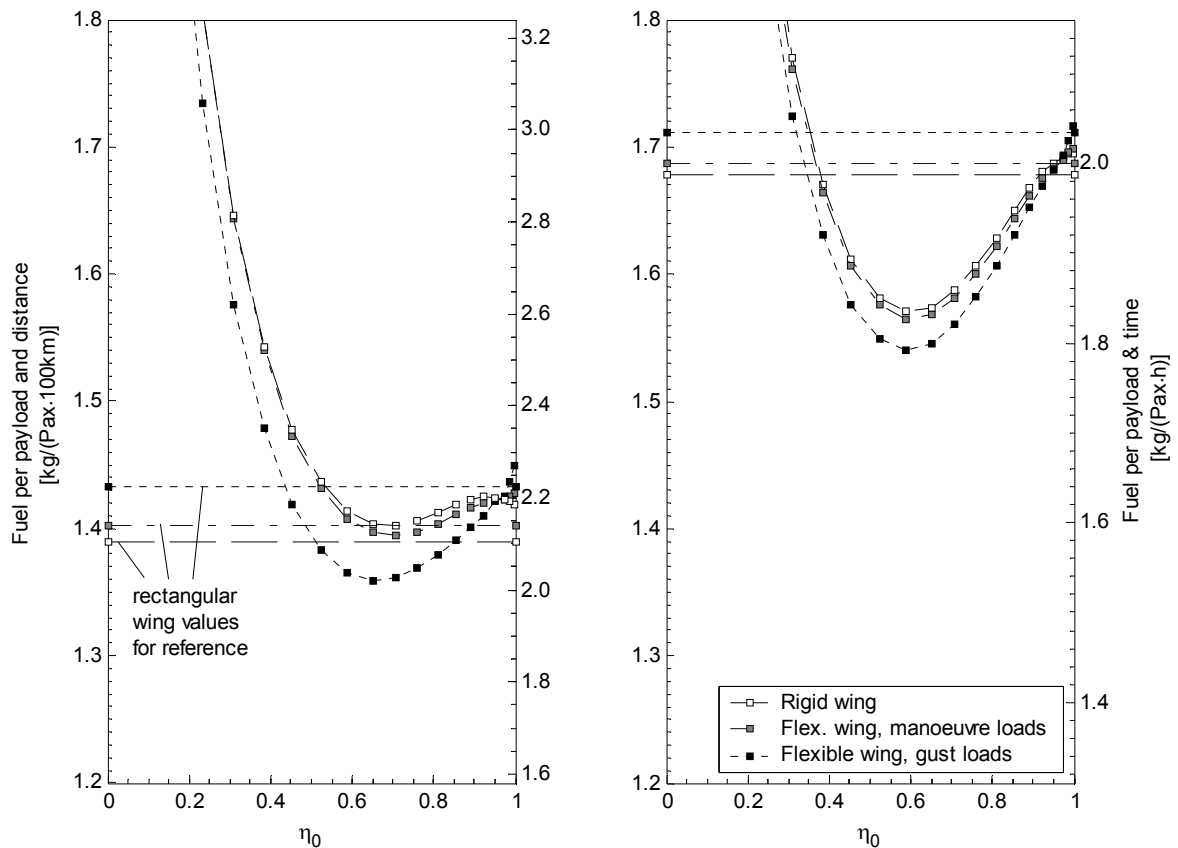


Fig. 76: Effect of slitting ratio and design load szenario on payload specific fuel consumption. Scaling of the vertical axis is adapted to fuel per payload and distance. Left: Maximum range condition. Right: Maximum endurance condition.

The effective wing span decreases due to bending while the normal load coefficients at inboard stations increase. The structural loads in terms of local bending moments decrease. This leads to the conclusion that the wing structural sizing based on a rigid structure can be conservative, at least to the extent that the limited scope of the current treatment allows to reason.

It is important to define the geometric properties of the wing boxes properly. The front spar is located at 15% chord and the rear spar at 35% chord. For unswept wings where the spanwise centres of pressure all appear at the quarter chord line this arrangement yields zero torsional moments and thus no aeroelastic twist. Beside, locating the front

spar at 15 percent chord allows a reasonable height of the shear webs for a NACA 0012 airfoil section and thus a close to optimum geometrical moment of inertia about the local wing box x-axes.

Fig. 76 compares the fuel consumption per payload unit of wings that are structurally designed to different criteria:

1. The data as well as the format of the line for the rigid wing has been taken from Fig. 73.
2. The square symbols with grey faces connected by a dash dot line illustrate the effect of sizing the wing regarding its deflection under ultimate manoeuvre loads. It is possible that the ultimate load factor could be maintained in a steady manoeuvre condition. Thus the angle of attack is adapted such as to exactly match the desired load: $L = L_{req}$.
3. The solid square symbols stand for the gust load case. For the computation a simplified model has been used. Instead of assessing the ultimate loads according to the procedure suggested in aircraft certification requirements (e.g. CS-23 [135]), the ultimate manoeuvre loads are assessed in the following fashion: First, considering the rigid wing, the ultimate load can be produced by an increase of angle of attack if the loads are not limited by the maximum lift coefficient. Confining the discussion to aircraft, this increase can either be produced by an input of the pilot via the longitudinal control effector or by a vertical gust assuming constant dynamic pressure. Now if the wing is flexible, it could be that the lift curve slope changes due to aeroelastic effects. If a manoeuvre is flown with fixed load factor, the pilot adjusts the control effector to compensate for the change in lift curve slope. This is not the case in a vertical gust situation. Hence, the gust loads are likely to be smaller than the manoeuvre loads compared to the rigid wing case.

Fig. 76 shows that the fuel consumption of the configuration that is structurally designed to the manoeuvre case under consideration of the aeroelastic deflection differs only little from the rigid wing result. The difference between the rigid wing and that one sized to the gust load condition is much greater. The gain in fuel efficiency per distance flown due to changing from a rectangular wing to a multi-winglet configuration is greater for a wing that is designed to gust loads than for the same wing being sized according to manoeuvre loads.

Close to a slitting ratio of $\eta_0 = 1$ the performance of the gust driven design becomes inferior to the wing designed to manoeuvre loads. This behaviour can be explained by

considering the torsional deformation of the wings. Plotted in Fig. 77 a) are the local centres of pressures. Due to the use of symmetrical sections, the locations do not vary with angle of attack (or lift coefficient). Moving outwards from the wing centre section the centres of pressure shift little but monotonically upstream. The positive loads of the outer sections exert a positive moment about the local wing box y-axes (which is also the elastic axis and also the quarter chord line for the current settings) due to the lever between the centres of pressure and the shear centre. This increases the geometrical angle of attack of the outer wing by about 1.00 deg at the maximum load factor of 4.4 with only a marginal difference between the two sizing conditions.

The lift curve slope is not anymore a function of the geometry only, but becomes also a function of lift. The slope starts with that of the rigid body at $\alpha = 0$ deg and increases progressively as the lift and thus the torsion increases. As discussed above, the compliance with the lift requirement allows adapting the angle of attack and compensating for the aeroelastic additional incidence if the manoeuvre load case is considered. The angle of attack is not adapted in the case of the gust load condition and hence the loads are greater which in turn produces a higher wing structure mass.

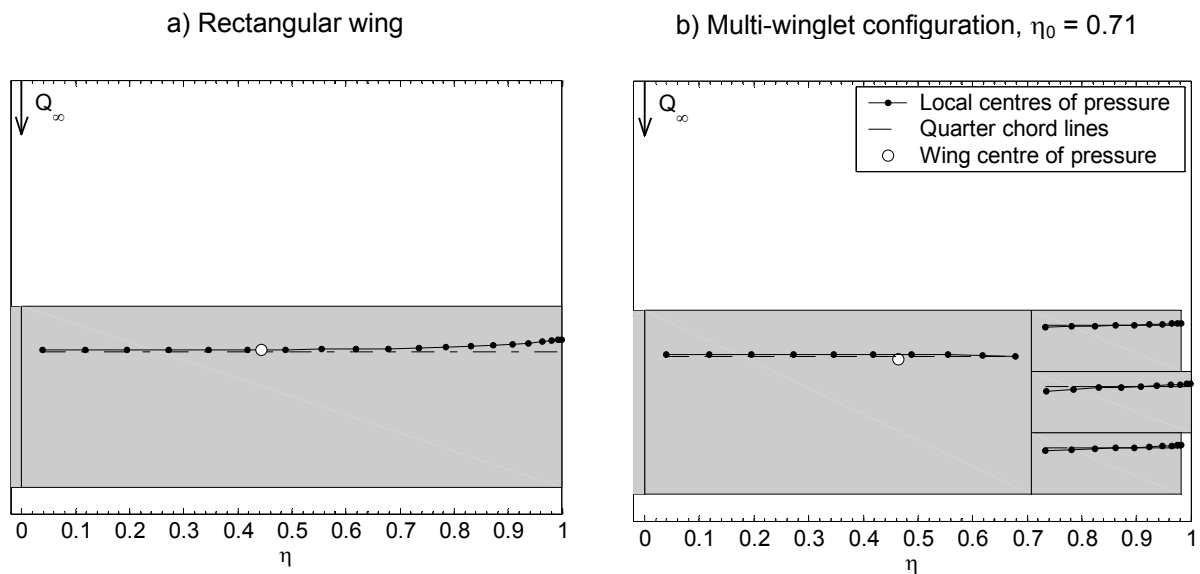


Fig. 77: Centres of pressure for rectangular wing and mutli-winglet configuration (only right hand side of wing are displayed of otherwise symmetrical configurations).

Slitting the wing as to produce a vertically fanned configuration yields higher aerodynamic loads on the trailing winglet compared to the trailing edge region of the rectangular wing. The common local spanwise centre of pressure as computed for all three winglets tends to move back towards to the trailing edge, although this is not explicitly shown in Fig. 77 b). Nevertheless, the effect is obvious because of the backward shift of the semi-span centre of pressure. The winglet cascade thus transmits a negative torsional load into the outer wingbox of the main wing which produces a

washout of -0.78 deg. This time the aeroelastic deformation of the wing produces a load alleviating effect under gust loads and hence would result in a lighter wing structural sizing.

Generally the effects described above can be reduced by

- moving the wing box towards the leading edge in order to locate the shear centre ahead of the centres of pressure
- using positively cambered surfaces that move the centres of pressure to the rear of the section
- increased wing stiffness by designing it to a higher than required ultimate load coefficient, thus changing from a strengths driven to a stiffness driven sizing concept.

It is worth mentioning that merely changing the design ultimate load factor will not make any difference with respect to the effect of aeroelastic torsion at least as regards first order influences. Doubling the ultimate load factor will double the required material thickness for a given wing layout. For a given wing box cross section, the polar moment of inertia is a linear function of the wall thickness and hence the wing tip deflection due to bending and washout due to aeroelastic torsion would be identical to the values of the wing designed to the lower loads.

The aft-shift of the centres of pressure has a positive, though small influence on the divergence velocity for wings where this aeroelastic phenomenon may be a design consideration. Although a quantitative analysis is beyond the scope of the present work, it must be recognized that reducing the stiffness of a wing, which is inevitable for multi-winglet configurations designed to strength requirements may have a detrimental effect on other aeroelastic characteristics such as flutter.

5.3.4 Discussion of Effects Attributable to Sizing and Model Assumptions

Lowering the slitting ratio has the consequence of decreasing induced drag but also of increasing structural mass figures of the wing. Because the initial induced drag reductions are more significant than the mass penalties, both effects result in a distinct minimum with respect to the payload specific fuel consumption both for maximum range and maximum endurance operating points. Profile drag increases with decreasing slitting ratio. The detrimental influence of profile drag on lift to drag ratio respectively endurance parameter is much more significant for the maximum range than it is for the maximum endurance operating point.

It was found that the gain in payload specific fuel consumption is relatively small as far as range performance is considered. Improvements of up to 1.47% in range (refer to

Tab. 30) could be achieved for slitting ratios between 56% and 85% compared to a rectangular wing under reference conditions defined in chapter 5.3.1.1.

Net effects are much greater for the maximum endurance condition. The gain in fuel efficiency sums up to 7.86% for the reference parameter setting (refer also to summary in Tab. 30). The range of slitting ratios that allow longer endurance is comparatively large spanning from 34% to 100%.

Refinement of the aerodynamic model comprised the incorporation of lift dependent profile drag, wing-winglet interference drag and cascade effects that may alter profile drag characteristics.

It was found that the aerodynamic load coefficients Δc_p at the leading winglet root for the maximum endurance operating point exceeds maximum sectional loadability limits without consideration of cascade effects. Basing the loadability limits on parameters that implicitly reflect the boundary layer state revealed that loadability limits most likely would have not been reached. This in turn resulted in reduced lift dependent profile drag such that detrimental interference effects associated with the wing-winglet intersection representing about 2% of the total drag were partly cancelled out by reduced lift dependent profile drag contributions. A maximum advantage of 6.31% in fuel efficiency compared to the rectangular wing was finally established for the maximum endurance condition and computation with mass model 1.

While consideration or disregard of above mentioned effects have an influence on the wing performance on the order of the net benefits due to multi-winglets for the maximum range condition, the net benefit for the maximum endurance condition is large enough to be preserved irrespective of the model settings.

The parametric study started with a rigid wing model sized according to a manoeuvre load scenario. However, the elasticity of a wing design may have a significant influence on wing sizing. It was found that multi-winglet cascades can have a positive effect on the structural sizing of gust critical designs, partly because of the greater elasticity and partly because of the backward sweep of local spanwise centres of pressure. The effect on manoeuvre critical designs can neither be qualified positive nor negative.

Tab. 30 summarises the relative impact of changing aerodynamic and mass models as well as structural design conditions on the fuel consumption of multi-winglet configurations with optimal slitting ratios compared to the basic rectangular wing values. It can be seen that the design load condition can easily have an influence on performance of the same order of magnitude as the net results obtained by considering aerodynamic effects and structure sizing according to a rigid wing model only.

Tab. 30: Relative changes of fuel consumption of multi-winglet configurations with optimal slitting ratios with respect to corresponding values of a rectangular wing.

Design designation	Aerodynamic model	Mass model	Max. range operation point	Max. endurance operation point
Reference condition	reference (chapter 5.3.1)	1	-1.47%	-7.86%
		2	-2.92%	-10.21%
Rigid wing	refined (chapter 5.3.2)	1	0.91%	-6.31%
Flexible wing, manoeuvre loads	refined (chapter 5.3.2)	1	-0.59%	-7.27%
Flexible wing, gust loads	refined (chapter 5.3.2)	1	-5.19%	-10.00%

An attempt to assess the error due to departure from the initially optimum operating conditions showed that a parametric study becomes more like comparing apples and oranges the more preconditions are set. This is exactly the opposite what was meant to be achieved by setting clear boundary conditions. However, a boundary condition which is fully acceptable in one discipline is likely to be inappropriate in another. For example, the impact of configuration changes on the profile drag and the wing structure mass are easy to track if the lift and the lift coefficient of the wing are kept constant. However, if an optimum lift to drag condition is to be maintained, there is no other way than to change the surface area which would in turn result in the need of scaling the whole wing in chord- and spanwise direction. Again, this would alter the chord based Reynolds numbers and profile drag. This example shall illustrate that boundary conditions meant to clarify the analysis and ease to keep track of what is going on, can easily lead to a misrepresentation of the problem and erroneous conclusions. The best practice from a physical point of view is thus to use design sensitive models with the least possible number of boundary conditions or constraints. It should be attempted to optimise configurations directly with regard to top level design requirements, accepting limited insight and control of individual physical effects and prediction models set up to reproduce them.

5.4 Systematic Variation of Geometry Parameters

5.4.1 Wing and Winglets with Rectangular Planform

The preceding chapter 5.3 focused on the effects of additional computational models for "higher order" effects on the performance of a multi-winglet configuration with three

winglets. The effects were illustrated by simply varying a single independent parameter, the slitting ratio.

This chapter puts emphasis on the actual configurational performance. Values of several parameters will be systematically combined and evaluated. The approach resembles the basic grid search optimisation technique if one is interested in finding particular extremal values.

The basic configuration is identical to the configuration used in chapter 5.3 except that a different panelling is used. The need for an altered discretisation is because the cos-distribution produces tip lattices with extremely small aspect ratios. Adding camber and twist to the wing results in a slight departure of the discrete trailing vortices out of the lattice planes because of the simple 5-leg vortex elements used. In the case of narrow tip lattices, the influence of the trailing vortices on the downwash at the collocation point can be larger than that of the bound vortex filaments. A vertical offset of a trailing vortex filament can produce significant sidewash and less than realistic downwash at a collocation point which can yield erroneous circulation values. Widening of the elements and restoring a reasonable lattice aspect ratio is a remedy to that problem. Hence, computations are performed with a reduced total number of 16 elements in the spanwise direction per wing half and an increased number of 9 elements in the chordwise direction.

The parameters that have been varied are:

1. slitting ratio η_0
2. winglet dihedral $\Upsilon_{wl,1}$
3. camber of the main wing tip m_t
4. winglet twist $\varepsilon_{wl,1}$

In order to reduce the number of independent parameters, the following constraints have been set on the grounds of symmetry considerations and the experience gained in chapter 5.3:

The winglet dihedral of the trailing winglet is $\Upsilon_{wl,3} = -\Upsilon_{wl,1}$ while the centrally located winglet remains at $\Upsilon_{wl,2} = 0$ deg. Similarly, the geometric washout of the winglets is set to $\varepsilon_{wl,3} = -\varepsilon_{wl,1}$ whereas $\varepsilon_{wl,2} = 0$ deg. The camber of the inner wing root is set equal to the tip value. The position of maximum camber is at 40% chord. The winglets start with some sectional camber at the root due to the constraint of a smooth attachment of lattice side edges but camber reduces to zero at the winglet tips.

The settings regarding the computational model are identical to those described in chapter 5.3.2 including cascade effects. The wing mass estimation is performed with model 2 (compare section 5.3.1.1) because it is deemed that this model is a closer

representation of practical sizing principles. Once again, the maximum range condition is compared to the maximum endurance condition.

Shown in Fig. 78 is the effect of varying the abovementioned parameters with respect to the span efficiency. The configuration without camber and twist attains the highest span efficiency value for the smallest slitting ratio 0.098 at 32 deg dihedral angle of the leading winglet. For slitting ratios around $\eta_0 = 0.9$ the span efficiency is slightly better for cambered configurations. The optimum dihedral does increase with increasing slitting ratio, a result that complies with findings of Löbert [12] and Hummel [50]. It can be observed that the most favourable values are obtained on the diagonal from the upper left hand corner to the lower right hand corner of Fig. 78. Apparently, combinations of positive camber and positive to negative twist of the winglets in the flow direction yield favourable lift distributions with respect to induced drag as already established in chapter 5.2. The dashed line in the upper left hand axes indicates the parameters of chapter 5.3 for reference. It is apparent that the dihedral setting is smaller than optimum regarding span efficiency in this case.

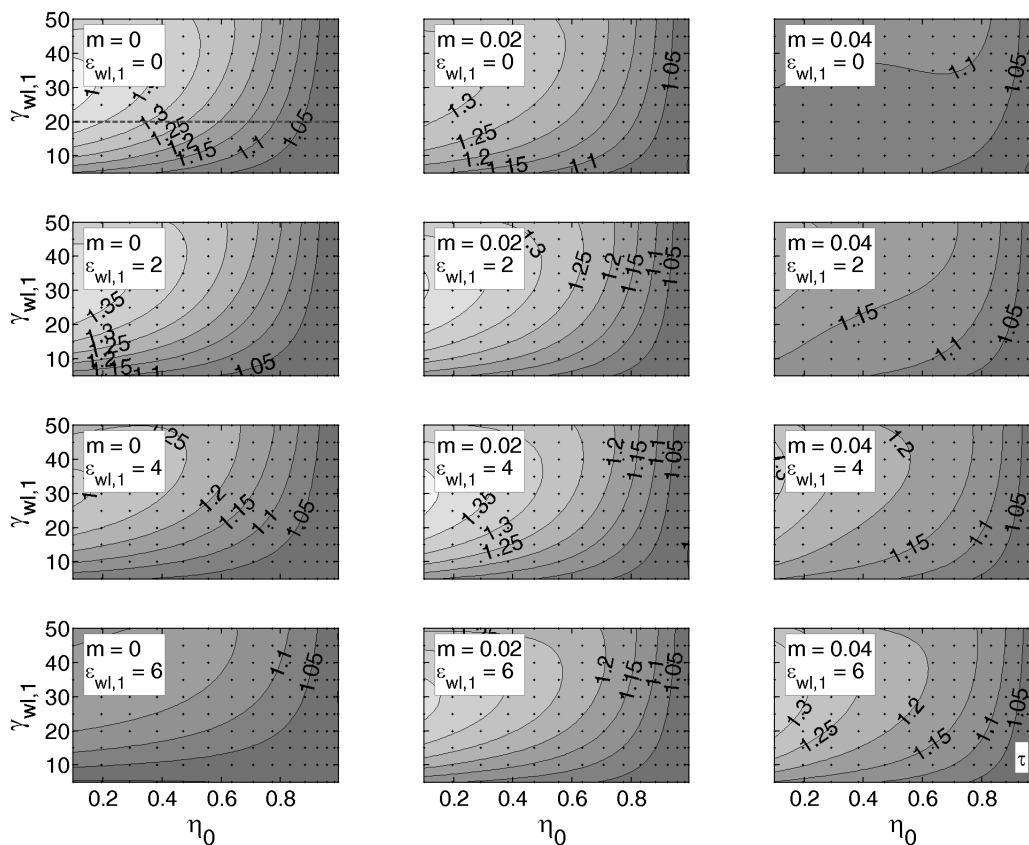


Fig. 78: Effect of varying slitting ratio η_0 , winglet dihedral $\gamma_{wl,1}$ [deg] and twist $\epsilon_{wl,1}$ [deg] as well as main wing camber m on relative span efficiency (with respect to rectangular wing value), $c_L = 0.4739$.

The results for the uncambered and untwisted configuration are virtually identical for the maximum range and the maximum endurance conditions (Fig. 79). This is to be expected since the span efficiency is independent of angle of attack for untwisted and uncambered wings. The small differences are due to the numerical discretisation, where the different trailing vortex sheet geometries are supposedly responsible for the greater part of the discrepancy. The differences between the cambered main wing surfaces are much larger for the operating conditions under consideration. The performance loss for the higher lift coefficient is much smaller compared to the uncambered surface. The camber produces a basic lift distribution which is independent of angle of attack. Adding the additional lift distribution due to angle of attack yields the total spanwise lift distribution. At the higher lift coefficient the influence of the additional lift distribution is larger and the apparently detrimental influence of the basic lift distribution is smaller.

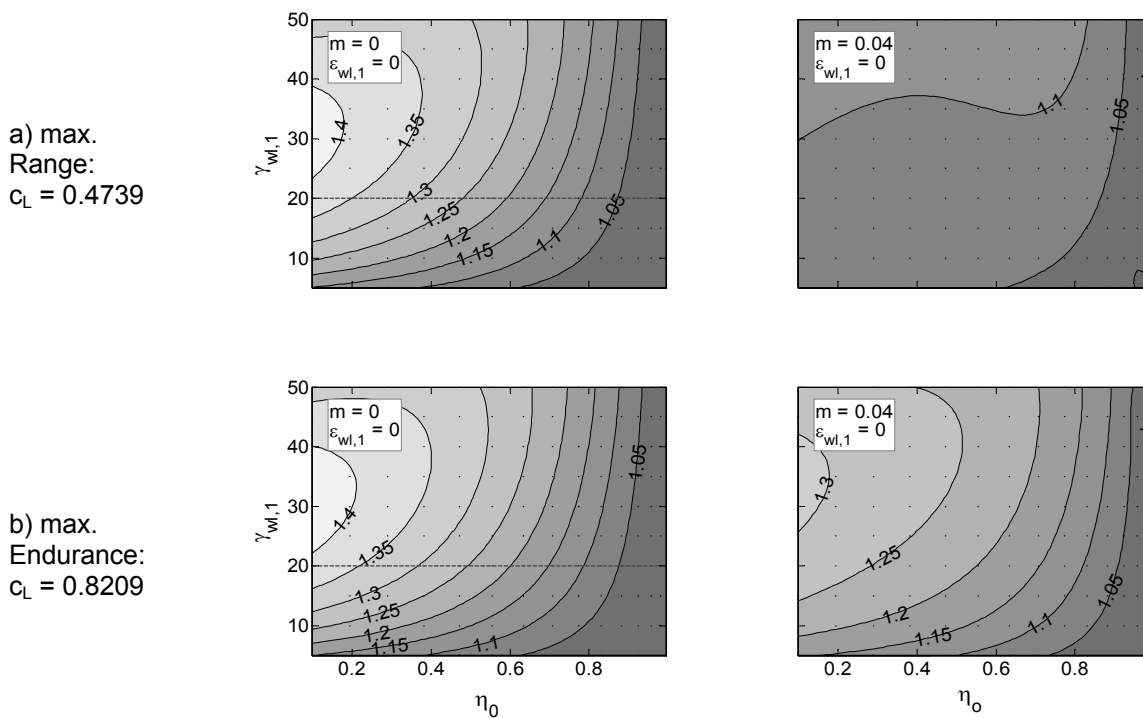


Fig. 79: Comparison of relative span efficiencies depending on parameter settings and operational conditions.

Fig. 80 shows the results for the all-up lift to drag ratio or equivalently the endurance parameter ratios, both with respect to the rectangular wing data. The best points for max. range and max. endurance operating points differ significantly.

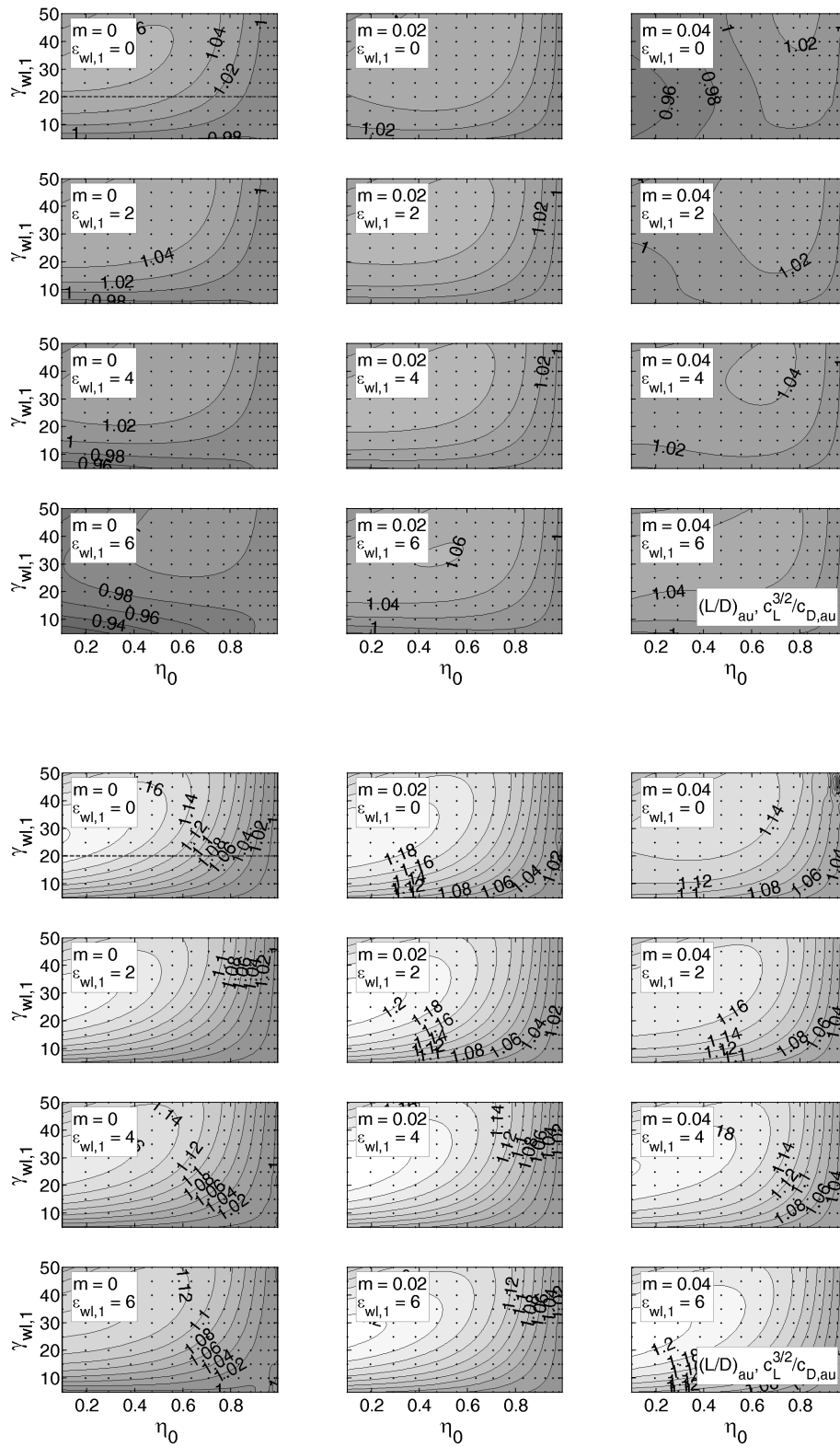


Fig. 80: Comparison of relative all-up lift to drag ratios and endurance parameters (values referred to rectangular wing reference). Upper part: Max. range, Lower part: Max. endurance.

For the first condition, there are optimum winglet dihedral angles at $30^\circ / 0^\circ / -30$ degs (leading to trailing winglets) and a slitting ratio of 0.383 for a main wing camber of 2% chord. Geometric twist angles are $+4.0 / 0.0 / -4.0$ degs. The best point for the latter condition is for smaller dihedral angles of $28 / 0 / -28$ degs, at η_0 approaching zero. The optimum is located between the subplots for 4% and 6% camber and 4 and 6 degs dihedral, respectively.

Because ultimate loads do not change for the two operating conditions considered, the differences with respect to the wing structural masses are small. Fig. 81 shows that the slitting ratio is the predominant parameter affecting wing mass. The findings from the parametric study for fixed winglet dihedrals of $20 / 0 / -20$ degs are thus equally valid for the current parametric variation. The areas to the left of the isolines are blanked out because the wing mass values are beyond the range of the grey-scale mapping.

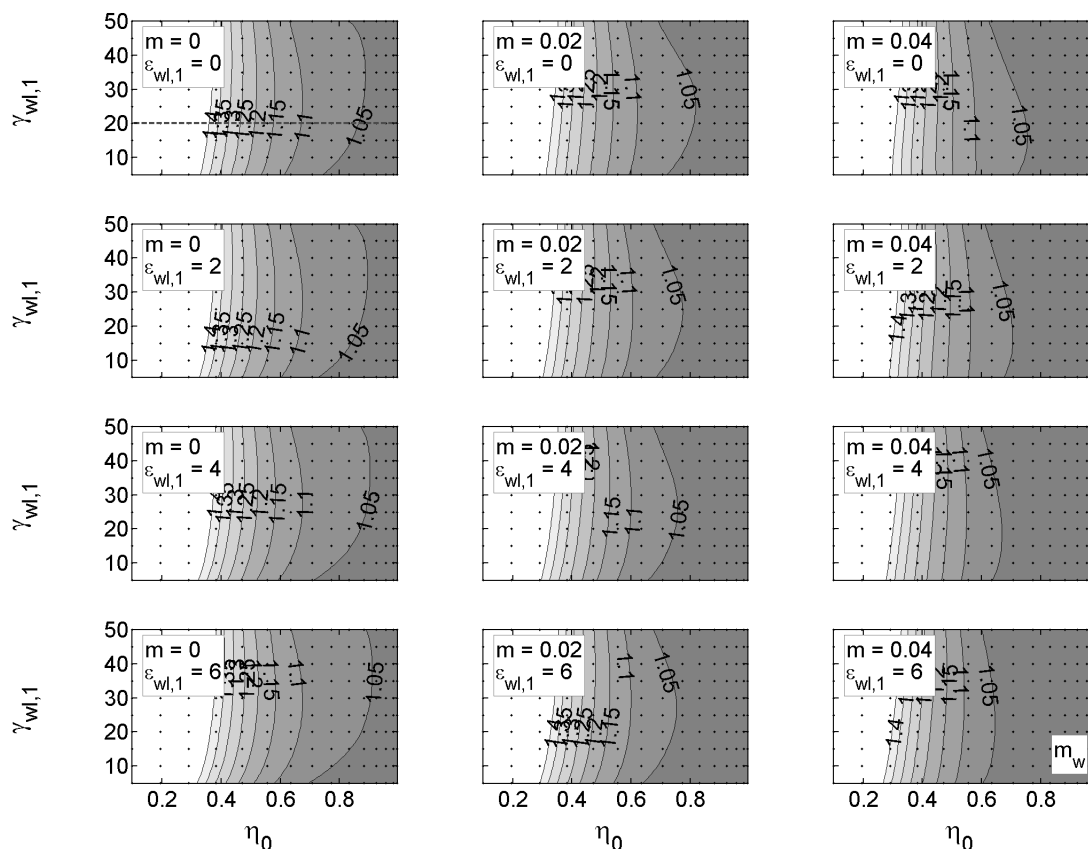


Fig. 81: Development of relative wing mass computed for the max. endurance condition.

Next, the fuel efficiency that is the product of payload and distance per fuel is depicted in Fig. 82. Note that this definition is the reciprocal value to the payload specific fuel consumption used in chapter 5.3.

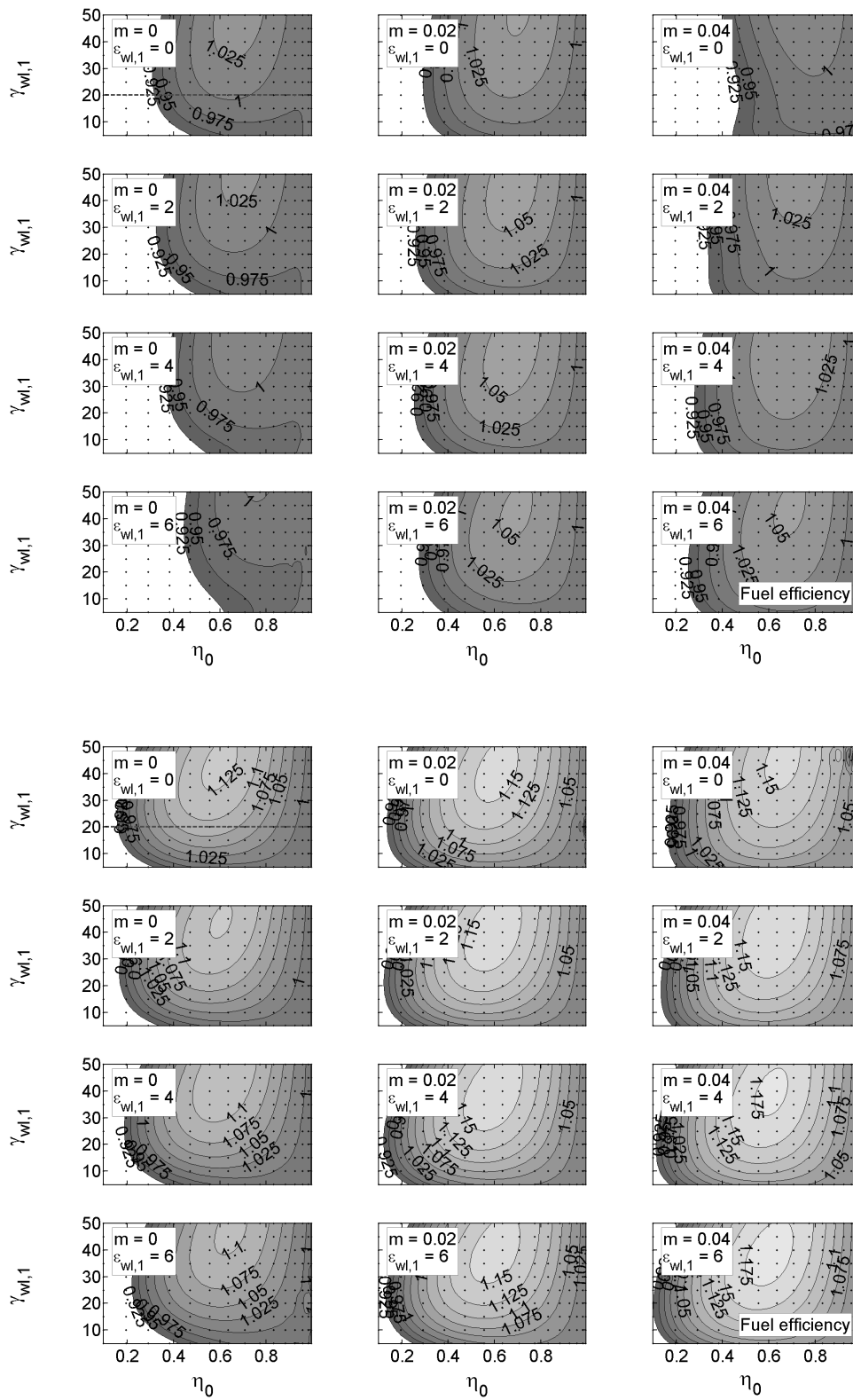


Fig. 82: Comparison of relative fuel efficiency (dependent parameter values referred to rectangular wing reference). Upper part: Max. range, Lower part: Max. endurance.

The results can be simultaneously interpreted as the product of payload and time per fuel since the dependent parameter values are expressed as ratios with respect to the rectangular wing performance. The fuel efficiency can be improved by up to 6.00% for maximum range conditions and up to 18.40% for maximum endurance compared to the planar rectangular wing according to Tab. 31, which summarises the optimum values of Fig. 80 and Fig. 82. These figures are significantly different to the best points of the initial univariate variation of the slitting ratio and show that the potential for optimisation is considerable.

It is also noticeable that the dihedral angles for the maximum endurance condition are consistently lower than those for the maximum range condition. However, the vertical extents of the configurations optimised according to the maximum endurance operation condition is larger as the parameter h/b testifies. This is because of the smaller slitting ratios, producing larger winglets. Moreover, a less fanned configuration allows better exploitation of favourable cascade interference, which is particularly important at the higher local load coefficients associated with the maximum endurance condition. The effect is, however, not excessively large because of the relatively high maximum sectional lift coefficients at chord based Reynolds numbers applicable to general aviation aircraft. The impact at lower Reynolds numbers typical for bird wings or low-cost wind-tunnel experiments such as discussed in chapter 5.2 is supposedly greater.

Tab. 31: Summary of optimal lift to drag ratios (Fig. 80) and fuel efficiency (Fig. 82) parameter combinations (values are nearest neighbours of real best points according to grid discretisation).

	Parameter	Rect. wing	Multi-winglet / Rect. wing	Υ [deg]	η_0	h/b	m	ε [deg]
max. Range	$(L/D)_{au} / C_L^{3/2} / C_{D,au}$	19.07 13.13	1.0723	30.0	0.383	0.309	0.02	4.0
	$n_{pax} \cdot m_{pax} \cdot R / m_F$ [100kg·100km/kg]	0.721	1.0600	45.0	0.707	0.207	0.02	4.0
	$n_{pax} \cdot m_{pax} \cdot T / m_F$ [100kg · h / kg]	0.400						
max. Endurance	$(L/D)_{au} / C_L^{3/2} / C_{D,au}$	16.01 14.51	1.2161	25.0	0.098	0.381	0.02	4.0
	$n_{pax} \cdot m_{pax} \cdot R / m_F$ [100kg·100km/kg]	0.600	1.1840	40.0	0.634	0.235	0.04	6.0
	$n_{pax} \cdot m_{pax} \cdot T / m_F$ [100kg · h / kg]	0.439						

Tab. 31 also shows that the maximum lift to drag respectively maximum endurance conditions occur at different parameter combinations. The difference is carried on to the fuel efficiency figures despite the fact that the strong deterioration of performance with

lessening slitting ratio and rising wing mass tends to bring optima closer together. Tab. 31 suggests that the slitting ratio, the camber of the main wing and the twist of the winglets preferably have to be adapted to the flight condition. This is consistent with findings from bird flight observations. Birds that utilise separated outer primaries not only in flapping flight spread these feathers out in soaring flight, but reduce the spread as well as wing camber in faster glides until they sweep wing tips back combined with a significant surface area reduction for high speed dives (compare Fig. 19). The outer primaries are folded away in such a way that they overlap and the gaps are closed. Wing profile drag is thus effectively reduced due to a smaller wetted area as well as larger mean Reynolds numbers.

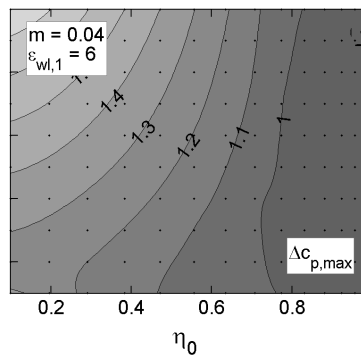
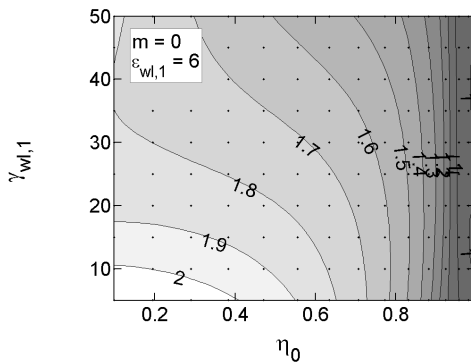
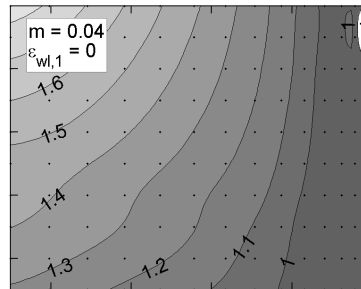
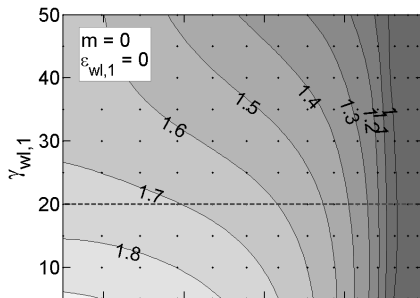
Plotted in Fig. 83 are the maximum local aerodynamic load coefficients. Dihedral provides some reductions of the maximum loading for the uncambered and untwisted wings at small slitting ratios because the effective angle of attacks are reduced. While the winglet geometrical twist has only a small influence, the positive main wing camber reduces the leading edge loads at the heavily loaded leading winglet root. The comparison shows that there is an optimum configuration, for which the level of the local loading, being referred to the maximum local loading of the rectangular wing, is smallest depending on the wing lift coefficient.

Again, this proves that flight performance of birds with slotted wing tips in fact depends on the ability to vary the wing camber. Adaptation of sectional performance is thus not only performed for adaptation of sectional characteristics but also to improve the aerodynamic load distribution of the wing.

a) max.
Range:

$$C_L = 0.4739,$$

$$\Delta C_{p,max,rect} = 0.5624$$



b) max.
Endurance:

$$C_L = 0.8209,$$

$$\Delta C_{p,max,rect} = 0.9760$$

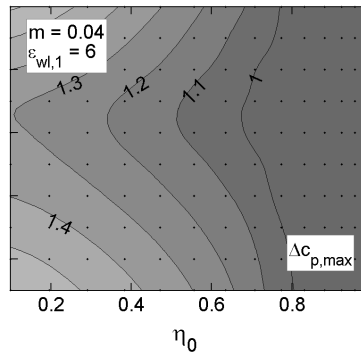
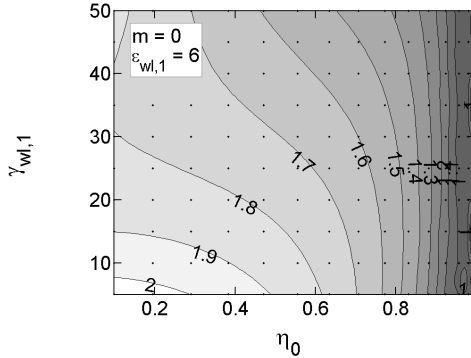
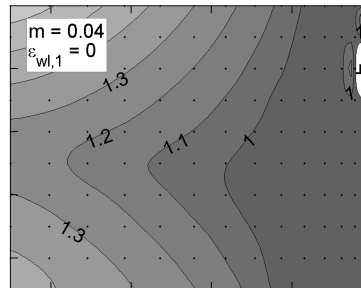
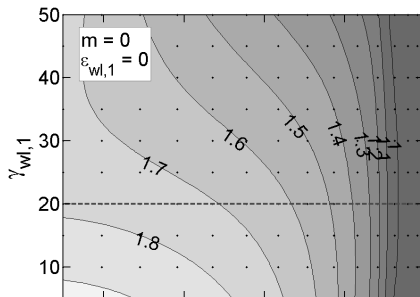


Fig. 83: Comparison of maximum local aerodynamic load coefficients at maximum range and maximum endurance conditions (values are given as ratios with respect to the respective rectangular wing values stated to the left of the diagrams).

5.4.2 Parametric Optimisation of Planform Shape

Another important parameter that affects the wing performance is the taper ratio of the wing or the taper ratios of wing parts respectively. Taper ratio is the ratio of the outer chord to the inner chord of a wing or a wing part and is a parameter governing the planform shape of a wing. Two taper ratios will be varied, one ratio for the inner wing and another one for the outer wing or the winglets. Because it would not be very meaningful to compare a highly optimised multi-winglet configuration with a suboptimal rectangular wing, the influence of altering the taper ratios is not only studied for the multi-winglet configuration but also for the initially rectangular planar wing.

It is possible to hold the wing reference surface constant by an appropriate scaling of the root, main wing tip and winglet tip chords. The chord of the inner wing tip is non-dimensionalised by the geometric mean chord of the wing. The chord is equal to the non-dimensionalised outer wing part root chord respectively the sum of the winglet root chords in streamwise direction.

$$\xi_{1,t} = \xi_{2,r} = \frac{2}{\eta_0 \cdot \left(1 + \frac{1}{\lambda_1}\right) + (1 - \eta_0) \cdot (\lambda_2 + 1)} \quad (88)$$

The non-dimensional main wing root and total wing tip chords are obtained from

$$\xi_{1,r} = \frac{\xi_{1,t}}{\lambda_1} \quad \text{and} \quad \xi_{2,t} = \xi_{2,r} \cdot \lambda_2$$

Total chords follow after multiplication with the geometric mean chord

$$c_{1,r} = \xi_{1,r} \cdot \bar{c}, \quad c_{1,t} = \xi_{1,t} \cdot \bar{c}, \quad c_{2,r} = \frac{\xi_{2,r} \cdot \bar{c}}{n_{wl}}, \quad c_{2,t} = \frac{\xi_{2,t} \cdot \bar{c}}{n_{wl}}$$

Root chords of multiple winglets are set equal. The same applies for the tip chords.

Two discrete taper ratios of 1.0 and 0.6 were set for the inner main wing part and values of 0.6 and 0.2 for the outer wing respectively the winglets. The geometric twist angles range from -4 (washout) to 4 deg (washin) with 2 deg increments for the outer wing of the planar configuration and a range from 0 to 6 deg for the leading winglet as before (also refer to assumptions in section 5.4.1).

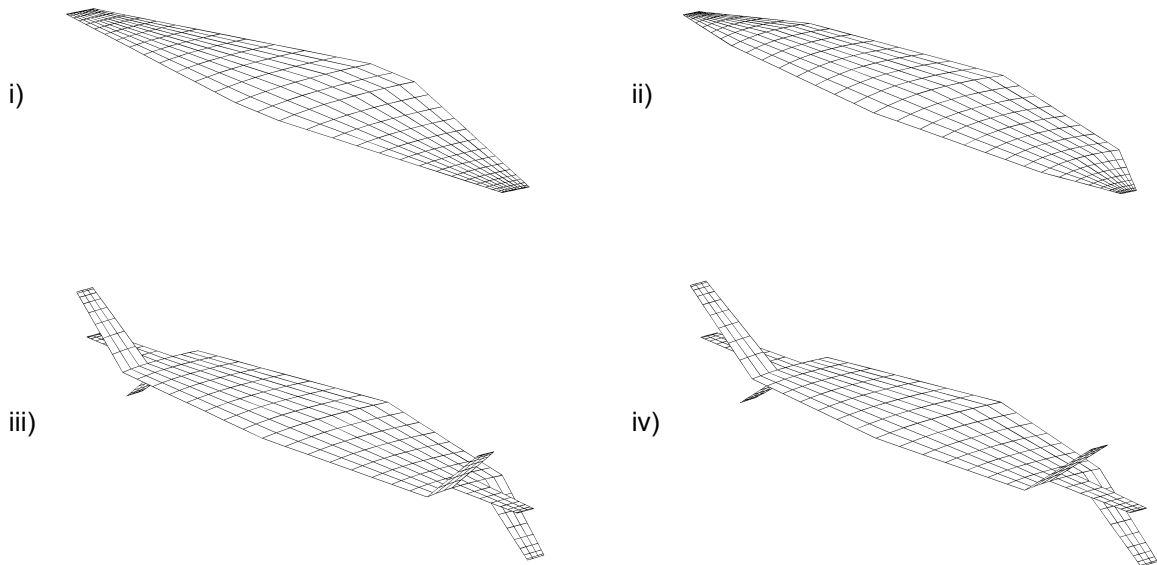
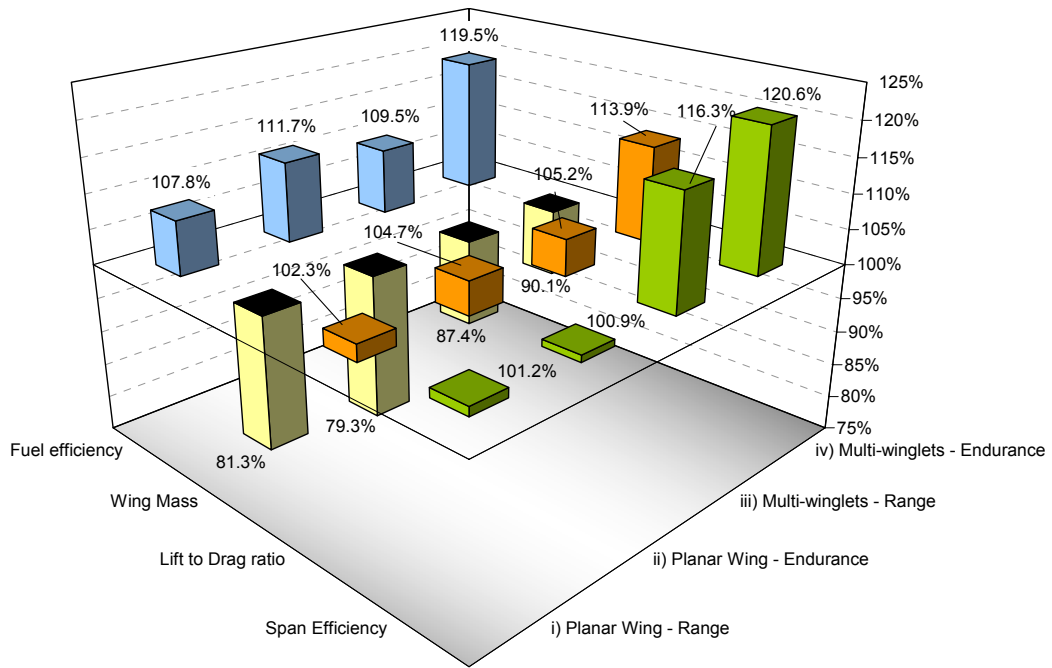


Fig. 84: Best points regarding fuel efficiency of planar and multi-winglet wings having the same wing spans. Percentages are given with respect to the basic rectangular wing. Values of independent parameters as below:

Parameters \ Design Case:	i)	ii)	iii)	iv)
dihedral [deg]:	0	0	40	35
kink location / slitting ratio:	0.1	0.71	0.71	0.63
main wing part camber:	0.02	0.04	0.02	0.02
twist of outer wing part / winglets [deg]:	4.0	4.0	4.0	4.0
inner wing taper ratio:	1.0	0.6	0.6	0.6
outer wing / winglet taper ratio:	0.2	0.2	0.6	0.6

Fig. 84 is a summary of the best points for span efficiency, lift to drag ratio, wing mass and fuel efficiency. Fuel efficiencies of planar as well as multi-winglet wings utilising taper are consistently better than the corresponding values of the rectangular wing. At a first glance, it will be observed that the optimum multi-winglet configurations have greater wing structure mass figures compared to the best planar wings but exhibit superior span efficiencies. Performance improvements over the basic rectangular wing are greater for the maximum endurance condition for planar wings as well as multi-winglet configurations. The performance gain of the multi-winglet compared to the best planar configuration for maximum range is only marginal and might easily be eaten up by additional mass fractions that are perhaps required for the non-planar configuration but that have been neglected so far (for example multi-winglet to wing attachment mass fractions).

The enhancement for the maximum endurance condition is more significant but the performance gap to the planar configuration is smaller compared to the planforms without taper described previously. It can thus be concluded that the planar configurations benefit more of planform optimisation than the multi-winglet configurations.

The present parametric study has been referred to an aircraft scenario but the trim drag was neglected so far. Trim drag, nevertheless, is unavoidable if a conventional system for longitudinal trim, stability and control is used. The trim drag of a general aviation aircraft is usually a one digit percentage fraction of the total aircraft drag, 4% being a typical value [115]. This assumes the utilisation of a conventional untwisted planar wing with a pitching moment coefficient of -0.05 corresponding to a section camber of $m = 4$. A brief assessment according to reference [115] reveals that this figure could reduce to about 3% for a symmetrical section or increase to about 4.5% for $m = 6$. These figures are assessed under the assumption that the horizontal tailplane sizes are adapted accordingly.

The actual pitching moments of the optimal configurations of the parametric study are given in Tab. 32. The mutual differences in trim drag between the optimum configurations for range and endurance are less than an estimated 0.35% of total drag.

Tab. 32: Pitching moment coefficients about the wing root quarter chord location for design operating points (reference surface area: 13.5 m², reference chord: 1.5 m).

Design Case	i)	ii)	iii)	iv)
$C_{M,25}$	-0.0427	-0.0778	-0.0585	-0.0686

These figures allow to conclude that the outcome of the present parametric study would not have been fundamentally different if the trim drag had been explicitly taken into account.

5.4.3 Numerical Multi-Winglet Optimisation

The preceding parametric study revealed optima for the payload specific fuel efficiency. Performance values were evaluated for a multi-dimensional matrix of independent discrete values for the independent parameters

- slitting ratio
- winglet dihedral
- main wing camber
- winglet geometric twist
- main wing taper ratio and
- winglet taper ratio.

This grid allowed identifying optima for fuel efficiency. Now, it will be checked whether the optimisation mode of VLM++ is able to find these optima more efficiently. In order to demonstrate the optimisation sequence graphically, the number of optimisation variables is limited to slitting ratio and winglet dihedral. The slitting ratio variation is constrained to discrete values in order to maintain consistency with the lattice arrangements used for the parametric study before. The computational basis is the best multi-winglet configuration for the maximum endurance operating condition from chapter 5.4.2. Cascade effects are considered using the dedicated optimisation mode of that program module. Fixed independent parameter values are

- main wing camber - $m = 0.02$
- winglet geometric twist - $\varepsilon_{wl,1} = 4 \text{ deg}$
- main wing taper ratio - $\lambda_m = 0.6$
- winglet taper ratio - $\lambda_{wl} = 0.6$.

Fig. 85 compares the grid search results with those obtained from numerical optimisation with the MATLAB function *fmincon*. The parameter range was extended to negative dihedral angles of the leading winglet (trailing winglet has positive dihedral in this case). The number of chordwise strips per wing half was fixed to 16 with a minimum number of one chordwise row of elements for the inner wing and a maximum of 15. Further constraints on the leading winglet dihedral angles and final key geometric values for the optimisation runs are summarised in Tab. 33.

The constraints are set so that the region of small dihedrals around zero is omitted in order to avoid numerical difficulties. Convergence was assumed to be obtained if the relative increments in the objective function decreased below $1 \cdot 10^{-4}$, in this case.

Tab. 33: Final results of winglet dihedral and slitting ratio optimisation.

Run	Starting point γ [deg] / η_0	Constr. $\gamma_{wl,1}$ [deg]	Line description (Fig. 85)	Number of steps for convergence	Final values		
					$\gamma_{wl,1}$ [deg]	η_0	Rel. fuel efficiency
1	+5.0 / 0.980	[5, 50]	solid line, \triangle	22	37.0	0.634	1.196
2	+5.0 / 0.098	[5, 50]	dash-dot line, ∇	28	36.0	0.634	1.196
3	-5.0 / 0.980	[-5, -50]	solid line, \triangleright	35	-39.5	0.707	1.184
4	-5.0 / 0.098	[-5, -50]	dash-dot line, \triangleleft	35	-39.5	0.707	1.184

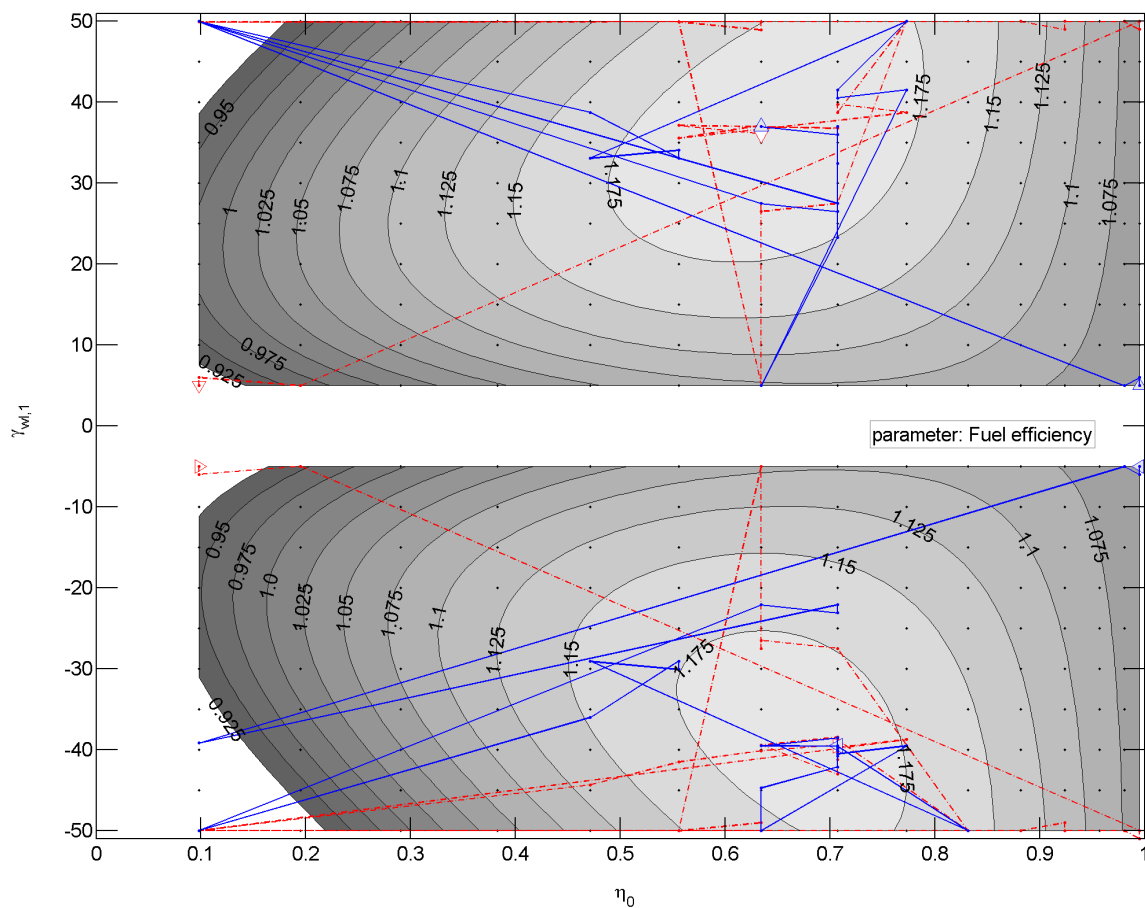


Fig. 85: Comparison of grid search results for maximum endurance (dots and contours) and optima found with non-linear constrained numerical optimisation (lines and triangles) using four different starting points. Contour values and shading indicate relative fuel efficiencies with respect to the basic planar rectangular wing.

Two optima develop, one for positive and one for negative leading winglet dihedral angles for winglets that make up for about a third of the semi-span of the wing. The area where relative payload per fuel and time is greater than 117.5% compared to the basic rectangular wing is larger for the accelerating cascade arrangement ($\gamma_{wl,1} > 0$ deg). This is mainly because of the positive camber of the main wing. Cascade effects in contrast play only a minor role because of the high loadability of the airfoil sections and the fact that sections mostly operate in the linear part of the lift polar.

The optimiser closes in to the lower (local) or the upper (global) optimum depending on the initial values of the dihedral angle. The traces give evidence that the convergence is rather sluggish, which might be due to the fact that the slitting ratio is basically an integer variable, which allows changes in prescribed discrete steps only.

6 Conclusion

It has long been theoretically confirmed that multi-winglet systems known from the avian world can reduce induced drag. However, the performance of technical adaptations of multi-winglet configurations actually fell often short of the expectations raised by theoretical predictions. It was the aim of this thesis to identify key points to explain the significant discrepancies between theory and practical application, which is of particular interest given the fact of the remarkable practical success of the configuration in nature. After critical areas were detected it was the idea to derive design guidelines for multi-winglet configurations aimed at avoidance or mitigation of particular problems. Another aim of the thesis was to identify multi-winglet configuration performance trends in comparison to planar wing concepts with emphasis on aircraft application. A computational approach was preferred to an experimental approach because of greater analysis versatility and the opportunity to assess configurations on a comprehensive multi-disciplinary basis.

A wing analysis tool termed VLM++ was set up for that purpose. It is based on an implementation of the basic vortex lattice method operating with horseshoe elements and element-wise constant circulations. The geometry module was tailored as to ease the set up of multi-winglet configurations on the basis of concise parameter sets. The core of the programme provides fundamental lift, pitching moment and induced drag characteristics. Interference effects among lifting surfaces with respect to these characteristics are inherently accounted for. Complementary models were added to represent the additional aerodynamic effects affecting wings equipped with multi-winglet cascades in incompressible, viscous flow. Additional effects that were explicitly considered by extensions of the basic analysis tool were

- profile drag (i.e. friction and pressure drag, including lift dependent components)
- interference drag due to viscous effects
- those that cascade arrangements exert on maximum aerodynamic loadability
- non-linear lift characteristics near stall.

Wing profile drag was computed by means of the flat plate analogy with prescribed locations for transition including extensions for thickness dependent drag as well as lift dependent profile drag components. The latter model was calibrated to resemble the characteristics of NACA 4-digit series airfoil sections.

A new, though purely empirical model for interference drag of winglet junctions due to viscous effects was set up on the basis of the data compiled in reference [95]. The model accounts for zero lift as well as lift dependent interference drag components.

In order to consider the influence of cascade arrangements on maximum and minimum lift capabilities of individual spanwise strips of a wing, the respective coefficients were correlated with the degree of energy recovery from the location of maximum kinetic energy at the minimum pressure location towards the trailing edge according to an approach suggested in reference [131]. Because the pressure distributions change if airfoil sections are placed in a cascade arrangement, the individual loadability limits also change. It has been claimed that increased trailing edge flow velocities in accelerating type cascade settings alleviate the chordwise pressure recovery and increase the maximum lift capabilities with the exception of the rearmost surface. The present method is based on section maximum and minimum lift coefficient data. Only the alterations of loadability are considered under the assumption that the stall type does not change, which is presumed to hold for many practical cases. The significance of this mechanism and the effectivity of the straightforward approach were proved by favourable correlations of computational results with multi-winglet experimental data.

The required chordwise pressure distributions were obtained by exploitation of family ties among various methods based on potential theory. First, continuous chordwise circulation distributions were adapted to the discrete vortex lattice results aided by Fourier approach functions from thin airfoil theory. Second, a model for the section thickness was added following the approach of Riegels [114]. The new hybrid method produces reasonable pressure distributions of three dimensional wings with sufficient accuracy for the present purpose where mutual interference due to thickness of the wing sections can be disregarded, an effect that is clearly not accounted for by the method. The method entails several additional computational steps. It is possible, though not proved, that the turn around times are in many cases smaller than that of panel methods where the thickness effect is explicitly modelled because of fewer elementary surfaces and consequently a significantly smaller number of influence coefficients to be computed. It has been shown that the current method produces reasonable wing pressure distributions on the basis of no more than three chordwise lattice elements.

Experiments documented in the literature indicated that hardly any multi-winglet configuration was tested where the flow was entirely attached on the whole surface, even at angles of attack where boundary layer separation is not normally encountered at wing configurations with plain closed tip wings. Because of this fact, non-linear lift effects near the stalling condition of individual wing sections were considered by means of the idea to alter the local lift curve slope by movement of the collocation point locations proposed in reference [95]. The generalised shape of the lift curve near the stalling condition, however, was prescribed by a priori selection of an expected stall type. The method is particularly suited to model conditions where the flow is just partly

separated. A distinct advantage of this approach is that the influence of partly separated flow on the wing load distributions and the induced drag is automatically accounted for.

The numerical model was compared with published low-speed wind tunnel data of reference [50] available for three multi-winglet configuration variants and a rectangular wing. The low Reynolds numbers of the experiments (the inner wing chord based Reynolds number was $0.433 \cdot 10^6$) made it necessary to adapt specific settings of the lift-dependent profile drag model beside adaptation of the sectional maximum and minimum lift coefficients. However, it was possible to match the given lift and drag characteristics of all four configurations using only one common parameter set. The adapted computational model with three vertically fanned-out winglets with +20, 0 and -20 degs dihedral and -10, -5 and 0 degs root incidences with respect to the main wing served as a first low Reynolds number basis for a parametric study.

Computations showed that multi-winglets can yield significant reductions of induced drag in the lower two digit percent range as compared to planar wing concepts having the same wing area and span. This reduction can only be achieved at the cost of increased profile and interference drag components. It was established that the skin friction and profile drag penalties for wing splitting are significantly less for turbulent than for laminar boundary layers.

Analysis of experimental results obtained for multi-winglet configurations and their comparison with numerical computations always showed that the computations were optimistic. It appears that the discrepancy between experiments and numerics is particularly large compared to other configurations including single winglets. The problem with analogue methods or numerical Trefftz plane optimisations is that the results are loadings of individual winglets, which are often impractical for 3D flow. For optimum loadings of a multi-winglet cascade with respect to induced drag, high loads on the upper- and lowermost winglets are prescribed. If the winglets are subsequently arranged in an accelerating grid configuration, it may prove impossible to get the stipulated load on the rearmost and at the same time lowermost winglet because of its inevitably limited loadability. Although not really dramatic, one must nevertheless acknowledge that induced drag gains are curtailed from the outset to some degree because of the practical difficulty to realise 2D optimum conditions. This is especially true if a range of operating points with near optimal performance figures is envisaged and not only a single one. This is a particular difference to planar wings and to a smaller degree also to configurations with conventional winglets where it is easier to practically establish the theoretical optimum conditions in three-dimensional flow.

A parametric variation of winglet number including the limiting case of only one winglet without dihedral (thus forming a planar tapered wing), which was based on a calibrated reference point, showed that the last mentioned configuration offers by far the best wing

lift to drag ratio as compared to a rectangular wing, a split tip configuration as well as multi-winglet configurations with 3, 4 and 6 winglets that all had principally the same span. The configuration with three winglets showed a marginal advantage of the best endurance parameter over the planar tapered wing. The lift capability of the split tip and multi-winglet configurations significantly reduced with increasing number of winglets without using the cascade model. Wing maximum lift coefficients were almost independent of winglet number if the cascade model was switched on, but neither of the multi-winglet configurations reached the lift capability of the tapered planar wing.

For aircraft application, the adaptability of individual winglet incidences by means of actuators is sometimes stated as a presumed prerequisite for good aerodynamic performance of multi-winglet wing tip devices. A more effective approach is cambering the main wing, which automatically alters the root incidences of the winglets attached to it. For constant overall lift conditions, the leading winglet is off-loaded due to a reduced local angle of attack while the rearmost located winglet has to sustain higher loads because of its greater incidence. It appeared that main wing camber and its adaptation are in fact of importance for good performance at various operating points characterised by different wing lift coefficients, at least for supercritical main wing section Reynolds numbers.

It was shown that multi-winglet configurations are at first hand an effective means to increase the endurance parameter $C_L^{3/2}/C_D$ (climb operation point, maximum endurance) but it was also shown that planar wings including the rectangular planform are superior to multi-winglet configurations regarding lift to drag ratios (best gliding performance, maximum range). It can be reasoned that an optimal configuration should combine optima of the two operating points, which would require that the winglets ought to be adaptable in a way that they are fanned out for climbing, but forming an unslotted closed wing tip in gliding flight or cruise, respectively. Birds, the natural example for the utilisation of multi-winglet cascade configurations, in fact demonstrate this because they spread their outer primaries while thermaling, but fold them up in fast gliding flight.

The current results corroborate the speculation that the success of the multi-winglet configuration in the avian world is in fact a consequence of exploitation of particular benefits as outlined in the introduction of the present thesis, including the effectiveness of the slotted outer primaries in producing thrust in flapping flight, which, in contrast, is hardly of interest for aircraft designed according to Cayley's paradigm where lift production and propulsion are clearly separate functions.

Besides the reference model mentioned above that was calibrated to low speed experimental data, a second datum wing configuration was established according to design specifications typical for a low speed general aviation aircraft wing. This datum configuration was used for a comprehensive parametric study including the

consideration of wing structural mass. The span and the wing loading measured in terms of the aircraft takeoff weight divided by the chord areas of the various wings were held constant. The aspect ratio of the basic planar rectangular wing that served as reference configuration was 6.0. Slitting ratio, winglet dihedral, main wing camber, winglet geometric twist, main wing taper ratio and winglet taper ratios were systematically varied in the course of the study.

It was found that the payload specific fuel consumption of a multi-winglet configuration is more sensitive to the assumptions made for the wing structure mass model compared to the sensitivity of a configuration having conventional wing tips. The reason for this behaviour is the fundamentally higher wing mass of the wing with slotted wing tips. Without changing the aerodynamic performance, higher design loads demand a proportional increase of wing structure material with the consequence that multi-winglet wing efficiency erodes quicker than that of the planar wing because of the more pronounced decay of payload capacity for a design scenario with fixed all-up mass and prescribed range or endurance requirements. This clearly shows that the non-planar configuration is not suitable for cases where high design load factors have to be considered, such as those encountered in the course of aerobatic aircraft design, for example.

Given that the parabolic drag polar is an acceptable model to represent aircraft drag characteristics, performance optima occur at maximum lift to drag ratio for range and the maximum of the parameter $c_L^{3/2}/c_D$ for endurance if power producing engines are assumed. The dynamic pressure was adapted to allow an assessment of both operating points without changing the total lift. Moreover, Reynolds numbers were held constant for both operating points. Optimum conditions were exactly applicable to the reference rectangular wing. Considering the optimum range operating point, the best multi-winglet configuration was found to have an advantage of just 1.58% in fuel efficiency (that is the reciprocal of the payload specific fuel consumption) over the best double-trapezoidal planar planform with the same chord area and span. This must be considered as a non-significant benefit if the accuracies of the analysis methods used are taken into account as well as the fact that no account was made for additional structure mass for fitting the winglets to the main wing. However, it seems that the higher Reynolds number of the general aviation scenario as compared to the low Reynolds number validation case has an advantageous effect on multi-winglet performance. In contrast to the maximum lift to drag ratio, the advantage in fuel efficiency at maximum endurance conditions is 6.98%. This figure is likely to be large enough to guarantee a benefit even if it proves true that numerical results are optimistic and that additional wing weight is to be added for winglet attachment to the main wing. This allows to conclude that a non-planar wing of moderate aspect ratio equipped with multi-winglet wing tip devices is in fact a better solution if a wing for achieving maximum endurance has to be designed, e.g. for an

aircraft optimised for surveillance tasks under the condition that the span is explicitly limited.

A particular shortcoming of the present method's horseshoe vortex geometries consisting of three respectively five filaments is the vertical spread of the trailing vortex filaments if the wing is cambered or twisted. This spread has caused problems, particularly if configurations were automatically optimised and the possibility of geometries with very narrow wing tip element spans and/or high wing tip camber was not explicitly excluded. It may happen that magnitude of the sideward component of the induced velocity at collocation or quarter chord points of affected elements is on the order of the downwash velocity component. At least a partial mitigation to this problem would be to use vortex rings as promoted in reference [4] instead of the horseshoe geometries. The trailing vortex legs of a forward ring element end at the quarter chord vertices of the following element located downstream. Hence, the trailing vortex filaments form a piecewise train that closely follows the section camber lines so that the aforementioned problem does not occur. Conceptually, the vortex ring approach is an identical "zero order" approach and as such fully compatible with the current implementation of the vortex lattice method with virtually no additional modelling efforts required. Compared to higher order lifting surface approaches or panel methods, the numerical efficiency and versatility is maintained. Also, the many extensions allowed for by the Pistolesi theorem can be maintained such as the adaptation of the local section lift curve slope by alteration of the relative collocation point positions.

It proved feasible to perform non-linear multi-variate configuration optimisations with the gradient based optimiser *fmincon* of MATLAB's Optimization Toolbox and VLM++ providing the objective function values. However, the interplay of both programmes leaves room for improvement. One obvious problem arises from the necessity to artificially smooth the outcome of the objective function. In the case of slitting ratio optimisation, this has been done by specifying the number of spanwise elements as an optimisation variable instead of the slitting ratio itself, in which case VLM++ would adjust the number of spanwise elements of main wing and winglets automatically. The problem in the latter case is that it cannot be excluded that the gradients determined by assessment of adjacent objective function evaluations become singular. Thus, the former practice was adopted, where the distance between neighbouring results is large enough to guarantee smooth gradients. The shortcoming of this approach is that the acceleration functions of the optimiser do not properly work on the coarse grid and the number of optimiser iterations is higher than expected. An aerodynamic analysis method that uses higher order approach functions (e.g. as described in reference [63]) for the spanwise circulation distributions could help in this particular respect as the necessity to alter the number of spanwise elements could be avoided with the

consequence of inherently smooth variation of the objective function with spanwise change of the slitting ratio.

A likely important effect that has not been considered in the frame of the present thesis is the influence of airfoil cascades on the boundary layer states as far as skin friction drag is concerned as brought up by Kroo [10]. The interference effect of multiple airfoils on the maximum loadability of wing sections and on the lift dependent profile drag has been approximately regarded by considering the effects of cascade arrangements on the pressure distributions, or more precisely on the pressure recovery and implicitly its effect on boundary layer separation. Favourable cascade arrangements of multiple lift producing surfaces positively alter the conditions where critical canonical trailing edge pressure coefficients occur. A favourable pressure gradient beginning at the leading edge of an airfoil also has a first order influence on the transition location because perturbations in the laminar boundary layer that finally lead to transition, if amplified, are actually damped. It is possible to obtain very low profile drag coefficients if one succeeds in establishing such a favourable pressure gradient over large portions of the wing section chord.

Many experimentalists reported on the problem of winglet root separation. In all those cases, a winglet utilising a moderately thick technical wing section was attached to a similar main wing tip section. A phenomenon reported by more than one author (e.g. [57], [80]) was the formation of a necklace vortex at winglet roots because the adverse pressure gradient ahead of the winglet caused the boundary layer at the usually rounded main wing tip side face to separate. Deeper insight on the interference phenomena at the winglet-wing intersection could be provided by detailed experimental and/or numerical investigations on the basis of Navier-Stokes methods.

It is still an open question in this context what role the thin primary feathers of birds with slotted wing tips play with respect to the root separation phenomenon. At a first glance it can be reasoned that it is rather unlikely that a necklace vortex can develop at the attachment location of wing primary feathers to the birds centre wing part. This is because of the lack of a significant stagnation region ahead of the thin outer primary feathers with its permeable leading edge vanes, second because of the smooth blending of the primary feather intersections with the main wing, and third because of the fact that subsequent slots formed by the feathers are not in line with respect to the freestream direction.

A potential advantage offered by multi-winglet configurations are the principally outstanding wake vortex properties because of the potential to produce low energy cores of the fully or partly rolled up trailing vortex systems. The flight experiments of multi-winglets on a Piper Pawnee 235 agricultural aircraft at the end of the 1970s (discussion of the experiments in [40]) already provided practical evidence by showing

that the amount of the sprayed droplets that were convected to locations above the aircraft reduced significantly as compared to all other wing tip devices tested. However, a challenging prerequisite for an exploitation of these properties for the improvement of wake vortex properties of large transport aircraft would be a wing design that advantageously combines the multi-winglet configuration with a suitable concept for aircraft lateral control as well as the integration of the high-lift system.

The present thesis has identified performance potentials of small general aviation aircraft equipped with multi-winglet wing tip devices. It was possible to derive a set of design guidelines based on the computationally established performance sensitivities which were determined by systematic variations of geometric parameters. Because the present findings are derived from numerical results, their verification by experimental evidence remains still an open task.

References

- [1] Prandtl, L.: Tragflügeltheorie - I. Mitteilung. Nachrichten der Gesellschaft der Wissenschaften zu Göttingen, Mathematisch-physikalische Klasse, 1918, pp. 151-177, reproduced in: Ludwig Prandtl - Gesammelte Abhandlungen. Erster Teil, eds.: Tollmien, W., Schlichting, H., Görtler, H., Springer Verlag, Berlin, 1961
- [2] Durand, William Frederick (ed.): Aerodynamic Theory. Vol. 1-6, first published by Julius Springer, 1934-1936, republication by Dover Publications, Inc., New York, 1963
- [3] Anderson, J. D.: Fundamentals of Aerodynamics. 2nd edition, McGraw-Hill, 1991
- [4] Katz, J., Plotkin, P.: Low-Speed Aerodynamics. 2nd edition, Cambridge University Press, 2001
- [5] Mason, W.H.: Class Notes for Applied Computational Aerodynamics. Virginia Polytechnic Institute and State University, 1997, http://www.aoe.vt.edu/~mason/Mason_f/CAtxtTop.html, date of visit: 01.02.2004
- [6] Houghton, E. L., Carpenter, P. W.: Aerodynamics for Engineering Students. 5th edition, Butterworth-Heinemann, 2003
- [7] Munk, Max: Isoperimetrische Aufgaben aus der Theorie des Fluges. Inaugural-Dissertation, Georg-August-Universität, Göttingen, 1919
- [8] Prandtl, L.: Tragflügeltheorie - II. Mitteilung. Nachrichten der Gesellschaft der Wissenschaften zu Göttingen, Mathematisch-physikalische Klasse, 1919, pp. 107-137, reproduced in: Ludwig Prandtl - Gesammelte Abhandlungen. Erster Teil, eds.: Tollmien, W., Schlichting, H., Görtler, H., Springer Verlag, Berlin, 1961
- [9] Prandtl, L.: Tragflächen-Auftrieb und -Widerstand in der Theorie. Jahrbuch der wissenschaftlichen Gesellschaft für Luftfahrtforschung, Vol. 5, 1920, pp. 37-65
- [10] Kroo, I.: Nonplanar Wing Concepts for Increased Aircraft Efficiency. VKI Lecture series on Configurations and Advanced Concepts for Future Civil Aircraft, June 6-10, 2005
- [11] Weber, J.: Theoretical Load Distribution on a Wing with Vertical Plates. A.R.C. Technical Report, R. & M. No. 2960, 1956
- [12] Löbert, G.: Der Flügel mit Gabelspitzen als Mittel zur Erhöhung der Wirtschaftlichkeit von Transportflugzeugen. DGLR-Jahrbuch 1977, Vol. 1, 1978

- [13] Cone, C. D.: The Theory of Induced Lift and Minimum Induced Drag of Nonplanar Lifting Systems. NASA TR-139, 1962
- [14] Krou, I.: Drag Due to Lift: Concepts for Prediction and Reduction. *Annu. Rev. Fluid Mech.* 2001, Vol. 33, pp. 587-617
- [15] Eppler, R.: Induced drag and winglets. *Aerospace Science and Technology*, No. 1, 1997, pp. 3-15
- [16] Maughmer, Mark D.: Design of Winglets for High-Performance Sailplanes. *Journal of Aircraft*, Vol. 40, No. 6, November-December 2003
- [17] In-Flight Separation of Vertical Stabilizer American Airlines Flight 587 Airbus Industrie A300-605R, N14053 Belle Harbor, New York, November 12, 2001. NTSB/AAR-04/04, October 26, 2004
- [18] Stache, M.: Evolutionsstrategisches Design von Tragflügelspitzen. *DGLR-Jahrbuch*, DGLR-2006-200, 2006, pp. 1131-1138
- [19] Prandtl, L.: Über Tragflügel kleinsten induzierten Widerstandes. *Zeitschrift für Flugtechnik und Motorluftschiffahrt*, Vol. 24, 1933, pp. 305-306, reprinted in: Tollmien, W., Schlichting, H., Görtler, H. (eds.): *Ludwig Prandtl - Gesammelte Abhandlungen*, Springer-Verlag, 1961
- [20] Jones, R. T., Lasinski, T. A.: Effect of Winglets on the Induced Drag of Ideal Wing Shapes. NASA TM 81230, September 1980
- [21] www.airliners.net, date of visit: 12.01.2007
- [22] Green, Sheldon I. (ed.): *Fluid Vortices*. Kluwer Academic Publishers, Dordrecht, 1995
- [23] Kaden, H.: Aufwicklung einer unstabilen Unstetigkeitsfläche. *Ingenieur-Archiv*, Vol. 2, 1931, pp. 140-168
- [24] Betz, A.: Verhalten von Wirbelsystemen. *Zeitschrift für angewandte Mathematik und Mechanik*, Vol. 12, No. 3, June 1932
- [25] Zheng, Z.C.: Betz Invariants and Generalization of Vorticity Moment Invariants. *AIAA Journal*, Vol. 39, No. 3, March 2001
- [26] Rossow, Vernon, J.: Extended-Betz Methods for Roll-Up of Vortex Sheets. *Journal of Aircraft*, Vol. 34, No. 5, September-October 1997
- [27] Kaufmann, W.: *Technische Hydro- und Aeromechanik*. 3rd edition, Springer-Verlag, 1963
- [28] Spreiter, J. R., Sacks, A. H.: The Rolling Up of the Trailing Vortex Sheet and its Effect on the Downwash behind Wings. *Journal of the Aeronautical Sciences*, Jan. 1951, pp. 21-32

- [29] Devenport, W. J., Rife, M. C., Liapis, S. I., Follin, G. J.: The structure and development of a wing-tip vortex. *Journal of Fluid Mechanics*, Vol. 312, 1996, pp. 67-106
- [30] Panton R. L., Oberkampf W. L., Soskic, N.: Flight Measurements of a Wing Tip Vortex. *Journal of Aircraft*, Vol. 17, No. 4, April 1980, pp. 250-259
- [31] Rossow, V. J.: On the Inviscid Rolled-Up Structure of Lift-Generated Vortices. *Journal of Aircraft*, Vol. 10, No. 11, November 1973, pp. 647-650
- [32] Rossow, V. J.: Theoretical Study of Lift-Generated Vortex Wakes Designed to Avoid Rollup. *AIAA Journal*, Vol. 13, No. 4, April 1975, pp. 476-484
- [33] Graham, W. R.: An assessment of the 2D vortex method in aircraft wake simulation. *Aeronautical Journal*, December 2001, pp. 653-666
- [34] Hinton, David, A., Tatnall, Chris, R.: A Candidate Wake Vortex Strength Definition for Application to the NASA Aircraft Vortex Spacing System (AVOSS). NASA TM 110343, September 1997
- [35] Crow, S. C.: Stability theory for a pair of trailing vortices. *AIAA Journal*, Vol. 8, No. 12, 1970, pp. 2172-2179
- [36] Stuff, R.: The Relationship Between Near- and Far-Field of Vortex Wakes from Aircraft with High Aspect Ratio Wings. *New Results in Numerical and Experimental Fluid Mechanics III, Contributions to the 12th STAB/DGLR Symposium*, Stuttgart, Wagner, S., et al. (eds.), Germany, 2000
- [37] Stumpf, E.: Numerical Study of Four-Vortex Aircraft Wakes. *New Results in Numerical and Experimental Fluid Mechanics III, Contributions to the 13th STAB/DGLR Symposium*, Munich, Breitsamter, C., et al. (eds.), Germany, 2002
- [38] Herzog, Karl: *Anatomie und Flugbiologie der Vögel*. Gustav Fischer Verlag, Stuttgart, 1978
- [39] Burton, R.: *Bird Flight: an illustrated study of birds' aerial mastery*. Facts on File Inc., New York, 1990
- [40] Videler, J. J.: *Avian Flight*. Oxford University Press, 1st edition, 2005
- [41] Spillman, J. J.: Wing tip sails; progress to date and future developments. *Aeronautical Journal*, December 1987
- [42] Hertel, Heinrich: *Struktur - Form - Bewegung*. Krauskopf-Verlag, Mainz, 1963
- [43] Lilienthal, O.: *Der Vogelflug als Grundlage der Fliegekunst*. 2nd edition, Verlag von R. Oldenbourg, Berlin, 1910
- [44] Tennekes, Henk: *Kolibris und Jumbo-Jets*. Birkhäuser Verlag, Basel, 1997

- [45] Patone, Giannino: Vogeldeckfedern, Ein Vorbild für Technische Rückstromtaschen an Tragflügeln. Dissertation, TU-Berlin, 1999
- [46] Ahlborn, F.: Zur Mechanik des Vogelfluges. Abhandlungen aus dem Gebiete der Naturwissenschaften, Naturwissenschaftlicher Verein Hamburg (ed.), Vol. 14, Hamburg, 1896
- [47] Oehme, Hans: On the Aerodynamics of Separated Primaries in the Avian Wing. in: Scale effects in animal locomotion, Pedley, T. J. (ed.), Academic Press, New York, 1977, pp. 479-494
- [48] Hummel, D.: The Aerodynamic Characteristics of Slotted Wing-tips in Soaring Birds. Proceedings of the 17th International Ornithological Congress, 1978, Berlin, 1980, pp. 391-396
- [49] Tucker, Vance, A.: Gliding Birds: Reduction of Induced Drag by Wing Tip Slots Between the Primary Feathers. Journal of Experimental Biology, Vol. 180, 1993, pp. 285-310
- [50] Hummel, D.: Recent Aerodynamic Contributions to Problems of Bird Flight. ICAS Proceedings, 11th Congress of the International Council of the Aeronautical Sciences, 10-16 September 1978, Lisboa, Portugal, Volume 1, pp. 115-129
- [51] Tucker, Vance, A.: Drag Reduction by Wing Tip Slots in a Gliding Harris' Hawk, *Parabuteo unicinctus*. Journal of Experimental Biology, Vol. 198, 1995, pp. 775-781
- [52] Pennycuik, C. J.: The Profile Drag of a Hawk's Wing, Measured by Wake Sampling in a Wind Tunnel. Journal of Experimental Biology, Vol. 165, 1992, pp. 1-19
- [53] Schmitz, F. W.: Aerodynamik des Flugmodells. Tragflügelmessungen bei kleinen Geschwindigkeiten, Vol. 1 & 2, Carl Lange, Duisburg, 1960
- [54] Freestone, M. M.: Aerodynamic Principles of Winglets. ESDU 98013, June 1998
- [55] Whitcomb, R. T.: Methods for reducing subsonic drag due to lift. AGARD Report No.654, Special Course on Concepts for Drag Reduction, April 1977
- [56] Hackett, J. E.: Vortex Drag Reduction by Aft-Mounted Diffusing Vanes. ICAS-80-13.4, 1980, pp. 542 - 552
- [57] Spillman, J. J.: The use of wing tip sails to reduce vortex drag. Aeronautical Journal, September, 1978, pp. 387-395
- [58] Dodson, R. O., Jr.: Comparison of Flight Measured, Predicted and Wind Tunnel Measured Winglet Characteristics on a KC135 Aircraft. KC135 Winglet Program

- Review, Proceedings of a symposium held at Dryden Flight Research Center, September 16, 1981, NASA Conference Publication 2211, 1982
- [59] Ishimitsu, K. K., VanDevender, N., Dodson, R. O., Brault, P. C., Byersm, B. A.: Design and Analysis of Winglets for Military Aircraft. Final Report, 16.06.-25.11.1975, Boeing Commercial Airplane Comp., AFFDL-TR-76-6, February 1976
- [60] Poisson-Quinton, Ph.: Parasitic and Interference Drag Prediction and Reduction. AGARD R-723, 1985
- [61] Faye, R., Laperte, R., Winter, M.: Blended Winglets for Improved Airplane Performance. Aero Magazine, No. 17, Boeing Commercial Airplane Company, January 2002
- [62] Kreuzer, Peter: Weiterentwicklung und experimentelle Überprüfung eines 3-D Panelverfahrens im Falle einer Tragflügelanordnung mit Winglets. Dissertation, Technische Hochschule Darmstadt, 1993
- [63] Horstmann, Karl-Heinz: Ein Mehrfach-Traglinienverfahren und seine Verwendung für Entwurf und Nachrechnung nichtplanarer Flügelanordnungen. DFVLR-FB 87-51, 1988
- [64] Heyson, Harry H., Riebe, Gregory D., Fulton, Cynthia E.: Theoretical Parametric Study of the Relative Advantages of Winglets and Wing-Tip Extensions. NASA TP 1020, September 1977
- [65] Ewald, B.: Ein Beitrag zur Leistungsverbesserung von Flugzeugen durch Nachrüsten von Winglets. DGLR-Jahrbuch 1977, Vol. 1, 1978
- [66] Kroo, I., Beckman, E.: Development of the SWIFT - A Tailless Foot-Launched Sailplane. Hang Gliding, Jan. 1991
- [67] Loptien, G. W.: The Effect of Winglets on the KC135A Aircraft. Final Report, 06/197511/1977, Air Force Flight Dynamics Lab, November 1978
- [68] 737-600/700/800/900 Airplane Characteristics for Airport Panning. Boeing Commercial Airplane Group, Rev. A, April 1998
- [69] Büscher, A., Radespiel, R., Streit, Th.: Two-Point-Design of Nonplanar Lifting Configurations using a Databased Aerodynamic Prediction Tool. DGLR-Kongress 2004
- [70] Drela, M.: A User's Guide to MSES 2.95. MIT Computational Aerospace Science Laboratory, 1996
- [71] Dunham, R. E.: Unsuccessful Concepts for Aircraft Wake Vortex Minimization. Wake Vortex Minimization, Proceedings of a symposium held at Washington, D.C., February 25-26, 1976, NASA SP-409, 1977

- [72] Nockemann, Martin: Geschwindigkeitsmessungen im nahen Nachlauf von Tragflügeln mit unterschiedlichen Randbögen und Winglets. Dissertation, RWTH-Aachen, Shaker Verlag Aachen, 1998
- [73] Willert, C., et al.: Application of Doppler Global Velocimetry in Cryogenic Wind Tunnels. 12th International Symposium on Applications of Laser Techniques to Fluid Mechanics, Lisbon, Portugal, 12-15 July 2004, Paper 25-3
- [74] Otto-Lilienthal-Museum Anklam. <http://www.lilienthal-museum.de>, website visited on 16.11.2006
- [75] Zimmer, H.: Die Bedeutung der Flügelendformen beim Tragflügelentwurf für Flugzeuge der zivilen Luftfahrt. DGLR Jahrbuch 1977, Band 1, 1978
- [76] Spillman, J. J., Ratcliffe, H. Y., McVitie, A.: Flight experiments to evaluate the effect of wing-tip sails on fuel consumption and handling characteristics. Aeronautical Journal, July 1979, pp. 279-281
- [77] Spillman, J. J., Fell, M. J.: The effects of wing tip devices on the performance of the BAe Jetstream. AGARD-CP-342, Aerodynamics of vortical type flows in three dimensions, 1983
- [78] Küppers, Udo: Randwirbelteilung durch aufgefächerte Flügelenden - Energiesparen nach biologischem Vorbild. Dissertation, TU-Berlin, Fortschrittsberichte der VDI-Zeitschriften, Reihe 7, Nr. 81, 1983
- [79] Kravchenko, S. A.: The Application of the Wing Tip Lifting Surfaces for Practical Aerodynamic. ICAS-96-4.6.4, 1996
- [80] Smith, Stephen C.: A Computational and Experimental Study of Nonlinear Aspects of Induced Drag. NASA Technical Paper 3598, 1996
- [81] Sunkomat, Eva: Erprobung eines mehrgliedrigen nichtplanaren Randbogens ("Fingerwinglets"). Idaflieg Berichtsheft, 1998
- [82] Smith, M. J., Komerath, N., Ames, R., Wong, O., Pearson, J.: Performance Analysis of a Wing with Multiple Winglets. AIAA-2001-2407, AIAA Applied Aerodynamics Conference, Anaheim, CA, 11-14 June 2001
- [83] Zimmer, H.: Die aerodynamische Optimierung von Tragflügeln im Unterschallgeschwindigkeitsbereich und der Einfluß der Gestaltung der Flügelenden. Dissertation, Institut für Aerodynamik und Gasdynamik, Universität Stuttgart, 1983
- [84] La Roche, U., La Roche, H.L.: Induced Drag Reduction using Multiple Winglets, looking beyond the Prandtl-Munk Linear Model. AIAA-2004-2120
- [85] Santos, Jonathan: Wing tip airfoils. US-Patent 4595160, 17.06.1986

- [86] Klug, Heinz, G.: Auxiliary wing tips for an aircraft. US-Patent 4722499, 02.02.1988
- [87] Mederer, Andreas: Hochauftriebsflügel. German Patent DE-2,149,956, 16.08.1973
- [88] Bunge, U.: Numerische Simulation turbulenter Strömungen im Kontext der Wechselwirkung zwischen Fluid und Struktur. Dissertation, TU Berlin, 2005
- [89] Cone, C. D.: The Design of Sailplanes for Optimal Thermal Soaring Performance. NASA TN D-2052, 1964
- [90] Thomas, F.: Grundlagen für den Entwurf von Segelflugzeugen. 2nd ed., Motorbuch Verlag, Stuttgart, 1984
- [91] Schlichting, H., Truckenbrodt, E.: Aerodynamik des Flugzeuges. Vol. 1, 2nd ed., Springer-Verlag, 1967
- [92] Wintzer, M., Sturdza, P., Kroo, I.: Conceptual Design of Conventional and Oblique Wing Configurations for Small Supersonic Aircraft. 44th AIAA Aerospace Sciences Meeting and Exhibit 9 - 12 January 2006, Reno, Nevada, AIAA-2006-930
- [93] Howe, D.: Aircraft Conceptual Design Synthesis. Professional Engineering Publishing, London, 2000
- [94] Antoine, Nicolas E., Kroo, Ilan M.: Framework for Aircraft Conceptual Design and Environmental Performance Studies. AIAA Journal Vol. 43, No. 10, October 2005
- [95] Truckenbrodt, E.: Zum Übergang von der erweiterten zur einfachen Traglinientheorie bei schiebenden und gefeilten Flügeln. Zeitschrift für Flugwissenschaften, vol. 5, No. 9, 1957, pp. 259-264
- [96] Montgomerie, B.: Methods for Root Effects, Tip Effects and Extending the Angle of Attack Range to $\pm 180^\circ$, with Application to Aerodynamics for Blades on Wind Turbines and Propellers. Swedish Defence Research Agency, FOI-R--1305--SE, ISSN 1650-1942, June 2004
- [97] Hoerner, S. F.: Fluid-Dynamic Drag. Hoerner Fluid Dynamics, 2nd edition, 1965
- [98] Carlson, Harry, W., Mack, Robert, J., Barger, Raymond, L.: Estimation of Attainable Leading-Edge Thrust of Wings at Subsonic and Supersonic Speeds. NASA TP-1500, 1979
- [99] Raymer, Daniel, P.: Aircraft Design, A Conceptual Approach. AIAA Education Series, 1989, pp. 298-302

- [100] Abbott, Ira, H., von Doenhoff, Albert, E.: Theory of Wing Sections. Dover Publications, New York, 1959
- [101] Torenbeek, E.: Synthesis of Subsonic Airplane Design. Delft University Press, 1982 Appendix F. Prediction of the airplane polar at subcritical speeds in the en route configuration, p. 500
- [102] Pfenninger, W.: Design Considerations of Large Global Range High Subsonic Speed LFC Transport Airplanes. AGARD Report No. 654, Special Course on Concepts for Drag Reduction, 28.03. - 01.04 1977, pp. 3-63 - 3-75
- [103] Lan, C. Edward: A Quasi-Vortex-Lattice Method in Thin Wing Theory. Journal of Aircraft, Vol. 11, No. 9, 1974, pp. 518-527
- [104] Hoerner, S. F.: Fluid-Dynamic Lift. Hoerner Fluid Dynamics, 1975
- [105] Bernstein, L.: A note on the potential contribution of wing-body interference drag to the total drag of an aircraft. Aeronautical Journal, November 1997, pp. 417-420
- [106] Tetrault, Philippe-Andre, Schetz, Joseph, A., Grossman, Bernard: Numerical Prediction of Interference Drag of Strut-Surface Intersection in Transonic Flow. AIAA Journal, Vol. 39, No. 5, May 2001, pp. 857-864
- [107] Kohler, M.: Windkanalversuche an Strebenknotenpunkten. Luftfahrt-Forschung, Vol. 15, No. 4, 06.04.1938, pp. 143-152
- [108] Englert, Sonja: Interferenzuntersuchungen an T-Leitwerken, Vorträge des Idaflieg-Wintertreffens 1988, Braunschweig, 1988
- [109] Biermann, D., Herrenstein, H.: The Interference Between Struts in Various Combinations, NACA Report No. 468, 1933
- [110] Critzos, C. C., Heyson, H. H., Boswinkle, R. W.: Aerodynamic Characteristics of NACA 0012 Airfoil Section at Angles of Attack from 0° to 180°. NACA TN 3361, 1955
- [111] Th. von Kármán, Burgers, J. M.: Aerodynamic Theory, Vol. 2, Durand, William Frederick, ed., 1935, p. 41
- [112] Drela, M.: XFOIL: An Analysis and Design System for Low Reynolds Number Airfoils. Conference on Low Reynolds Number Airfoil Aerodynamics, University of Notre Dame, June 1989
- [113] Riegels, F.: Das Umströmungsproblem bei inkompressiblen Potentialströmungen (I. Mitteilung). Ing.-Arch. Vol. 16, 1948, pp. 373-376
- [114] Riegels, F.: Das Umströmungsproblem bei inkompressiblen Potentialströmungen (II. Mitteilung). Ing.-Arch. Bd. 17, 1949, pp. 94-106

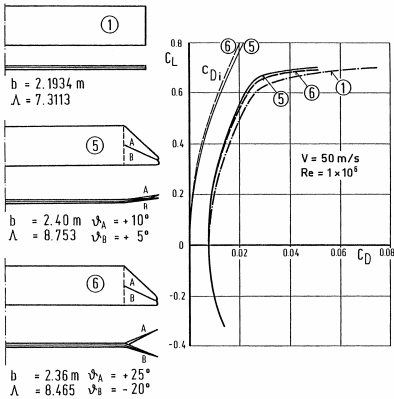
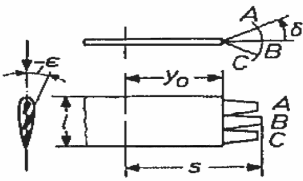
- [115] Roskam, J.: Airplane Design - Part VI: Preliminary Calculation of Aerodynamic, Thrust and Power Characteristics. Roskam Aviation and Engineering Corporation, 1987
- [116] Roskam, J.: Airplane Design - Part V: Component Weight Estimation. Roskam Aviation and Engineering Corporation, 1985
- [117] Kroo, I.: LinAir 4 - A Nonplanar, Multiple Lifting Surface Aerodynamics Program. Desktop Aeronautics, 2003
- [118] Schlichting, H., Truckenbrodt, E.: Aerodynamik des Flugzeuges. Vol. 2, 2nd ed., Springer-Verlag, 1969
- [119] Torenbeek, E.: Development and Application of a Comprehensive, Design-Sensitive Weight Prediction Method for Wing Structures of Transport Category Aircraft. Delft University Press, Report LR-693, 1992
- [120] Wiedemann, Johannes: Leichtbau - Band 2: Konstruktion. 2nd edition, Springer-Verlag, Berlin, 1996
- [121] Ardema, Mark D., Chambers, Mark C., Patron, Anthony P., Hahn, Andrew S., Miura, Hirokazu, Moore, Mark D.: Analytical Fuselage and Wing Weight Estimation of Transport Aircraft. NASA TM 110392, May 1996
- [122] Jupp, J.: Wing aerodynamics and the science of compromise. Aeronautical Journal, November 2001, pp. 633-641
- [123] Hirschel, E., H., Prem, H., Madelung, G. (eds.): Luftfahrtforschung in Deutschland. Die deutsche Luftfahrt, Bernard & Graefe Verlag, Bonn, 2001
- [124] Adair, D., Horne, W. C.: Turbulent separated flow over and downstream of a two-element airfoil. Experiments in Fluids 7, 1989, pp. 531-541
- [125] Feistel, T. W., Corsiglia, V. R., Levin, D.: Wind-Tunnel Measurements of Wing-Canard Interference and a Comparison with Various Theories. Society of Automotive Engineers 810575, 1982, pp. 2026-2039
- [126] van Dam, C.P.: The aerodynamic design of multi-element high-lift systems for transport airplanes. Progress in Aerospace Sciences, Vol. 38, 2002, pp. 101-144
- [127] Jacobs, E. N., Sherman, A.: Airfoil Section Characteristics as Affected by Variations of the Reynolds Number. NACA Report No. 586, 1937, pp. 227-267
- [128] Nenadovitch, M.: Recherches sur les Cellules Biplanes d'Envergure Infinie. Publications Scientifiques et Techniques du Ministère de l'Air, No. 86, Institut Aérotechniques de St.-Cyr, Paris, 1936

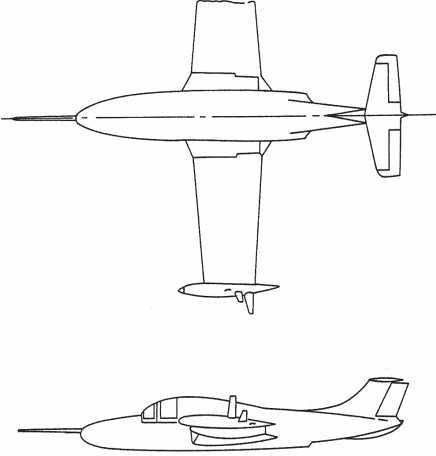
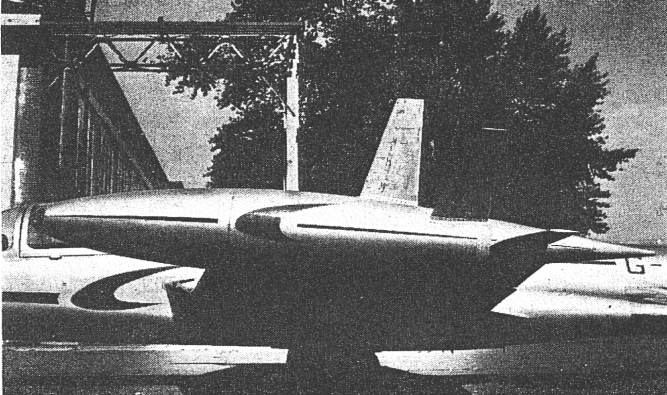
- [129] Gault, D. E.: A correlation of low-speed, airfoil section stalling characteristics with Reynolds number and airfoil geometry. NACA TN 3963, 1957
- [130] Spreiter, R., Steffen, P.J.: Effect of Mach and Reynolds Numbers on Maximum Lift Coefficient. NACA TN 1044, 1946
- [131] Smith, A. M. O.: High-Lift Aerodynamics. Journal of Aircraft, Vol. 12, No. 6, 1975, pp. 501-530
- [132] Page, F. H.: The Handley Page Slotted Wing. Aeronautical Research Council, R&M No. 834, London, 1922
- [133] Carmichael, B. H.: What Price Performance. Soaring, No. 18, May/June 1954
- [134] Horstmann, K. H.: Neue Modellaufwindverteilungen und ihr Einfluß auf die Auslegung von Segelflugzeugen. 15. OSTIV Congress, Räyskälä, Finland, 1976
- [135] EASA Certification Specifications for Normal, Utility, Aerobatic, and Commuter Category Aeroplanes - CS-23, European Aviation Safety Agency, 14.11.2003

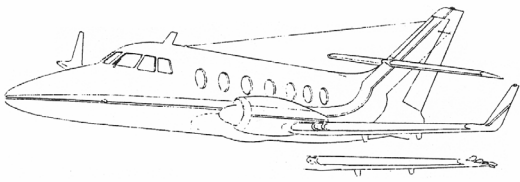
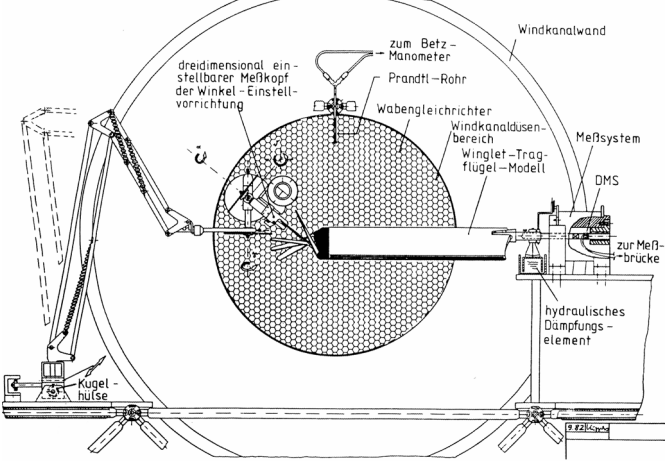
Appendix A: Synopsis of Experiments with Split-Tip and Multiwinglet Configurations Documented in the Open Literature

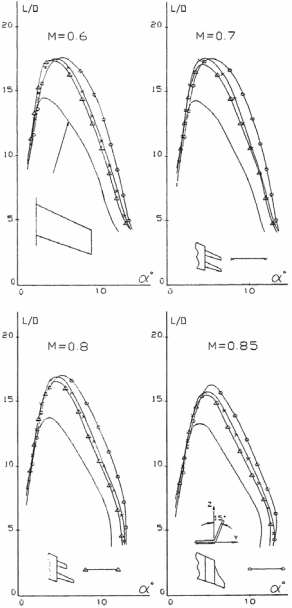
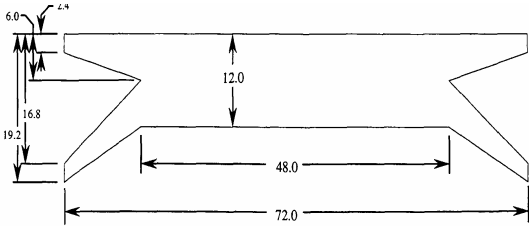
Tab. A1 contains figures illustrating the tested configurations. Summaries regarding experimental aim, conduction and results are presented adjacently. Bibliographic as well as quantitative data is compiled in Tab. A2 from references where such data was available.

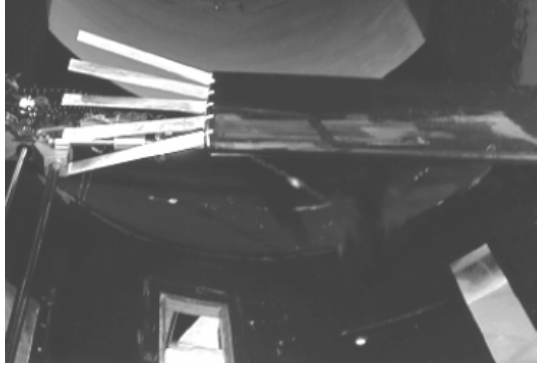
Tab. A1: Published data from windtunnel and flight test studies considering split-tip and multi-winglet configurations.

Author / Title	Year	Reference	Link to Tab. A2
Configuration	Comment		
Lilienthal, O.: "Der Vogelflug als Grundlage der Fliegekunst"	1910	[43]	-/-
	<ul style="list-style-type: none"> - Gliding flights performed - Attempts to utilise flapping multi-winglets to propel the machine were not successful 		
Zimmer, H.: "Die Bedeutung der Flügelendformen beim Tragflügelentwurf für Flugzeuge der zivilen Luftfahrt"	1978	[75]	1
	<ul style="list-style-type: none"> - Comparison of experimental configurations: multi-winglet, split tip, winglet, normal wingtips - Low-speed / low Reynolds number measurements indicate better aerodynamic performance of split tip configurations than multi-winglet configurations with 4 non-planar winglets - Split tip arrangement with dihedral angles of +10 / +5 deg (leading / trailing winglet) slightly better in terms of lift to drag ratio than configuration with greater fan out of +25 / -20 deg 		
Hummel, D.: "The Aerodynamic Characteristics of Slotted Wing-tips in Soaring Birds"	1978	[50]	2
	<ul style="list-style-type: none"> - Comparison of multi-winglet wing with rectangular wing of identical span - Maximum lift to drag ratio of multi-winglet was 0.3% less than that of the rectangular wing but endurance parameter $c_L^{3/2}/c_D$ was 11.7% greater 		

Author / Title	Year	Reference	Link to Tab. A2
Configuration	Comment		
Spillman, J. J.: "The use of wing tip sails to reduce vortex drag"	1978	[57]	3
	<ul style="list-style-type: none"> - Winglets mounted at the tip tank of a jet trainer aircraft M.S. 760 Paris - Reynolds number effects are shown for configurations with three winglets: the total drag coefficient is inferior to that of the original configuration without winglets for lift coefficients lower than 0.42 for the wind tunnel test whilst the flight test results show superior performance of the tip sails across the whole range of lift coefficients 		
Spillman, J. J., Ratcliffe, H. Y., McVitie, A.: "Flight experiments to evaluate the effect of wing-tip sails on fuel consumption and handling characteristics"	1979	[76]	4, 5
	<ul style="list-style-type: none"> - Further measurements on M.S. 760 equipped with three multi-winglets - Aerodynamic performance for trimmed flight conditions: <ul style="list-style-type: none"> ▷ without winglets: $c_{D0} = 0.210$, $k = 0.079$ ▷ with winglets: $c_{D0} = 0.220$, $k = 0.058$ - 9% reduction in minimum fuel flow occurred at $c_L = 0.54$ without winglets and $c_L = 0.60$ with winglets - Fuel flow becomes equal at higher flight speed corresponding to $c_L = 0.23$ - Handling qualities: increased roll damping - Lift off speed reduced 		

Author / Title	Year	Reference	Link to Tab. A2
Configuration	Comment		
Spillman, J. J., Fell, M. J.: "The effects of wing tip devices on the performance of the BAe Jetstream"	1983	[77] (part a))	-/-
	<ul style="list-style-type: none"> - Comparisons of planar wing-tip datum drag data of a BAe Jetstream wind-tunnel model with data measured after attaching conventional winglets or alternative multi-winglets to the wing tips - Uncambered multi-winglet sections performed better than cambered ones at multi-winglet chord based Reynolds numbers of $4.65 \cdot 10^4$ - Always regions of boundary layer separation for single and multi-winglet configurations - Multi-winglets, however, had a lead over the basic wing above $c_L = 0.38$, single winglets above $c_L = 0.52$ 		
Küppers, U.: "Randwirbelteilung durch aufgefächerte Flügelenden - Energiesparen nach biologischem Vorbild"	1983	[78]	-/-
	<ul style="list-style-type: none"> - Automatic configurational optimisation of winglet incidences and dihedrals by means of a genetic algorithm coupled with an automatically controlled manipulator - Small improvements in lift to drag ratio and endurance parameter compared to conventional rectangular wing tip - Experimental setup appears to have produced unreliable results (only wingtip in open jet wind-tunnel, lift derived from root bending moment for assumed fixed centre of pressure) 		

Author / Title	Year	Reference	Link to Tab. A2
Configuration	Comment		
Kravchenko, S. A.: "The Application of the Wing Tip Lifting Surfaces for Practical Aerodynamic"	1996	[79]	6
	<ul style="list-style-type: none"> - Experimental investigation of various winglet and multi-winglet configurations at subsonic and transonic Mach numbers - Comparison of a single winglet with 75 deg dihedral with two smaller planar winglets on a wing with 20 deg quarter chord sweepback shows that the maximum lift to drag ratio of both configurations is about 20% greater than that of a planar wing with a conventional tip and a span equal to the multi-winglet configuration (aspect ratio 4.1, taper ratio 0.8) (M = 0.60, 0.70, 0.80) - M = 0.85: lift to drag ratios of single winglet are 22.5% greater than base wing, multi-winglets are just 18% better - Average performance of single winglet configuration is generally better at other lift coefficients than that for maximum lift to drag ratio 		
Smith, Stephen C.: "A Computational and Experimental Study of Nonlinear Aspects of Induced Drag"	1996	[80]	7
	<ul style="list-style-type: none"> - Numerical and experimental study of split tip configuration effects on lift dependent drag - Experimental results: elliptical wing: $\tau_{ell} = 0.972$ split tip wing: $\tau_{st} = 1.096$ 		

Author / Title	Year	Reference	Link to Tab. A2
Configuration	Comment		
Sunkomat, E.: "Erprobung eines mehrgliedrigen nichtplanaren Randbogens ("Fingerwinglets") "	1998	[81]	8
	<ul style="list-style-type: none"> - Outer wing of Janus Ce equipped with multi-winglet cascades - Span reduced from 20.0 to 18.6 m - Alternative conventional wintip at 18.6 m span - Winglet layout was Trefftz-plane optimised - Initially problems with root separation on winglets 3 and 4 solved by reducing incidence 		
Smith, M. J., Komerath, N., Ames, R., Wong, O., Pearson, J.: "Performance Analysis of a Wing with Multiple Winglets"	2001	[82]	9
	<ul style="list-style-type: none"> - Main wing: NACA0012, winglets: flat pates with rounded leading edges - No L/D advantage compared to wing with winglets removed - Lift curve slope of multi-winglet configuration slightly larger 		
La Roche, U., La Roche, H.L.: "Induced Drag Reduction using Multiple Winglets, looking beyond the Prandtl-Munk Linear Model"	2004	[84]	-/-
	<ul style="list-style-type: none"> - Original wing span of prometheus motor-glider reduced from 23 m to 12 m - multi winglet spans were 1.0 m each, winglets staggered but no dihedral - Maximum lift to drag ratio dropped from 43 to 24 		

Tab. A2: Experimental data of split-tip and multi-winglet configurations.

abbr. meaning

mw main wing

wl winglets

bw basic reference wing

mwl wing with split-tip or multi-winglets

1- elliptical

2- rectangular

3- trapezoidal

1- symmetrical

2- cambered

3- camb., lam.

No	Authors	Title	Year of Ref.	Wing Planform		AR		Section		nWL	eta0
				bw	mwl	bw	mwl	mw	wl		
1	Zimmer, H.	Die Bedeutung der Flügelendformen beim Tragflügelentwurf für Flugzeuge der zivilen Luftfahrt	1978	2	2	7.31	8.75	1	1	2	0.78
2	Hummel, D.	The Aerodynamic Characteristics of Slotted Wing-tips in Soaring Birds	1978	2	2	4.00	4.47	1	1	3	0.71
3	Spillman, J. J.	The use of wing tip sails to reduce vortex drag	1978	2	2	5.12	7.09	2	2	3	0.89
4	Spillman, J. J.	The use of wing tip sails to reduce vortex drag	1978	2	2	5.12	7.09	2	2	3	0.89
5	Spillmann, J. J., et. al.	Flight experiments to evaluate the effect of wing-tip sails on fuel consumption and handling characteristics	1979	2	2	5.12	7.09	2	2	3	0.89
6	Kravchenko, S. A.	The Application of the Wing Tip Lifting Surfaces for Practical Aerodynamic	1996	3	3	3.81	5.58	3	3	2	0.8
7	Smith, Stephen C.	A Computational and Experimental Study of Nonlinear Aspects of Induce Drag	1996	1	2	6.66	6.66	1	1	2	0.67
8	Sunkomat, E.	Erprobung eines mehrgliedrigen nichtplanaren Randbogens ("Fingerwinglets")	1998	3	3	21.2	21.2	3	3	5	0.93
9	Smith, M. J., et. al.	Performance Analysis of a Wing with Multiple Winglets	2001	2	2	8.00	10.80	1	1	5	0.8

1- wind tunnel test

2- flight test

No	Dihedral [deg]					Root Incidence [deg]					Winglet Sweep [deg]					Method	Reynolds Numbers		(L/D)max			cL ^{3/2} / cD			ΔGain
	1	2	3	4	5	1	2	3	4	5	1	2	3	4	5		mw	wl	bw	mwl	Gain	bw	mwl	Gain	
1	10	5				-4.5	0				38	20				1	1.00E+06	3.00E+05	24.8	29.0	16.7%	17.7	20.9	18.0%	1.4%
2	20	0	-20			-10	-5	0			0	0	0			1	4.30E+05	9.20E+04	16.98	16.93	-0.3%	10.52	11.9	13.2%	13.5%
3	90	45	0			?	?	?			12	12	12			2	1.14E+06	1.07E+05	9.1	10.4	14.5%	9.1	11.3	25.1%	10.7%
4	90	45	0			?	?	?			12	12	12			2	7.48E+06	7.02E+05	11.5	14.7	27.9%	9.7	13.0	33.9%	6.0%
5	90	45	0			?	?	?			12	12	12			2	7.48E+06	7.02E+05	12.3	14.0	14.0%	10.0	12.5	24.7%	10.6%
6	0	0				-5	-3				30	30				1	1.50E+06	2.00E+05	14.4	17.6	22.2%				
7	0	0				0	0				-4	38				1	1.12E+06	3.80E+05	17.4	18.5	6.3%	14.24	14.64	2.8%	-3.5%
8	15	->	->	->	-20	-ve	->	->	->	0	0	0	0	0		2	1.75E+06	1.51E+05	38.7	39.4	1.8%	36.92	37.38	1.2%	-0.6%
9	20	10	0	-10	-20	0	0	0	0	0	0	0	0	0		1	2.90E+05	3.60E+04	10.9	10.0	-8.2%	7.3	7.3	0.0%	8.2%

Appendix B: Interference Drag Model

B.1 Introduction

Although interference drag is a constantly treated engineering and research topic as recent publications prove (e.g. [105], [106]), there is still no publication that is more comprehensive than the compilation of experimental data by Hoerner [97].

The appendix documents the derivation of design sensitive empirical models based on aforementioned data for the prediction of interference drag that is caused by viscous effects (e.g. boundary layer separation) of

- wing-wall intersections
- T-junctions
- wing-winglet intersections and
- wing-multiwinglet intersections.

Tab. B1 gives an overview on some of the aerodynamic effects relevant for various intersection types.

Tab. B1: Interference effects in incompressible flow.

Configuration	Effects Related to Pressure Distribution	Boundary Layer (BL) Effects	No. of Corners
Wing-Wall (ww)	- For inviscid fluid, the wing pressure distribution would be identical to a configuration with the wing mirrored about the wall plane of symmetry and the wall removed.	- Usually fully developed turbulent wall BL. - Separation ahead of wing leading edge stagnation region due to adverse pressure gradient for wings with no or just moderate sweep at root.	2
T-Junction (T)	1. In the case of simple junctions of identical sections, superimposed pressure distributions cause severer adverse pressure gradients and make the configuration prone to premature BL separation. 2. Above effect can be alleviated according to Kohler [107], Whitcomb [55] or Englert [108] by moving the intersecting surface (the vertical part of the "T") downstream so that the minimum pressure regions do not coincide.	- BL's develop from the leading edge regions and thus have significantly smaller thickness compared to the wall boundary layer of the wing-wall interference case. - In contrast to a straight wall, pressure drag can be exerted onto each aerodynamically shaped part of the configuration. - Earlier BL separation is to be expected in the narrower corner in case of non-orthogonal junctions.	2

Configuration	Effects Related to Pressure Distribution	Boundary Layer (BL) Effects	No. of Corners
Wing-Winglet (wwl)	<ul style="list-style-type: none"> - Fundamentally, the situation is similar to the T-junction. - Cross flow components come into play for lift producing surfaces such as wing-winglet configurations. 	<ul style="list-style-type: none"> - It is possible to design a smoothly rounded junction of intersecting surfaces which eases design for low interference drag compared to the case of T-junctions where fillets must be used for this purpose. 	1
Wing-Multi-winglet (wmwl)	<ul style="list-style-type: none"> - The pressure distribution on the outer parts of the main wing part is shifted downstream due to the presence of the winglets. - Pressure distribution in the connection area of the main wing is distorted by consecutive drop and rise of pressures (suction side) due to the winglets attached to it (chordwise pressure distribution becomes wavy). 	<ul style="list-style-type: none"> - It must be expected that flow separation cannot entirely be avoided, especially if it happens that the spanwise winglet attachment points to the main wing are one after another lined up in the flow direction. - BL load can be relieved by: <ol style="list-style-type: none"> 1. Use of slot flow effects to convey "tired" fluid away from the surfaces so that it cannot impinge on consecutive wings. 2. Spanwise staggering so that the connections of wings to winglets do not directly line up in the streamwise direction. 	1

B.2 Interference Drag of Perpendicular Wing-Wall Intersections

Hoerner collected experimental results of several publications on wing-wall interference and plotted the data versus thickness to chord ratio (ref. [97] p. 8-10, Fig. 23) and lift coefficient (p. 8-10, Fig. 24) respectively. The data can be matched by the following regression function:

$$c_{D,int,bas,c^2} = a_{cl} \cdot c_l^2 \cdot \left(\frac{t}{c}\right)^3 + b \cdot \left(\frac{t}{c}\right)^\lambda + d_{tc0} \quad (B.1)$$

- c_l - sectional lift coefficient at wing root
- (t/c) - maximum thickness to chord ratio
- $a_{cl} = 8.0$ - empirical coefficient
- $b = 0.75$ - empirical constant [97]
- $d_{tc0} = -0,0003$ - interference drag coefficient for flat plate
- $\lambda = 3$ - exponent for wing-wall interference.

The comparisons in Fig. B1 show that the agreement with measurement data obtained for a wing placed between end plates and having an AR = 2 and symmetrical sections at $Re_c = 1 \dots 2 \cdot 10^6$ is satisfactory. In order to obtain the drag increment for an aircraft,

the results must be multiplied by the number of intersections (typically two for a wing-fuselage intersection).

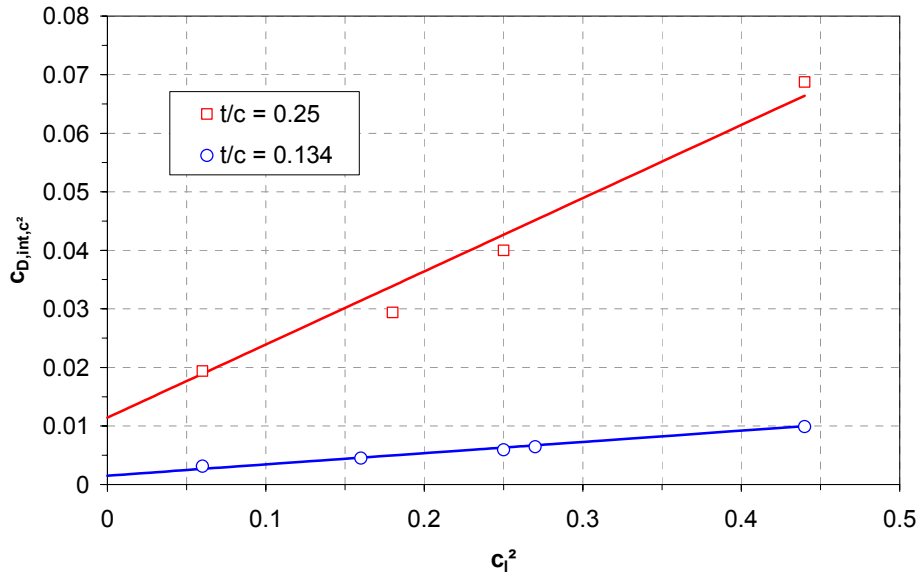


Fig. B1: Wing-wall interference drag versus lift coefficient.

B.3 Inclined Wing-Wall Interference Drag

The measurement data give evidence that lateral inclination of the wing against the wall increases interference drag most likely because of increased separation in the narrower of the two corners (see lower part of Fig. B2). The boundary layers of two wings having symmetrical wing sections placed in a biplane configuration at zero angle of attack merge after some distance from the leading edges if the distance between the surfaces is small enough. If the boundary layers are turbulent, the close spacing may inhibit the re-energising of the boundary layers with freestream fluid to a certain extent. Moreover, both wing sections produce a convergent-divergent channel flow. Minimum pressure will be decreased compared to the situation where the surfaces are individually placed in an unbounded fluid and the adverse pressure gradient will be consequently greater which may cause the boundary layers to separate before reaching the trailing edges with a subsequent rise of pressure drag. Contrarily, positive as well as negative sweep yield a decrease in interference drag, partly due to a lower effective thickness to chord ratio (primarily if wing is being swept, not sheared) and partly due to mitigation of necklace vortex formation ahead of the root section due to separation of the wall boundary layer caused by the adverse pressure gradient towards the stagnation zone at the wing leading edge root (upper part of Fig. B2).

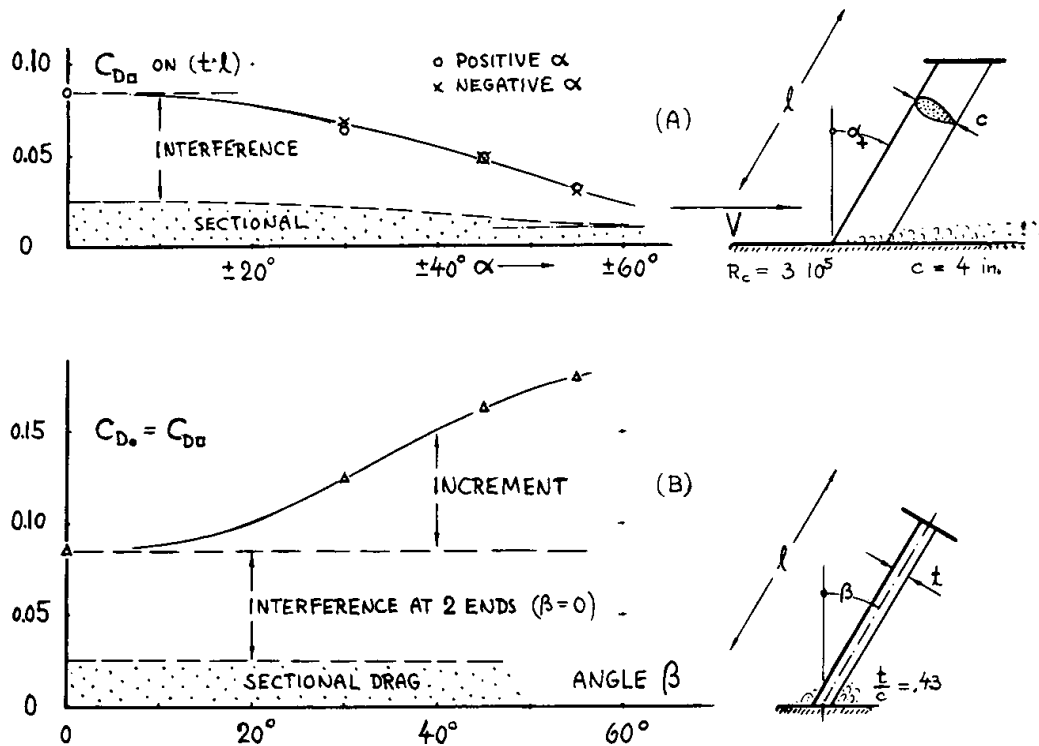


Fig. B2: Total drag of a strut as a function (A) of sweep angle and (B) of lateral angle of inclination ([97], chapter XIII, Fig. 25).

The trends will be used to extend the basic model (eq. (B.1)) for sweep and dihedral effects. The sweep correction is only applied to the term that is independent of lift because it is expected that stagnation pressures at the leading edge do not change significantly with angle of attack of the wing root section.

$$C_{D,int,ww,c^2} = k_{int,dih} \cdot \left[a_{cl} \cdot c_l^2 \cdot \left(\frac{t}{c}\right)^3 + b \cdot \cos(\Lambda_{le})^2 \cdot \left(\frac{t}{c}\right)^\lambda + d_{tc0} \right] \quad (B.2)$$

where Λ_{le} - leading edge sweep, replaces α used in Fig. B2

The total interference drag due to dihedral will be broken down into two parts, one part stands for the inner and the other part for the outer corner. To start with, the equation for the inner corner is

$$k_{int,dih,i} = \frac{|\gamma|}{\pi} + g \begin{cases} |\gamma| \leq \frac{\pi}{2}: & g = 0 \\ |\gamma| > \frac{\pi}{2}: & g = \sin\left(|\gamma| - \frac{\pi}{2}\right)^2 \end{cases} \quad (B.3)$$

and for the outer corner respectively

$$k_{\text{int,dih,o}} = 1 - \frac{|\Upsilon|}{\pi} + g \begin{cases} \pi - |\Upsilon| \leq \frac{\pi}{2}: & g = 0 \\ \pi - |\Upsilon| > \frac{\pi}{2}: & g = \sin\left(\frac{\pi}{2} - |\Upsilon|\right)^2 \end{cases} \quad (\text{B.4})$$

with $\Upsilon = \pi/2 - \beta$ - dihedral angle [rad]

β - lateral inclination angle as defined in [97] and shown in Fig. B2.

The lateral inclination correction factor for the wing-wall case is

$$k_{\text{int,dih}} = k_{\text{int,dih,i}} + k_{\text{int,dih,o}} \quad (\text{B.5})$$

which assumes a numerical value of 1.0 for $\Upsilon = \pi/2$.

If the wing or strut is mounted to the corner of a fuselage with square cross section and, if the one angle becomes larger than 180 degrees, the inclination correction factor becomes zero.

B.4 Interference Drag of T-junctions

In case of the wing-wall interference it is important to consider the boundary layer properties, i.e. the thickness of the wall boundary layer. The experimental data upon which eq. (B.1) is based have been obtained for thicknesses of the wall boundary layer of $\delta/c = 10\%$, which, according to Hoerner, is typical for wing-fuselage junctions. For T-junctions of wings or struts at zero lift, there is no boundary layer ahead and thus interference drag results can be expected to differ from the wing-wall case. The parameters of the basic equation (B.1) are altered, so that the data given in Figure 26 of chapter 8 of ref. [97] can be closely matched as shown in Fig. B3 using following factors:

- $a_{\text{cl}} = 8.0$ - empirical coefficient
- $b = 15$ - empirical coefficient
- $d_{\text{tc0}} = -0,0005$ - empirical offset for T-junction [97]
- $\lambda = 4$ - exponent for T-junction.

An additional factor $k_{\text{int,det}}$ will be introduced catering for the design quality of the assembly. Values for the additional factor are stated in Fig. B3. Properly designed fillets may reduce the interference drag by up to 75%.

$$C_{\text{D,int,T,c}^2} = k_{\text{int,det}} \cdot C_{\text{D,int,bas,c}^2} \quad (\text{B.6})$$

The factor thus takes into account the efficiency of fillets and fairings.

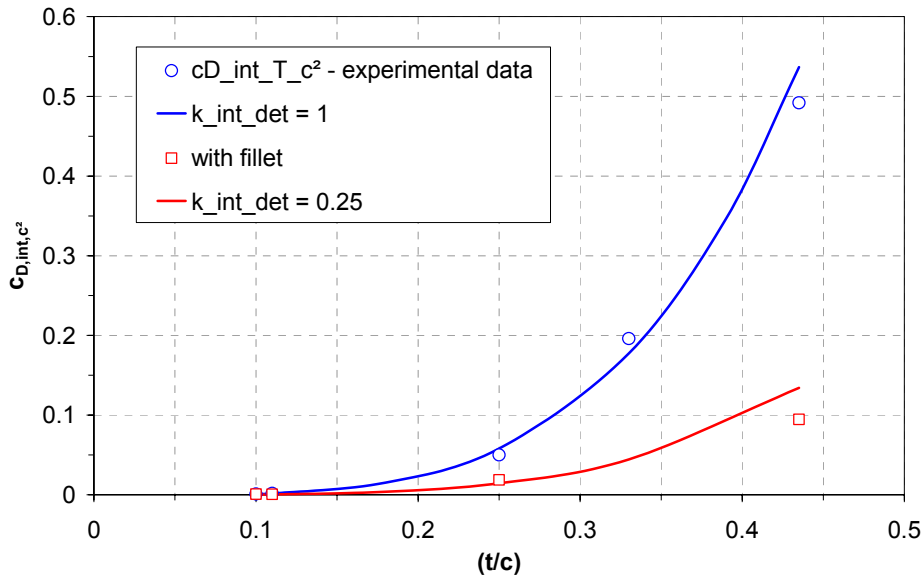


Fig. B3: Measured and calculated zero lift interference drag coefficients of T-junctions (Measurement data from reference [97]).

Reference [97] contains no data for the development of interference drag under conditions where the surfaces that make up the T-junction are aerodynamically loaded. Furthermore, no data is given for T-junctions with streamwise offsets that would allow assessing the effectiveness of tailored local chordwise pressure distributions with respect to interference drag reduction as discussed in Tab. B1.

B.5 Wing-Winglet Interference Drag

The experimental interference drag data for right angle intersections of wings with NACA 0010 sections obtained for $Re_c = 1.0 \cdot 10^6$ are useful for the calibration of the present method (compare Fig. 31 of ref. [97]). In contrast to the T-junction, the dihedral effect must be considered

$$C_{D,int,wwl,c^2} = C_{D,int,bas,c^2} \cdot k_{int,dih} \cdot k_{int,det} \quad (B.7)$$

Once again, no data is given for lift producing conditions. The measurement data for the sharp corner with $r/c = 0.0$ can be matched with the same settings as used for the T-junction. The factor $k_{int,dih}$ in equation (B.5) is set to $k_{int,dih,i}$ because, by definition, only one interference corner is active. It is thus assumed that the interference drag for orthogonal junctions is exactly half the drag found in the case of T-junctions.

Biermann and Herrenstein [109] determined the interference drag of streamline struts intersecting at various angles from $\Upsilon = 0$ up to 164 degrees. With the factors set as for the T-junction and considering the dihedral effect for only one corner, the agreement of the present model with the measurement data is satisfactory (Fig. B4).

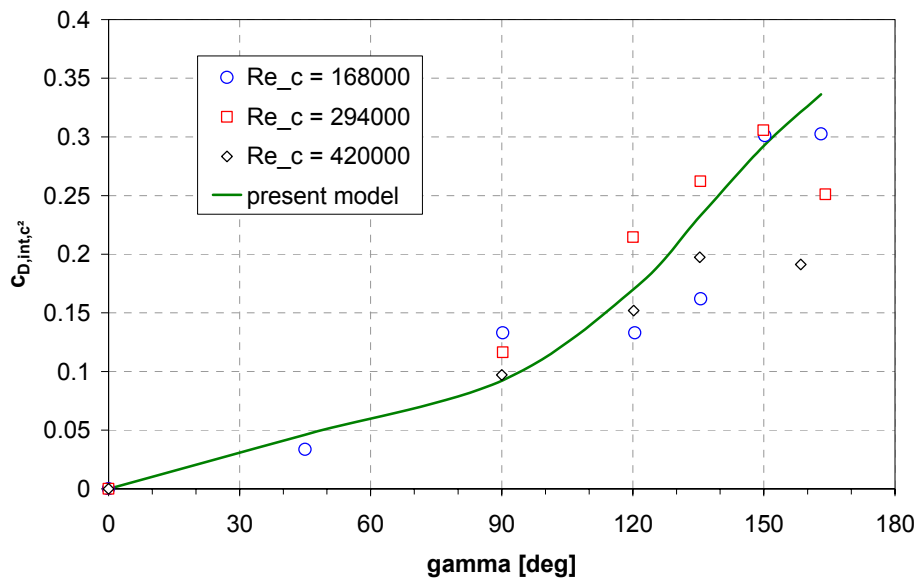


Fig. B4: Interference drag coefficients of symmetrical streamline struts intersecting at various angles (measurement data at zero lift, $(t/c) = 1/3$, reference [109]).

B.6 Multiwinglet Configurations

Interference between two streamlined struts in tandem configuration with $(t/c) = 1/3$ is substantially different to that of bluff bodies such as circular cylinders or spheres (original reference [109], discussion in [97]). A favourable interference is found in the case of bluff bodies in tandem configuration, particularly if the spacing between the bodies is less than three times the diameter of the bodies. Contrarily, the total drag of two streamlined struts that are identical in shape is virtually unaffected by streamwise stagger. A drag increase of no more than 25% above the sum of drag forces measured for both struts independently is found for close-coupled struts with $x/c = 1$ (x -distance between trailing edge of leading strut and leading edge of trailing strut), declining to zero at $x/c > 1.5$. For $x/c = 1$ the forward strut experiences net thrust whereas the rear strut experiences increased drag. An interpretation by Hoerner is that the flow separates from the rear of the second strut because of the momentum deficit within the wake coming from the first strut. This increases drag on the rear strut while the increased static pressure between the two struts is pushing the first one forward. So far only zero lift conditions are considered. It must once again be assumed that the behaviour is different in lift producing conditions but detailed experimental data is not available.

Smith [80] reports on flow separation at the root of the rear winglet of his split tip configuration due to the flow separation on the outer sideward face of the inner wing just ahead of the attachment of the downstream winglet. However, the effect is expected to be less significant for wing-winglet combinations than for wing-wall intersections for geometrical reasons and hence the effect is covered by supplemental drag increments.

According to common practice, the interference drag coefficients are based on the "chord area" c^2 . A question arises what the suitable reference area may be for configurations with unequal chords on both sides of the intersection. The most plausible reference area appears to be $c_{t,0} \cdot c_r(i)$ ($i = 1 \dots n_{wl}$) shown as shaded surfaces in Fig. B5 for single (a) and multiwinglet configurations (b). According to the suggested procedure, the total reference areas of both configurations are equal. To distinguish reference areas of individual winglets the index " $c^* 2$ " will be used, where $c^* 2(i) = c_{t,0} \cdot c_r(i)$.

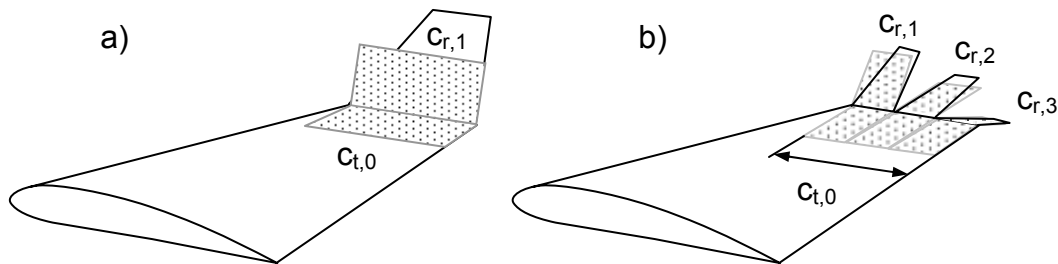


Fig. B5: Reference surfaces for interference drag: a) Wing-winglet b) Wing-multi-winglet.

Streamwise arrangements of elements may feature reduced but more likely increased drag as discussed above. For the current state of the model, the multiwinglet configuration would have a smaller interference drag than the single winglet configuration because of smaller mean dihedral angles. Experimental results nevertheless give evidence that it is much harder to design a multi-winglet configuration with small interference drag than to accomplish this task for a single winglet configuration. Sunkomat [81] reports on flow separation on the latter two winglets of a five-winglet system, where the local incidences had been set to values required for maximum span efficiency. Separations were removed by a reduction of the incidences of the affected surfaces. Nevertheless, it can be reasonably expected that profile drag and especially interference drag in surface junction regions tend to be increased.

To alleviate some of the shortcomings of the basic concept, the following approach is suggested. In addition to the basic interference drag, an increment is added for multiwinglet systems. The following interference drag coefficient expression is referred to the winglet root chord length squared.

$$c_{D,int,wmwl,cr^2}(i) = \left[a_{cl} \cdot c_{l,r}(i)^2 \cdot \left(\frac{t}{c} \right)_i^3 + b \cdot \left(\frac{t}{c} \right)_i^\lambda + d_{tc0} \right] \cdot k_{int,dih}(i) \cdot k_{int,det}(i) \cdot \frac{c_{t,0}}{c_r(i)} + \Delta c_{D,int,ts,cr^2}(i) \quad (B.8)$$

The Δ -term shifts the streamwise interference drag distribution so that the trailing elements ('ts' trailing surfaces) experience higher drag. This add-on represents the often

higher risk of separation on trailing surfaces of lifting surface cascades. Looking at a slotted slat-wing-flap system at high lift, it will frequently be observed that the flow remains attached on the slat and main wing upper surface but separates on the suction side of the flap. The profile drag of the trailing surface in this case will consequently be much higher than that of the other elements.

$$\Delta C_{D_{int,ts,cr^2}}(i) = C_{d,p,r}(i) \cdot k_{ts}(i) \quad (B.9)$$

where $C_{d,p,r}(i)$ - profile drag coefficient of root section of winglet i

$$k_{ts}(i) = a_{ts} \cdot \left(\frac{i-1}{n_{wl}-1} \right)^2 \cdot \ln(0.75 \cdot n_{wl}) \quad | \quad n_{wl} \geq 2$$

$a_{ts} = 1.5$ - calibration factor

i - streamwise winglet index starting with 1

n_{wl} - number of winglets

The factor $k_{ts}(i)$ introduces an increase of the functional value with increasing number of winglets n_{wl} because it is supposed that the interference drag also grows. The factor is applied to the local profile drag $C_{D,p,r}(i)$.

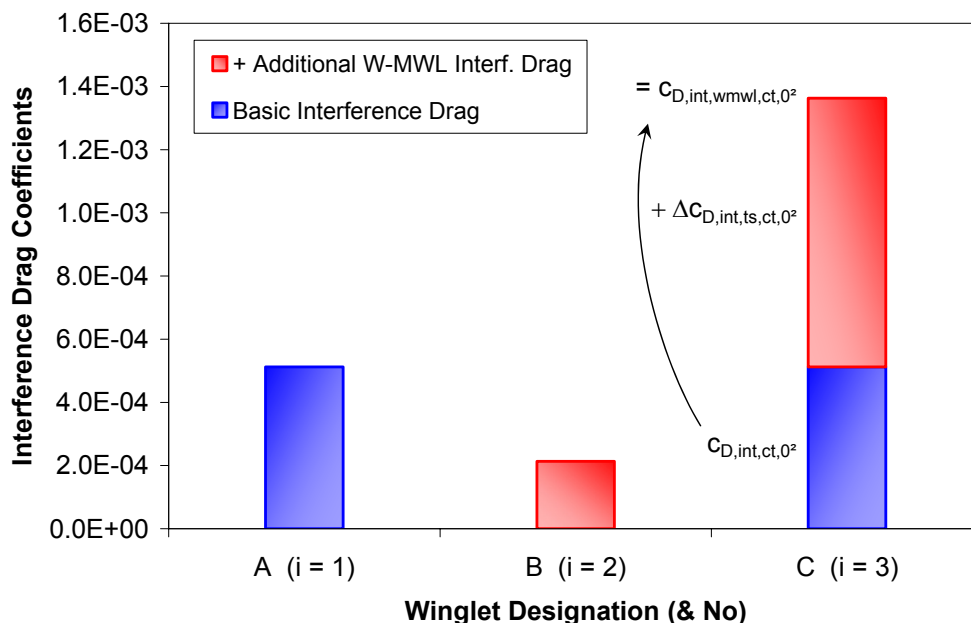


Fig. B6: Cumulative plot of basic and additional interference drag contributions of a wing-multiwinglet (M-MWL) assembly ($n_{wl} = 3$, drag coefficients with respect to the inner wing tip chord area $c_{tip,0}^2$, winglets set at $+45^\circ$, 0° , -45°).

Fig. B6 depicts the basic and additional interference drag contributions as a function of winglet number. The values were obtained for a multiwinglet cascade attached to a

rectangular wing (local lift coefficient at the inner wing tip to which the winglets were attached was 0.51, chord base Reynolds number = $6.6 \cdot 10^6$).

It should be mentioned that although the individual winglets will be given individual interference drag increments, the results cannot be expected to be always accurate. However, more confidence can be placed in the resulting total interference drag value

$$D_{\text{int,wmwl}} = q \cdot \sum_{i=1}^{n_{\text{wl}}} C_{D,\text{int,wmwl},cr^2}(i) \cdot C_r(i)^2 \quad (\text{B.10})$$

Appendix C: Hybrid Method to Estimate Chordwise Pressure Distributions on the Basis of VLM Results

C.1 Introduction

The concentrated vortex singularities make it impossible to directly derive useful contour velocities and pressure distributions from vortex lattice solutions. To overcome this problem, special relations between different methods that are commonly based on potential theory can be exploited to set up a hybrid method for the estimation of the surface pressure distribution based on three-dimensional VLM results.

A starting point is the similarity between the discrete vortex lattice method with its "lumped" vortex elements and the thin airfoil theory based on continuous circulation distributions. The basic thin airfoil theory tackles mean line problems only. However, Riegels [113], [114] successfully extended the theory for sections of finite thickness. The present method suggests to use the three-dimensional VLM results for individual chordwise strips of lattice elements to approximate chordwise circulation distributions similar to those obtained from thin airfoil theory. The thickness effect is then added following the lead of Riegels' approach in order to obtain pressure distributions for all chordwise strips of the configuration. Finally, velocities induced by other lifting surfaces that are tangent to the mean line of each wing section are superposed. Corrections for wing sweep based on simple sweep theory are applied where applicable.

C.2 Chordwise Pressure Distributions of Wing Sections

Riegels developed an extension of thin airfoil theory method that incorporates the thickness effect by studying results obtained by means of a conformal mapping technique despite the fact that the final method is solely based on singularity distributions. Riegels used a circulation distribution for the angle of attack and the camber effects, and separately a source/sink model for the thickness effect. The particular speciality of the approach is that Riegels discretised the section geometry by means of a Fourier-approach

$$\left(\frac{y}{c}\right)(\varphi) = \frac{1}{2} \left(\sum_{i=1}^{n_i} a_i \cos i\varphi + \sum_{i=1}^{n_i} b_i \sin i\varphi \right) \quad (\text{C.1})$$

where	$a_i = 2 \cdot m \cdot a_{i,c}$	- Fourier coefficients for the mean line
	m	- maximum relative camber (maximum elevation of the camber line above the chord line divided by the chord length)
	$a_{i,c}$	- Fourier coefficients for generic mean line shape

- $b_i = 2 \cdot (t/c)_{\max} \cdot b_{i,t}$ - Fourier coefficients representing thickness distribution
 $b_{i,t}$ - generic shape of the thickness distribution.

The transformation of the chordwise coordinate ξ into a continuous coordinate φ guarantees a unique allocation of each point on the profile contour (see illustration in Fig. C1).

$$\begin{aligned}
 \xi &= \frac{1}{2} \cdot (1 + \cos \varphi) & 0 \leq \varphi \leq 2 \cdot \pi \\
 &= \cos^2 \frac{\varphi}{2}
 \end{aligned} \tag{89}$$

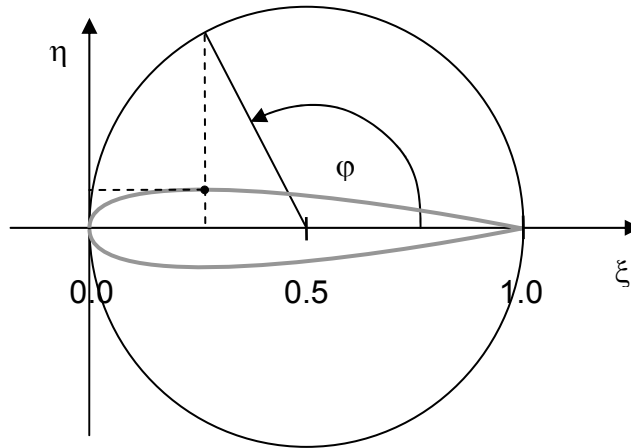


Fig. C1: Cosine mapping of airfoil section contour.

The advantageous properties of Fourier series regarding analytical integration lead to a useful solution for the contour velocities

$$\frac{Q_t}{Q_\infty} = \frac{\left\{ \cos \alpha \left(\sin \varphi + \sum_{i=1}^{n_{i_c}} i a_i \cos i \varphi + \sum_{i=1}^{n_{i_t}} i b_i \sin i \varphi - \sum_{i=1}^{n_{i_c}} i a_i \right) + \sin \alpha (1 - \cos \varphi) \left(1 + \sum_{j=0}^{n_j} \beta_j \cos j \varphi \right) \right\}}{\sqrt{\sin^2 \varphi + \left(\sum_{i=1}^{n_{i_t}} i b_i \cos i \varphi - \sum_{i=1}^{n_{i_c}} i a_i \sin i \varphi \right)^2}} \tag{C.2}$$

with $\beta_0 = \sum_1^{n_{i_t}} i b_i$; $\beta_j = 2 \sum_{i=1}^{n_{i_t}} [(2i + j - 1) \cdot b_{2i+j-1} + 2i b_{2i+j}]$

from which the incompressible pressure distribution immediately follows from $c_p = 1 - (Q_t/Q_\infty)^2$. Infinite numbers of Fourier terms for camber n_{i_c} and thickness n_{i_t} are stated in the original reference. However, for practical use, realistic results can already be obtained if the Fourier series are truncated after a much lesser finite number of terms

determined by the required accuracy of the approximation and/or the number of elementary solutions available for which a Fourier series approximation is required.

Examining the nominator of eq. (C.2) from left to right, the first expression $\sin \varphi$ in the $\cos \alpha$ -term stands for the freestream velocity component that is tangent to the section contour. While the b-sum stands for the source distribution at the mean line that is required for the cancellation of the freestream velocity components normal to the thickness distribution the a-sums represent the perturbation velocities at the contour due to the circulation distribution caused by camber. The basic effect of inclining the chord line against the freestream direction is accounted for by the expression $\sin \alpha (1 - \cos \varphi)$. The β -sum is a thickness correction to this term. The denominator root cancels singular leading edge contour velocities that would otherwise occur except for one specific angle of attack. It has been shown by Riegels that the equation is identical to an equivalent and exact expression from conformal mapping as far as the airfoil section is symmetrical, i.e. all a's are zero and the angle of attack is zero. Yet the Fourier coefficients must be found.

The cosine series in equation (C.1) stands for the mean line shape and the sine series for the thickness distribution. There is only one set of thickness coefficients $b_{i,t}$ for the NACA 4 digit thickness distribution. Experience has shown that already five coefficients yield satisfactory results: $b_{1,t} = 0.436$, $b_{2,t} = -0.149$, $b_{3,t} = -0.0158$, $b_{4,t} = -0.0142$, $b_{5,t} = -0.00673$. If a different thickness contour has to be used or if the position of the maximum thickness is changed, the coefficients must be adapted accordingly.

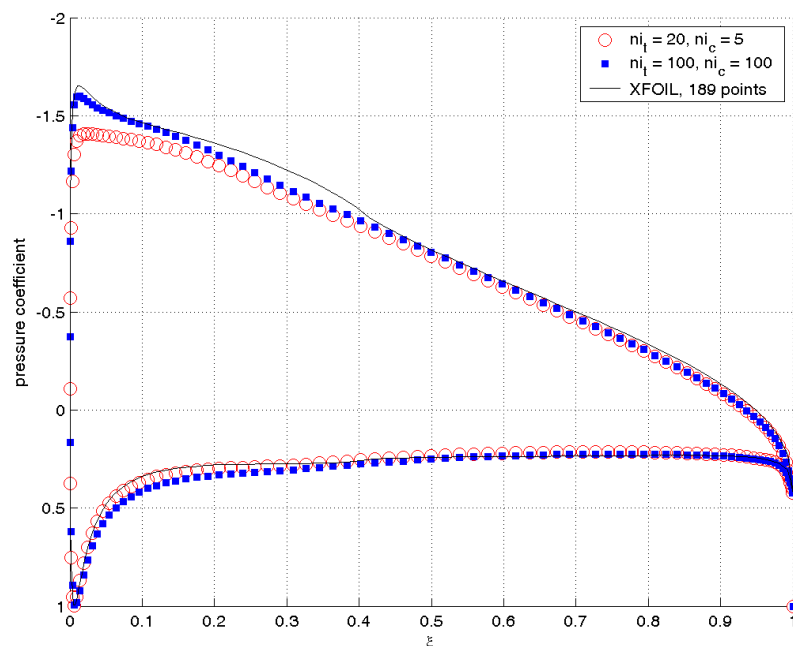


Fig. C2: Comparison of NACA 4412 pressure distributions ($\alpha = 5$ deg, $M_\infty = 0$).

Fig. C2 compares the results of Riegels' method with those obtained from the surface panel programme XFOIL [112]. It can be noticed that a close approximation of the panel results was only achieved after increasing the number of Fourier coefficients, both for thickness and camber. However, the accuracy for the lower number of coefficients appears acceptable for conceptual design purposes.

For the actual application in connection with the vortex lattice method, the coefficients $a_{i,c}$ are not directly taken from the camber shape as in the original method. Instead they are derived from the chordwise circulation distributions that result from the vortex lattice computation. The rationale is that the coefficients a_i do not only represent the geometric mean line shape but also the chordwise circulation distribution according to thin airfoil theory, which will be changed by mutual interference of multi-airfoil systems. Also, the local effective angle of attack is derived from the circulation distribution because it will in general be different from that measured between the freestream and the chordline. This offers the chance of incorporating three dimensional effects in the computation of the chordwise pressure distributions. Interference effects are thus automatically included as far as angle of attack and camber effects are concerned. What is not considered is the interference due to thickness. If two symmetrical sections, e.g. NACA 0015, are placed parallel to the stream and on top of each other with a vertical gap in between, the pressure distributions of a single surface would be identical to the one obtained for a single airfoil alone. Pressure distributions are thus only valid for lifting surfaces in unbounded fluids and for cases where the interference due to thickness does not play an important role. It is assumed that the last condition applies to multi-winglet cascades which are predominantly staggered in horizontal direction. Caution is advised if the pressure distributions at intersections of lifting surfaces are studied if they have finite thicknesses, especially if the intersection is not smoothed.

The fact that the circulation distribution $\gamma(\varphi)$ is directly affected by the geometric coefficients a'_i can be readily seen from equation 8.15 of reference [111]

$$\frac{\gamma(\varphi)}{2 \cdot Q_\infty} = \sum_{i=1}^{nc} a'_i \cdot \frac{\cos i\varphi - 1}{\sin \varphi} \quad (C.3)$$

In contrast to eq. (C.2), this equation is only applicable in the context of thin airfoil theory and if small perturbation assumptions are satisfied.

In either case, i.e. eq.'s (C.2) or (C.3), it can be shown that the first coefficient mainly represents the negative value of the angle of attack. If the effective angle of attack assumes the value of the coefficient $-a'_1$, a_1 must be set to zero if to be used in eq. (C.2). Unfortunately, a'_1 also contains a part of the camber distribution, i.e. the effective mean line incidence. For symmetrical sections and those with a chordwise symmetrical mean line and a position of maximum camber at half chord (such as NACA X5XX), the

coefficient a_1 becomes zero. The error with regard to the angle of attack is zero in this particular case, such that $\alpha = -a'_1$. For other camber lines, the pressure distributions obtained from eq. (C.2) will be identical to that of the underlying thin airfoil theory if zero thickness is stipulated. Whatever the correct subdivision may be, if α is set to $-a'_1$, the Riegels' a_1 defined by the camber shape is contained in the angle of attack. An inconsistency exists since the camber coefficient as part of the angle of attack affects the thickness part, which is the second sum in the nominator of equation (C.2). If the camber coefficient a_1 would be explicitly determined it would only affect the first term and hence the outcome would be different. Thickness increases the lift curve slope to values greater than the corresponding slope of $2 \cdot \pi$ of thin airfoil theory. With the unfavourable effect present, the lift curve slope would be even slightly higher. Nevertheless, the systematic relative error in lift curve slope for a NACA 4412 airfoil section is just 0.28%.

Practically the coefficients a_i are derived from the discrete chordwise circulation distribution as delivered by the vortex lattice method by means of solving a set of linear simultaneous equations built from eq. (C.1). It is possible to determine as many coefficients ($a_1 \dots a_{nc}$) as the number of chordwise lattice elements allows. Realistically the upper limit of coefficient number is limited to five because the interpolation can result in oscillations of the solution if larger numbers are used. For camber shapes without an inflection point a minimum number of two elements is required to represent a camber effect. Actually a_2 is the most important coefficient because it describes the shape of a circular arc with a maximum at half chord location.

C.3 Approximation of Continuous Chordwise Circulation Distributions from VLM-Results as a Prerequisite to Obtain Wing Pressure Distributions

The lumped vortex model is the fundamental basic feature of vortex lattice methods. A single lumped vortex representation of a flat plate which is placed at the quarter chord location in connection with the requirement of zero normal flow at the three-quarter chord location produces the same total circulation and thus the same lift as a vortex distribution that induces constant downwash along the chord. Furthermore, the pitching moments are identical in both cases (zero about the quarter chord). The flat plate profile can also be discretised with two or arbitrarily more such basic elements while the basic properties regarding lift, circulation and pitching moment are retained. The continuous thin airfoil circulation distribution mentioned above is approached in the limit of the number of chordwise elements increasing towards infinity using the approximation

$$\gamma_{d,i} = \frac{\Gamma_i}{c_i} \quad (\text{C.4})$$

where Γ_i - circulation of lattice element i
 c_i - chordlength of surface element i .

This property is exploited for finding the camber coefficients from which the continuous circulation distribution can be calculated. Although the distribution approximated on the basis of the discrete lattice circulations and equation (C.4) resembles that of the continuous distribution, it is not identical. This can be shown by a single lumped vortex. According to thin airfoil theory the circulation is

$$\Gamma = \pi \cdot \alpha \cdot Q_\infty \cdot c$$

so that the circulation per chord is

$$\gamma_d = \pi \cdot \alpha \cdot Q_\infty$$

The expression can be divided by the angle of attack and the free stream velocity leaving an average value for the approximation of the chordwise load distribution of

$$g_d = \frac{\gamma}{\alpha \cdot Q_\infty} = \pi$$

The equation for the circulation distribution of a flat plate is known from thin airfoil theory (reference [111]):

$$g_c = \frac{\gamma}{\alpha \cdot Q_\infty} = 2 \cdot \frac{1-\xi}{\sqrt{\xi-\xi^2}} \quad (\text{C.5})$$

Evaluation at the quarter chord point where $\xi = 0.25$ yields

$$g_c = 2 \cdot \sqrt{3} = 3.464$$

If one would try to approximate the load distribution on the basis of the discrete load value g_d , the approximated value would be $g_c/g_d = 1.103$, i.e. about 10% too small. For more than one element the discrete load values can be computed according to the standard VLM approach. The equation stipulating the Neumann boundary condition at the $3/4$ -chord location on the chordwise lattice element j is

$$\sum_i^n \frac{g_{d,i}}{1/2 + j - i} = 2 \cdot \pi$$

This equation can be used n times to set up a set of simultaneous linear algebraic equations, which can be solved as described in section 3.1.1.2 of the main text for the vector

$$\mathbf{x} = \begin{pmatrix} g_{d,1} \\ \vdots \\ g_{d,i} \\ \vdots \\ g_{d,n} \end{pmatrix}$$

which contains the dimensionless circulations of an chordwise array of lattice elements. The coefficient matrix is established as follows

$$A(j,i) = \frac{1}{1/2 + j - i} \quad i = \{1, \dots, n\}, j = \{1, \dots, n\}$$

and the right hand side vector is simply

$$b(j) = 2 \cdot \pi$$

The resulting loads g_d marked out at the lattice quarter chord locations are depicted in Fig. C3 along with the respective values for the continuous distribution g_c according to eq. (C.5). The difference of both distributions for $n = 16$ is small, except for the first and the last elements as far as the ratios of the continuous to the discrete values are concerned (see lower subplot of Fig. C3). Referring to the upper part of Fig. C3, the small loading at the trailing edge makes the deviation virtually invisible. The difference at the leading edge is more distinct and the ratio of the continuous value divided by the discrete value approaches 1.1284 in the limit of the number of elements n approaching infinity. The difference at the leading edge predominantly affects the resolution of the suction peak. Since thin airfoils always exhibit singular velocities at the leading edge at ξ approaching 0 with the exception of one angle of attack (e.g. $\alpha = 0$ deg for flat plates), it is expected that the correction factor can not only be applied to a flat plate configuration but cambered mean lines as well.

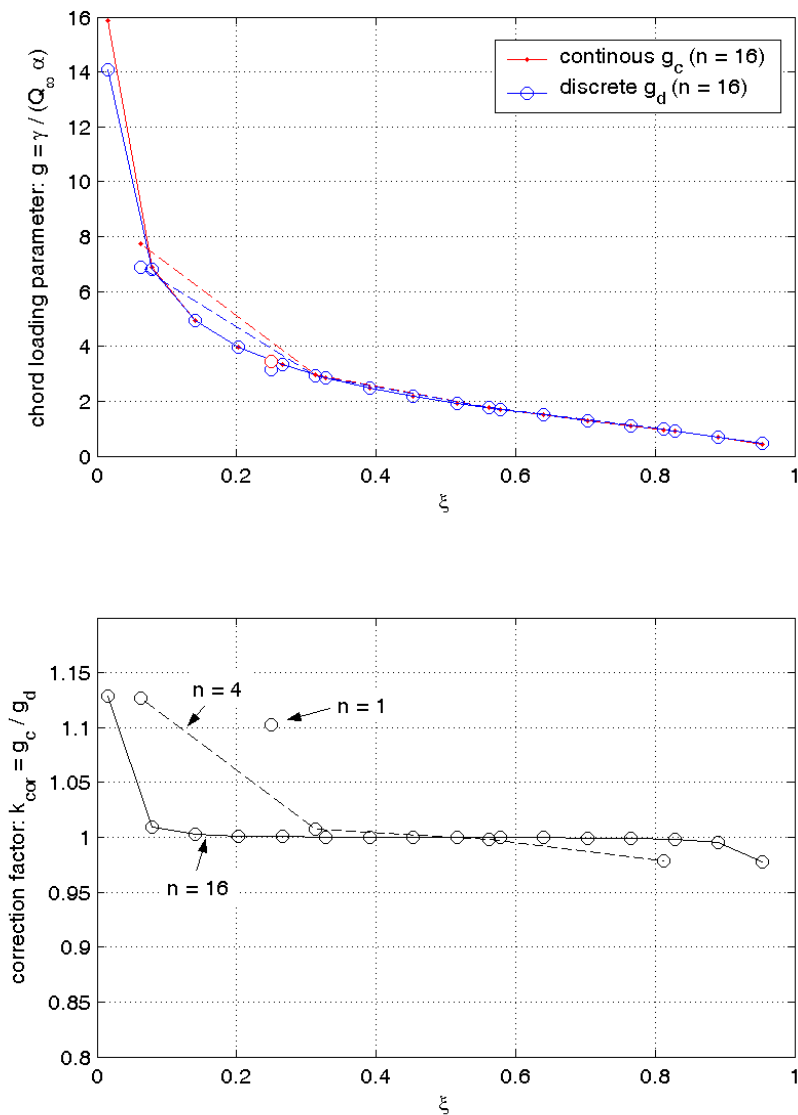


Fig. C3: Comparison of discrete and continuous load distributions for a flat plate.

Tab. C1 and Fig. C4 compare corrected chordwise circulation distributions of NACA 4412 and NACA 0012 sections with three different chordwise lattice discretisations. The lattice circulations have been corrected as described above:

$$\gamma_{d,i,cor} = k_{cor,i} \cdot \gamma_{d,i} \quad i = \{1, \dots, n\}$$

The discrete corrected circulation values are inter- respectively extrapolated at five chordwise locations and form the basis for the determination of the Fourier coefficients a_i . Interpolation is not required for $n_i = 5$. Comparing the circulations obtained from the vortex-lattice computation, it will be observed that the symmetrical section NACA 0012 does not exhibit any dependence on the number of chordwise lattices in contrast to the cambered NACA 4412 section.

Tab. C1: Comparison of two-dimensional lift coefficients from VLM (*) and those obtained from hybrid model (†) with derived Fourier coefficients a_i and consideration of thickness effect. Results of Riegels' method obtained with geometrically determined mean line Fourier coefficients for reference.

NACA			4412			0012				
i_{adap}	ξ_{25}	ni	VLM adaptation			Riegels	VLM adaptation			Riegels
			5	50	250		5	50	250	
1	0.05	$\gamma_{d,i,cor}$	38.8	43.4	42.7		39.8	39.8	39.8	
2	0.25		22.6	23.8	23.9		15.8	15.8	15.8	
3	0.45		17.6	17.7	17.7		10.1	10.1	10.1	
4	0.65		12.9	13.2	13.2		6.7	6.7	6.7	
5	0.85		8.3	8.5	8.5		3.8	3.8	3.8	
$c_l(t/c = 0)$			1.459*	1.531*	1.537*	1.537	1.091*	1.091*	1.091*	1.091
$c_l(t/c = 0.12)$			1.540†	1.603†	1.612†	1.660	1.193†	1.174†	1.175†	1.210
$c_l(t/c = 0.12) / c_l(t/c = 0)$			1.056	1.047	1.049	1.080	1.094	1.077	1.077	1.109

The circulation correction works excellent for symmetrical airfoil sections while the correction is not as perfect for the cambered section as the dependency on the number of chordwise lattices attests.

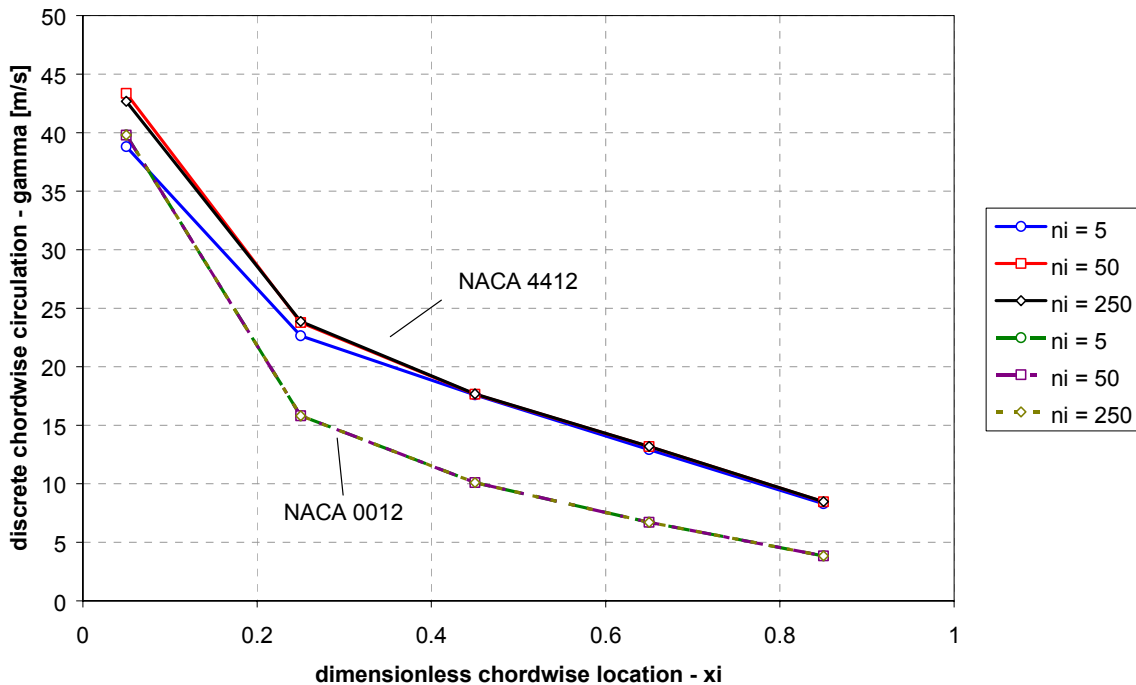


Fig. C4: Comparison of adapted chordwise circulations of NACA 4412 and NACA 0012 airfoil sections for three different lattice discretisations.

Lift coefficients derived from the adapted pressure distributions are without exception higher than the mean line values of the vortex-lattice method due to the thickness effect but they are always lower than what would be expected from the basic model of Riegels.

Overall, the quality of the approximation is just modest. However, the errors in the local pressure distributions do not give way to ambiguous results regarding the approximation of high lift effects. Furthermore, the magnitudes of errors vary continuously so that they don't suddenly increase in a stepwise manner at a certain parameter combination.

C.4 Comparison of Present Method with Experimental Pressure Distributions of a Wing-Flap Configuration

The chordwise pressure distributions of the two-element wing-flap configuration of reference [124] obtained for quasi-two-dimensional flow conditions are compared with the present model in Fig. C5.

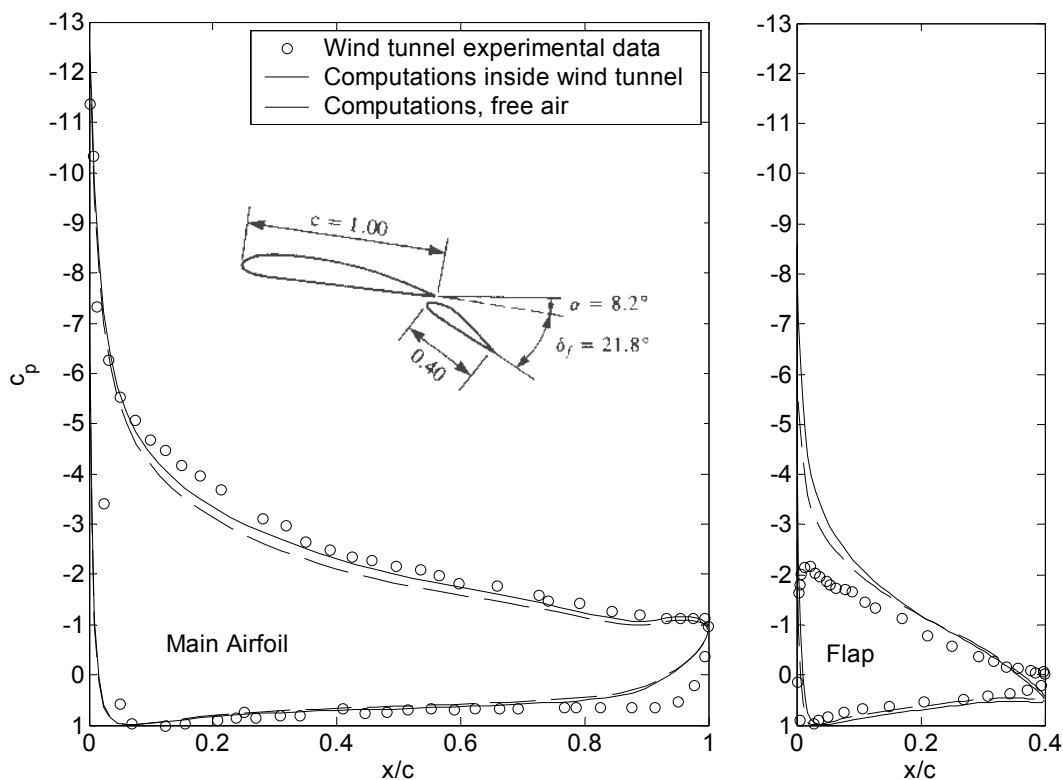


Fig. C5: Two-dimensional experimental and computed chordwise pressure distributions, main wing with NACA 4412 and flap with NACA 4415 airfoil section.

Lift increases in the presence of wind tunnel walls as a comparison of the corresponding curves with and without explicit considerations of walls proofs. Pressure characteristics,

however, are not perfectly resembled despite the wall corrections. One reason for the discrepancy at the suction side of the airfoil section could be the inability of the computational method to account for interference effects due to thickness. The wind tunnel model had a chord of 0.9 m, which is quite large for the wind tunnel test section height of only 2.13 m. Super velocities due to the reduction of the effective tunnel cross section could additionally contribute to lower pressures at the upper main airfoil contour. However, the current method is able to predict the reduced pressure at the trailing edge of the main airfoil section contributing to the ability of the section to sustain an experimental lift coefficient of 3.19. Adair and Horne [124] report that boundary layer separation occurred over the aft 7% of the flap chord. As a consequence, the suction peak reduces and the pressure recovery towards the trailing edge of the flap is less for the experiment compared to the computed result because separation was not considered. This also partly explains the lower load in the experiment compared to the numerical result. A similar difference between the measurements and numerical data obtained from a panel code is documented in reference [4]. The weaknesses of the current method become obvious especially at locations where the thickness of the airfoils plays a significant role as, for example, at the trailing edge of the main wing pressure side. The missing stagnation effect at the leading edge of the flap because of neglecting the thickness effect in the basic VLM solution has the consequence of a more gradual pressure recovery towards the trailing edge on the pressure side of the main element.

C.5 Pressure Distributions for Three-Dimensional Cases

So far only sectional characteristics have been considered. Turning attention towards three dimensional problems, some additional effects need to be considered. A swept back wing, either of infinite or finite span, has an attachment line but does not have a forward stagnation point. The pressure coefficient at the attachment line is less than one in incompressible flow because only the velocity component normal to the leading edge "stagnates" but the tangential flow component does not. The attachment line is the connection of the spanwise loci where the streamlines divide fluid that is going to pass on the upper and that what is going to pass on the lower side of the wing. Because three dimensional effects with regard to the pressure distribution are not automatically considered like in three dimensional panel codes, an explicit correction must be formulated. A straightforward correction is by means of simple sweep theory, which will be used here. According to this theory, only the flow component which is perpendicular to a constant chord (sweep-) line can be perturbed by the wing whereas the component parallel to the sweep line passes the surface unperturbed. Parallel and perpendicular flow components comprise the free stream and induced velocity components. They are computed for the mean line surface, more precisely for each lattice quarter chord point as illustrated by Fig. C6.

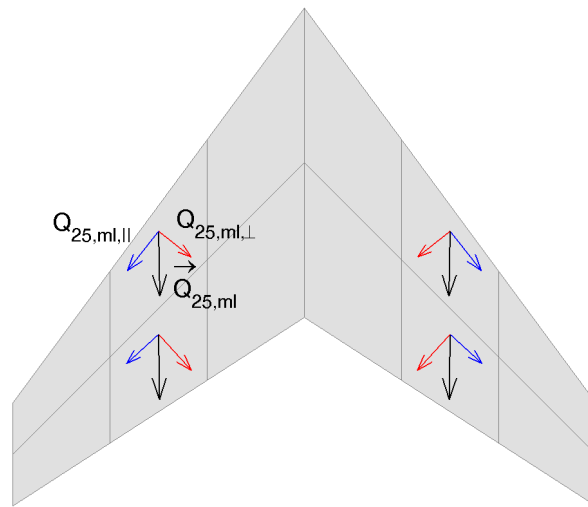


Fig. C6: Decomposition of mean line velocity vectors into components parallel and perpendicular to local quarter chord lines.

It is the linear nature of the Laplace equation that allows the superposition of its solutions, either velocity potentials or velocities. This principle is exploited in order to find the correct pressure distribution. The contour velocities of equation (C.2) are modified as described henceforth. The basic wing sections are placed so that the local chord lines are roughly parallel to the body x-axis. Nevertheless, according to simple sweep theory the section perpendicular to the sweep line(s) is the effective one. The relative thickness of the effective airfoil section increases since the effective chord is smaller than the geometrical chord length. Although not strictly exact but, nevertheless, an acceptable approximation is the correction

$$\left(\frac{t}{c}\right)_{\max,\perp} = \left(\frac{t}{c}\right)_{\max} / \cos \Lambda_{25}$$

based on the section quarter chord sweep angle. The velocity ratio of equation (C.2) is corrected in the following way

$$\left(\frac{Q_t}{Q_\infty}\right)_{3d} = \frac{\sqrt{\left[\left(\frac{Q_t}{Q_\infty}\right)_{2d} \cdot Q_{25,ml,\perp}\right]^2 + Q_{25,ml,\parallel}^2}}{Q_\infty}$$

and finally the pressure coefficient for incompressible three dimensional flow becomes

$$c_{p,3d} = 1 - \left(\frac{Q_t}{Q_\infty}\right)_{3d}^2$$

Appendix D: Effect of Gap on the Maximum Lift Capability of Wing-Canard Configurations - Comparison of Computational Results with Experimental Data

This section is dedicated to the validation of the maximum lift adaption method. Experiments on a generic wing-canard configuration are documented in reference [125]. A two-view sketch of the model is shown in Fig. 42 of the main part. Both, long and short coupled configurations had been tested. Variations of the vertical position of wing and canard showed a pronounced maximum lift gain at the canard for the configuration where the canard was positioned close to and above the wing. A maximum lift coefficient loss occurred for positions of the canard vertically below the wing.

Both surfaces, wing and canard, utilised the LS(1)-0413 (also known as GA(W)-2) airfoil section. The sections geometry was approximated by a modified NACA 4-digit airfoil section with a relative thickness of 13% where the position of maximum thickness was moved aft to $x/c = 0.38$. Camber was set to 2.2% with the maximum ordinate at 50% of the chord. A fair approximation was obtained, which was mainly limited by the restricted versatility of the simple NACA 4-digit mean lines shape.

The canard surface had an area one-half that of the main wing and was always set at 2° incidence with respect to the wing. The aspect ratio of both surfaces was 6. The chord of the rectangular main wing was 1ft (0.3048 m). The distance of the quarter chord location of the canard ahead of the main wing quarter chord line was 1.63 of the main wing chord for the close coupled configuration. Moving the main wing up and down altered the vertical arrangement. Three vertical configurations were tested: 1. canard high (0.5 of the main wing chord up), 2. co-linear, 3. canard low (0.5 of the main wing chord down). The Reynolds number based on the main wing chord was $1.4 \cdot 10^6$. The basic maximum lift coefficients were adapted to the experimental data for the isolated surfaces. The maximum lift coefficient was found to be 1.67 for the isolated main wing surface and 1.49 for the canard with respect to the individual chord lengths. It is worth mentioning that the lift coefficients discussed henceforth are always referred to the main wing surface area.

The influence of the wind tunnel walls of the 7- by 10-foot test section was always explicitly considered with a coarse paneling as illustrated in Fig. D1. The main effect of the walls is to increase the lift curve slopes slightly. The tunnel wall correction did not include blockage or volume displacement effects which, however, were expected to be small. This assumption is expected to hold at least as far as the wings do not experience significant flow separation at high angles of attack. Thickness would cause the wall pressure coefficients to be shifted to slightly lower values in the case of attached flow but nonetheless without any net effect on the lift curve slope. While tunnel

walls and section thickness increase lift curve slopes, viscous effects actually reduce them. For the latter reason, the sectional lift curve slopes were reduced by 18% for the canard and 8% for the main wing in order to better match the experimental ones.

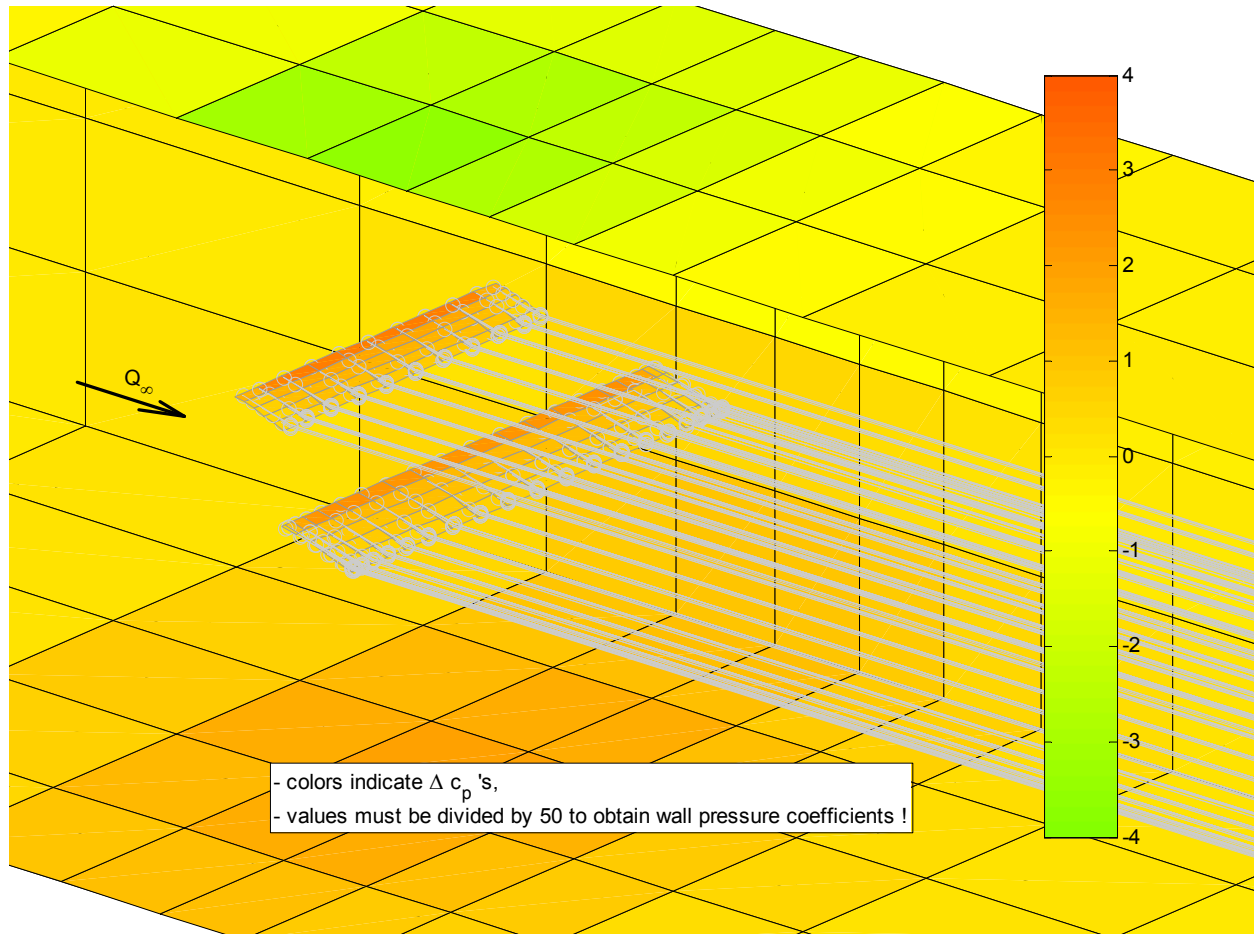


Fig. D1: Wing with close-coupled canard in the upper position situated in wind tunnel test section. Left side wall and one-half of top wall removed for clarity. Canard shown at maximum lift condition: $\alpha = 13.0^\circ$, $c_L = 1.85$. Bound and trailing vortices indicated by grey lines.

Feistel et al. [125] already encountered problems to match lift curves from vortex lattice computations with those obtained from the wind tunnel experiments. The numerical lift coefficients were too low for a given angle of attack with a constant offset. The poor camber line discretisation with only six chordwise panels was identified as a probable reason for the discrepancy. An incidence increment of 1.4° solved the problem. The incidences for the current computation were set to even higher values: 3.4° for the main wing and 4.7° for the canard.

Lift polars were computed with the cascade as well as the post-stall model switched on. The results for the canard high case are compared to the experimental data in Fig. D2.

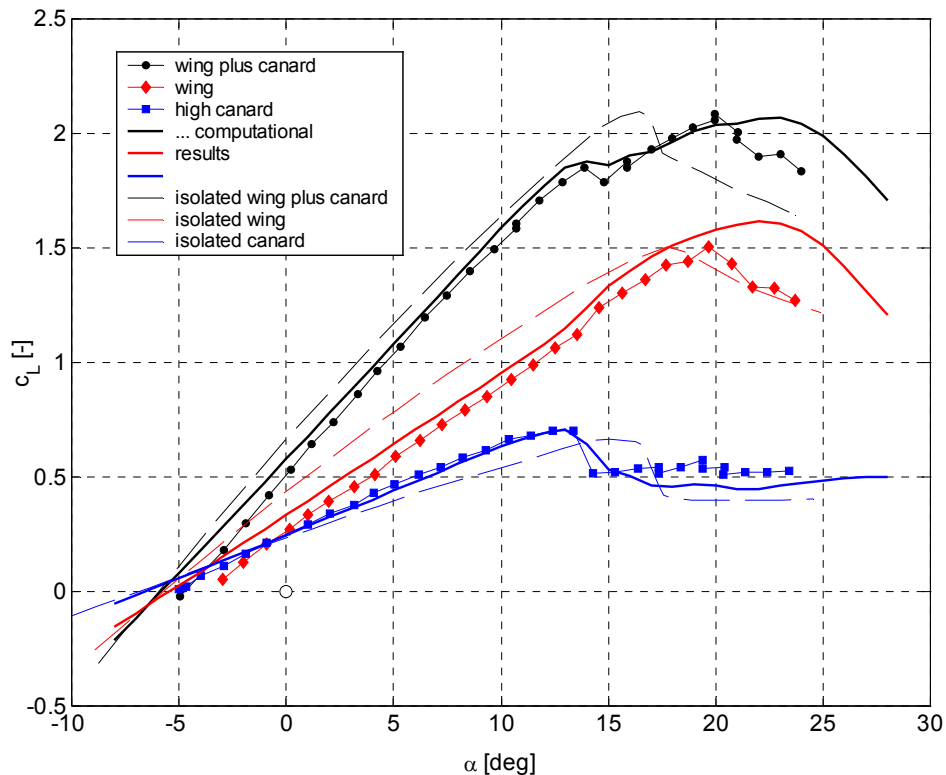


Fig. D2: Experimental results for a close coupled wing-canard configuration with the canard located in a higher position than the wing compared to computational results; dashed lines indicate experimental lift characteristics for isolated surfaces (wind tunnel walls included in computational model).

The lift curve slope and the lift coefficient at zero angle of attack of the main wing decreases compared to the isolated wing due to the downwash effect of the canard ahead. The upwash of the wing on the canard has the opposite effect.

The agreement of the computational lift curves with the experimental results is fair. After the canard came to pass the maximum lift condition with the subsequent drop of aerodynamic loading, the downwash that the canard induces on the main wing decreases. Hence, the effective angle of attack of the main wing increases and so does the lift. This effect is well represented by the current computational method.

Means for transition fixing were not applied to the wind tunnel model. While the shape of the lift curve of the canard resembles that of a leading edge stall, the main wing shape with its kink rather resembles that of a combined leading and trailing edge stall.

At an angle of attack of almost 20° , the main wing reaches its maximum lift coefficient which is virtually identical to that of the isolated wing. The maximum lift coefficient and the corresponding angle of attack predicted by the present computational method is too

high. Because of the lower than measured post-stall lift level of the canard, the all-up maximum lift coefficient is correct again.

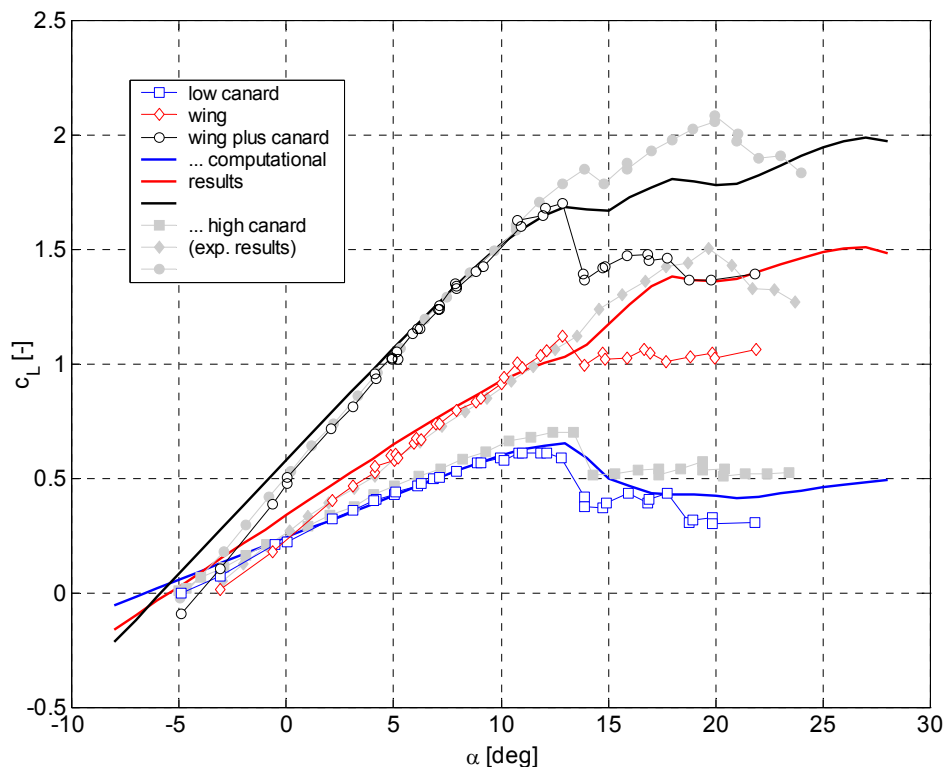


Fig. D3: Experimental results for a close coupled wing-canard configuration with the canard located in a lower position than the wing compared to computational results; experimental data for high canard configuration for reference (wind tunnel walls included in computational model).

The computational results for the low canard position are much less promising (Fig. D3). Again, the canard stalls first but at a lower maximum lift coefficient because of the adverse arrangement that fundamentally resembles a compressor cascade. The predicted maximum lift coefficient is obviously too high. A severe discrepancy is observable for the lift behaviour of the main wing because the lift coefficient is predicted to attain a maximum value of 1.51 at $\alpha = 27.0^\circ$ in contrast to a measured value of just 1.21 at $\alpha = 12.9^\circ$. The problem is that canard and wing become almost collinear with respect to the freestream direction at an angle of attack of about 12° such that the low momentum wake of the canard deteriorates the flow conditions on the main wing such that this surface experience a premature stall. Such convective processes cannot be simulated by the current method such that the computational result is erroneous.

However, the primary aim was to assess the flow conditions up to the point where flow separation significantly affects the configuration performance. The pivot point after

which the results of the current computational method should be assessed with greater care is the point where the first section of the whole configuration arrives at the maximum lift condition.

Fig. D4 summarises experimental and computational results for the canard alone, which stalled first in each case. It is obvious that the low canard with its imposed adverse pressure gradient experiences a decreased loadability compared to the isolated surface. In contrast, the lift capability of the configuration with the canard in a high position and an imposed favourable pressure gradient is increased. The numerical result correctly reproduces this trend although the magnitude of the effect is significantly underestimated for the configuration with the low canard.

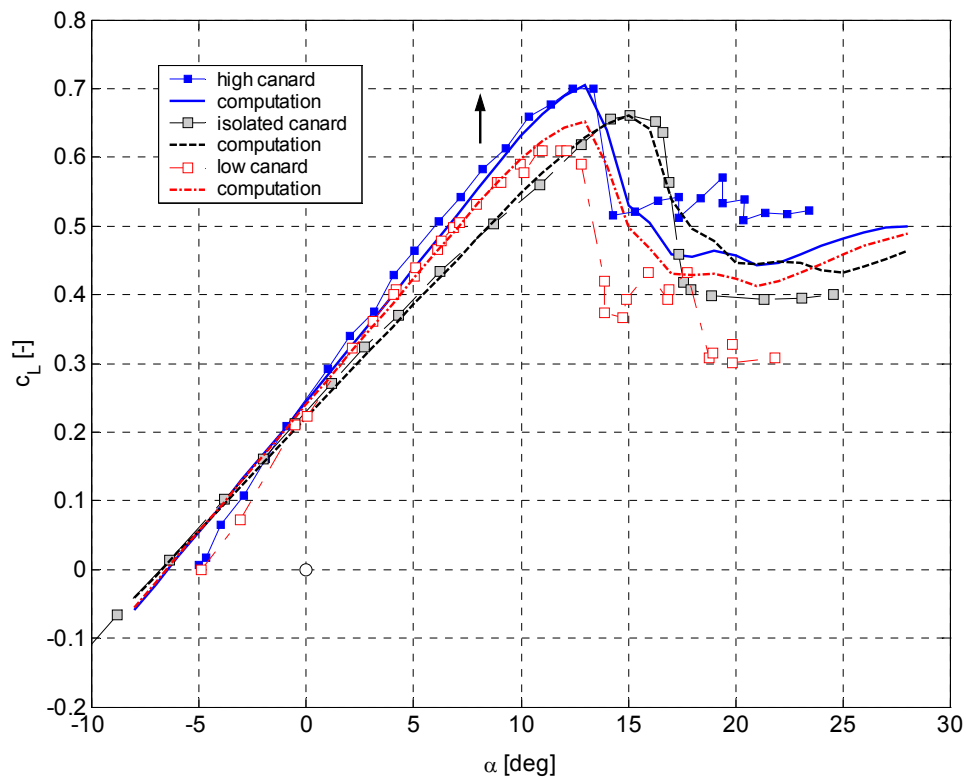


Fig. D4: Experimental and computational lift characteristics of isolated canard as compared to results for low and high canard locations for close coupled combination with wing (wind tunnel walls included in computational model).